A Saturation-Dependent Dissipation Source Function for Wind-Wave Mod elling Applications

by

José Henrique Gomes de Mattos Alves

A dissertation submitted for the
degree of Doctor of Philosophy
at

The University of New South Wales
Australia

December
2000

Table of Contents

Acknowledgements

Although a PhD project is in essence a solo journey travelled by its author, its path intersects several other roads. When I look back in time I see many of these benign crossroads in my path. When I decided to move forward into this project, my first step (and many of the steps that I took thereafter) was out of a crossroads where I stood with my parents, Carlos and Sylvia. Their unconditional support and encouragement were very important to keep my heart and mind in one piece all the way since then.

This work would not have been possibly made without the valuable and unique supervision provided by Professor Michael L. Banner. His intense dedication to Science and creativity in approaching apparently unsolvable problems in the field of wind-wave and air-sea interactions research, were an inspiration that I wish to carry on in my future research. I am also very grateful to Professor Ian R. Young for co-supervising my research activities. His clear-minded and objective attitude towards solving scientific problems, which often kept me from losing the track in difficult moments, are also qualities that I wish to carry on in the future.

Amongst many friends and colleagues that offered me support, Professor Eloi Melo played a crucial role in many decisive moments that led me into this project. I also thank Dr. Jose Lima not only for the good time we had together running along the cliffs between Coogee and Bondi to chill out from our PhD projects, but mostly for the support he and his family offered during my first year in Australia. I am immensely grateful to Maria Fenn for her kind, patient and always positive attitude that inspired me so much in more recent times.

The following colleagues enriched the contents of this thesis with valuable suggestions, discussions and technical support: Alex Babanin, Eva Bauer, Diana Greenslade, Peter Janssen, Vladimir Makin, Russel Morrison, Hendrik Tolman and Gerbrant van Vledder. I also acknowledge the support of staff and students from the School of Civil Engineering of the Australian Defence Force Academy, in Canberra, and from the School of Mathematics of The University of New South Wales, in Sydney.

I gratefully acknowledge the Manly Hydraulics Laboratory, Steedman Science and Engineering, the Australian National Antarctic Research Expeditions, Lawson and Treloar Ltd., the Australian Bureau of Meteorology, the Department of Transport of Western Australia and Woodside Petroleum S. A. for kindly providing the wind and wave data sets used in many parts of this thesis. I am also grateful for the computational support provided by the Supercomputer Facility of the Australian National University, the Centre for Environmental Modelling and Prediction of The University of New South Wales and the High Performance Computing and Communications Centre of the Australian Bureau of Meteorology.

Finally, I am very grateful to the Conselho Nacional de Desenvolvimento Cientifico e Tecnologico (CNPq), in Brazil, for providing a PhD scholarship that ultimately allowed the realisation of this project.

Abstract

This study proposes a new formulation of the spectral dissipation source term S_{ds} for wind-wave modelling applications. This new form of S_{ds} features a nonlinear dependence on the local wave spectrum, expressed in terms of the azimuthally integrated saturation parameter $B(k) = k^4 F(k)$. This saturation-dependent formulation for spectral dissipation rates is based on a new framework for the onset of deep-water wave breaking due to the nonlinear modulation of wave groups. The new form of S_{ds} is successfully validated through numerical experiments that include exact nonlinear computations of fetch-limited wind-wave evolution and hindcasts of two-dimensional wave fields made with an operational wind-wave model.

Simulations of the fetch-limited evolution of wind waves made with an exact nonlinear wave model demonstrate that the nonlinear dependence of this new dissipation source term on a local saturation spectrum generates predictions of integral spectral parameters that agree closely with observations. The inclusion of a weighting function proportional to the ratio $k/\overline{k}$ and a weak dependence on an integral steepness parameter increases the control of properties of the high wavenumber spectral tail.

Exact nonlinear computations with the new saturation-dependent form of S_{ds} also demonstrate that (i) computed spectral parameters generated under different wind intensities conform to similarity theory, (ii) dissipation rates of swell components agree closely with observations and (iii) this new form of S_{ds} may be successfully used in combination with several commonly-used forms of S_{in}. In comparison to other dissipation source terms used in state-of-the-art wind-wave models, the newly-proposed form of S_{ds} generates integral spectral parameters that agree more closely with observations, also providing more flexibility in controlling properties of the wave spectrum within the high wavenumber range.

Numerical experiments with an operational implementation of the WAM model are also made to assess the performance of the saturation-dependent form of S_{ds}. Results of these experiments show that changes in the specification of the dissipation source term have a profound impact on the quality of hindcasts. The newly-proposed saturation-dependent form S_{ds}^{bs} provides an overall improvement of hindcast of sea-states in terms of significant wave heights, although discrepancies in the hindcasts of peak periods indicate that further refinement is needed. Model runs using the new form of S_{ds} provided greatly improved hindcasts of significant wave heights during severe sea-state events. These improvements demonstrate the potential usefulness of the new saturation-dependent form of S_{ds} in operational wind-wave forecasting applications.

Chapter 1

Introduction

Since the pioneering wave prediction method of Sverdrup and Munk (1947), a large literature of theoretical and observational studies has provided a broad understanding of the processes involved in wind-wave generation. These studies have led to the development of highly sophisticated wave forecasting methods, based on numerical models that provide not only reliable predictions of average properties of the wave field, such as the significant wave height H_s and the peak period T_p, but also details of the full directional wave spectrum. Spectral wind-wave models have, therefore, become an important source of information for ocean engineering and scientific research.

Engineering and environmental applications of wind-wave models include navigation, operation and design of coastal and offshore structures, safety of nautical sports and leisure activities, planning and execution of rescue operations, coastal management and many others. On the scientific side, they assist in investigations of dynamical processes occurring at the air-sea interface, including gas transference, drift and diffusion of pollutants and other chemicals, heat exchange, distribution of surface stress and enhancement of ocean currents, to mention a few.

Most wind-wave models presently used in operational sea-state forecasting are based on the numerical solution of the radiative transfer equation. This general equation describes the evolution of the wave spectrum resulting from several driving mechanisms represented via parametric functions (source terms). In deep water, it is generally accepted that wind-wave growth is driven by the balance between three physical processes: wind forcing, resonant nonlinear wave-wave interactions and energy dissipation by breaking, turbulence and viscosity. Associated source terms are represented in shorthand notation by the symbols S_{in}, S_{nl} and S_{ds}, respectively.

Extensive analytical and observational efforts have led to the development of acceptable parameterisations of S_{in} based on a measure of the wind speed to wave phase speed ratio. Recent operational wind-wave models express this ratio in terms of the friction velocity u_*, as this parameter is supported by theoretical arguments (Miles, 1957; Janssen, 1991). Difficulties involved in the direct observation of u_* in the field have led to the development of alternative parametric S_{in} forms, based on the 10-m height wind speed U_{10} (Snyder et al., 1981) or the wind speed at a half-wavelength height $U_{\lambda/2}$ (Donelan and Pierson, 1987; Donelan, 1999). Other forms of S_{in} have been derived through direct modelling of the wave boundary layer (Gent and Taylor, 1976; Makin and Chalikov, 1979; Riley et al., 1982; Al Zanaidi and Hui, 1984; Chalikov and Makin, 1991; Chalikov and Belevich, 1993).

The source term S_{nl} represents weak resonant nonlinear wave-wave interactions that transfer energy within a wave field. This mechanism has been shown to have a dominant influence in the evolution of the wave spectrum (Hasselmann et al., 1973; Resio and Perrie, 1991; Young and Van Vledder, 1993). Wind-wave models use exact or approximate forms of S_{nl} based on the theory of nonlinear interactions in a homogeneous wave field developed independently by Hasselmann (1962) and Zakharov (1968).

Wave breaking (white-capping) and wave-turbulence interactions are believed to be the dominant dissipative processes within a wind-generated sea. Viscous dissipation is disregarded, as it is not a significant sink of energy at the scales of motion found in typical wave fields within ranges considered in wave models. Due to the extreme difficulties involved in observing wave breaking and wave-turbulence interactions in the field, dissipation is the least understood physical process associated with wave development.

Present state-of-the-art models used in operational applications compute spectral dissipation rates through parametric functions based on general theoretical arguments. Examples are the WAM (Hasselmann et al., 1988; Komen et al., 1994), SWAN (Booij et al., 1998) and WAVEWATCH (Tolman, 1997) models. Conceptual forms yet to be implemented into numerical models have also been proposed by Phillips (1984, 1985), Donelan and Pierson (1987) and Donelan (1996). A review of existing operational and conceptual S_{ds} forms may be found in Donelan and Yuan (1994).

The WAVEWATCH III model is implemented operationally at the Ocean Modelling Branch of the National Centres for Environmental Prediction NCEP/NOAA (USA). It uses a S_{ds} term divided in two explicit constituents: a low-frequency dissipation part strongly dependent on the peak frequency f_p that also includes rates of energy loss due to oceanic turbulence and a diagnostic high-frequency dissipation part. Model performance assessments and comparisons of the WAVEWATCH dissipation function with results obtained with the WAM Cycle 4 version are presented in Tolman and Chalikov (1996).

The WAM model has a dissipation function that was developed on the assumption that wave breaking is a weak-in-the-mean process, depending linearly on an integrated measure of the spectral steepness (Hasselmann, 1974). An extensive assessment of the dissipation function used in the WAM Cycle 3 release under idealised fetch-limited evolution scenarios is presented in Banner and Young (1994). New results from an assessment of the performance of the S_{ds} form used in the more recent WAM Cycle 4 release are presented in Chapter 5, along with a summary of the main findings of Banner and Young (1994).

Phillips (1984) suggests a dependence of spectral dissipation rates on a measure of spectral saturation defined by the nondimensional parameter $B(k,\theta) = k^4 F(k,\theta)$, where $F(k,\theta)$ is the directional wavenumber spectrum at a spectral component with wavenumber k and direction θ. The local value of $B(k,\theta)$ provides a measure of the degree of saturation when compared to a threshold value B_s, representing an upper limit for the growth of the energy density at that wavenumber. The saturation spectrum $B(k,\theta)$ may also be seen as a local measure of steepness in wavenumber space.

According to Phillips (1984, 1985), dissipation rates within the high wavenumber region of the wave spectrum (the equilibrium range) can be conveniently described by a nonlinear function of $B(k,\theta)$. Nonlinearity would be required to produce a source term with dissipation rates that are very small when $B < B_s$ and increase rapidly for values of B close to or higher than B_s. A similar conceptual model is presented in Donelan and Pierson (1987). These general ideas are the basis of the high-frequency form of S_{ds} used in the WAVEWATCH III model (Tolman and Chalikov, 1996). Field observations reported more recently by Donelan (1996) indicate that spectral dissipation rates at the spectral peak region may also be described by a nonlinear function of $B(k,\theta)$.

Banner et al. (2000) show that breaking probabilities of dominant wave groups are well described by a nonlinear function of a local steepness parameter. Their measurements also suggest that such a nonlinear dependence is potentially applicable to understanding the breaking probability of high frequency waves. These results are consistent with well-accepted concepts and numerical experiments that describe breaking of deep water waves as a process dominated by nonlinear wave group modulation. An analysis of this latter topic is provided in Banner and Tian (1998) and a brief overview is given in Chapter 3.

This study introduces a new dissipation source term S_{ds} for wind-wave modelling applications. This new S_{ds} formulation includes a parameterisation of dissipation rates associated with breaking due to nonlinear group modulation, based on the results of Banner and Tian (1998) and Banner et al. (2000). Breaking due to group modulation is represented by a term that depends nonlinearly on a local measure of wave steepness shown to be directly proportional to the saturation spectrum. Consequently, this new form of S_{ds} is also consistent with the concepts outlined in Phillips (1984, 1985) and Donelan (1996).

Although the newly-proposed form of S_{ds} incorporates state-of-the-art concepts concerning the physics of deep water wave breaking, the existing knowledge on the dynamical behaviour of wind-waves does not allow a direct quantification of parameters describing important aspects of the breaking process. These unknown features include the intensity of breaking events, the influence of long wave components on the evolution of shorter waves, the consequences for breaking of wave directionality and the interaction between waves and background upper-ocean turbulence levels, amongst others. Consequently, the development of a general parametric form of S_{ds} and the proper specification of its parameter values depend heavily on numerical modelling and tuning.

Following the approach outlined in Banner and Young (1994), the present study investigates a saturation-dependent form of S_{ds} using a wind-wave model with a full solution for the nonlinear term S_{nl}, and no constraints to the growth of high-frequency spectral components within a suitable range. This approach allows a more comprehensive analysis of model performance with a minimum of restrictions on spectral development. Operational models, on the other hand, use approximate S_{nl} parameterisations and a diagnostic (fixed) tail proportional to a power of the wavenumber k at frequencies above $6.25k_p$ $(2.5f_p)$, where k_p and f_p are the spectral peak wavenumber and frequency, respectively.

As the exact solution of S_{nl} requires a large amount of computational effort, a comprehensive performance analysis of the new S_{ds} formulation presented in Chapter 5 is limited to the evolution of wave spectra under idealised fetch-limited conditions. A review of relevant fetch-limited observations used for model validation are provided in Chapter 4. Preliminary tests of the new S_{ds} involving the operational implementation of the WAM model at the Bureau of Meteorology, Australia, are presented in Chapter 6. Although these test are made with a more limited range of model configurations, they allow an assessment of the impact of the new S_{ds} under more realistic forcing conditions. Chapter 6 also describes a comparison of model results to measurements from a network of surface buoys.

Recent efforts towards improving wind-wave model skill have been focused on two major areas: the improvement of forcing surface-wind fields and the assimilation of *in situ* and remote observations into operational wave forecasts. Results presented in Chapters 5 and 6 indicate that a better specification of source terms that represent the driving physical mechanisms of wind-wave evolution is still a source of improvements in model skill, with potential benefits for applications involving operational forecasting scenarios.

An overview of the structure of this thesis is as follows:

- **Chapter 2** presents a short historical overview of wind-wave modelling and an outline of its major concepts and governing equations;
- **Chapter 3** introduces the main concepts and a general form of a new saturation-dependent dissipation source term for wind-wave modelling applications;
- **Chapter 4** provides a review of the observational data base used for the purposes of model validation;
- **Chapter 5** includes the results of testing the dissipation source term under idealised fetch-limited conditions;
- **Chapter 6** presents a preliminary analysis of the impact of the new dissipation source term on the skill of an operational wind-wave model;
- **Chapter 7** contains the conclusions outlining the main results and foreshadowed future directions.

A bibliography section and lists of tables, figures and symbols are provided at the end of the thesis.

Chapter 2

Wind-Wave Dynamics and Modelling

The foundation of modern numerical wave prediction is arguably the sea state forecasting method reported by Sverdrup and Munk (1947). Their pioneering technique, however, was based on wave measurements with low resolution and inaccurate assessment of wind conditions, as demonstrated later in a series of landmark papers published by Pierson and Moskowitz (1964). Furthermore, that method was based on the description of a single monochromatic wave, not allowing even a rough description of wave generation processes and more complex situations, dependent on a full representation of the wave field.

The introduction by Pierson et al. (1955) of the concept of a wind-wave spectrum provided a more realistic and complete representation of the sea state, triggering a period of fast development in the field of wave prediction. A great leap forward was the formulation of a spectral transport equation by Gelci et al. (1957), allowing the evolution of wave spectra to be described mathematically as a result of a net source function, representing simultaneously wind input and energy dissipation.

More realistic descriptions of the wind input source function became available in the ensuing years. Important concepts were consolidated by Phillips (1957) and Miles (1957) through mathematical theories explaining the process of wave generation by the wind. The theoretical breakthroughs of the time did not provide means of describing the spectral rates of energy dissipation. This was due to both the lack of sound mathematical theories and technical difficulties involved in observing wave breaking in deep water. The issue of describing properly the spectral dissipation rates of wind-waves remains a scientific challenge to the present day. As documented in Phillips (1981), Phillips (1960) and Hasselmann (1962) identified and described mathematically a third process later found to be crucial for predicting the evolution of wind wave spectra: the weak nonlinear interactions between waves due to a resonant mechanism.

These early ideas provided the basic framework of modern wind-wave modelling and operational forecasting. Its general assumption is that the evolution of wind-wave spectra results from the balance between three forcing functions accounting for the wind input, the nonlinear wave-wave interactions and the dissipation of energy mainly through white capping and bottom friction. These forcing mechanisms are usually included in mathematical models that may also describe modifications of the wave field caused by wave-current interactions and depth-induced transformations.

2.1 Wind-wave model classification

2.1.1 First- and second-generation models

Early wave prediction models were based typically on a wind forcing input term representing Phillips' and/or Miles' mechanisms. Non-linear wave-wave interactions were treated as a secondary effect that could be neglected in a first approximation. When present, these nonlinear interactions were parameterized through simple expressions based on integral properties of the spectrum. The dissipation function was treated indirectly as a limiter that prevented the wind-sea regions of the spectrum (high wavenumbers) from exceeding an arbitrarily prescribed saturation level.

These early wind-wave models were later called first-generation (1G) models (SWAMP, 1985). Despite their successful application for many years, it was uncertain whether they represented correctly even some known aspects of the physics of wave generation. For instance, to produce predictions that matched observations, the wind input source terms of 1G models had to be increased significantly above observed values or theoretical estimates of energy transfer rates from wind to waves.

Unknown aspects of the physics of wave generation were revealed when more accurate measurements of wind wave growth under fetch-limited conditions became available. A landmark contribution in that direction was the Joint North Sea Waves Project (JONSWAP), described in Hasselmann et al. (1973). The JONSWAP observations demonstrated the importance of nonlinear wave-wave interactions to the growth of low frequency spectral components, also revealing other important aspects of the dynamics of wave spectra. These findings provided the framework for the advent of more efficient source term parameterisations, included in second-generation (2G) wind-wave models.

Source functions employed in 1G models predicted the evolution of spectral components separately, as the source terms did not include coupling across spectral components. The introduction in 2G models of a source term that explicitly accounted for the nonlinear wave-wave interaction required coupling between individual components. Due to these differences, 1G models are also know as decoupled discrete models, while 2G models are called, alternatively, coupled models.

The nonlinear wave-wave coupling in second-generation models is usually addressed by a parametric function of a few spectral parameters. Depending on the frequency ranges covered by the parameterisation, second generation models can be further sub-classified as coupled hybrid and coupled discrete models. A complete overview of classification criteria and particular characteristics of 1G and 2G models is presented in SWAMP (1985).

Dissipation is not explicitly accounted for in the majority of reported first- and second-generation models. In some cases it is included as an arbitrarily imposed saturation level that limits the growth of individual components in the high frequency range. An explicit dissipation source term is rarely used in 1G and 2G models. Even then its purpose is to allow model tuning, having no connection with the physical properties of dissipative processes.

SWAMP (1985) reports the results of extensive numerical experiments simulating idealised and realistic wind wave evolution scenarios using several 1G and 2G models. The inter-comparison reveals that:

1 Models from both classes yield significantly different relations between space and time variables and spectral parameters in the development of a wind sea, as a result of their different parameterisations of source terms and of the wave spectrum;

2 Models from both classes suffer from limitations of the parameterisation of wave-wave nonlinear interactions. Their performance is limited to idealised cases for which the parametric forms were designed. Under complex situations the models fail to reproduce observations;

3 Parameterisations of the directional spreading of energy in models from both classes can be a source of significant errors in cases involving turning or inhomogeneous wind fields.

idealisedAccording to SWAMP (1985), these difficulties could only be overcome with the development of third-generation (3G) models, with discretised parameterisations of the nonlinear interaction term that had the same number of degrees of freedom as the discrete representation of the spectrum. Computations of the spectral evolution would then be performed through explicit integration of a dynamical equation without prior restrictions on the spectral shape.

2.1.2 Third-generation models

A first attempt to produce a third-generation (3G) model was based on a computational method introduced by Hasselmann and Hasselmann (1981). The method solved the exact six-dimensional integral expression proposed by Hasselmann (1962), describing explicitly the mean exchange of energy between wave components within a spectrum. The resulting numerical model included a representation of the dissipation source term suggested by Hasselmann (1974), incorporating general assumptions about the physics of energy dissipation through whitecap breaking. The resulting model was called EXACT-NL.

An alternative technique to compute explicitly nonlinear energy transfers was introduced by Webb (1978) and Masuda (1981). The method, which produced a smooth and stable computation of the nonlinear source function S_{nl}, was included in a 3G model developed by Tracy and Resio (1982). Their model used a polar wavenumber-direction grid with radial wavenumber coordinates following a geometric progression, which, they claimed, produced slight improvements over the computational efficiency of EXACT-NL. A 3G model based on Tracy and Resio (1982) was used by Banner and Young (1994) in a comprehensive investigation of source terms employed in state-of-the-art spectral wind-wave models. The method proposed by Webb (1978) and Masuda (1981) was also used in a 3G model described in Polnikov (1994).

The solution of S_{nl} employed in the EXACT-NL model and in codes based on the Webb (1978) and Masuda (1981) approach still demanded large computational effort, even when simple cases were considered. Nevertheless, its success in predicting overall characteristics of the wave spectrum under idealised conditions motivated the development of more efficient S_{nl} algorithms. The objective was to produce a computationally-efficient 3G model that would allow operational predictions of the sea state on basin and global scales, as these still relied solely on 1G and 2G models.

The Wave Modelling (WAM) group (Hasselmann et al., 1988) was formed with the aim of formulating a useful model out of the achievements attained with EXACT-NL (Komen et al., 1994). This group united leading scientists in the field to develop jointly a 3G model that could be implemented operationally on global and regional scales. Hasselmann et al. (1988) and Komen et al. (1994) report the progress made and the achievements of the joint effort that resulted in the WAM model. Its subsequent success may be greatly attributed to the development of the discrete interaction approximation (DIA) by Hasselmann and Hasselmann (1985), an algorithm that provided an approximate solution of S_{nl} with very low computational cost.

Despite the state-of-the-art status of the WAM model, Banner and Young (1994) have shown that there are still critical shortcomings in the formulation of its source functions, particularly regarding the dissipation term S_{ds}. Bender (1996) and Tolman (1992) criticise the numerics used in the standard WAM version, pointing out limitations and suggesting modifications to the original advection scheme. Despite known problems and the need for improvements, over 50 research groups and forecasting centres worldwide have been running the WAM model since its first release in 1988.

Since the advent of the DIA algorithm, other 3G models have been developed independently from the WAM group. Ris (1997) and Booij et al. (1999) report on the implementation of a 3G model for application in shallow waters and enclosed basins. Tolman and Chalikov (1996) present a wave model with new formulations for the wind input and the dissipation source terms, as well as innovations to the numerical propagation scheme used in WAM. Lin and Huang (1996*a*,*b*) describe a wave model to study the air-sea interaction processes in the coastal region. An in-depth discussion of several aspects of the physics and numerics of state-of-the-art 3G models is found in Lin (1998) and Tolman et al. (1998).

2.2 Wave Dynamics and the Wave Spectrum

The displacement of the air-sea interface due to the presence of wind waves is described mathematically by the Navier-Stokes equation for a two-layer fluid. Recent studies have shown that the numerical solution of this equation is a useful tool in modelling small scale processes associated with wind-waves. These include surf zone dynamics (Bradford, 2000), interaction with porous structures (Liu et al., 1999), breaking-induced air entrainment (Mutsuda and Yasuda, 2000) and runup on sloping beaches (Lin et al., 1999), amongst others.

The direct solution of the Navier-Stokes equation, however, is not practical in cases involving the study of wind-wave generation, as the sea surface in this case is displaced by waves of different shapes and scales. A first simplification of the Navier-

Stokes equation is made by reducing the problem to a description of a one-layer fluid motion, as the density of air (typically 1.2 kg m^{-3}) is much smaller than the density of water (typically 1025 kg m^{-3}). Further simplifications are made by assuming that forcing, dissipation and nonlinear processes involved in the evolution of the wave field are higher-order effects. These are then included as corrections to the approximate solution through source functions.

The remaining problem regards the almost chaotic nature of typical wind-wave fields. This is addressed by introducing the concept that the sea surface elevation η is determined by the sum of a large number of regular wave components with frequencies f, wavelengths λ, directions θ and amplitudes a. A further assumption, proven to be acceptable in practical applications, is that individual waves are plane, sinusoidal and have a small amplitude-to-wavelength ratio. Consequently, their dynamical behaviour is described by two-dimensional, linearised equations applied independently to each wave component. A detailed mathematical treatment of this problem is provided by Dean and Dalrymple (1990), Tucker (1991) and Komen et al. (1994). A brief account based on these references is provided below.

The governing equation of the motion of independent wave components becomes the two-dimensional linearised Euler equation for a one-layer fluid. Normal modes of the linearised Euler equation are obtained by solving a boundary value problem with known periodic and free-surface boundary conditions. The solution for the free-surface displacement associated with an arbitrary wave-field component with angular frequency $\omega = 2\pi f$ and wavenumber $\mathbf{k} = 2\pi/\lambda$ becomes

$$\eta(\mathbf{k}, \omega; \mathbf{x}, t) = a \exp\left\{i\left(\mathbf{k} \cdot \mathbf{x} - \omega t\right)\right\}. \tag{2.1}$$

where $\mathbf{x}$ is the position vector and t is time.

Irrotationality of linear, periodic and barotropic modes associated with (2.1) are then described by a velocity potential (ϕ) given by

$$\phi(\mathbf{x}, t) = -i\omega a \frac{\cosh k(z+h)}{k \sinh kh} \exp i(\mathbf{k} \cdot \mathbf{x} - \omega t). \tag{2.2}$$

The resulting waves are dispersive: wave components with different frequencies propagate with different velocities. Furthermore, wavenumbers are related to frequencies by a dispersion relationship which, in water of "infinite" depth, becomes

$$\omega^2 = gk. \tag{2.3}$$

In finite-depth water, equation (2.3) becomes a nonlinear function of wavenumber and depth. The present study, however, will only consider waves propagating in "infinite" depth, as it is concerned solely with the evolution of deep-water waves.

A general expression for the total free-surface displacement η is obtained by superposing the solution (2.1) of the entire ensemble of linearised wave components, resulting in

$$\eta(\mathbf{x}, t) = \int_{-\infty}^{+\infty} \hat{\eta}(\mathbf{k}) \exp\{i(\mathbf{k} \cdot \mathbf{x} - \omega t)\} d\mathbf{k}. \tag{2.4}$$

Equation (2.4) may be rewritten in terms of a discrete Fourier series, convenient for the purposes of numerical modelling. The continuous integral form is, in this case, replaced by a discrete sum of components with central wavenumbers k_c that are representative of contributions to η from wavenumbers within the bandwidth $k_c \pm \Delta k/2$. Discrete amplitudes are then defined as

$$a_{\mathbf{k}_c} = \int_{\mathbf{k}_c - \frac{1}{2}\Delta\mathbf{k}}^{\mathbf{k}_c + \frac{1}{2}\Delta\mathbf{k}} \hat{\eta}(\mathbf{k}) d\mathbf{k}. \tag{2.5}$$

The corresponding mean energy of a discrete wave component is given by

$$F_{\mathbf{k}_c} = \frac{1}{2}|a_{\mathbf{k}_c}|^2. \tag{2.6}$$

Conversely, the continuous energy density may finally be defined in terms of the mean energy of discrete components as

$$F(\mathbf{k}) = \frac{F_{\mathbf{k}}}{\Delta\mathbf{k}}. \tag{2.7}$$

The quantity $F(\mathbf{k})$ is known as the wavenumber spectrum. $F(\mathbf{k})d\mathbf{k}$ represents the average amount of energy per unit area carried by an ensemble of wave or spectral components within a bandwidth $d\mathbf{k}$ centred at the wavenumber k, in a large area or basin and within a given time lag. An illustration of a typical wave spectrum is shown in Figure 2.1.

The wave spectrum may also be formally derived through assumptions about the statistics of the sea-surface displacement η. As the probability distribution of η is nearly Gaussian (Komen et al., 1994, section I.2), an approximate description of its statistical properties is given by the covariance function

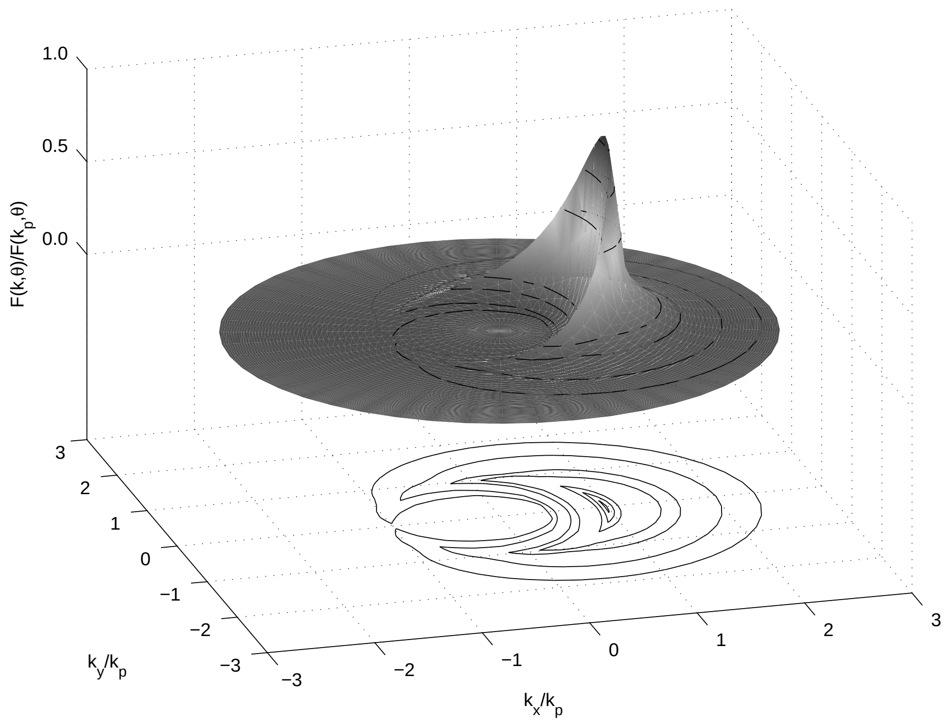

Figure 2.1: *Typical directional wavenumber spectrum $F(k, \theta)$. Energy densities are normalised by the spectral maximum $F(k_p, \theta)$ in the vertical axis. Wavenumbers are normalised by the spectral peak wavenumber k_p in the horizontal axes.*

$$\mathcal{F} =< \eta(\mathbf{x}, t_0)\eta(\mathbf{x} + \mathbf{r}, t_0 + t) >, \tag{2.8}$$

where $\mathbf{x}$ is the position vector, $\mathbf{r}$ is a spatial separation vector, t_0 is the time of the first observation of η, t is a time lag and the brackets denote the ensemble average.

Following Phillips (1966), the wave spectrum for a homogeneous, stationary wave field is defined as a function of $\mathcal{F}$ given by

$$\Phi(\mathbf{k}, \omega) = (2\pi)^{-3} \int\int_{-\infty}^{+\infty} \mathcal{F} \times \exp\left[-i\left(\mathbf{k} \cdot \mathbf{r} - \omega t\right)\right] d\mathbf{r}dt, \tag{2.9}$$

where $\mathbf{k}$ is the wavenumber vector and ω is the angular frequency. The term $\Phi(\mathbf{k},\omega)$ has the property that $\int\int \Phi(\mathbf{k},\omega)d\mathbf{k}d\omega = \overline{\zeta}^2$, the mean squared wave height, representing the mean distribution of wave energy with wavenumber module $k = |\mathbf{k}|$ and frequency ω propagating in the direction θ, as discussed by Banner (1990). Reduced forms of (2.9), such as equation (2.7), are used in a wide range of applications. Some important reduced forms are

(i) the directional wavenumber spectrum (2.7)

$$F(k,\theta) = 2\int_0^{\infty} \Phi(\mathbf{k},\omega)d\omega, \tag{2.10}$$

(ii) the omnidirectional wavenumber spectrum

$$< F > (k) = \int_{-\pi}^{+\pi} F(k,\theta)kd\theta, \tag{2.11}$$

(iii) the azimuthally integrated wavenumber spectrum

$$F(k) = \int_{-\pi}^{+\pi} F(k,\theta)d\theta, \tag{2.12}$$

(iv) the directional frequency spectrum

$$\varphi(\omega,\theta) = 2\int_0^{\infty} \Phi(\mathbf{k},\omega)kd\mathbf{k}, \tag{2.13}$$

(v) the (one-dimensional) frequency spectrum

$$\overline{\varphi}(\omega) = \int_{-\pi}^{+\pi} \phi(\omega,\theta)d\theta. \tag{2.14}$$

2.3 Governing Equation of Spectral Evolution

A mathematical description of how the wave field changes in space and time in response to interactions with the environment (perturbations) is essential to sea-state prediction. Following Komen et al. (1994, Section I.2.7), it is possible to distinguish two classes of perturbation leading to changes in wave properties. The first is related to the presence of spatial gradients of environmental parameters that modify the motion of waves. These gradients are relevant when waves propagate on strong currents or in a shallow sea of variable depth. Most perturbations of this class become important in problems concerning wave evolution in coastal waters. A formal treatment of the problem is found in Watson and West (1975), Jonsson (1990) and Mei (1983), to mention a few.

The second class of perturbation leads to variations that are slow compared to the characteristic time scale of the components of a wave field. These will affect waves propagating at all depths, given the propagation times are long enough so they can become effective. Slow time scale perturbations are associated with the main driving mechanisms of deep water waves (wind forcing, dissipation and nonlinear wave-wave interactions), the main topic of this thesis. Therefore, they are considered in detail below.

Slow time scale perturbations are represented by a sum of forcing functions (source terms) applied to individual spectral components $F(k,\theta)$. Their contribution to the evolution of deep water wave spectra is described by the energy balance equation

$$\left\{\frac{\partial}{\partial t} + \mathbf{c}_g \cdot \frac{\partial}{\partial \mathbf{x}}\right\} F(k,\theta) = \sum_{\mathrm{all}\, i} S_i, \tag{2.15}$$

where c_g is the group velocity of a spectral component with wavenumber k and direction θ, $F(k, \theta)$ is the two-dimensional wavenumber-direction spectrum, and the source terms S_i are parametric functions describing several driving mechanisms. When currents and depth-related processes are significant, the energy density of spectral components is no longer conserved. In these cases, a more general governing equation describing the evolution of the wave action density $N = F(k, \theta)/\omega$, should be used (Komen et al., 1994, Section I.2.10).

2.3.1 Source functions

Source terms represent the main physical mechanisms that transform the wave spectrum in space and time. Experimental evidence supports the idea that, in deep water, these processes are well represented by a system of three functions S_{in}, S_{nl} and S_{ds}, accounting respectively for wind input, resonant nonlinear wave-wave interaction and whitecap dissipation. The right hand side of equation (2.15) is, therefore, replaced with

$$\sum_{\text{all}i} S_i = S_{in} + S_{nl} + S_{ds}. \tag{2.16}$$

These three source terms do not exhaust all possible mechanisms that may affect deep-water wind-waves. They do, however, appear to account for the major fluxes of energy to and within the wave spectrum. Consequently, it is generally assumed that they represent the dominant driving mechanisms in the evolution of deep water waves. In shallow waters, depth induced effects and wave-current interactions become significant, requiring the inclusion of additional terms that will not be considered in this study.

2.3.1.1 Wind input

Energy fluxes from the atmosphere into the sea surface are the result of shear and normal wind stresses at the air-sea interface. The transfer of energy into the wave field is dominated by normal stresses exerted on the sea surface. Ripples develop rapidly over an initially undisturbed sea surface as they interact with the turbulent structure of the wind field. The growth of waves at this stage is a linear function of time described in Phillips (1966). This mechanism becomes ineffective as the ripples grow into steep wavelets that distort the structure of the atmospheric boundary layer. The growth then becomes exponential with time.

An initial theory describing the exponential growth of wind-waves was proposed by Miles (1957) and confirmed later through several field experiments. Miles' approach, further improved by Fabrikant (1976) and Janssen (1989, 1991), became known as the quasilinear theory of wind wave generation. Reviews of this topic are given by Phillips (1966), Komen et al. (1994) and Young (1999).

Although the spectral growth rates due to wind forcing may be represented by a sum of linear (Phillips, 1966) and exponential (Miles, 1957) growth mechanisms, the majority of wind-wave models used in operational applications neglect the linear term. An exception is the SWAN model (Booij et al., 1998, 1999), which employs a parameterisation of the linear growth mechanism reported by Cavaleri and Rizzoli (1981) and modified by Tolman and Chalikov (1996). The linear growth mechanism due to (Phillips, 1966) is neglected in this thesis.

A general form of S_{in} based on the critical-layer theory of Miles (1957) is given by

$$S_{in}(k,\theta) = \frac{\rho_{air}}{\rho_{sea}} \beta \omega \mathcal{G}\left(U_r, c\right) F(k,\theta), \tag{2.17}$$

where ρ stands for the densities of air and sea, β is a growth rate parameter and $\mathcal{G}(U_r, c)$ is a function of the wave age, defined as the ratio between a reference wind speed U_r and the phase speed c of a spectral component with wavenumber k and direction θ.

Snyder and Cox (1966) proposed the first empirical wind input function based on direct observations of wind-wave growth rates. Their S_{in} term was also supported by field measurements reported by Barnett and Wilkerson (1967). In both cases, however, spectral growth was assumed to depend on wind input alone. The validity of this approach was challenged when results from the JONSWAP experiment (Hasselmann et al., 1973) demonstrated the importance of nonlinear wave-wave spectral interactions to wind-wave growth.

Attempts to observe wave growth in isolation from other spectral evolution mechanisms were reported by Dobson (1971) and Snyder (1974). The conflicts in results from these two studies underpinned the staging of a combined experiment conducted by Snyder et al. (1981) in the Bight of Abaco, Bahamas. This successful experiment reconciled the inconsistencies in the previous studies, indicating that the form of the input term was proportional to a linear function of the ratio between the 5m-height wind speed U_5 and the wave phase speed c, given by

$$S_{in}(k,\theta) = \frac{\rho_{air}}{\rho_{sea}} \beta \omega \left(\frac{U_5}{c} \cos\theta - 1 \right) F(k,\theta), \tag{2.18}$$

with observed values of β varying between 0.2 and 0.3. In wind-wave modelling applications, U_5 is usually replaced by U_{10}, which requires a small adjustment to the parameter β.

Despite the limited range of observed inverse wave ages $[1 < U_{10}/c < 3]$ during the Bight of Abaco experiment, the input function (2.18) was successfully employed in the first operational versions of the WAM model up to Cycle 3 (Komen et al., 1994). As this form of S_{in} appears several times in the following Chapter, it will be represented by the symbol S_{in}^S. The form (2.18) received further support from experimental results reported in Hasselmann and Bösenberg (1991).

Field measurements reported by Hsiao and Shemdim (1983) and Donelan and Pierson (1987) expanded the observations of growth rates to a wider range of wave ages U_{10}/c. Their results were supportive of a form of S_{in} proportional to the square of the wave age, as proposed earlier by Plant (1982). The quadratic dependence was particularly evident in spectral components with phase speed c much less than U_{10}, corresponding to strongly-forced, high-wavenumber waves.

As shown in Young (1999), field observations indicate that equation (2.18) is only a good approximation to the growth rates of spectral components around the spectral peak. Its extrapolation to higher frequencies leads to an underestimation of their growth rates, as demonstrated later by Janssen (1989, 1991). A parametric form of S_{in} that addressed the need of higher energy input rates within the higher wavenumber range was provided by Yan (1987)

$$S_{in}(k,\theta) = \left\{ \left[0.04 \left(\frac{u_*}{c} \right)^2 + 0.00544 \frac{u_*}{c} + 0.000055 \right] \cos\theta - 0.00031 \right\} \omega F(k,\theta), \tag{2.19}$$

where the friction velocity u_* is used rather than U_{10} in the definition of the inverse wave age parameter.

Equation (2.19) is included in several versions of the WAM and SWAN models. It was also used by Banner and Young (1994) in their comprehensive investigation of the performance of spectral dissipation source terms. For weakly-forced spectral components, expression (2.19) reduces to the Snyder et al. (1981) form (2.18). At higher wavenumbers it provides growth rates that are proportional to the square of u_*/c. The symbol S_{in}^{Y} will be used throughout this thesis to represent this form of S_{in}.

Applications of (2.19) in wind-wave modelling usually adopt a wind-speed dependent (sea-state independent) drag coefficient formulation to convert given U_{10} fields into corresponding estimates of u_*. In our validation experiments, model results from runs that use (2.19) are compared to evolution curves given by equations (4.13) and (4.14) of Chapter 4. Results from Banner and Young (1994) indicate that the impact of using (2.19) with a sea-state dependent u_* is negligible. Alternatively, this study uses a modified version of (2.19), derived to accommodate direct U_{10} forcing by replacing u_* with $U_{10}/26$ [for $U_{10} = 10$m/s this is equivalent to deriving u_* using the drag coefficient due to Wu (1982)]. Results from these alternative model runs are, therefore, compared to equations (4.10) and (4.11).

The importance of including the influence of the sea-state in estimates of the friction velocity, particularly at early wave evolution stages, was demonstrated by Janssen (1989, 1991). His arguments were supported by field observations reported in Maat et al. (1991). An approach to formulating S_{in} that addresses this sea-state dependence of u_* is provided by the quasilinear theory of wind-wave generation (Fabrikant, 1976; Janssen, 1989, 1991). In this study, a quasilinear of S_{in} is used for the validation of alternative forms of S_{ds}. The chosen quasilinear form of S_{in}, which is also used in the latest WAM Cycle 4 model release, was proposed by Janssen (1991), as follows:

$$S_{in} = \frac{\rho_{air}}{\rho_{water}} \beta(\Upsilon, z_0) \Upsilon^2 \omega F(k, \theta), \tag{2.20}$$

where Υ is a function of wave age

$$\Upsilon = \left(\frac{u_*}{c} + z_\alpha \right) \cos\theta, \tag{2.21}$$

with $z_\alpha = 0.011$. The growth rate coefficient (Miles' parameter) β in (2.20) is given by

$$\beta = \frac{1.2}{\kappa} \mu \ln^4 \mu, \tag{2.22}$$

where $\kappa = 0.4$ is the von-Karman constant and μ is a function of the wave phase speed c, the roughness length z_0 and the wave age parameter Υ

$$\mu = \frac{g z_0}{c^2} \exp \frac{\kappa}{\Upsilon}, \tag{2.23}$$

with roughness length determined from the Charnock relation $z_0 = 0.009 u_*^2/g$.

One important characteristic of the quasilinear form (2.20) is that the growth parameter β, the wave age Υ and the roughness length z_0 are all defined in terms of a total sea-surface stress $\tau = u_*^2$ that has a strong dependence on the wave-induced stress τ_w. As this parameter depends on the high wavenumber spectral energy densities, the wind forcing levels S_{in} have to be determined iteratively through a coupling mechanism that successively adjusts u_* and the wave spectrum itself, until the solution converges. In the remainder of this thesis, this form of S_{in} will be represented by the symbol S_{in}^J.

Non-dimensional growth rates $\gamma/f = (\rho_{air}/\rho_{sea})\beta\omega\mathcal{G}(U_r, c)/f$ computed from the form S_{in}^S, S_{in}^Y and S_{in}^J are compared to observations in Figure 2.2. All source functions were computed based on a JONSWAP spectrum with $f_p = 0.25$Hz, $U_{10} =$ 10m/s and spectral parameters given by Lewis and Allos (1990). The form S_{in}^J was determined approximately using a u_* derived through a sea-state dependent parameterisation of the roughness length z_0 proposed by Donelan et al. (1993).

Both forms S_{in}^Y and S_{in}^J agree well with observations in all ranges of the wave age parameter u_*/c. The form S_{in}^S agrees well with values of γ/f up to $u_*/c = 0.2$, corresponding to waves travelling with phase speed of the same order of magnitude as the 10m-height wind speed U_{10}. At higher wavenumbers (i.e., $u_*/c > 0.2$), it underestimates the growth rates considerably. Although all forms of S_{in} agree well with data within the range $0.05 < u_*/c < 0.2$, S_{in}^J predicts growth rates that are lower than those of S_{in}^Y and S_{in}^S.

The form of S_{in} due to Snyder et al. (1981) is still regarded as a robust parameterisation of S_{in} that is widely used in research and operational forecasting, despite

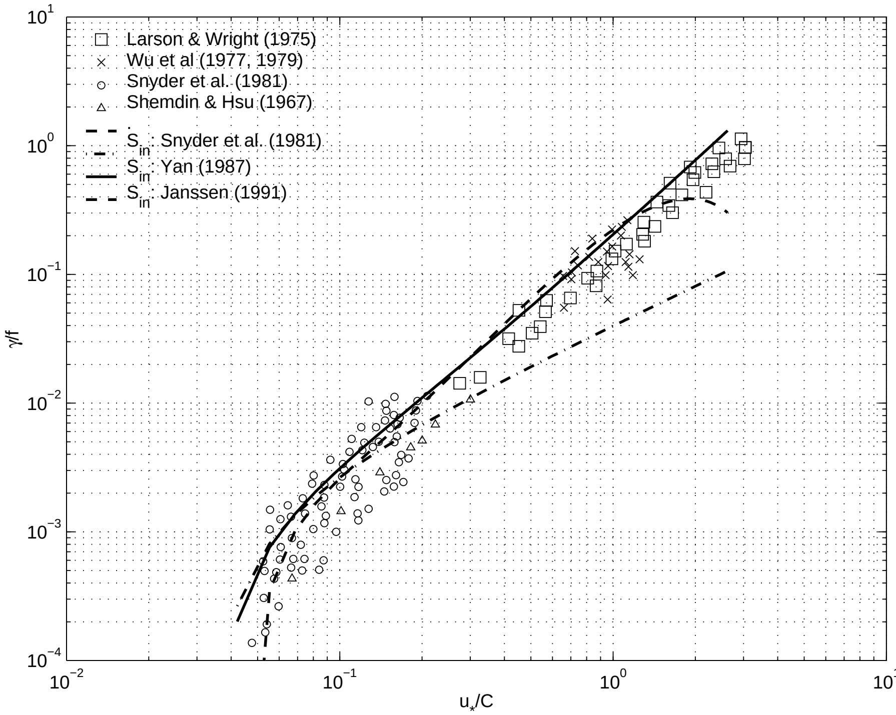

Figure 2.2: *Non-dimensional growth rates $\gamma/f = S_{in}F^{-1}(k,\theta)/f$ as a function of the wave age parameter u_*/c. Values computed from S_{in} forms due to Snyder et al. (1981) (dash-dotted line), Yan (1987) (dashed line) and Janssen (1991) (continuous line) are plotted against field observations from several studies. [Adapted from Plant (1982) and Young (1999)]*

its underestimation of spectral growth rates at higher wavenumbers. The forms S_{in}^{Y} and S_{in}^{J}, however, are preferred in more recent wind-wave models (Komen et al., 1994; Booij et al., 1998). The objective of the present study is to provide a comprehensive assessment of a new formulation for the dissipation term S_{ds}. Therefore, our analyses of model performance will address results obtained independently with these three forms of S_{in}.

Other forms of S_{in} based on the direct modelling of the turbulent boundary layer flow over the moving sea surface have been proposed by Gent and Taylor (1976), Makin and Chalikov (1979), Riley et al. (1982), Al Zanaidi and Hui (1984), Chalikov and Makin (1991) and Chalikov and Belevich (1993). The form of S_{in} proposed by Chalikov and Belevich (1993) is presently used successfully in the operational wave model WAVEWATCH III (Tolman and Chalikov, 1996). Consistent with the approach adopted in Banner and Young (1994), the present study does not include the validation of new forms of S_{ds} using alternative wind input source terms derived through direct modelling. This will be the topic of future research.

2.3.1.2 Nonlinear wave-wave interactions

Nonlinear wave-wave interactions are higher order perturbations that induce energy fluxes between spectral components through resonant mechanisms. Their importance in wind-wave modelling became evident through the theoretical work of Phillips (1960), Hasselmann (1962) and Zakharov (1968) and their subsequent experimental confirmation during the JONSWAP experiment (Hasselmann et al., 1973).

A historical review of the development of nonlinear interaction theory is given by Phillips (1981). Details of the computational techniques developed to solve S_{nl} are reviewed by Young and Van Vledder (1993). Komen et al. (1994) and Young (1999) present a comprehensive overview of the theory and its applications in numerical modelling of wind waves. The following summary is based on these references.

Nonlinear wave-wave interactions involve a set of four waves known as quadruplets. They exchange energy whenever resonant conditions defined by

$$\begin{cases} \mathbf{k}_1 + \mathbf{k}_2 = \mathbf{k}_3 + \mathbf{k}_4 \\ \omega_1 + \omega_2 = \omega_3 + \omega_4 \end{cases} \tag{2.24}$$

are satisfied simultaneously. Equations (2.24) form a coupled system linked through a dispersion relationship which, in deep water, has the form $\omega^2 = gk$.

The nonlinear interaction term S_{nl} is expressed as a function of the wave action density $N(\mathbf{k}) = F(\mathbf{k})/\omega$ through the integral

$$\begin{aligned}\frac{\partial N_1}{\partial t} = \int\int\int & G(\mathbf{k}_1, \mathbf{k}_2, \mathbf{k}_3, \mathbf{k}_4)\times \\ & \delta(\mathbf{k}_1 + \mathbf{k}_2 - \mathbf{k}_3 - \mathbf{k}_4) \times \delta(\omega_1 + \omega_2 - \omega_3 - \omega_4) \times \\ & [N_1 N_3 (N_4 - N_2) + N_2 N_4 (N_3 - N_1)]\, d\mathbf{k}_1 d\mathbf{k}_2 d\mathbf{k}_3.\end{aligned} \tag{2.25}$$

Numerical integration of equation (2.25) represents a major challenge in wind-wave research. The main difficulties arise from the complexity of the coupling coefficient G and the fact that the integral on the right hand side of (2.25) is six-dimensional.

A first spectral wind-wave model with a full solution to the nonlinear interactions term (EXACT-NL) was developed by Hasselmann and Hasselmann (1981). Their method consisted of a symmetric integration technique that reduced significantly the computational time required to solve (2.25). A second numerical method that allowed a full solution of S_{nl} with further reductions of computational effort was provided by Tracy and Resio (1982), based on the integration technique proposed by Webb (1978) and Masuda (1981). Following Banner and Young (1994), exact nonlinear computations of fetch-limited evolution described in Chapter 5 were made with a model that uses the Tracy and Resio (1982) algorithm.

The development of a parametric approximation to (2.25) known as the discrete interaction approximation (DIA) by Hasselmann and Hasselmann (1985), allowed the advent of the WAM model (Hasselmann et al., 1988). It was the first third-generation model to be applied successfully in two-dimensional cases, including regional and global wind wave predictions. The DIA algorithm is also included as a resource to solving S_{nl} in other operational wind-wave models. Examples are the WAVEWATCH-III model (Tolman and Chalikov, 1996) and the SWAN model (Booij et al., 1998). Research on developing other computationally-efficient solution techniques for S_{nl} have been reported recently by Lin (1998), Lavrenov and Ocampo-Torres (1999) and Van Vledder et al. (2000). However, tests of these alternative S_{nl} forms involving more complex wind-wave generation scenarios have not yet been reported. Therefore, the usefulness of these new techniques in more general applications is still to be demonstrated.

2.3.1.3 Spectral dissipation rates

Wave breaking plays a significant role in the evolution of deep-water wind-waves. In wind-wave modelling, spectral dissipation rates are assumed to be mostly determined by wave breaking. The probability of breaking and the magnitude of dissipation rates of individual waves or wave groups have been successfully observed in the field and in the laboratory, as reported in reviews by Banner and Peregrine (1993) and Banner and Tian (1998). Nevertheless, the description of spectral dissipation rates in more complex two-dimensional wave fields remains an elusive task. Thus, spectral dissipation is the least understood driving mechanism in the modelling of wind-wave evolution.

Hasselmann (1974) proposed a first source term describing explicitly spectral dissipation rates for wind-wave modelling applications. In this theoretical model, he described whitecaps as randomly distributed pressure pulses situated on the forward face of breaking waves, exerting negative work on the water surface. He further assumed that white-caps persisted only for a small fraction of the period of the breaking wave, conserved shape and position in relation to the wave profile during the duration of the breaking event and were geometrically similar, regardless of the observed wave length.

These assumptions yielded a dissipation function that depends linearly on the wave spectrum $F(k, \theta)$. The general form of the dissipation source term proposed by Hasselmann (1974) is given by

$$S_{ds}(k, \theta) = \gamma_{ds} F(k, \theta). \tag{2.26}$$

This general quasilinear form of S_{ds} carries the underlying assumption that the damping factor γ_{ds} is the same for all spectral components at any scale. As the pressure-induced decay is assumed to be randomly distributed at all scales of the wave spectrum, it may be included in the definition of the damping factor γ as a function of an overall steepness of the wave field, expressed in terms of the total energy E_{tot} and of a representative wavenumber such as its mean value $\overline{k}$. Other dissipative effects, such as the attenuation of shorter waves within the wake of white-caps produced by the breaking of dominant waves (Banner et al., 1989), may also be directly included in the definition of γ. This effect may be represented by the ratio $\omega/\overline{\omega}$. The combination of these parameters were the basis of the form of S_{ds} proposed by Komen et al. (1984), which is given by

$$S_{ds}(k,\theta) = -C_{ds}\bar{\omega}\left(\frac{\omega}{\overline{\omega}}\right)^{n}\left(\frac{\hat{\alpha}}{\hat{\alpha}_{PM}}\right)^{m} F(k,\theta) \tag{2.27}$$

where $\overline{\omega}$ is the mean radian frequency

$$\overline{\omega} = \frac{\int\int \omega F(k,\theta) k dk d\theta}{E_{tot}}, \tag{2.28}$$

$\hat{\alpha}$ is an integral steepness parameter $E_{tot}\overline{k}^2$ and $\hat{\alpha}_{PM} = 4.57 \times 10^{-3}$ is the overall steepness of a fully-developed Pierson and Moskowitz (1964) spectrum. The parameters m and n in (2.27) were determined numerically by Komen et al. (1984). Optimal values were found to be $m = n = 2$. The resulting dissipation function was adopted in earlier versions of the WAM model up to Cycle 3.

The S_{ds} form (2.27) was later modified by Janssen (1989) to be used in combination with the quasilinear S_{in}^{J} form (2.20). The quasi-linear S_{in}^{J} produced higher levels of input at higher frequency components due to its quadratic dependence on the wave age u_*/c. In order to obtain a proper balance within the high frequency tail, Janssen (1989) proposed the following form of S_{ds}, presently used in WAM Cycle 4:

$$S_{ds}(k,\theta) = -C_{ds}\left(\frac{\hat{\alpha}}{\hat{\alpha}_{PM}}\right)^{m}\left[(1-\delta)\frac{k}{\overline{k}} + \delta\left(\frac{k}{\overline{k}}\right)^{2}\right]\overline{\omega}F(k,\theta), \tag{2.29}$$

where δ is a weighting factor controlling the magnitude of linear and quadratic functions of the ratio $k/\overline{k}$. This weighting function provides the means of controlling dissipation rate levels at higher wavenumbers, without significant changes to S_{ds} levels around the spectral peak.

The effectiveness of the form of S_{ds} (2.27) due to Komen et al. (1984) was evaluated in a comprehensive numerical study on the evolution of fetch-limited waves made by Banner and Young (1994). Their major findings are summarised in Chapter 5, which also presents the results of an assessment of the form of S_{ds} given by equation (2.29). The following Chapter introduces the conceptual framework for the development of a new form of S_{ds} that depends nonlinearly on the local wave spectrum. Other alternative forms of S_{ds} are proposed and investigated in Tolman and Chalikov (1996) and Holthuijsen et al. (2000), for example.

Chapter 3

Modulating Wave Groups, Onset of Breaking and Spectral Dissipation Rates

Modulating wave groups are strongly associated with the onset of breaking in deep water waves. Early evidence on this process was given by Donelan et al. (1972), who casually observed from a plane and a ship that wave breaking occurred periodically, whenever individual wave crests advanced through a group and reached a critical amplitude associated with the group envelope maximum. This process is shown schematically in Figure 3.1. Subsequent field, laboratory and numerical experiments have provided support to these early observations. Recent reviews of the topic are presented in Banner and Peregrine (1993), Banner and Tian (1998) and Banner et al. (2000).

The first open ocean experiment to investigate the relation of breakers and wave groups was performed by Holthuijsen and Herbers (1986). Two-thirds of their observations of breaking waves occurred in one-third of the wave groups. In other words, around 70% of the observed breakers were associated with wave groups. As their observations indicated that breaking generally occurred near the centre of a wave group, they concluded that "the occurrence of breakers in groups supports, to some extent, the model of ocean wave breaking suggested by Donelan et al. (1972)".

Holthuijsen and Herbers (1986) also observed that the onset of breaking could not be predicted by a *local* wave steepness threshold, as had been proposed in earlier

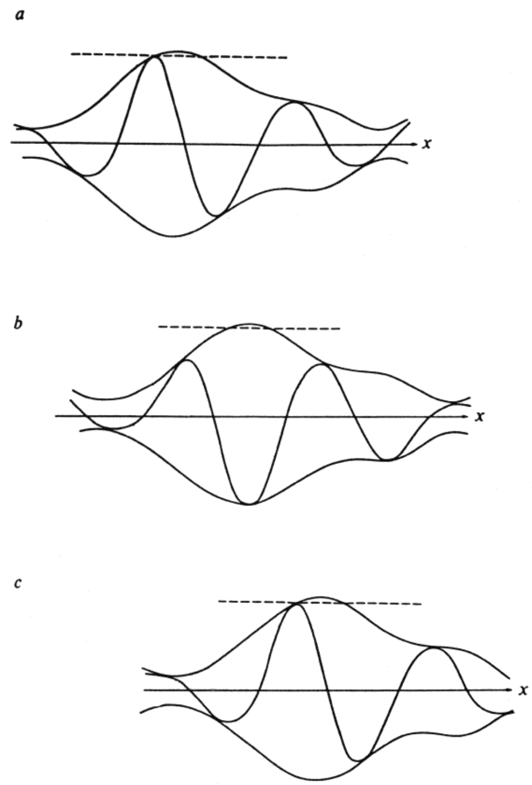

Figure 3.1: *Schematic view of a modulating wave group propagating from left-to-right [panels (a) to (c)] showing the surface elevation, the group envelope and a hypothetical breaking threshold (dashed line). Individual waves break as they advance towards the centre of the group. [Adapted from Donelan et al. (1972).]*

theoretical studies. Furthermore, they observed that waves would break with steepness much lower than the expected theoretical values (e.g., Longuet-Higgins, 1975), as had been shown earlier by the classical numerical experiments on breaking of unsteady deep water waves reported by Longuet-Higgins and Cokelet (1976).

Using a fully nonlinear free surface model, Dold and Peregrine (1986) studied the two-dimensional evolution of wave groups to breaking as a function of the initial dominant wave slope $(ak)_0$ and the number of waves N in one modulation interval.

Their results demonstrated that, for a given N, recurrence towards the initial wave group configuration or breaking occurred whenever $(ak)_0$ was, respectively, below or above a threshold value. They also observed that a wide range of values of local wave steepness occurred prior to breaking and, therefore, did not provide a robust breaking criteria.

A measure of initial group slope was also found to be a good predictor of the onset and strength of breaking by Rapp and Melville (1990), who observed breaking in two-dimensional focusing wave groups generated in a laboratory tank. Their input packet amplitude ak_c was approximately constant for breaking wave groups with a wide range of bandwidths, as shown in Figure 3.2, panel (a). Their results also indicated that wave slopes immediately before, and at breaking, were scattered within a wide range of values, providing further evidence that breaking criteria based on local steepness values were not robust.

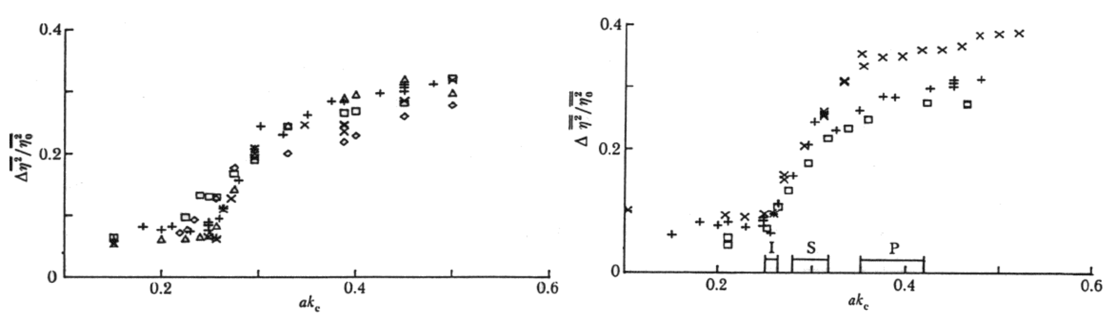

Figure 3.2: *Loss of excess momentum flux against ak_c for (a) five packet bandwidths and (b) three packet centre frequencies. Incipient, spilling and plunging event are marked with I, S and P. [Adapted from Rapp and Melville (1990).]*

Banner and Tian (1998) recently confirmed these earlier results through an extensive set of numerical experiments simulating the onset of breaking in unforced, nonlinear modulating wave groups. Their simulations suggested the existence of a universal threshold dependent on relative growth rates of the mean energy density, which discriminated wave groups that would either proceed to breaking or undergo recurrence. Examples of breaking and recurring wave groups are shown in Figure 3.3.

Following Dold and Peregrine (1986), Banner and Tian (1998) confirmed that breaking or recurrence depended on the initial steepness $(ak)_0$ and the number of waves N in one wave group cycle. Furthermore, in groups with more than four waves ($N > 4$), corresponding to typical open ocean wave groups (Longuet-Higgins, 1984), they found that the threshold initial steepness required for the onset of breaking was approximately constant, as shown in Figure 3.4. This outcome is consistent with the laboratory results of Rapp and Melville (1990).

Banner and Tian (1998) also investigated the effects of upper ocean shear on the breaking onset of deep water waves. Strong shear superimposed onto modulating nonlinear wave groups resulted in marginal differences to the main characteristics of breaking (steepness and evolution time to breaking) relative to cases with no shear. Strong wind forcing was also not of primary importance to the evolution to breaking (M. L. Banner, private communication).

Directional effects associated with the convergence of wave groups travelling in different directions may also be an important factor in estimating the spectral dissipation rates of wind-waves. This problem has been investigated in laboratory experiments reported recently by Kolaini and Tulin (1995), She et al. (1997), Nepf et al. (1998) and Wu and Nepf (2000). Their results, which are considered in more detail below, confirm that directionality can affect substantially both the onset and the intensity of breaking events.

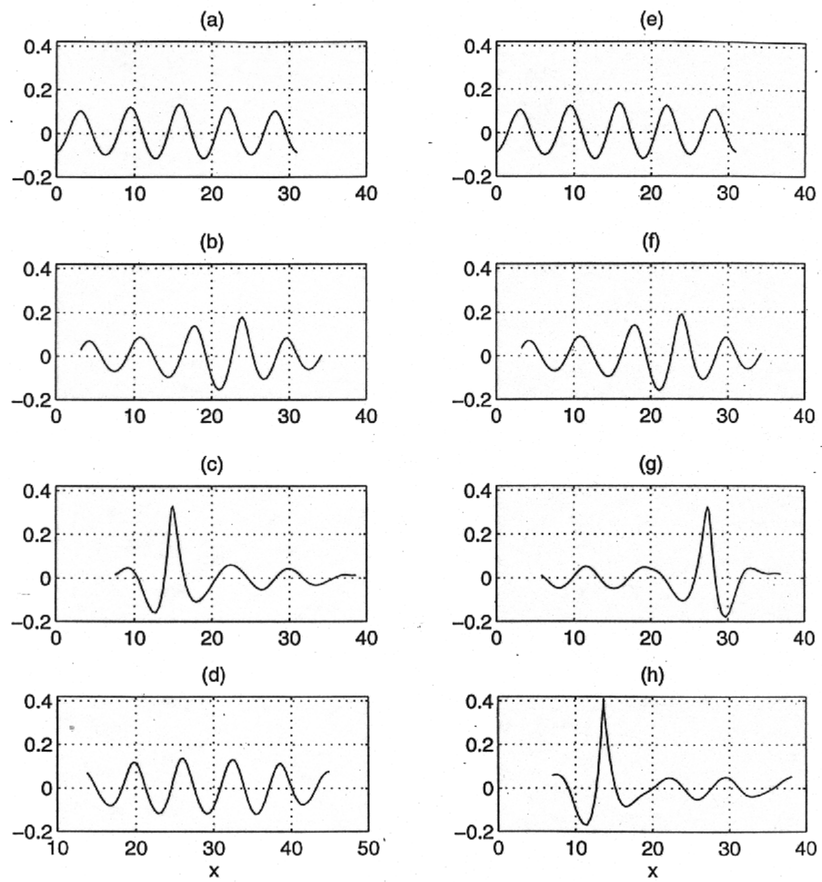

Figure 3.3: *Free-surface profile showing wave groups that evolve towards recurrence (left-hand side panels) or breaking (right-hand side panels). Propagation is from left to right. The associated times in the left-hand panels, from (a) to (d), are t = 0, 40, 85 and 165 wave periods; in the right-hand panels, the times are t = 0, 40, 70.1 and 74.9 wave periods, from (e) to (h). Recurrent waves in panels (a) to (d) are associated with threshold initial steepness values indicated by circles in Figure 3.4, which also indicates the threshold steepness of breaking waves [panels (e) to (h). [Adapted from Banner and Tian (1998).]*

3.1 Spectral representation of wave groups

Information about group structure and its variation in space and time are lost when the wave spectrum, an ensemble average of linearised wave components that share a common frequency or wavenumber, is used. As a consequence, parameters describing the onset of breaking based on the evolution of actual nonlinear wave groups, such as the universal growth-rate threshold reported in Banner and Tian (1998), cannot be directly incorporated into spectral wind-wave models. Snyder and Kennedy (1983), however, suggest a tentative approach to recover first-order properties of wave dynamics from an average description of the sea surface. Their approach consists of: (i) finding appropriate functions relating spectral energy densities to properties of breaking wave groups and (ii) proposing appropriate functions to partition this transfer among spectral components. The present study follows these general guidelines, adding a third step: testing and optimising the spectral dissipation function via numerical modelling.

Since it is assumed presently that breaking is strongly related to wave group dynamics, this requires the introduction of the concept of a wave spectrum representing average properties of *groups* of coherent waves, instead of the classical picture of the wave spectrum being composed of average amplitudes or energy densities of a large number of superposed *regular* waves. The sea surface would then be schematically represented by a superposition of wave groups randomly distributed. This conceptual model of wind-seas is treated formally in Komen et al. (1994, section I.2.6).

The idea of a sea surface composed of a collection of wave groups finds observational support in recent studies reported in Shen and Mei (1993) and Donelan et al. (1996). Shen and Mei (1993) investigated the effects of turbulent winds in the equilibrium range of wave spectra using records of surface elevation from the Bohai Sea, China. Their wavelet analysis shows that spectral components in the high frequency spectral range are intermittent and inhomogeneous, with structure resembling that of wave groups, as shown in Figure 3.5. Nevertheless, their analysis does not allow one to

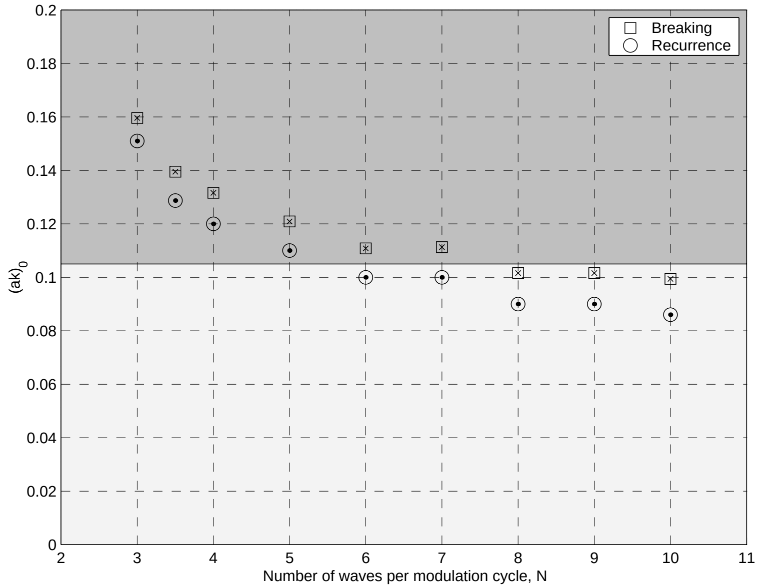

Figure 3.4: *Initial group steepness for different values of the number of waves in one group cycle N. Thresholds of breaking and recurrent events as a dissipative function of N are indicated by squares and circles, respectively. Shaded areas partitioned at a mean threshold $(ak)_0$ indicate recurrence (lighter) or breaking (darker) zones. [Adapted from Banner and Tian (1998).]*

differentiate the signature of free groups, occurring on different scales, from bound harmonics of the dominant waves.

Donelan et al. (1996) applied their wavelet directional method (WDM) to measured and synthetic sea surface elevation data to demonstrate that the underlying order in apparently chaotic wind-seas may be explained by the superposition of wave groups. Their new analysis technique also provided wave spectra that, despite having narrower directional energy distributions, were generally consistent with spectra computed through more traditional Fourier and Maximum Likelihood methods. An example is given in Figure 3.6. Their results are indications that the wave spectrum is a robust representation of average characteristics of wind-seas composed of coexisting wave groups.

The following sections introduce a conceptual model that relates local spectral densities to average properties of wave groups. This model is combined with observational evidence to construct a new source function for wind-wave modelling applications that estimates spectral dissipation rates due to breaking of waves at the spectral peak. This framework is then broadened to include higher wavenumbers, through the introduction of parameters controlling other processes that may be relevant at the shorter scales.

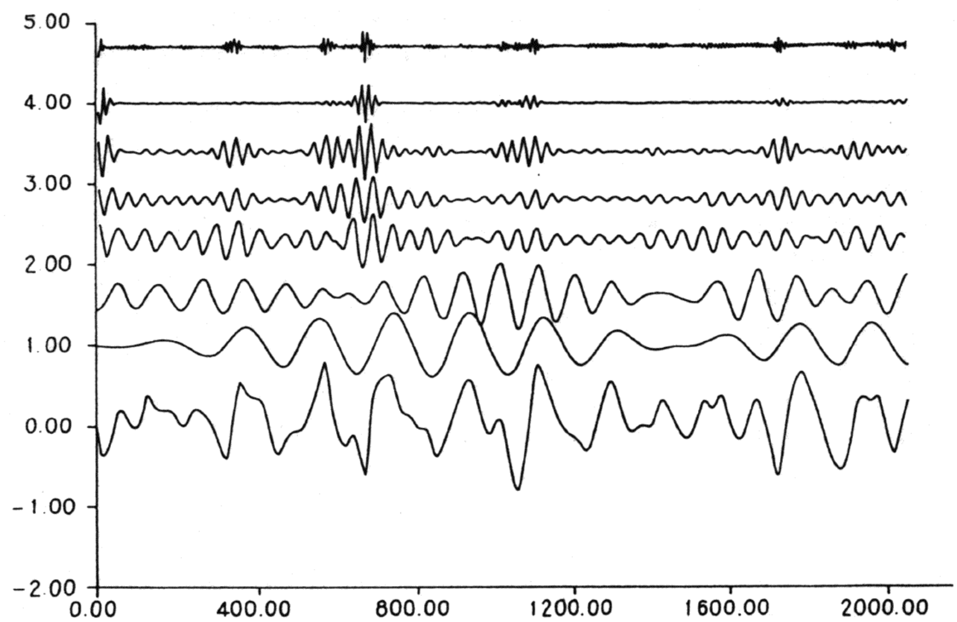

Figure 3.5: *Wavelet transforms of a record of surface elevation from the Bohai Sea, China. The original record corresponds to the time series in the bottom (mean level 0.00). The wavelet decomposition of the original signal corresponds to the remaining time series, with the shortest modes at the top. [Adapted from Shen and Mei (1993).]*

3.2 A threshold breaking parameter

Laboratory and numerical experiments indicate that a measure of initial wave group steepness may be the natural choice of a parameter that controls the onset of breaking. Therefore, a spectral parameter such as the initial group steepness $(ak)_0$ or the initial packet slope $(ak)_r$, would potentially be used as an indicator of breaking probability and of wave energy dissipation rates associated with breaking.

However, numerical experiments indicate that the onset of breaking is not only controlled by a steepness parameter, but also depends on properties such as the number of waves per group and the envelope geometry (depth of modulation), among others. Furthermore, the initial wave steepness cannot be directly derived from the wave spectrum, as the latter provides simply an average measure of the energy density of a large number of wave groups, with a common central wavenumber k_c but an unknown number of waves per modulation cycle.

These conceptual difficulties may be addressed by assuming that the stochastic nature of group lengths in open ocean waves averages out the variation with N of initial group steepness. An average threshold or initial steepness of stochastically distributed wave groups would then be directly proportional to a significant spectral steepness, derived from the observed wave spectrum.

Using observations of breaking waves from Lake Washington (USA), the Black Sea and the Southern Ocean, Banner et al. (2000) investigated the functional dependence between the breaking probability of dominant waves b_T and a significant spectral peak steepness defined by

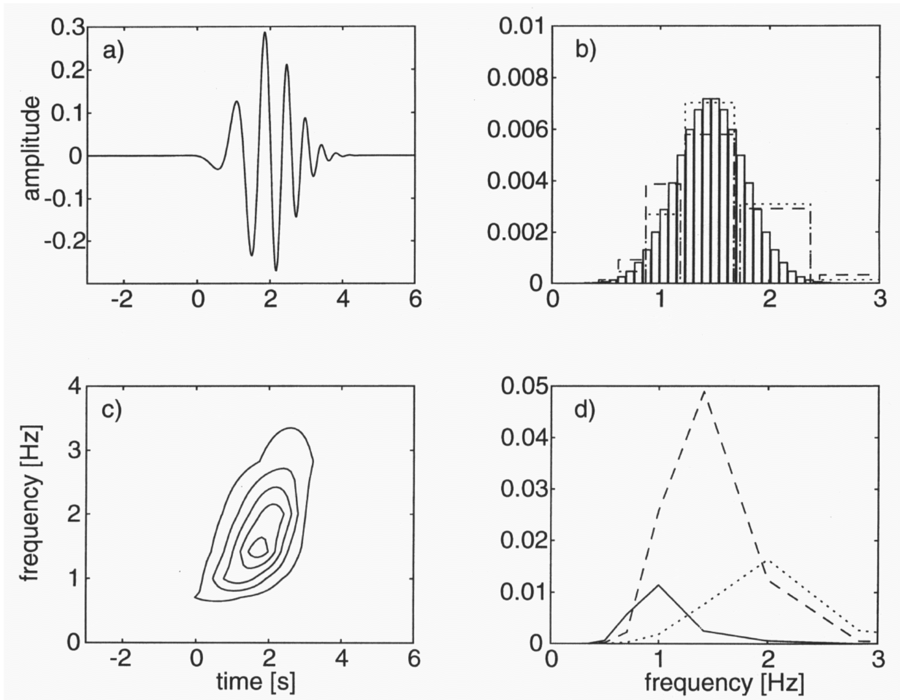

Figure 3.6: *A comparison of Fourier and wavelet analyses of the Gaussian wave group shown in panel (a). Solid bars and dashed boxes in panel (b) are the Fourier and wavelet spectra, respectively. Panel (c) shows a contour of the wavelet spectrum on the same time scale as (a). The one-dimensional wavelet spectrum at 1s, 1.5s and 2s is shown in panel (d). [Adapted from Donelan et al. (1996).]*

$$(ak)_p = \frac{H_p k_p}{2}, \quad \text{where} \quad H_p = 4\left(\int_{0.7f_p}^{1.3f_p} \varphi(\omega)d\omega\right)^{1/2}. \tag{3.1}$$

Figure 3.7 shows the number of breakers per wave period b_T as a function of $(ak)_p$ from their analysis of Lake Washington and Black Sea data. This figure indicates that (i) breaking probabilities are well correlated with $(ak)_p$; (ii) higher values of b_T are associated with dominant waves with higher mean steepness; and (iii) a threshold value of $(ak)_p$ around 0.05-0.06 determines whether breaking occurs or not.

The combination of their data sets demonstrated that b_T was strongly correlated with the transformed variable $[(ak)_p - (ak)_r]$, where $(ak)_r = 0.055$ was the average spectral peak threshold steepness value determined from the data. These results are shown in Figure 3.8. Rewriting the transformed variable as $[(ak)_p/(ak)_r - 1]$ indicates more clearly that $b_T = 0$ whenever $(ak)_p \leq (ak)_r$.

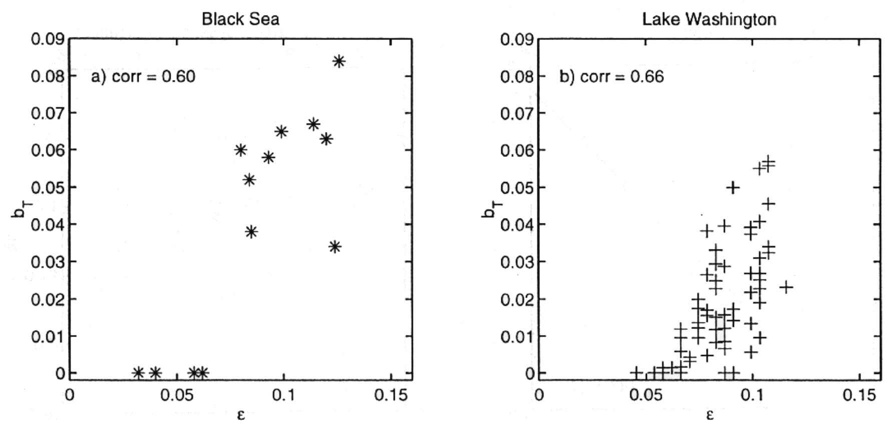

Figure 3.7: *Observed dominant wave breaking probability b_T against the dominant wave steepness $(ak)_p$ [represented by ε in the figure] at two locations: (a) Black sea and (b) Lake Washington. Correlation coefficients based on a linear fit are indicated in the top left of each panel. [Adapted from Banner et al. (2000).]*

The significant spectral peak steepness (3.1) is computed by integrating the wave spectrum at a range of frequencies within ±30% of the spectral peak frequency f_p. This range corresponds to the peak enhancement region of a JONSWAP spectrum (Hasselmann et al., 1973). According to Longuet-Higgins (1984), the superposition of wave components within that spectral range produces wave groups with three or more waves per modulation, corresponding to typical open ocean wave group lengths.

The resulting truncated spectrum, therefore, is assumed to be representative of statistically averaged properties of dominant wave groups. The whole idea is consistent with the model spectrum proposed by Donelan et al. (1996). In fact, a spectrum truncated within $0.7f_p$ and $1.3f_p$ resembles that of Figure 3.6, panel (b). Nevertheless, it does not represent the energy distribution of a single group, but the average properties of a large number of dominant wave groups randomly distributed on the sea surface.

3.3 Dissipation rates within the spectral peak

The dissipation rate of spectral energy density $S_{ds}(k,\theta)$ may be expressed as the product of a breaking strength coefficient Q and $\Gamma(k,\theta)$, the breaking crest length per unit area introduced by (Phillips, 1985), through an expression of the form

$$S_{ds}(k_p,\theta) \propto Q\Gamma(k_p,\theta), \tag{3.2}$$

By definition, the breaking probability of dominant waves b_T is a function of $\Gamma(k,\theta)$ given by

$$b_T = \int_{\bar{\theta}-\Delta\theta/2}^{\bar{\theta}+\Delta\theta/2} \int_{k_p-\Delta k}^{k_p+\Delta k} c\frac{\Gamma_p(k,\theta)}{f} kdkd\theta, \tag{3.3}$$

where $\bar{\theta}$ is a mean direction and $\Delta\theta$ is the directional spread of the dominant waves.

There are no observations presently available that allow a reliable parameterisation of the breaking strength coefficient Q (Melville, 1996). However, laboratory measurements by Rapp and Melville (1990) suggest that it is related to a mean excess slope relative to a reference threshold initial steepness, which, in their case, is the input packet slope ak_C. Their results are summarised in Figure 3.2, panel b, showing the loss of excess momentum flux, a measure of the breaking strength, as a function of ak_C.

Assuming that the significant spectral peak steepness $(ak)_p$ represents ak_c for the open ocean case, the breaking strength coefficient may be rewritten as a function in the form $Q = C_Q[(ak)_p/(ak)_r]^m$. The breaking probability of dominant waves b_T is described in Banner et al. (2000) as a function of the form $b_T = C_{bt}[(ak)_p - (ak)_r]^n$. The parameter b_T may also be approximated by a function of the form $b_T = C_{bt}[(ak)_p/(ak)_r]^n$.

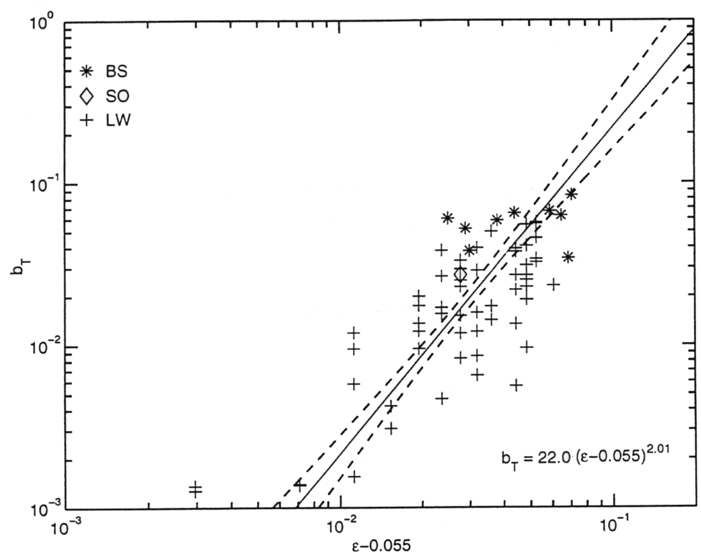

Figure 3.8: *Observed dominant breaking probability b_T against the steepness parameter $(ak)_p - (ak)_r$ [indicated as $\varepsilon - 0.055$ in the figure] at three locations: Black Sea (◯), Lake Washington (+) and Southern Ocean (◊). Continuous and dashed lines are the linear regression and ±90% confidence limits corresponding the equation in the bottom right. [Adapted from Banner et al. (2000).]*

As b_T and Q may both be expressed as functions of $[(ak)_p/(ak)_r]$, and $\Gamma(k,\theta)$ is directly proportional to b_T, a function describing the dissipation rate of energy density for dominant waves will have the form

$$S_{ds}(k,\theta) = C_{ds}\left[\frac{(ak)_p}{(ak)_r}\right]^p \omega F(k,\theta), \tag{3.4}$$

where C_{ds}, $(ak)_r$ and the exponent p are, to a first approximation, all constants. Following Banner et al. (2000), the spectral peak steepness $(ak)_p$ is given by (3.1). The resulting expression implies that the dissipation rates of dominant waves depend primarily on spectral properties of the dominant waves themselves. This is a departure from the concept that dissipation rates should be described by a quasilinear function of the wave spectrum proportional to an integrated spectral parameter, proposed originally by Hasselmann (1974).

The parameters C_{ds}, $(ak)_r$ and p in (3.4) cannot be determined directly due to the lack of observations of spectral dissipation rates. Their values have to be determined numerically by trial and error, in such a way that model results match optimally the available field observations of wind-wave growth.

The term dependent on the ratio $[(ak)_p/(ak)_r]$ represents the combination of the probability b_T and the strength of breaking events. Banner et al. (2000) have shown that for values of $(ak)_p$ lower than $(ak)_r$, the probability of breaking is zero. Therefore, if the spectral dissipation rates (3.4) were to represent exclusively white-cap dissipation, that term would have to asymptote to zero whenever $(ak)_p \leq (ak)_r$. However, this would also imply in assuming that no other processes, such as interactions between dominant waves and background levels of turbulence in the upper ocean, contribute to the spectral dissipation rates.

Two possibilities will be investigated numerically in the next Chapter using expression (3.4): (i) dissipation vanishes or becomes very small whenever the breaking probability is zero; and (ii) dissipation due to background turbulence is still effective even after breaking ceases to occur at a given wavenumber. These two conditions correspond to assuming that the term $[(ak)_p/(ak)_r]^p$ asymptote to zero or to one, respectively, whenever $(ak)_p < (ak)_r$. In this second case, dissipation rates due to wave-turbulence interactions are accounted for through the constant C_{ds}, in a first approximation.

3.4 Dissipation rates at higher frequencies

Consistent with the idea that wind-seas are a superposition of coherent wave groups, the concept of a steepness criterion controlling the onset of breaking may be extended to the high frequency range of the wave spectrum. Observational support for this idea is provided by Rapp and Melville (1990). They reveal that the onset and strength of moderate breaking in wave packets with different scales and frequency bandwidths have very similar dependences on an average steepness parameter, as seen in Figure 3.2. In addition, preliminary field observations reported in Banner et al. (2000) suggest that the dependence of the breaking probability on a steepness parameter is statistically similar at the spectral peak and at frequencies higher than the spectral peak frequency.

In practical terms, however, extending the concept of a significant spectral steepness similar to (3.1) using an arbitrarily chosen central wavenumber $k_c > k_p$ would produce a mean slope measure with significant bias, as pointed out by Banner et al. (2000). This would result from integrating the spectrum at ranges that have very different shapes: approximately symmetrical at the spectral peak and rapidly decreasing with frequency above the spectral peak. Within the high wavenumber range, such integration may also introduce undesirable contributions from bound harmonics into the computed mean slope.

To overcome this difficulty, a spectral steepness that depends directly on the equivalent significant wave height is proposed

$$H_c = 4\left(C_{sp}F(k_c)k_c^2\frac{\Delta k_c}{k_c}\right)^{1/2}, \tag{3.5}$$

where $F(k_c)$ is the azimuthally integrated spectral density $F(k_c) = \int_0^{2\pi} F(k_c,\theta)d\theta$ and Δk_c is the physical wavenumber bandwidth. At the spectral peak, values of H_c and H_p need to match. A proportionality constant C_{sp} is, therefore, included to account for the differences of approximating in (3.5) the integral term defining H_p in (3.1). Equation (3.5) is equivalent to convolving a window function, representing the actual shape of the *local* spectrum, with a rectangular spectrum $F(k) = constant$, within the range $k_c \pm \Delta k_c$.

Consistency of $H_c(k_c)$ at different central wavenumber scales requires a constant relative wavenumber bandwidth $\Delta k_c/k_c$. After rearranging constants in (3.5), an equivalent spectral steepness parameter may finally be defined as

$$(ak)_c = (C_B B(k_c))^{1/2}, \tag{3.6}$$

where $B(k_c) = F(k_c)k_c^4$ is the azimuthally integrated spectral saturation parameter [following the notation introduced by Phillips (1984) and Donelan and Pierson (1987)], and the proportionality, shape and bandwidth constants are all implicitly included in the coefficient C_B. One major advantage of using the spectral saturation $B(k_c)$ as the parameter controlling dissipation rates due to group modulation is that the exact shape of local wave group spectra is no longer important.

The validity of this approximation at any value of k_c would require the assumption that the shapes of wave group spectra are geometrically similar at all scales. Support for the similarity of spectral shapes at the spectral peak is provided by Donelan et al. (1985). Figure 3.9 reproduces a plot of their normalised frequency spectra at a wide range of development stages. This figure suggests that the triangular shapes of wave spectra at the spectral peak are approximately self-similar.

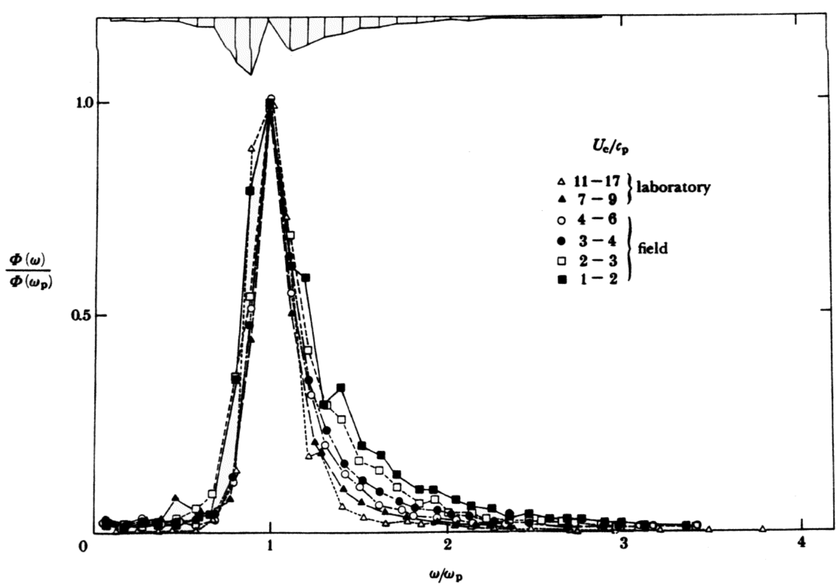

Figure 3.9: *Normalised frequency spectra from measurements reported in Donelan et al. (1985). Spectra are grouped into classes of the wave age parameter U/c_p. [Adapted from Donelan et al. (1985)]*

Preliminary evidence that the concept of geometrical similarity may be extended into other ranges of the wave spectrum is provided by Banner et al. (2000). They compared the dependence of the breaking probability b_T on a spectral steepness parameter at the spectral peak with that of a band centred at $2.56k_p$. The steepness parameter at the high-frequency range was determined through the integration of: (i) the unmodified spectrum and (ii) the spectrum convoluted with a triangular window resembling the spectral peak shape. Integrations were carried within a fixed 30% relative frequency bandwidth. The dependences were more consistent when the triangular window was applied.

Other physical processes may be important in determining the dissipation rates of waves at scales much shorter than the dominant waves. A well-known effect in the laboratory is the rapid attenuation of short waves in the wake of a large breaker, as described in Banner et al. (1989). Laboratory measurements by Mitsuyasu (1966) and Phillips and Banner (1974) indicate that augmented surface drift near the crest of long waves may also attenuate or entirely suppress shorter waves. Although not documented in the field, it is assumed that these two effects may be represented by a weighting function proportional to the local wavenumber relative to the average wavenumber $\overline{k}$, operative only at $k > \overline{k}$. An alternative way of expressing the influence of longer wave components on the dissipation rates of shorter waves dependent on a cumulative mean steepness parameter has recently been proposed by M. A. Donelan (private communication). The impact of its use will be the subject of future research.

The combination of these processes leads to a general function describing spectral dissipation rates, given by

$$S_{ds}(k,\theta) = C_{ds}\left(\frac{B(k)}{B_r}\right)^{p/2}\left(\frac{k}{\overline{k}}\right)^{n}\omega F(k,\theta), \tag{3.7}$$

where the reference saturation level B_r, the coefficient C_{ds} and the exponents p, m and n are all constants to be determined numerically.

The general structure of equation (3.7) resembles that of the dissipation source term proposed by Komen et al. (1984). Both may be reduced to the general form $S_{ds} = \gamma F(k, \theta)$, with the factor γ dependent on a steepness parameter. However, in the new saturation-dependent form of S_{ds} [hereafter referred to as S_{ds}^{ab}], γ is a function of the wavenumber k that depends nonlinearly on the steepness of the local wavenumber spectrum, becoming $\gamma(k) \propto F(k)^{p/2}(k/\overline{k})^n$ at any particular time. In opposition, the form of S_{ds} used in the WAM model [hereafter referred to as S_{ds}^{w}] has $\gamma(k, \theta) \propto constant(k/\overline{k})^n$ at any given wavenumber, as it is defined as a quasilinear function of the integrated spectral energy E_{tot} and this has a single value, independent of the wavenumber k, at any particular time.

These conceptual distinctions produce significant differences in practical terms, as shown in Figure 3.10. Panels (a), (b), (c) and (d) show the spectral dissipation rates estimated by the new form S_{ds}^{ab} and by the WAM Cycle 4 form of S_{ds}^{w} [equation (2.29)] at four stages of evolution: (a) young wind-seas ($U/c_p = 3$), (b) mature wind-seas ($U/c_p = 1.5$), (c) approaching full development ($U/c_p = 1$) and (d) fully developed seas ($U/c_p = 0.8$). To enhance their differences, both forms of S_{ds} have been normalised by the maximum absolute value of S_{ds}^{w} at a given development stage. Spectra used to compute dissipation rates were produced through exact nonlinear simulation of fetch-limited evolution.

Figure 3.10 shows that the nonlinear dependence of S_{ds}^{ab} on the azimuthally integrated local wavenumber spectrum $F(k)$ has a dramatic impact on the estimates of dissipation rates around the spectral peak region. As the wave spectrum evolves

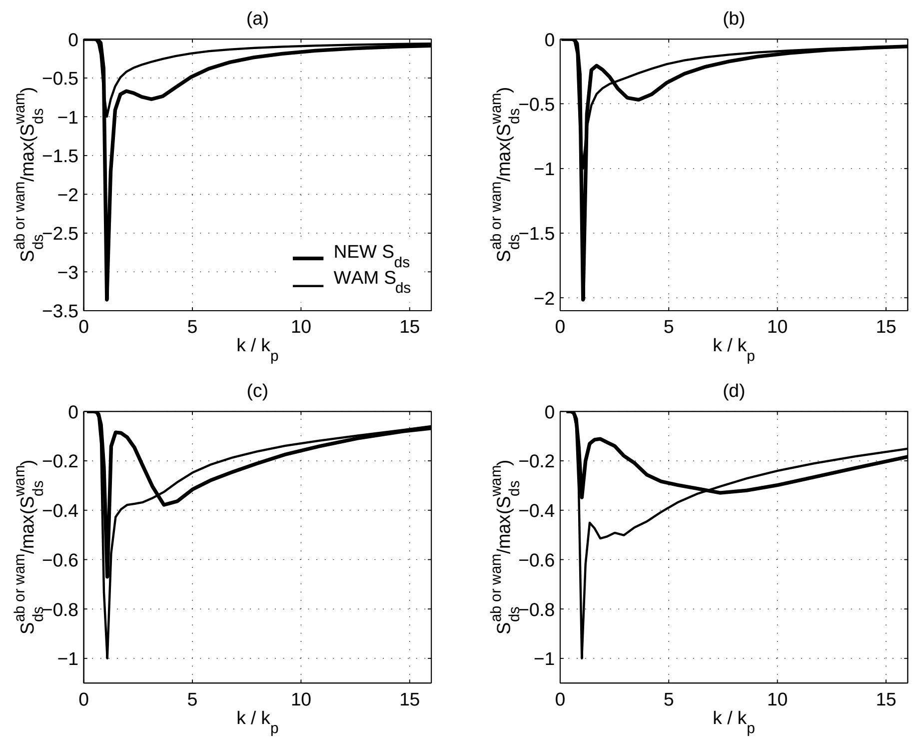

Figure 3.10: *Spectral dissipation rates estimated by the new form S_{ds}^{ab} (thick lines) and by the WAM Cycle 4 form of S_{ds}^{w} [equation (2.29)] (thin lines) at four stages of evolution: (a) young wind-seas ($U/c_p = 3$), (b) mature wind-seas ($U/c_p = 1.5$), (c) approaching full development ($U/c_p = 1$) and (d) fully developed seas ($U/c_p = 0.8$). To enhance their differences, both forms of S_{ds} have been normalised by the maximum absolute value of S_{ds}^{w} at a given development stage.*

from young wind-seas [panel (a)] towards full development [panel (d)], the ratio $R_{ab/wam} = S_{ds}^{w}/S_{ds}^{ab}$ around the spectral peak decays from $R_{ab/wam} = 3$ to $R_{ab/wam} = 0.3$, an order of magnitude change. The larger dynamic range of S_{ds}^{ab} at the peak is a consequence of its nonlinear dependence on $B(k)$, which decays quite dramatically as the spectral peak becomes less forced by the wind field, when the wave spectrum evolves under constant forcing. This nonlinear dependence also results in the strong features of the dissipation rates around the spectral peak. The term S_{ds}^{w} produces smoother features due to its quasilinear dependence on the wave spectrum.

Within the spectral tail ($k > 6.25k_p$), this ratio remains approximately constant at different evolution stages, and their differences in magnitude ($2 < R_{ab/wam} < 1.5$) are modest. In S_{ds}^{ab}, the narrower dynamic range of dissipation rates at higher wavenumbers (relative to that of the spectral peak) is due to the smaller variations in the wave spectrum $F(k)$ at $k >> k_p$ in different development stages. The reason for a better agreement between S_{ds}^{ab} and S_{ds}^{w} at higher wavenumbers is that, in both cases, dissipation rates depend on the ratio of the local wavenumber k to the mean wavenumber $\overline{k}$. At higher wavenumbers, both forms of S_{ds} become strongly dependent on this ratio, as it becomes much larger than the respective steepness terms.

Recent laboratory observations have shown the importance of three-dimensional effects to the onset of breaking (Kolaini and Tulin, 1995; She et al., 1997; Nepf et al., 1998; Wu and Nepf, 2000). The azimuthally-integrated saturation $B(k)$ in (3.7), however, averages out details about the directionality of waves at any given wavenumber. This may be seen as a shortcoming in the new formulation, particularly at wavenumbers above the spectral peak. At the spectral peak, the directional spreading is generally narrow enough to justify ignoring directional effects, as supported by observations reported in Banner et al. (2000).

At wavenumbers higher than the spectral peak, the directionality of the wave spectrum becomes larger, as demonstrated by Donelan et al. (1985) and Banner (1990). Observations reported in Wu and Nepf (2000), however, indicate that strongly directional waves may result in three-dimensional focusing, leading to an increase in dissipation rates. Therefore, a dependence of S_{ds} on an azimuthally integrated saturation $B(k)$, rather than on the two-dimensional saturation $\mathcal{B}(k, \theta)$, may be seen as a simple way of parametrising the effect of enhanced dissipation at higher wavenumbers due to directional effects.

Numerical experiments discussed in Chapter 5 indicated a more practical reason for using the azimuthally integrated saturation $B(k)$ in (3.7), instead of $\mathcal{B}(k, \theta)$. These experiments showed that a dependence on $\mathcal{B}(k, \theta)$ resulted in spectral dissipation rates with a narrow directional distribution, which led to the unbounded growth of energy densities propagating at large angles in relation to the wind direction, particularly at wavenumbers higher than the peak. A closer examination of model results revealed that S_{ds} was not strong enough to damp the vigorous energy transfer to larger angles provided by S_{nl} at higher wavenumbers. This led to a significant broadening of the wave spectrum and, in some cases, to the explosive growth of energy at lower wavenumbers. This problem was solved with a form of S_{ds} proportional to $B(k)$.

A final condition on the consistency of this new saturation-dependent form of S_{ds} with observations reported in Rapp and Melville (1990) and Banner et al. (2000) is the cancellation of contributions from the term representing energy loss due to wave breaking whenever $B(k) < B_r$. If other dissipative processes (e.g., straining of shorter waves and wave-turbulence interactions) are to remain active as background sources of energy losses after the contribution from breaking at a given wavenumber has ceased, the term $(B(k)/B_r)^{p/2}$ cannot strictly vanish when $B(k) < B_r$. For convenience, it is assumed that this term asymptotes to unity. In this way, the remaining terms will set the background dissipation of spectral components with reduced steepness, such as swell and waves travelling faster than the forcing wind speed.

Chapter 4

Observations of Fetch-Limited Evolution

Field observations of wind-wave evolution under fetch-limited conditions provide a simple and robust method for the development and validation of numerical models. The main reason for this is the availability of data from several field studies conducted since the landmark JONSWAP experiment (Hasselmann et al., 1973). In addition, these studies have shown that several properties of fetch-limited wave spectra are described by simple nondimensional relations determined empirically according to the similarity theory of Kitaigorodskii (1962, 1973).

Fetch-limited conditions develop when a uniform steady wind blows perpendicular to a long and straight shoreline, as illustrated in Figure 4.1. If the wind persists for long enough, the wave spectrum reaches a stationary state. Its descriptive parameters then become exclusively a function of wind speed and fetch, which is defined as the distance from the coastline along the wind direction (x in Figure 4.1).

The broad arrow in Figure 4.1 represents the wind speed U_z at some arbitrary level z. A hypothetical line of 10 wave gauges extends from the shoreline into deeper waters along the wind direction. Figure 4.2 illustrates the variation of significant wave height H_s along the line of wave gauges at two wind speeds U_z = 15 and 20ms^{-1}. For a given wind speed U_z that has blown for long enough, values of H_s at any fetch X will remain unchanged at all times.

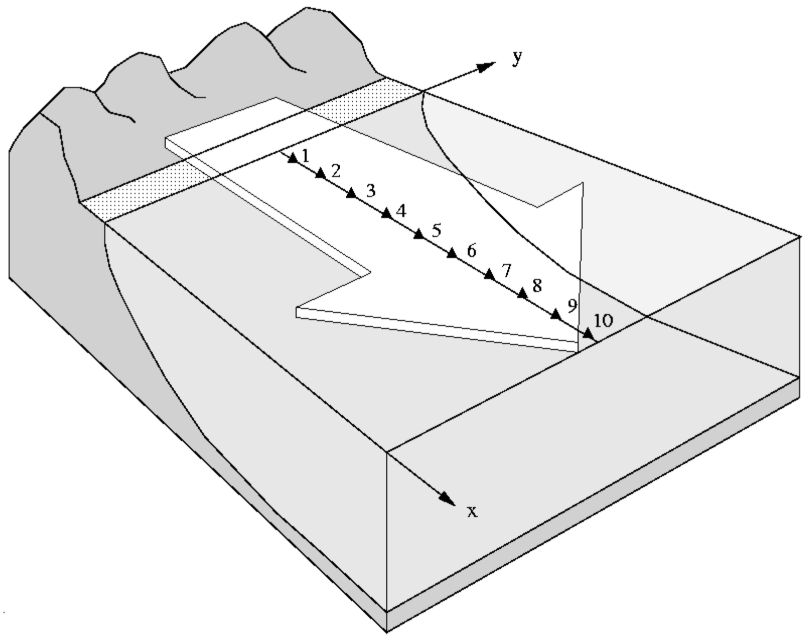

Figure 4.1: *Fetch-limited conditions develop when a steady wind field blows perpendicularly (along the x direction) from a long and straight coastline extending along the y direction. The wind field is illustrated by a broad clear arrow. Wave heights at the 10 wave gauges extending from the shoreline in the wind direction are shown in Figure 4.2. The depth is sufficiently deep to avoid bottom interaction effects at all points.*

4.1 Evolution curves

The evolution of H_s as a function of fetch corresponding to Figure 4.1 is shown in Figure 4.2. It is an approximate picture of what is observed in the field. The curves of H_s indicate that the wave energy grows proportionally to a power of the fetch until reaching an asymptotic evolution limit. Different growth regimes may be discriminated by the wave-age parameter c_p/U_z, relating the phase speed of the dominant waves c_p to the reference wind U_z. The fetch-limited growth region may then be subdivided into two regimes called young wind-seas and old wind-seas. These are followed by full development. Their along-fetch dimensions as well as the asymptotic H_s values are all functions of the wind speed U_z.

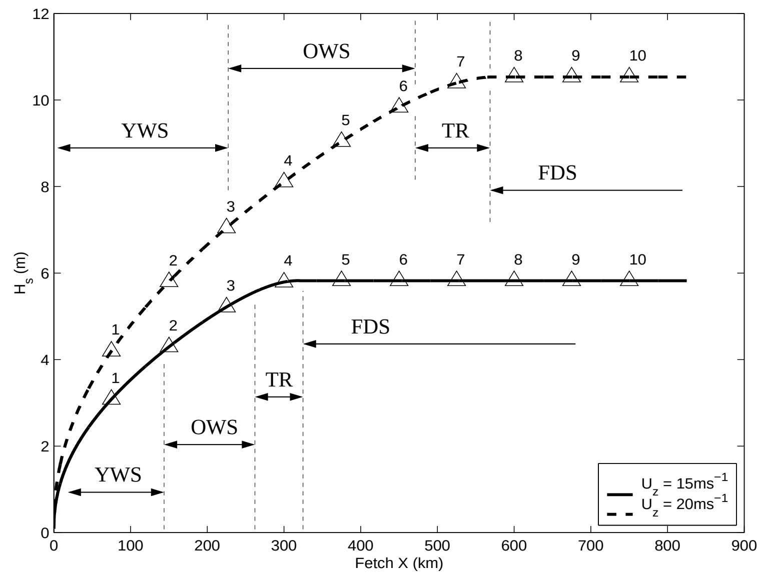

Figure 4.2: *Significant wave heights H_s from the fetch-limited evolution diagram in Figure 4.1. Values associated with two hypothetical conditions with wind speeds $U_z = 15$ and 20ms^{-1} are shown. In each case, ranges classified according to the stage of wave evolution are indicated. These are: young wind seas (YWS), old wind seas (OWS), fully-developed seas (FDS) and a transitional region (TR).*

Similar evolution curves may be produced to describe the fetch-limited evolution of other spectral parameters, as these will also be functions of wind speed and fetch only. Of particular interest to model validation studies are evolution curves describing the downshift of the spectral peak frequency f_p and the growth of the total wave energy E_{tot}, which is related to the significant wave height through the expression $H_s = 4\sqrt{E_{tot}}$.

General forms used to express the relationship between fetch, wind speed and parameters describing fetch-limited wave spectra are provided by the similarity theory of Kitaigorodskii (1962, 1973). The following nondimensional parameters are traditionally used:

a) Non-dimensional fetch

$$\chi_0 = \frac{gX}{U_0^2} \tag{4.1}$$

b) Non-dimensional peak frequency

$$\nu_0 = \frac{f_p U_0}{g} \tag{4.2}$$

c) Non-dimensional energy

$$\varepsilon_0 = \frac{g^2 E_{tot}}{U_0^4}, \tag{4.3}$$

where U_0 is a reference wind speed (U_z in the example from Figures 4.1 and 4.2) and g is the gravity acceleration.

According to similarity theory, the nondimensional parameters χ_0, ν_0 and ε_0 are variables that lie on universal curves provided that the reference wind speed U_0 is defined appropriately.

Kitaigorodskii (1962) originally proposed that U_∞, the geostrophic wind speed above the atmospheric boundary layer, would provide the most appropriate scaling. In practice, it should be replaced by a quantity that can be routinely measured or estimated. Within the wave modelling community a preference is shown towards using the friction velocity u_*, as reflected in Komen at al. (1994, sections II.8.4 and III.6.4). Experimental studies supporting u_* scaling include Janssen et al. (1987) and Davidan (1996).

Many experimentalists, however, criticise that choice because u_* is rarely measured directly, but is usually estimated through assumptions about the wind profile over the sea surface. Therefore, parameterised u_* estimates may introduce uncertainties that add to instrumental errors. Consequently, U_{10}, the wind speed at 10m height, which is routinely measured, has been taken as the natural scaling parameter by many investigators (Bretschneider, 1966; Mitsuyasu et al., 1975; Hasselmann et al., 1973; Kahma, 1981; Donelan et al., 1985; Walsh et al., 1989; Ebuchi et al., 1992; Donelan et al., 1992; Young and Verhagen, 1996).

Another alternative is $U_{\lambda/2}$, the wind speed at a height corresponding to half the wave-length (λ) of the dominant waves, as proposed by Donelan and Pierson (1987). More recently Resio et al. (1999) have proposed a dynamically-scaled wind speed U_r, taken at a height that is linearly related to the wavelength of the spectral peak. At present, however, there is no experimental evidence supporting the use of $U_{\lambda/2}$. Evidence presented by Resio et al. (1999) in favour of U_r is based on a single data set reported by Ewing and Laing (1987), who caution that their own measurements may not represent fully-developed conditions.

A review of several fetch-limited data sets made by Kahma and Calkoen (1992) has shown that observations do not provide conclusive evidence that rule out either U_{10} or u_* scaling. Both scalings appear to produce evolution curves of integral spectral parameters that fit observations with similar error levels. However, it is well-accepted that the friction velocity u_* is related to U_{10} through the expression

$$u_*^2 = U_{10}^2 C_D, \tag{4.4}$$

where C_D is the drag coefficient at a height of 10 m. For any known parameterisation of C_D, the resulting dependence between u_* and U_{10} is nonlinear. Furthermore, a generally accepted wind profile in neutral stability conditions is defined by

$$U_z = U_{10} \frac{\ln(z/z_0)}{\ln(10/z_0)} \tag{4.5}$$

provides expressions for $U_{\lambda/2}$ and U_r, that also depend nonlinearly on U_{10}. Consequently, relations (4.4) and (4.5) imply that if expressions (4.1), (4.2) and (4.3) are all universal when U_{10} is used, they will no longer be universal when u_*, $U_{\lambda/2}$ and U_r are used, or vice-versa. A more detailed examination of scaling wind speeds is conducted in the following sections.

Regardless of the choice of scaling wind speed, field observations suggest that nondimensional fetch-limited evolution of ε_0 and ν_0 as a function of χ are given by functions in the form:

$$\varepsilon_0 = C_\varepsilon \chi^m \ \text{ and } \ \nu_0 = C_\nu \chi^n, \tag{4.6}$$

where C_ε and C_ν are proportionality coefficients and m and n are exponents determined empirically.

Equations (4.6) are only valid when estimating the fetch-limited evolution of spectral properties from young to old wind-seas development stages, when the wave field is actively growing. At full development the spectral parameters no longer depend on the fetch X. Consequently, nondimensional relations for fully-developed seas are given by

$$\varepsilon^{lim} = \frac{E_{tot}^{lim} g^2}{U_0^4} \ \text{ and } \ \nu^{lim} = \frac{f_p^{lim} U_0}{g}, \ \text{ at } \ \chi \geq \chi_{min}, \tag{4.7}$$

where the superscript *lim* refers to the asymptotic values and χ_{min} is the minimum nondimensional fetch at which fully-developed seas are observed.

A common practice in wind-wave research is to establish dimensional relationships between wave parameters and other environmental variables using H_s, while nondimensional formulas are usually expressed in terms of E_{tot}. The same convention will be applied throughout the present investigation. Consequently, expressions (4.6) and (4.7) are readily converted into equivalent dimensional forms given by

$$H_s = 4\left(C_\varepsilon \frac{U_0^{2(2-m)}}{g^{(2-m)}} X^m\right)^{1/2} \quad \text{and} \quad f_p = C_\nu \frac{g^{(n-1)}}{U_0^{(2n-1)}} X^n, \tag{4.8}$$

and

$$H_s^{lim} = C_{hs} U_0^p \quad \text{and} \quad f_p^{lim} = C_{fp} U_0^q, \quad \text{at} \quad X \geq X_{min} = \frac{\chi_{min} U_0^2}{g}, \tag{4.9}$$

where X_{min} is the dimensional minimum length to full development corresponding to χ_{min}, C_{hs} and C_{fp} are proportionality coefficients and the exponents p and q are determined empirically.

To be consistent with similarity theory, observed wind and wave parameters need to satisfy equations (4.7) and (4.9) simultaneously, implying that the exponents in (4.9) should be $p = 2$ and $q = -1$. This conditional dependence is used by Alves et al. (2000) to investigate the adequacy of alternative wind speeds in describing three data sets representative of fully-developed conditions.

Suitable field observations within the transition between fetch-limited growth and full development are presently not available. Therefore, the dependence between spectral parameters and fetch within that range of fetches is unknown. Since the approach of the present study is to compare model results and evolution curves only within ranges that are supported by observations, the exact treatment of the transitional range is not of great importance. For simplicity, the choice was towards an extrapolation of the evolution curves with a sharp cutoff at the transition to full development.

In a comprehensive reanalysis of several fetch-limited data sets, Kahma and Calkoen (1992) derive values for the proportionality coefficients and exponents in equations (4.6) and (4.7). Their results also show that observations do not provide conclusive evidence ruling out either U_{10} or u_* scaling, as both appear to produce evolution curves that fit observations with similar error levels. In contrast, analysis of fully-developed sea events reported by Alves et al. (2000) indicate that U_{10} appears to be more robust as a scaling parameter than u_*. The results of Alves et al. (2000) also indicate that U_{10} provides nondimensional relations that are consistent with similarity theory while scaling with u_* fails to do so.

As the search for the most appropriate scaling wind speed remains an elusive issue, a consistent alternative is to make a choice in terms of the definition of the wind forcing source term S_{in}. Support for this approach is provided by results reported in Komen et al. (1994) and in Chapter 5 of the present study. They indicate that whenever scaling is done with a wind speed different from that used in the formulation of S_{in}, nondimensional spectral parameters derived from model runs at different wind speeds produce a family of evolution curves. Conversely, evolution curves that collapse onto a single line, thus satisfying similarity theory, are obtained when the scaling wind speed is consistent with the definition of S_{in}.

Three alternative forms of S_{in} described in Chapter 2 are used in the model validation experiments presented in the following Chapters. They are defined in terms of scaling wind speeds that can be either U_{10} or u_*. Estimates of u_*, in turn, are also made using two different formulations of C_D that are, respectively, dependent and independent of sea-state. Comparison of model results and observations should, therefore, use three sets of evolution curves. The present study uses the evolution curves derived by Kahma and Calkoen (1992, 1994), as described below.

Other empirical fetch-limited evolution curves are examined in comprehensive reviews presented in Donelan et al. (1992), Banner and Young (1994) and Young (1999). A brief review of relevant field experiments is provided below. For the sake of clarity, investigations using U_{10} and u_* scaling are described separately. This brief review is followed by a description of the corresponding Kahma and Calkoen (1992, 1994) evolution curves.

4.1.1 U_{10} scaling

Wiegel (1963) provides a compilation of fetch-limited observations available prior to 1960. They were the basis of early wave forecasting methods, consisting basically of nondimensional evolution curves scaled by the wind speed at an arbitrary height U_z. Figure 4.3 is a comprehensive summary of observed nondimensional integral parameters, plotted against nondimensional fetch. Wiegel (1963) used this figure to highlight the large scatter of observations, attributed mainly to a lack of uniformity in the selection of the measuring wind height.

Efforts towards unifying the height of wind observations near the sea-surface were consolidated in the investigations of Pierson and Moskowitz (1964), which are de-

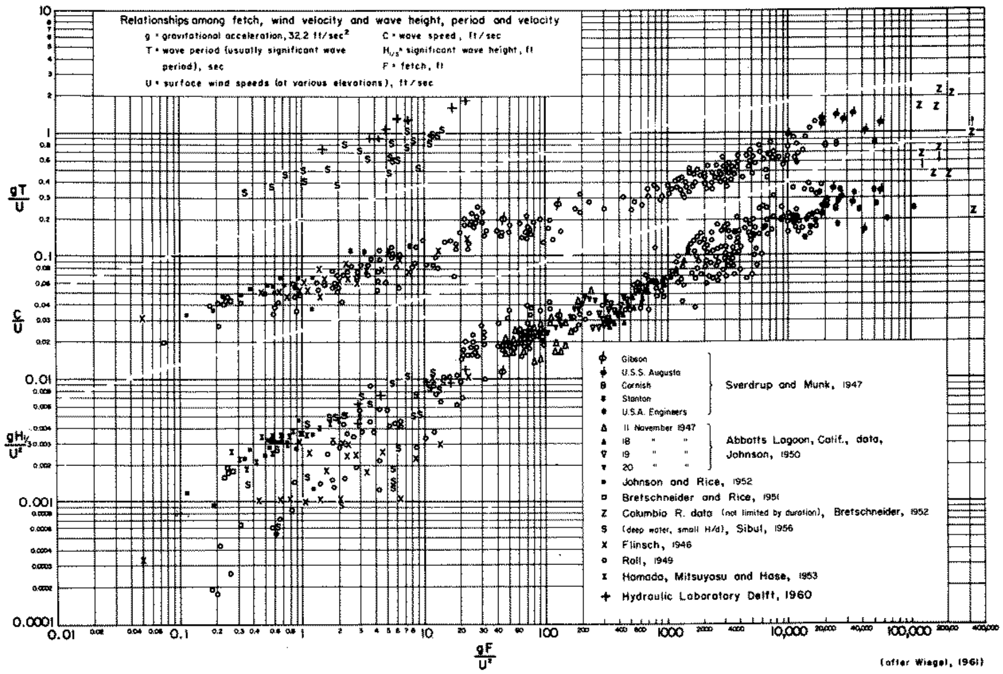

Figure 4.3: *Plot of nondimensional integral spectral parameters derived from observations available prior to 1960, adapted from Wiegel (1963).*

scribed briefly below in a section dedicated to fully-developed seas. Their comprehensive studies preceded a major international scientific initiative that synthesised the major trends of the time: the Joint North Sea Wave Project (JONSWAP), described in detail by Hasselmann et al. (1973).

Observations of fetch-limited evolution of wind-waves during the JONSWAP experiment were made near the coast of Northern Germany during 1969. The JONSWAP data set consisted of 121 events corresponding to "ideal" fetch-limited conditions. Hasselmann et al. (1973) merged these observations with data from several other studies, both in the field and in the laboratory, to obtain more robust nondimensional evolution curves scaled with U_{10}. They also derived a general parametric form describing fetch-limited spectra (the JONSWAP spectrum) based on an analytical expression previously proposed by Pierson and Moskowitz (1964).

Figure 4.4 shows observations of nondimensional integral spectral parameters (total energy E_{tot} and peak frequency f_p) from the JONSWAP experiment. Also shown are two other data sets used by Hasselmann et al. (1973) to derive their evolution curves. These were measurements made in the field by Burling (1959) and in the laboratory by Mitsuyasu (1968). Also shown are the evolution curves proposed by Hasselmann et al. (1973).

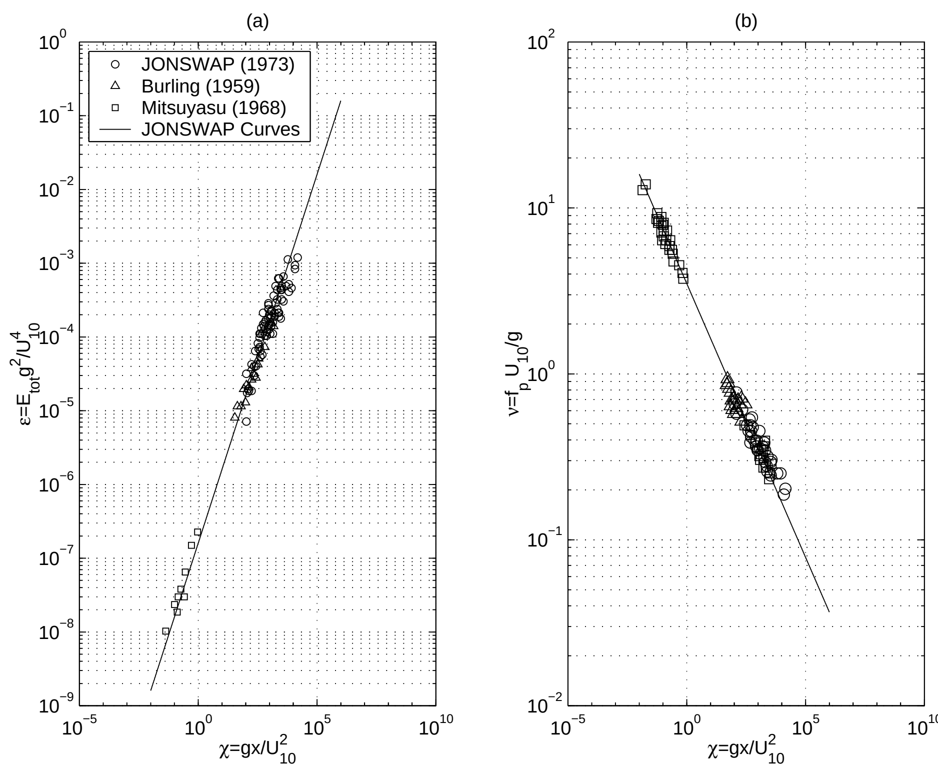

Figure 4.4: *Plot of nondimensional integral spectral parameters derived from observations used by Hasselmann et al. (1973) to derive the JONSWAP evolution curves, also shown as continuous lines in panels (a) total energy ε and (b) peak frequency ν.*

Several field experiments made subsequently provided nondimensional evolution curves scaled with observations of U_{10}. Relevant investigations were conducted by Kahma (1981) in the Bothnian Sea, Donelan et al. (1985) in Lake Ontario, Canada, Walsh et al. (1989) in the eastern coast of the USA and Ebuchi et al. (1992) in the Sea of Japan, to mention a few. These different data sets, together with the JONSWAP results, confirmed the power law evolution of integral spectral parameters with fetch, as represented by equations (4.6). Nevertheless, coefficients derived empirically from separate data sets produced evolution curves that diverged considerably.

Kahma and Calkoen (1992) reanalysed the JONSWAP data and results from investigations in the Bothnian Sea (Kahma, 1981) and Lake Ontario (Donelan et al., 1985). Their reanalysis divided these data sets according to whether the atmospheric stability conditions observed during fetch-limited events were stable or unstable. The partitioning of observations into stability groups significantly reduced the scatter between data sets, providing a consistent explanation for the differences in previously reported evolution curves.

Using a combination of observations from the Bothnian Sea, Lake Ontario and the JONSWAP experiment, Kahma and Calkoen (1992) derived unified expressions for the evolution of U_{10}-scaled nondimensional total energy ε and peak frequency ν given by

$$\varepsilon = 5.2 \times 10^{-7} \chi^{0.9}, \tag{4.10}$$

and

$$\nu = 2.18 \chi^{-0.27}. \tag{4.11}$$

These relations are representative of fetch-limited evolution under neutral atmospheric stability conditions. As the wind input source functions used in the present study were developed under the assumption of neutral stability, relations (4.10) and (4.11) are used to assess the performance of model results obtained with S_{in} defined in terms of U_{10}. Their range of validity, expressed in terms of the nondimensional fetch, is approximately $1 \times 10^2 \leq \chi \leq 1 \times 10^4$

4.1.2 Friction velocity scaling

Charnock (1955) provided a first assessment of the impact of using the friction velocity u_* to derive relations between spectral parameters and the wind field. Based on this early assessment, Kitaigorodskii (1962) suggested that u_* would be a practical alternative to replace the geostrophic wind speed U_∞ in defining the nondimensional variables (4.1), (4.2) and (4.3). His assumption was that when determined properly, u_* would be unaffected by (i) the variability of wind with height, (ii) distortions in the atmospheric boundary layer induced by the passage of waves and (iii) atmospheric stability effects.

Pierson (1964) argued that this approach was not consistent because u_* is proportional to the square of the total sea-surface stress τ, which is divided in two parts: one that transfers momentum into the wave field and another that generates the wind-drift layer. He reasoned that only the fraction of τ that transfers momentum into the wave field should be relevant to relate spectral parameters to the wind field. Since this fraction cannot be easily separated from the total stress, his conclusion was that u_* would not be the most practical choice for scaling purposes. In his view, a better option was the wind speed at a fixed height above the sea surface U_z.

The absence of a consensus in this conceptual arena required direct experimental evidence. Early efforts in that direction are reported in Ross (1978) and Liu and Ross (1980). Combining airborne laser altimeter and surface buoy measurements of wind-waves in Lake Michigan, they investigated the consequences of u_* scaling to the parameterisation of nondimensional relations between spectral parameters and fetch, also taking into account atmospheric stability effects.

Prior to Kahma and Calkoen (1992), Liu and Ross (1980) successfully reduced the scatter of their observations by simply separating U_{10}-scaled nondimensional spectral parameters from stable and unstable atmospheric conditions. Their main focus, however, was to investigate the effects of u_*. They found that the scatter of observations was further reduced when spectral parameters were rescaled with estimates of u_* that took into account atmospheric stability effects. Thus, their rescaling with u_* provided a single nondimensional expression describing the evolution of spectral parameters with fetch regardless of atmospheric stability conditions.

The results of Liu and Ross (1980) were based on 114 observations made during only two events of wave development under stable and unstable conditions, respectively. Kahma and Calkoen (1992) used a larger database with more than 200 observations from several fetch-limited events at three different locations. Their results showed that replacing U_{10} with u_* as the scaling variable reduces only slightly the scatter when data sets from stable and unstable conditions are combined. More importantly, however, the analysis of data divided into two groups, according to stability regimes, did not reveal significant differences in scatter between data scaled by either U_{10} or u_*.

Consequently, Kahma and Calkoen (1992) argued that u_* scaling brought no clear advantage over U_{10}. However, as values of u_* from the analysed data sets were estimated from measurements of U_{10}, they cautioned that their results do not imply that the true friction velocity, if measured or calculated accurately, could not change the outcomes. They, however, conclude that "our opinion is that the U_{10}-scaled [evolution] equations are considerably more accurate than the ones scaled by u_*, because less uncertain calculations were involved".

The investigation of Komen et al. (1984) and the quasi-linear theory of wave generation (Fabrikant, 1976; Janssen, 1989, 1991) have provided input source function S_{in} defined in terms of u_*. Wind-wave models use u_* determined indirectly from U_{10} through equation (4.4), where the drag coefficient is determined from empirical formulas or techniques that include or not sea-state influences on the total stress at the sea surface.

Covering these two possibilities, Kahma and Calkoen (1994) provided different evolution curves to describe the fetch-limited development of nondimensional spectral parameters, depending on the algorithm used to estimate u_* from U_{10}. Using once more the results from their composite dataset as representative of neutral atmospheric stability and the sea-state independent formulation of C_D proposed by Wu (1982)

$$C_D = (0.8 + 0.065U10) \times 10^{-3}, \tag{4.12}$$

a first pair of evolution curves describing ε and ν is given by

$$\varepsilon_* = 6.5 \times 10^{-4} \chi_*^{0.9}, \tag{4.13}$$

and

$$\nu_* = 4.90 \times 10^{-1} \chi_*^{-0.27}, \tag{4.14}$$

where $\varepsilon_* = E_{tot} g^2 / u_*^4$, $\chi_* = Xg/u_*^2$ and $\nu_* = f_p u_* / g$.

Analogous sea-state dependent relations are obtained by using an empirical wave-dependent z_0 proposed by Donelan (1990) and the Charnock relation $z_0 = \alpha_{ch} u_{**}^2 / g$

$$\varepsilon_{**} = 2.2 \times 10^{-4} \chi_{**}^{0.96}, \tag{4.15}$$

and

$$\nu_{**} = 6.68 \times 10^{-1} \chi_{**}^{-0.29}, \tag{4.16}$$

where the double-star subscript refers to parameters estimated from U_{10} through a sea-state dependent drag coefficient. In either sea-state dependent or independent cases, these evolution curves are valid within the range of nondimensional fetches $3 \times 10^4 \leq [\chi_* \text{ or } \chi_{**}] \leq 3 \times 10^6$.

4.1.3 Full-development limits

At a limiting nondimensional fetch χ_{lim}, it is assumed that the wave field reaches an asymptotic growth limit (the full-development limit) that is constant for all $\chi > \chi_{lim}$. Early attempts to estimate fully-developed asymptotic spectra and integral parameters as a function of wind speed were made by Sverdrup and Munk (1947), Pierson et al. (1955), Darbyshire (1959) and Bretschneider (1966). As a consequence of technical limitations and nonstandard procedures to observe the wind speed over the sea surface, these studies provided asymptotes $\varepsilon_{0,lim}$ and $\nu_{0,lim}$ that were in strong disagreement.

Aiming at the elimination of discrepancies found in earlier studies, Moskowitz (1964), Pierson and Moskowitz (1964) and Pierson (1964) analysed a carefully-chosen data set representative of fully-developed seas made with a state-of-the-art ship-borne wave gauge and selected according to strict criteria. Special attention was given in the selection of the height of wind measurements. Their results provided universal relations for fully-developed asymptotic limits and an analytical form describing the entire frequency spectrum (the "PM spectrum"). Wave parameters were nondimensionalised by the 19.5m-height wind speed $U_{19.5}$.

4.1.3.1 The Pierson-Moskowitz limits

Using observations of significant wave height H_s, Moskowitz (1964) expressed the relationship between H_s and $U_{19.5}$ through

$$H_s = 0.023 U_{19.5}^2. \tag{4.17}$$

Moskowitz (1964) integrated the PM spectrum as an alternative to recomputing (4.17). He justified this procedure based on limitations in the wave recorder and on the unreliability of spectral estimates at frequencies higher than 0.25Hz . Although the analytical form would give only an approximation to the spectral densities at all scales, he argued that it would eliminate errors in the high frequency region.

Integration of the PM spectrum resulted in

$$H_s = 0.021 U_{19.5}^2. \tag{4.18}$$

Equation (4.18) may be converted directly into the associated nondimensional total energy asymptote ε. Assuming a logarithmic wind profile given by (4.5), $U_{19.5}$ may be replaced by U_{10}, yielding

$$\varepsilon_{10,lim}^{an} = \frac{E_{pm}^{an} g^2}{U_{10}^4} = 3.64 \times 10^{-3}, \tag{4.19}$$

where the superscript *an* refers to a value derived from integration of the analytical spectrum and E_{pm} is the total energy of a PM spectrum computed from any given value of U_{10}.

Alternatively, equation (4.17) gives an asymptote ε that is based on direct observations of the wave spectrum

$$\varepsilon_{10,lim}^{obs} = \frac{\overline{E_{pm}^{obs}} g^2}{U_{10}^4} = 4.24 \times 10^{-3}, \tag{4.20}$$

where the superscript *obs* now refers to a value derived from observations.

Individual values of the peak frequency are not provided by Moskowitz (1964). Therefore, an asymptotic peak frequency value $\nu_{10,lim}$ may be derived from the average spectra described in Pierson and Moskowitz (1964), giving

$$\nu_{10,lim} = \frac{f_{pm} U_{10}}{g} = 0.13. \tag{4.21}$$

4.1.3.2 Rescaling the PM Limits with u_*

Asymptotic limits may be found alternatively with u_* scaling. The expressions first derived by Komen et al. (1984), which are now widely used as benchmarks for validation of numerical models, used an estimated u_* computed from a single value of $U_{10} = 15\text{ms}^{-1}$ and a drag coefficient $C_D = 1.8 \times 10^{-3}$. Using equation (4.4), this resulted in $u_* = 0.64$ m s^{-1}. Asymptotic limits were then obtained through integration of the PM spectrum, giving

$$\varepsilon^{an}_{*,lim} = \frac{g^2 E^{an}_{pm}}{u_*^4} = 1.1 \times 10^3 \tag{4.22}$$

and

$$\nu^{an}_{*,lim} = \frac{f_{pm} u_*}{g} = 5.6 \times 10^{-3}. \tag{4.23}$$

These asymptotic limits have been widely used for the validation of wind-wave models (e.g., Banner and Young, 1994; Komen at al., 1994; Ris, 1997; Schneggenburger, 1998; Hersbach, 1998).

To satisfy the similarity theory of Kitaigorodskii (1962, 1973), these nondimensional parameters should be universal, i.e. they should hold for all plausible values of the adopted scaling wind speed, which in equations (4.22) and (4.23) is u_*. The PM spectrum, however, was designed to provide a universal spectral form as a function of $U_{19.5}$. Universality still holds when employing U_{10}, as the differences between $U_{19.5}$ and U_{10} are generally small (around 7%).

The friction velocity u_* is determined indirectly through equation (4.4) using a drag coefficient that is typically a nonlinear function of the observed U_{10}. Therefore, scaling the PM spectrum with u_* given different values of U_{10} will produce nondimensional spectra (and corresponding integral parameters ε_* and ν_*) that are non-universal quantities, as the PM spectrum is a universal form only when U_{10} or $U_{19.5}$ are used. In fact, using an array of plausible values of $U_{10} = [5, 10, 15, 20$ and $25]$ m s^{-1} results in $E_{pm} = [0.02, 0.38, 1.91, 6.05$ and $14.77]\text{m}^2$. After introducing these quantities into the left hand side of equations (4.19) and (4.21) the nondimensional total energy and peak frequency values all converge to $\varepsilon_{10,lim} = 3.64 \times 10^{-3}$ and $\nu_{10,lim} = 0.13$, respectively.

Using equation (4.4) and a drag coefficient $C_D = (0.8 + 0.065U_{10}) \times 10^{-3}$ due to Wu (1982), which is consistent with Komen et al. (1984), results in $u_* =$ [0.1677, 0.3808, 0.6320, 0.9165 and 1.2311] ms^{-1}. Introducing these values into equations (4.22) and (4.23) gives $\varepsilon_{*,lim} =$ [2.9, 1.7, 1.1, 0.8 and 0.6] $\times 10^3$ and $\nu_{*,lim} =$ [4.4, 5.0, 5.6, 6.0 and 6.4] $\times 10^{-3}$. The results are clearly divergent, indicating that universality may not hold for nondimensional PM spectral parameters scaled by u_* (this viewpoint would be consistent with Pierson and Moskowitz (1964), as they assumed that the universality of parameters at full development was valid only for the $U_{19.5}$ case). These conclusions served as motivation for a comprehensive review of asymptotic evolution limits of fully-developed seas reported in Alves et al. (2000). The next section presents a summarised overview of their main findings.

4.1.3.3 New observations of fully-developed seas

Relatively few attempts to measure fully-developed seas have been reported since the pioneering contributions of Pierson and Moskowitz in 1964. According to Donelan et al. (1992) “there is a daunting list of reasons why such field observations have not yet been reported. Perhaps the most significant lies in the unrealistic assumption of stationarity and homogeneity over the time and length scales required to achieve full development".

Pierson (1991) enumerates other important limitations: "For large areas of light winds, there are usually waves that have propagated into that area from somewhere else" and "a constant wind over an area, say, 10° of longitude by 5° of latitude leads to conceptual difficulties because the wind is divergent and the great circle paths of the spectral components are different on each side of the fetch". Evidence against the concept of fully-developed seas is explored in more detail by Glazman (1994).

On the other hand, at least three recent studies of wave growth under fetch-limited conditions (Ewing and Laing, 1987; Walsh et al., 1989; Donelan et al., 1992) give support to the concept of fully-developed seas. The results of these three studies, however, were inconclusive. Ewing and Laing (1987) found integrated spectral energy asymptotes that fell systematically below the Pierson and Moskowitz (1964) asymptotes. Walsh et al. (1989) provides an asymptotic energy growth level that, despite being consistent with equation (4.18), is based on a single fetch-limited event. Donelan et al. (1992) provide evidence of a transition between fetch-limited growth and full development towards and asymptotic value slightly higher than (4.18). However, the observation of conditions for the occurrence of actual fully-developed seas were frustrated due to strong wind variability, the presence of gradients in wind and wave propagation and irregular fetch geometry at the observation site.

Based on climatologies of winds and waves described in Young and Holland (1996), Alves et al. (2000) selected two potential sources for new data representative of fully-developed seas: the Arabian Sea and the Southern Ocean. The Arabian Sea

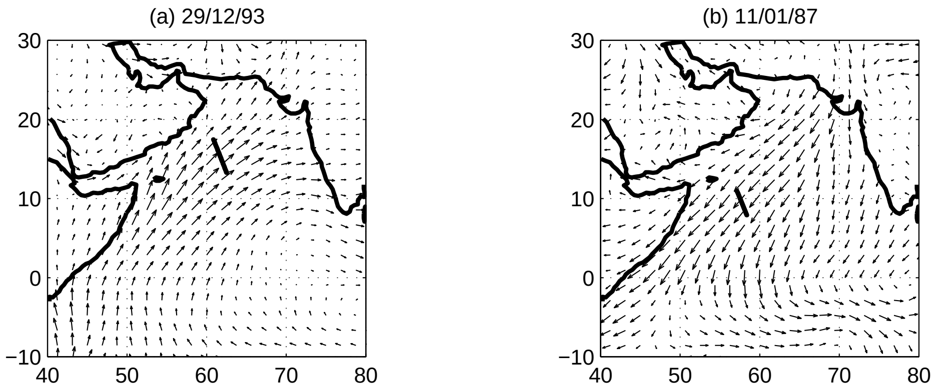

Figure 4.5: *Surface winds U_{10} from the Arabian Sea from two events observed on (a) 29/12/1993 and (b) 11/01/1987, corresponding to winter and summer monsoon periods, respectively. Black bars within the oceanic region indicate selected satellite passes. Scales are in degrees of latitude and longitude.*

is exposed to a strong south-westerly jet that develops close to the African coast, associated with the Asian Winter Monsoon. This pattern reverts during the Summer Monsoon, when weaker but persistent northeasterly winds develop from the coast of India. These two scenarios are illustrated in Figure 4.5. The Southern Ocean is known for its large extra-tropical storms and strong westerly winds, providing ideal conditions for the development of intense and persistent winds covering long fetches, as seen in Figure 4.6.

The new data sets analysed by Alves et al. (2000) consisted of 42 altimeter observations of H_s within the Arabian Sea and 25 spectra measured with a surface buoy near Macquarie Island, in the Southern Ocean. Analyses carried out with observations of H_s from the Arabian Sea resulted in U_{10}-scaled asymptotes $\varepsilon_{10,lim}$ and $\nu_{10,lim}$ that satisfied similarity theory. In opposition, u_* yielded relations that did not satisfy similarity theory. Spectra measured near Macquarie Island also provided expressions relating U_{10} to asymptotic spectral parameters that satisfied similarity theory and u_*-scaled expressions that did not. These results were confirmed by an analysis of a combination of these two data sets with observations reported in Moskowitz (1964).

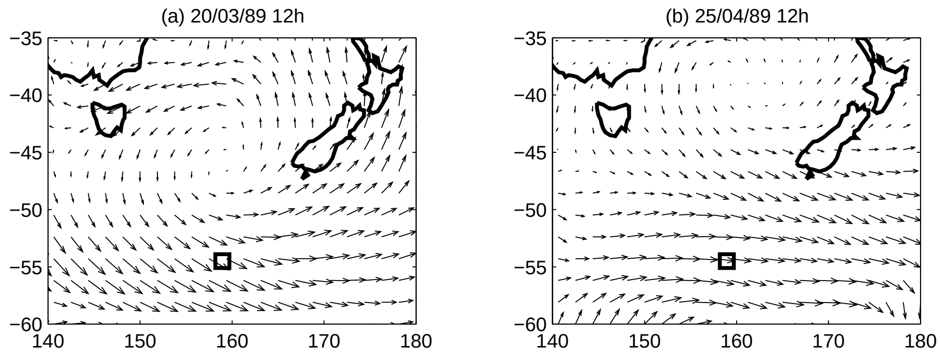

Figure 4.6: *Surface winds U_{10} showing two fully-developed wind-sea events observed in the Southern Ocean. In panel (a), a polar high pressure system, pictured on 20/03/1989, remains approximately stationary over the Tasman Sea. Panel (b) shows consistent westerly winds over a large area on 25/04/1989. Scales are in degrees of latitude and longitude.*

More importantly, Alves et al. (2000) produced a combined data base with 121 observations representative of fully-developed conditions by merging Arabian Sea, Macquarie Island and Moskowitz (1964) data sets. The unavailability of f_p measurements from both the Moskowitz (1964) and the Arabian Sea data sets limited their joint analysis to observed values of H_s (E_{tot}). Their combined analyses provided a U_{10}-scaled asymptote $\varepsilon_{10,lim}$ that was statistically identical across individual data sets.

A plot of dimensional and U_{10}-scaled nondimensional asymptotes is shown in Figure 4.7, panels a and c, respectively. The average value computed from the combined data set was

$$\varepsilon_{10,lim} = [4.26 \pm 0.18] \times 10^{-3}. \tag{4.24}$$

The resulting $\varepsilon_{10,lim}$, which is also based in observations of E_{tot} from the original Moskowitz (1964) data set, is 20% higher than the value obtained through integration of the analytical PM spectrum $\varepsilon^{an}_{10,lim} = 3.64 \times 10^{-3}$.

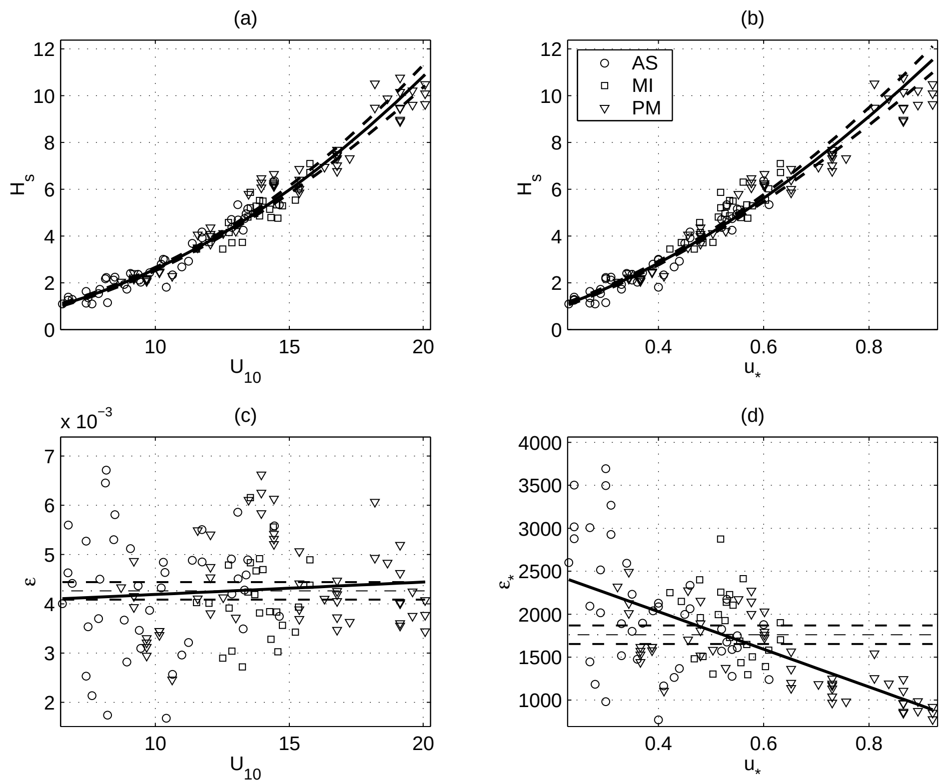

Figure 4.7: *Plot of significant wave height H_s from the combination of data from the Arabian Sea [AS], Macquarie Island [MI] and Moskowitz (1964) [PM] against (a) U_{10} and (b) u_*. The asymptotes ε and ε_* are plotted against U_{10} and u_* in panels (c) and (d), respectively. Continuous lines in all panels show the linear least squares fit between indicated variables. Dashed lines in panels (a) and (b) are the 95% confidence intervals of the mean. In panels (c) and (d), dash-dotted lines show average values of indicated asymptotes, while dashed lines show corresponding 95% confidence limits.*

Although u_*-scaled asymptotes $\varepsilon_{*,lim}$ were statistically different across individual data sets, suggesting the inadequacy of the friction velocity as a scaling parameter, Alves et al. (2000) computed an average value from the combined data set, resulting in

$$\varepsilon_{*,lim} = [1.76 \pm 0.11] \times 10^3. \tag{4.25}$$

Frequency spectra from Macquarie Island provided a nondimensional asymptote ν that was slightly different to the value $\nu_{10,lim} = 0.13$ derived from the Moskowitz (1964) data set

$$\nu_{10,lim}^{obs} = 0.122 \pm 0.005. \tag{4.26}$$

The corresponding u_*-scaled parameter was also different to the value $\nu_{*,lim} = 5.6 \times 10^{-3}$ proposed by Komen et al. (1984)

$$\nu_{*,lim}^{obs} = [4.68 \pm 0.21] \times 10^{-3}. \tag{4.27}$$

Results from validation experiments presented in Chapter 5 adopt the asymptotic evolution limits proposed by Alves et al. (2000) as upper bounds to the evolution curves provided by Kahma and Calkoen (1992). However, as the evolution limits proposed by Moskowitz (1964), Pierson and Moskowitz (1964) and Komen et al. (1984) are widely used in wind-wave modelling applications, they are also included in the analyses presented in the following Chapters.

4.2 Properties of fetch-limited wave spectra

Fetch-limited spectra are generally represented by parametric expressions derived from observations. These expressions are usually based on the concept that there exists a power-law dependence of the energy density levels at ranges much higher than the spectral peak on the angular frequency ω. This dependence may also be expressed in terms of the frequency f or the wavenumber k. Phillips (1958) called this part of the wave spectrum the equilibrium or saturated range. Assuming that the amplitudes of high wavenumber spectral components were controlled by wave breaking, he proposed, on dimensional grounds, the following relationship describing the shape of the equilibrium range:

$$F(\omega) = \alpha_p g^2 \omega^{-5}, \tag{4.28}$$

where α_p is the Phillips constant.

An alternative conceptual model was proposed by Toba (1973), who argued that spectral density levels within the equilibrium range would also depend on the wind intensity, represented by the friction velocity u_*. Again on dimensional grounds, he obtained a relationship in the form

$$F(\omega) = \alpha_t g^2 u_* f^{-4}, \tag{4.29}$$

where α_t is a proportionality constant.

Phillips' equilibrium range model was used by Pierson and Moskowitz (1964) to describe the high frequency range in a parametric expression representing fully-developed wave spectra (the PM spectrum). The parameterisation of fetch-limited spectra observed during the JONSWAP experiment (Hasselmann et al., 1973) derived by Hasselmann et al. (1976) and Müller (1976) was an improvement of the

PM spectrum that included a spectral peak enhancement factor, but maintained Phillips' equilibrium range model at higher frequencies. The resulting JONSWAP spectrum is obtained through the expression

$$F(\omega) = \alpha_j g^2 2\pi\omega^{-5} \exp\left[-1.25\left(\frac{\omega}{\omega_p}\right)^{-4}\right] \daleth^{\iota} \tag{4.30}$$

where the exponent controlling the peak enhancement, ι, is given by

$$\iota = \exp\left\{-\frac{\left(\omega - \omega_p\right)^2}{2\sigma^2\omega_p^2}\right\}, \tag{4.31}$$

and where α_j is once more the Phillips constant, $\daleth$ is a peak enhancement factor and σ is the spectral width parameter. The JONSWAP spectrum (4.30) reduces to the PM spectrum when $\iota = 1$.

Directional spectra may be produced through multiplying (4.30) with a directional spreading function, giving $F(\omega, \theta) = F(\omega)D(\omega, \theta)$. Initial conditions of most numerical experiments described in the present study were prescribed by a JONSWAP spectrum with directional spreading given by a parametric form due to Longuet-Higgins et al. (1963)

$$D(\omega, \theta) = D_0 \cos^{2s}\left(\frac{\theta - \overline{\theta}}{2}\right). \tag{4.32}$$

where G_0 is a normalising constant, $\overline{\theta}$ is the mean direction and s is a bandwidth parameter. Alternative values for s are given by Mitsuyasu et al. (1975), Hasselmann et al. (1980) and Kuik et al. (1988).

More recent field observations of wind-wave spectra reported in Mitsuyasu et al. (1975), Kahma (1981), Donelan et al. (1985) and Banner (1990) support the use of a parametric form similar to (4.29). A parametric expression describing fetch-limited spectra with a high frequency tail proportional to ω^{-4} is provided by Donelan et al. (1985)

$$F(\omega) = \alpha_d g^2 \omega^{-4} \omega_p^{-1} \exp\left\{-\left(\frac{\omega_p}{\omega}\right)^4\right\} \daleth^{\iota}, \tag{4.33}$$

where α_d is the equilibrium range parameter, $\daleth$ is the peak enhancement factor, ι is an exponent controlling the peak enhancement given by equation (4.31) and σ is the spectral peak width parameter, all given by functions of the wave age parameter U_{10}/c_p [see Donelan et al. (1985) or Komen et al. (1994)]. The directional spreading function associated with (4.33) is also provided by Donelan et al. (1985)

$$D(\omega, \theta) = 0.5 D_d \mathrm{sech}^2 D_d(\theta - \theta(\omega)), \tag{4.34}$$

where the spreading parameter D_d is a function of the ratio ω/ω_p given by

$$D_d = \begin{cases} 2.61\left(\frac{\omega}{\omega_p}\right)^{1.3} & : \; 0.56 < \omega/\omega_p < 0.95 \\ 2.28\left(\frac{\omega}{\omega_p}\right)^{-1.3} & : \; 0.95 \leq \omega/\omega_p < 1.6 \\ 10^{-0.4+0.8393\exp\left\{-0.567 ln((\omega/\omega_p)^2)\right\}} & : \; \omega/\omega_p \geq 1.6 \end{cases} \tag{4.35}$$

The expression for D_d for $\omega/\omega_p \geq 1.6$ was proposed by Banner (1990) from high wavenumber stereo photogrametric data.

Computational experiments described in the following Chapter were made with a numerical model that solves the evolution of the wavenumber spectrum $F(k,\theta)$. Expressions (4.28) to (4.35), therefore, were converted from their frequency-directional form through

$$F(k,\theta) = \varphi(\omega,\theta)\frac{\mathrm{d}\omega}{\mathrm{d}k}. \tag{4.36}$$

The parametric spreading function (4.34) and associated values of the parameter D_d were derived from an extensive observational data base reported in Donelan et al. (1985) and Banner (1990). Therefore, they provide observational references for the directional distribution of energy at several ranges of the wave spectrum. These will be used in the following Chapter to assess model performance in association with the model for the wavenumber spectral slice in the wind direction ($\theta = \theta_{wind}$) proposed by Banner (1990)

$$F_B(k,\theta_{wind}) = 4.5\times 10^{-5}\left(\frac{U_{10}}{c_p}\right)^{1/2} k^{-4}, \tag{4.37}$$

where c_p is the phase speed of waves at the spectral peak.

4.3 Summary of validation parameters

The following Chapter presents results of several numerical experiments designed to validate new formulations of the dissipation source function S_{ds} presented in Chapter 3. The validation strategy consists basically of comparing computed fetch-limited integral spectral parameters E_{tot} and f_p with target nondimensional evolution curves proposed by Kahma and Calkoen (1992). According to the specification of the S_{in} term, target curves are given by (i) U_{10}: equations (4.10) and (4.11), with asymptotic limits given by (4.24) and (4.26); (ii) a sea-state independent u_*: equations (4.13) and (4.14); or a sea-state dependent u_*: equations (4.15) and (4.16), with asymptotic limits given by (4.25) and (4.27).

A brief assessment of model performance in terms of two-dimensional properties of the wave spectrum is also made through analyses of the following diagnostic parameters suggested by Banner and Young (1994)

(i) Mean level $\overline{\alpha}_B$ and mean slope $\overline{n}_B$ of the wind direction slice of the wavenumber spectrum $F(k, \theta_{wind})$ derived from the power-law relationship proposed by Banner (1990)

$$\overline{F}(k, \theta_{wind}) = \overline{\alpha}_B \times 10^{-5} \left(\frac{U_{10}}{c_p}\right)^{1/2} k^{-\overline{n}_B}, \tag{4.38}$$

where $\overline{\alpha}_B$ and $\overline{n}_B$ were determined using a least square fit to wavenumbers within $6.25k_p \leq k \leq 25k_p$.

(ii) Mean spectral width $\overline{\theta}(k)$

$$\overline{\theta}(k) = \frac{\int_0^{\pi/2} \theta F(k, \theta) d\theta}{\int_0^{\pi/2} F(k, \theta) d\theta} = \frac{\int_0^{\pi/2} \theta D(k, \theta) d\theta}{\int_0^{\pi/2} D(k, \theta) d\theta}, \tag{4.39}$$

with the $D(k, \theta)$ satisfying $F(k, \theta) = F(k) D(k, \theta)$.

This spectral width parameter $\overline{\theta}(k)$ is representative of the directional distribution of model spectra. Comparisons are made with data reported in Banner

(1990) for $\overline{\theta}(k)$ at $k = k_p$ and $4k_p$, respectively. Alternative expressions for the width parameter that are independent of the shape of the spreading function are provided by Kuik et al. (1988), for example. Equation (4.39) is adopted in the present study to allow a comparison of the new modelling results with those reported in Banner and Young (1994).

(iii) Relative spectral tail (local) energy parameter ϵ_B

$$\epsilon_B = \frac{F(k, \theta_{wind})}{F_B(k, \theta_{wind})}, \tag{4.40}$$

which provides a measure of changes in the tail energy levels in relation to the parametric equilibrium range model of Banner (1990) F_B, given by equation (4.37). Both terms in (4.40) are evaluated at $k = 6.25k_p$ and $k = 12.25k_p$ within the spectral slice in the wind direction θ_{wind}.

Chapter 5

Exact Nonlinear Computations of Fetch-Limited Evolution

This Chapter presents the results of numerical experiments designed to validate the newly-proposed forms of S_{ds} described in Chapter 3. These experiments consisted of simulations of the fetch-limited evolution of wind-waves, computed with with the exact nonlinear wind-wave model described in Tracy and Resio (1982). Validation was made against the nondimensional evolution curves proposed by Kahma and Calkoen (1992, 1994), with asymptotic limits based on Pierson and Moskowitz (1964) and Alves et al. (2000). The validation strategy aimed at determining the S_{ds} implementations that brought model results to an optimal agreement with these target evolution curves.

Details of the experimental setup are presented in the following section. Results are reported subsequently in three sections. Section 5.2 is dedicated to experiments made with a version of the new dissipation function that depends nonlinearly on an integrated spectral peak steepness parameter, given by equation (3.4). These tests are initially made with the form of S_{in} due to Yan (1987). The performance of the more general form of S_{ds} given by equation (3.7), which is dependent on a nonlinear function of the azimuthally integrated saturation spectrum $B(k)$, is explored in Section 5.3. This form of S_{ds} is tested using three different forms of S_{in} due to Snyder et al. (1981), Yan (1987) and Janssen (1991), respectively.

Section 5.3 also includes a comparative analysis of the performance of the new dissipation function relative to the forms of S_{ds} used in Cycles 3 and 4 of the WAM model. Section 5.4 provides a preliminary evaluation of model results in terms of the width of directional spreading of the wavenumber spectrum. Finally, section 5.5 presents a brief analysis of computed rates of swell decay in comparison to the observations of Snodgrass et al. (1966). Assessments of model performance in all sections are made against the set of empirical parameters described in Chapter 4.

5.1 Experimental setup

Fetch-limited conditions occur when spatially homogeneous and time-invariant winds blow perpendicularly off a straight coastline. The resulting wave field will be governed by the one-dimensional form of the energy balance equation (2.15), given by

$$\left\{ \frac{\partial}{\partial t} + c_g \cos\theta \frac{\partial}{\partial x} \right\} F(k,\theta) = S_{in} + S_{nl} + S_{ds}, \tag{5.1}$$

where x is the spatial dimension aligned with the wind direction.

In theory, a further simplification of equation (5.1) may be made by eliminating the unsteady term $\partial F(k,\theta)/\partial t$, as fetch-limited evolution is a steady-state process. On the numerical side, however, sensitivity tests discussed below indicated that retaining the time dependent term of equation (5.1) compensated for limitations of its numerical solution, allowing a better convergence of model results towards an equilibrium state. This was particularly important at short fetches, when the wind-sea is young and the spectral energy density is concentrated at very short wavelengths.

The drawback of retaining $\partial F(k,\theta)/\partial t$ in the numerical solution of (5.1) was a resulting increase by one order of magnitude in the demands of computational time. A compromise option was to use the simple time-independent solution, with $\partial F/\partial t = 0$, during preliminary assessments and tuning of alternative S_{ds} forms made in section 5.2. These preliminary exercises, therefore, were made using what was called the basic setup. The transient term was included later to allow a more precise analysis of evolution at very short fetches. This model implementation was called the short-fetch setup. A description of both implementations follows below.

5.1.1 Basic setup

The basic setup was used in most of the experiments described in Section 5.2. It consisted essentially of using the steady-state form of the fetch-limited action balance equation (5.1), which was solved numerically with a first-order forward-difference numerical scheme. Following Komen et al. (1984), Hasselmann and Hasselmann (1985), Banner and Young (1994) and Tolman (1992), the numerical model had a spatial step Δx dynamically adjusted to maintain numerical stability and accuracy.

The directional wavenumber spectrum $F(k,\theta)$ was discretised into a polar grid with 53 angular bands defined in the range $\pm 120°$ and 43 wavenumbers within the bandwidth limited by 2.26×10^{-3} and 3.83 rad m^{-1}. Wavenumbers were logarithmically spaced according to the relationship $k_n = 1.13k_{n-1}$. This wavenumber grid configuration, with Δk defined in term of a geometric progression, is a property of the WRT method (Webb, 1978; Tracy and Resio, 1982) that allows a reduction of the computational effort required for the exact solution of the S_{nl} integral (2.25).

The chosen wavenumber bandwidth allowed the analysis of model performance from intermediate development stages up to full development. The wavenumbers represented in the computational grid remained the same throughout the computations, in opposition to using a variable wavenumber grid as reported in Tolman (1992) and Lavrenov and Ocampo-Torres (1999). Consequently, the maximum breadth of the nondimensional spectral range, defined in terms of the peak wavenumber k_p, varied from $4k_p$ ($2f_p$) at initial evolution stages to approximately $64k_p$ ($8f_p$) at full development. In opposition to most operational models that impose a parametric tail above $6.25k_p$ ($2.5f_p$), source terms were integrated explicitly at all wavenumber represented in the polar wavenumber grid of the basic setup.

In the WRT method for solving the S_{nl} term, only the vectors $\mathbf{k}_1$ and $\mathbf{k}_3$ and their corresponding energy densities are taken from the polar wavenumber grid. Corresponding loci of the $\mathbf{k}_2$ and $\mathbf{k}_4$ vectors are computed according to the resonant condition (2.24), and their energy densities are interpolated directly from the polar wavenumber grid. Changes of energy density associated with each pair of $\mathbf{k}_1$ and $\mathbf{k}_3$ vectors are computed by integrating a modified version of (2.25) around the corresponding loci of resonant $\mathbf{k}_2$ and $\mathbf{k}_4$ pairs. Following Tracy and Resio (1982), Young and Van Vledder (1993) and Banner and Young (1994), the loci of the $\mathbf{k}_2$ and $\mathbf{k}_4$ vectors were discretised into 50 points.

As pointed out by Banner and Young (1994), some of the loci defining the interacting $\mathbf{k}_2$ and $\mathbf{k}_4$ vectors extend beyond the high wavenumber cutoff of the polar grid at $k_{max} = 3.83$ rad m^{-1}. The contributions from these higher wavenumbers to S_{nl} was evaluated by extrapolating the energy density at k_{max} towards higher wavenumbers with a diagnostic tail. According to Banner and Young (1994), computational results are generally insensitive to the exact shape of the tail extension above a high enough cutoff wavenumber k_{max}. Nevertheless, a diagnostic spectral tail proportional to k^{-4}, which agrees with observations reported in Toba (1973), Donelan et al. (1985) and Banner (1990), was adopted in the present study.

5.1.2 Short-fetch setup

The short-fetch setup was designed to eliminate two major limitations of the basic setup, both associated with having the fixed wavenumber grid cutoff at $k_{max} = 3.83$ rad m^{-1}. The first has to do with the relatively short spectral wavenumber grid range that is resolved during early stages of evolution: only up to approximately $4k_p$ for a wind speed U_{10} =10 m s^{-1}, and an initial spectral peak frequency $f_p^0 = 0.5$ Hz. The second limitation regards the ratio k_{max}/k_p: as the wave field evolves with fetch, k_p decays and this ratio varies widely from 4 to 64, as mentioned in the previous subsection.

These two limitations may not be very important for the purposes of testing a new form of S_{ds} that affects primarily the spectral peak, as done in Section 5.2. The general form of S_{ds} (3.7) tested in Sections 5.3 and 5.4, however, is designed to specify dissipation rates at all scales, including the spectral tail above $6.25k_p$. Therefore, the experimental design for its proper assessment should include a numerical wavenumber grid extending well above $6.25k_p$. Furthermore, for a fair assessment of spectral properties at several evolution stages, it is appropriate that the ratio k_{max}/k_p remains constant throughout the computations.

The extension of the spectral grid towards higher wavenumbers is limited by restrictions on the validity of the Taylor series expansions used by Hasselmann (1962) to derive the S_{nl} integral (2.25). Banner and Young (1994) argue that the limit to the validity of S_{nl} can be expressed in terms of the ratio of the root-mean-square wave height H_{rms} to the shortest wave wavelength λ_{short}, with $k_{max} = 2\pi/\lambda_{short}$. The expansion is valid provided $H_{rms}/\lambda_{short} < \mathrm{O}(1)$. Based on their computations of fetch-limited evolution that had a maximum $H_{rms} = 1.85$m, Banner and Young (1994) chose a limiting wavenumber $k_{max} = 3.83$ rad m^{-1}.

However, when the condition $H_{rms}/\lambda_{short} < \mathrm{O}(1)$ is applied to a range of computed H_{rms} values at several fetch-limited evolution stages, it is found that k_{max} may be extended to wavenumbers greater than 3.83 rad m^{-1}, without affecting the validity of the S_{nl} expansion. Figure 5.1, panel (a), shows the evolution of H_{rms} against wave age U_{10}/c_p of a typical fetch-limited model run. Panel (b) shows the associated estimates of the ratio k_{max}/k_p, obtained by using the condition $H_{rms}/\lambda_{short} <$ O(1). Values of k_{max}/k_p vary from 27 to 63 as the wave field develops from young wind-seas into full development (e.g., $U_{10}/c_p < 1$).

Based on the results shown in Figure 5.1, the numerical grid used in the short-fetch setup consisted of 50 wavenumbers logarithmically spaced with $k_{max} = 25k_p^0$ ($f_{max} = 5f_p$), where k_p^0 is the peak wavenumber of the spectrum used to the computations. The lowest wavenumber in the spectral grid was defined as $k_{min} = k_{max}/\xi^{N-1}$, where the geometric progression factor ξ was set to 1.166 after extensive sensitivity tests considering computational costs and numerical convergence were made.

Absolute values of the initial wavenumber $k_p^0 = (2\pi f_p^0)^2/g$ were selected to match the nondimensional peak frequency $\nu = f_p U_{10}/g$ corresponding to the lowest nondi-

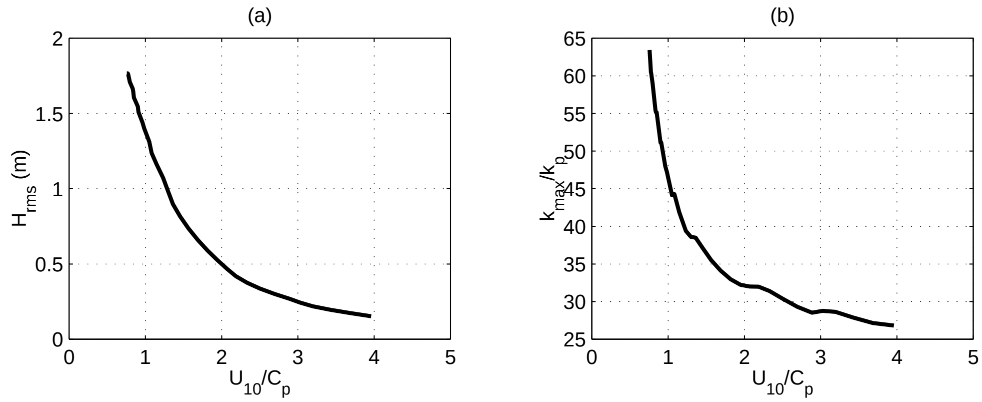

Figure 5.1: *Panel (a) shows the evolution of the root-mean-square wave height H_{rms} against wave ages U_{10}/c_p from a typical example of fetch-limited evolution. The forcing wind speed is U_{10} = 10 m s^{-1}. Panel (b) shows the corresponding ratio k_{max}/k_p computed according to the condition of validity of the S_{nl} expansion $H_{rms}/\lambda_{short} < O(1)$.*

mensional fetch χ_{min} within the valid range of the Kahma and Calkoen (1992, 1994) evolution curves. With U_{10} as the scaling wind speed, an initial nondimensional fetch $\chi_{min} = 1 \times 10^{-2}$ resulted in $\nu_{min} = 0.63$, which led to $k_p^0 = (2\pi\nu_{min}/gU_{10})^2$. Table 5.1 summarises the resulting absolute values of k_p^0, k_{min} and k_{max} corresponding to the three wind speed regimes used in this study, $U_{10} = 7.5, 10$ and 15ms $^{-1}$.

	U_{10} m s^{-1}		
	7.5	10.0	15.0
f_p^0	0.86 Hz	0.61 Hz	0.43 Hz
k_p^0	2.96 rad m^{-1}	1.48 rad m^{-1}	0.74 rad m^{-1}
k_{min}	0.04 rad m^{-1}	0.02 rad m^{-1}	0.01 rad m^{-1}
k_{max}	74.18 rad m^{-1}	37.09 rad m^{-1}	18.55 rad m^{-1}
N_k	50	50	50
ξ	1.166	1.166	1.166

Table 5.1: Configuration of wavenumber grids used in the short-fetch setup at three wind speed regimes $U_{10} = 7.5, 10$ and 15ms $^{-1}$. Parameters listed are initial peak frequency f_p^0, initial peak wavenumber k_p^0, lowest wavenumber of the grid k_{min}, highest wavenumber of the grid k_{max}, number of grid points N_k and geometric progression factor ξ.

The resulting array of wavenumber grids shown in Table 5.1 solves the limitations of the basic setup associated with the absolute value of k_{max}. The problem of having a ratio k_{max}/k_p that varies with fetch, however, remains, since the WRT code for solving S_{nl} used in the present study requires a fixed numerical wavenumber grid throughout the computations. A simple solution was to limit the explicit computation of source terms to the range $0.25k_p \leq k \leq 25k_p$, setting spectral densities below $0.25k_p$ to zero and approximating the spectrum within $25k_p < k \leq k_{max}$ with a diagnostic tail proportional to k^{-4}.

Experiments initialised at a nondimensional fetch $\chi_{min} = 1 \times 10^2$ involved explicit computations of source terms at very high wavenumbers. As the magnitude of the source terms is generally proportional to a high power of the wavenumber (e.g., Phillips, 1985), numerical instabilities at the spectral tail were observed in early evolution stages. This problem was substantially reduced by reintroducing the time-dependent term $\partial F(k, \theta)/\partial t$ of equation (5.1) into the numerical solution. Following a suggestion made by H. Tolman (personal communication, 1999), the new numerical scheme consisted simply of iterating each spatial propagation step of the two-point numerical grid over time until convergence towards a steady-state was reached.

5.1.3 Initial conditions

All model runs were initialised with a modified JONSWAP spectrum (Hasselmann et al., 1973). Parameters of the JONSWAP spectrum were specified through an adaptation of the expressions provided by Lewis and Allos (1990), which provided an optimal match to the Kahma and Calkoen (1992, 1994) fetch-limited evolution curves at different wind speeds and initial fetches. Experiments described in Section 5.2 were made with a single wind speed U_{10} = 10 m s $^{-1}$, and the initial peak frequency set to $f_p^0 = 0.55$Hz. In the short-fetch experiments of Sections 5.3 and 5.4, the initial peak frequency $f_p^0 = \sqrt{gk_p^0}$ was set according to Table 5.1 and three wind speeds $U_{10} = 7.5$, 10 and 15 m s $^{-1}$ were used.

5.1.4 Computed spectral parameters

The output of the numerical model consisted primarily of "raw" files with the two-dimensional wave spectrum and associated source terms at the polar wavenumber grid resolution. Other output files used for real time assessment and quality control included integral spectral parameters and general information about model runs. Raw files were post-processed using Matlab subroutines that computed the following parameters:

(i) total energy E_{tot}, determined through discrete integration of the computed wavenumber spectrum $F(k, \theta)$, according to

$$E_{tot} = \sum_{k=k_0}^{k_{max}} F(k, \theta) k \Delta k \Delta \theta, \tag{5.2}$$

for cases using the basic setup, and

$$E_{tot} = \sum_{k=0.25k_p}^{25k_p} F(k, \theta) k \Delta k \Delta \theta, \tag{5.3}$$

for experiments made with the short-fetch setup;

(ii) peak frequency f_p, derived directly from the dispersion relation $f_p = \sqrt{gk_p/2\pi}$, with peak wavenumber k_p computed according to Young (1995)

$$k_p = \frac{\sum_{\text{all }\theta} \sum_{k=0.25k_p^0}^{k=25k_p^0} kF^4(k,\theta)\Delta k \Delta\theta}{\sum_{\text{all }\theta} \sum_{k=0.25k_p^0}^{k=25k_p^0} F^4(k,\theta)\Delta k \Delta\theta}, \tag{5.4}$$

which provides a smooth estimate of k_p;

(iii) average spectral tail level $\overline{\alpha}_B$, average spectral tail slope exponent $\overline{n}_B$ and relative energy density ratio ϵ_B of the wavenumber spectral slice in the wind direction, computed according to item (i) of Section 4.3;

(iv) mean spectral width $\overline{\theta}(k)$ at k_p and $4k_p$, computed according to item (ii) of Section 4.3.

Other post-processing subroutines were available to produce plots of source terms at arbitrary output time steps and comparisons of integral parameters from model runs with observations.

5.1.5 Validation strategy

The validation strategy of the experiments described in this Chapter consisted in manually tuning parameters of the new forms of S_{ds}, aiming at an optimal fit of model results to spectral parameters associated with observations of fetch-limited wind-wave evolution. The primary goal was to reproduce with less than 10% bias the observed power-law evolution of integral spectral parameters E_{tot} and f_p with fetch, followed by a proper transition of these parameters towards the full-development limits. A secondary goal was to make a preliminary assessment of the effects of the new forms of S_{ds} on the shape of the wavenumber spectrum.

This validation approach was based primarily on the results of Banner and Young (1994), who provide an extensive performance analysis of the form of S_{ds} due to Komen et al. (1984) [hereafter, this form will be represented by the symbol S_{ds}^{w3}]. The analyses of Banner and Young (1994) showed that no tunings of S_{ds}^{w3} led to model results that reproduced properly observational data. The major problems are summarised in Figure 5.2, which compares results of the model runs made by Banner and Young (1994) with S_{ds}^{w3} against (i) observations of fetch-limited evolution of E_{tot} and f_p [panels (a) and (b)] and (ii) observations of the changes in the spectral shape parameters $\overline{\alpha}_B$, $\overline{n}_B$ and $\overline{\theta}$ with wave age c_p/u_* [panels (c) through (f)].

Using the two different forms of S_{in} due to Snyder et al. (1981) and Yan (1987), Banner and Young (1994) demonstrated that all variants of the Komen et al. (1984) dissipation term fail to reproduce the observed evolution curves of integral spectral parameters. Examples are shown in panels (a) and (b) of Figure 5.2, which show the nondimensional evolution of u_*-scaled E_{tot} and f_p against fetch from runs made with the Yan (1987) wind input term.

Figure 5.2, panel (a), shows that all variants of S_{ds} produced growth curves with no portion approximating a power law. When dissipation rates were set to provide a match of model results to observations at short fetches, the growth rate continuously decreased with fetch (dashed line associated with case Y10UT). Conversely, if dissipation rates were relaxed to allow a proper transition towards full development, growth rates became too large at short-fetches (dashed line associated with case Y10UTO4). A similar trend is observed in the evolution of f_p shown in panel (b).

Panels (c) through (f) of Figure 5.2 show that variants of S_{ds}^{w3} failed to reproduce observations of properties related to the shape of the wavenumber spectrum.

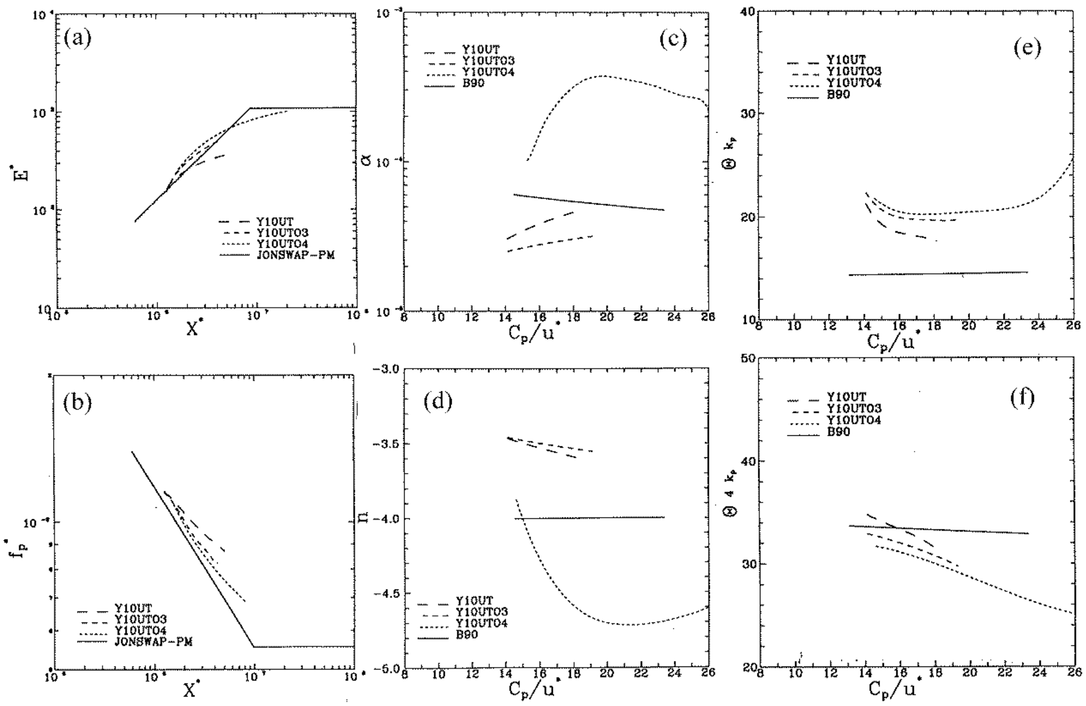

Figure 5.2: *Results of the Banner and Young (1994) experiments: Evolution curves of nondimensional (a) total energy $\varepsilon_* = E_{tot}g^2/u_*^4$ and (b) peak frequency $\nu_* = f_p u_*/g$ versus nondimensional fetch $\chi_* = Xg/u_*^2$ and (c) tail level $\overline{\alpha}_B$, (d) tail slope $\overline{n}_B$ and widths of directional spreading (e) at the peak wavenumber $\overline{\theta}(k_p)$ and (f) at a higher wavenumber $\overline{\theta}(4k_p)$ against inverse wave age c_p/u_* [adapted from Figures 11, 12 and 13 of Banner and Young (1994)].*

According to Banner and Young (1994), the directional width at the spectral peak wavenumber k_p was generally broader [panel (e)] and at high wavenumbers narrower [panel (f) shows the value at $4k_p$] than the observational data. Finally, panels (c) and (d) show that using S_{ds}^{w3} resulted in spectral tail levels $\overline{\alpha}_B$ and slope exponents $\overline{n}_B$ that were substantially different to observations.

Based on the results of Banner and Young (1994), attention was initially directed towards adjusting S_{ds} to provide higher dissipation rates at earlier development stages (young wind-seas at short-fetches) and, simultaneously, lower dissipation rates closer to full development. These were the basic aims of the experiments described in

Section 5.2, dedicated to the validation of the form of S_{ds} dependent on an integral peak steepness parameter, given by equation (3.4) of Chapter 3. Hereafter, this form will be represented by the notation S_{ds}^{peak}.

Validation tests of (3.4) were made using the basic model setup. Wind forcing was initially computed with the form of S_{in} due to Yan (1987), given by equation (2.19), and a single wind speed $U_{10} = 10\text{ms}^{-1}$. The consistency of these initial results was then verified by forcing the model with two other wind speeds corresponding to $U_{10} = 7.5$ and 15ms^{-1} and, finally, by extending the simulations to $\chi = 1 \times 10^2$ using the short-fetch setup.

Experiments described in Sections 5.3 and 5.4 were focused on validating the general form of S_{ds} dependent on the integrated saturation $B(k)$, given by equation (3.7) of Chapter 3 [hereafter, this form will be represented with the symbol S_{ds}^{b}]. Dissipation parameters were initially tuned to provide optimal model performance using the Yan (1987) form of S_{in} and three different forcing wind speeds.

Model results in sections 5.3 and 5.4 were compared to fetch-limited observations scaled with both u_* and U_{10}. As discussed in Chapter 2, the Yan (1987) input function was modified to allow proper comparisons with the U_{10}-scaled fetch-limited curves. The robustness of the general S_{ds} term (3.7) was finally validated with the two input source terms of Snyder et al. (1981) and Janssen (1991), presently used in several versions of the WAM (Komen et al., 1994; Günther et al., 1992) and SWAN (Booij et al., 1999) models.

5.2 Dissipation rates at the spectral peak

Experiments described in this section were made to validate S_{ds}^{peak}. As this function is primarily designed to provide dissipation rates of components within the spectral peak, the levels of dissipation at higher wavenumbers ($k > 9k_p$) were specified by a function of the integrated spectral steepness parameter $E_{tot}k_p^2$, weighted by the ratio $(k/\overline{k})^2$. This formulation is similar to the form of S_{ds} due to Janssen (1989), given by equation (2.29). Sensitivity tests indicated that this source function, in combination with S_{ds}^{peak}, provided the required source term balance at the spectral tail, where the Yan (1987) form of S_{in} becomes dependent on the inverse of the wave age parameter c/u_* squared.

The chosen combination of dissipation functions favoured stability of the numerical solution at high wavenumbers and, therefore, a clearer assessment of the spectral peak reaction to the new form of S_{ds}. Consequently, the new dissipation function (3.4) was applied below $k = 1.7k_p$, while the form (2.29) was used above $k = 9k_p$. A smooth transition within $1.7k_p \leq k \leq 9k_p$ was provided by a linear combination of these two forms of S_{ds}, determined through a weighting parameter given by $(9k_p - k)/(9k_p - 1.7k_p)$. The computation of dissipation rates using a form of S_{ds} divided in two parts was also explored in Tolman and Chalikov (1996).

5.2.1 Integrated S_{ds} with a fixed exponent p

The numerical experiments described in this subsection consisted of 17 model runs designated by a progressive sequence of letters from A to Q [henceforth referred to as the ABIF series]. Experiments were performed in a DEC Alpha 8200/5 server

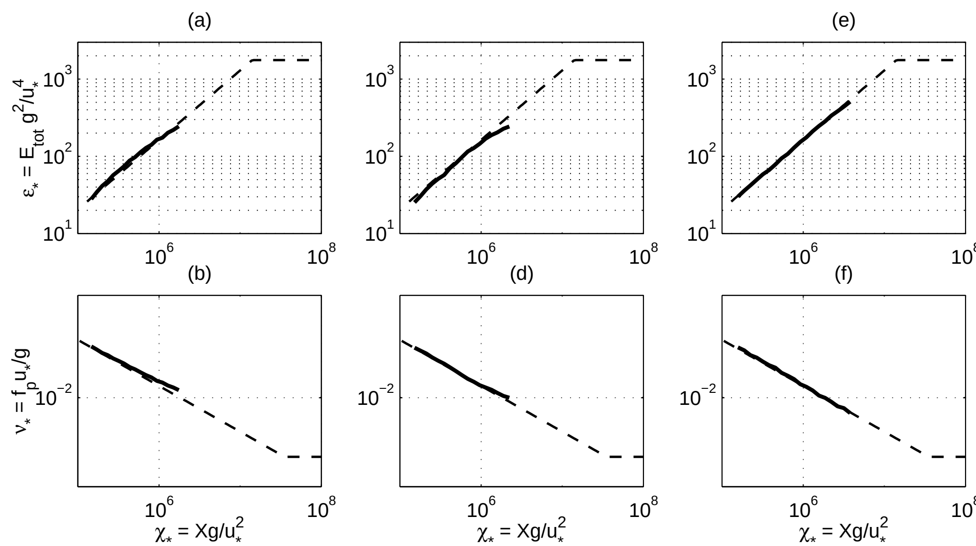

Figure 5.3: *Evolution of nondimensional total energy ε_* and peak frequency ν_* obtained from runs ABIF-K [panels (a) and (b)], ABIF-M [panels (c) and (d)] and ABIF-P [panels(e) and (f)]. These results are shown with solid lines. The dashed lines represent the target growth curves of Kahma and Calkoen (1992, 1994).*

with 4 CPUs running at 300 MHz. Computational times for typical runs with 10000 model cycles were approximately 10 hours. As in Banner and Young (1994), runs were terminated as soon as obvious trends were apparent. Validation of model results was made against the evolution curves given by (4.13) and (4.14), which are consistent with a form of S_{in} specified in terms of the sea-state-independent u_*.

Seeking an optimal fit to the target evolution curves only within their ranges of validity (e.g., up to $\chi_* = 3 \times 10^6$), the dissipation parameters of S_{ds}^{peak} were initially adjusted according to $0.04 \leq (ak)_r \leq 0.05$ and $p = [2,\ 4,\ 6]$ (subsequently a lower $(ak)_r$ was also used), with the constant C_{ds} tuned to give appropriate overall dissipation rates in each case. From 17 test cases, runs ABIF-K, ABIF-M and ABIF-P provided the best overall results. Figure 5.3 shows the evolution of nondimensional total energy ε_* and peak frequency ν_* obtained from these three runs. Corresponding dissipation parameters are listed in Table 5.2.

Run code	S_{ds}		
	C_{ds}	p	$(ak)_r$
ABIF-K	3.00×10^{-5}	2	0.040
ABIF-M	2.00×10^{-5}	4	0.050
ABIF-P	2.30×10^{-5}	6	0.050
ABIV-P	1.25×10^{-5}	6	0.038

Table 5.2: Dissipation parameters used in runs ABIF-K, -M and -P.

Results shown in Figure 5.3 indicate that the increased nonlinear dependence of spectral peak dissipation rates on the ratio $(ak)_p/(ak)_r$, obtained by changing progressively the exponent p from 2 to 6, resulted in a nearly unbiased match of model results to observed evolution curves of both E_{tot} and f_p for the case with $p = 6$ (run ABIF-P). This was a consequence of choosing a value of $(ak)_r$ that was smaller or greater than $(ak)_p$ at early stages of evolution or close to full development, respectively. This choice is consistent with the concepts about dissipation rates due to nonlinear group modulation outlined in Chapter 3.

A variation of run ABIF-P, designated ABIFPA, with $C_{ds} = 2.0 \times 10^{-5}$, $p = 6$ and $(ak)_r = 0.04$ was used to extend the validation of S_{ds}^{peak} towards the full-development limits. Resulting evolution curves of ε_* and ν_* from this model run are shown in Figure 5.4, panels (a) and (b), respectively. Panels (c) and (d) show the percentage bias between these parameters and the corresponding evolution curves within the range of valid fetch-limited observations (e.g., $\chi_* \leq 3 \times 10^{-6}$). In both cases the agreement of model results with observations within the valid fetch-limited range was remarkable, as the absolute percentage bias is never larger than 4%. As expected, model results diverged when the computed evolution curves approach the full-development limits.

The results of run ABIFPA were better understood through a more careful analysis

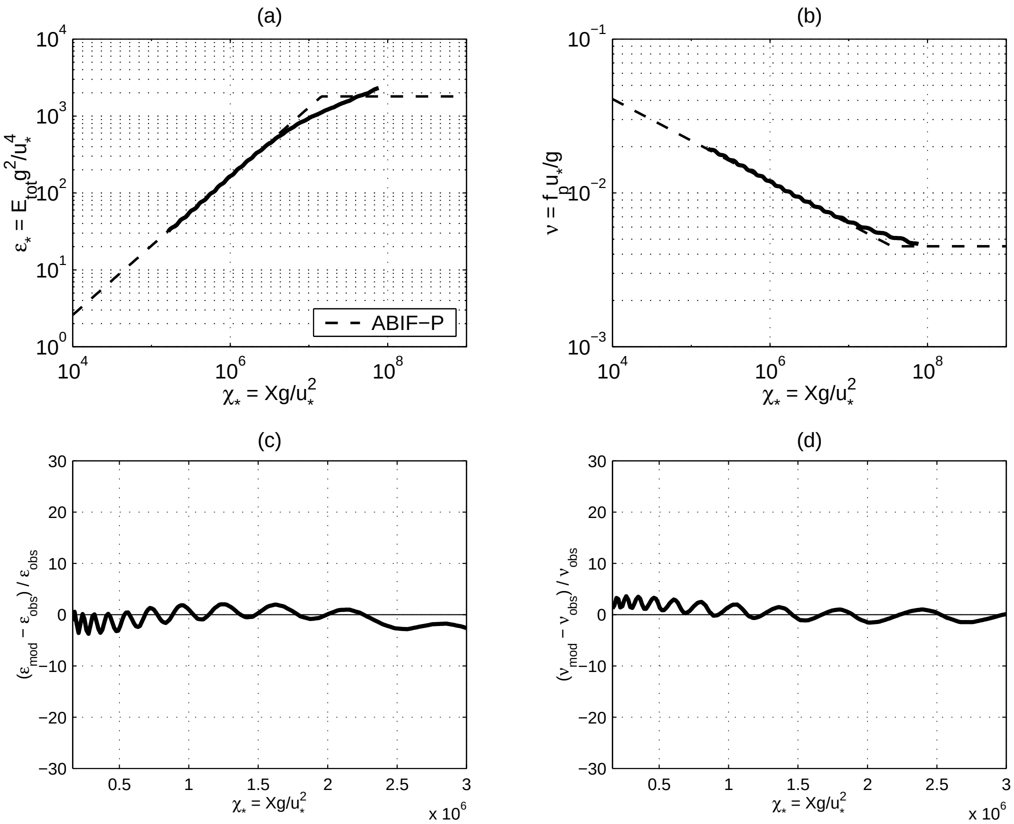

Figure 5.4: *Evolution curves from model run ABIFPA: (a) nondimensional total energy ε_* and (b) nondimensional peak frequency ν_*. Panels (c) and (d) show the percentage bias between these parameters and the corresponding Kahma and Calkoen (1992, 1994) evolution curves (shown as dash-dotted lines) within the valid range of fetch-limited observations (e.g., up to $\chi_* < 3 \times 10^{-6}$).*

of the source term balance associated with the transformation of young wind-seas into mature wind-seas and, finally, into fully-developed seas. In theory, input rates to the spectral peak become progressively smaller from young to mature wind-seas, vanishing at full development. At the spectral tail, input rates remain approximately constant at all development stages.

During early stages of development, nonlinear energy fluxes given by S_{nl} are characterised by a pronounced negative lobe at frequencies slightly above the spectral peak. The energy withdrawn from wavenumbers within this negative lobe is spread towards lower and higher wavenumber ranges. The fluxes are particularly strong at wavenumbers lower than the spectral peak. At full development, the levels of S_{nl} within the spectral tail become a small fraction of S_{in}. At the spectral peak, however, S_{nl} remains fairly active, as demonstrated numerically by Komen et al. (1984). Consequently, a transition of the wave field towards a fully-developed stationary state depends on a proper balance of this positive S_{nl} lobe and S_{ds}.

Figure 5.5 shows the balance of azimuthally-integrated source terms from run AB-IFPA at two stages of development, corresponding to young wind-seas [panels (a), (b) and (c)] and to the point where the solution diverges from the full-development limits [panels (d), (e) and (f)]. Levels of the source terms shown in Figure 5.5 were normalised by the maximum value of S_{in}. Panels on the left-hand side are associated with model results that matched well the target fetch-limited curves in Figure 5.4. Not surprisingly, the source term balance seems to correspond to the expected behaviour.

The panels on the right-hand side of Figure 5.5, however, reveal that although the levels of S_{in} had virtually vanished at the spectral peak, strong energy fluxes to this region continued to be provided by S_{nl}. As these nonlinear fluxes were not sufficiently damped by S_{ds}, the integral spectral pastep-likerameters estimated in run ABIFPA continued evolving beyond the asymptotic full-development limits, as seen in Figure 5.4.

These results confirm that a transition towards the asymptotic full-development limits may only exist if the positive lobe of S_{nl} at the spectral peak is balanced by S_{ds}, as pointed out by Komen et al. (1984). As discussed in Chapter 2, this idea was the basis of the dissipation source terms used in the WAM model. In the next

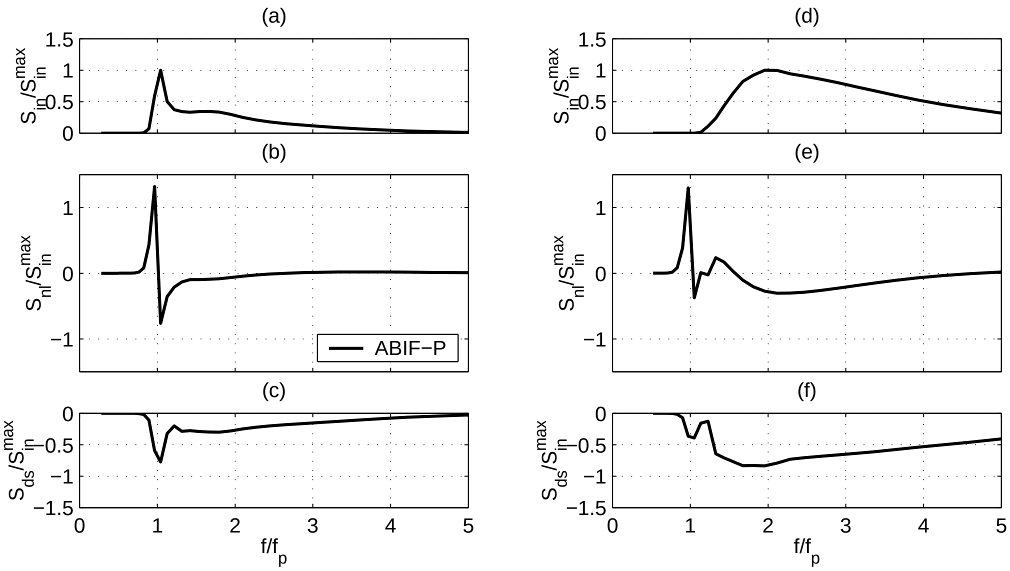

Figure 5.5: *Source term balance from run ABIF-P at an early development stage [panels (a), (b) and (c)] and at the point where spectral evolution has surpassed the full-development limits [panels (d), (e) and (f)]*

subsection, this problem is solved through an approach that remains faithful to the idea that dissipation rates of dominant waves depend nonlinearly on the more local parameter $(ak)_p$, and, more generally, on the saturation spectrum $B(k)$.

5.2.2 Variable exponent p

Experiments described in this subsection were designed to investigate the idea that although dissipation rates due to group modulation become vanishingly small when $(ak)_p < (ak)_r$, the wave field is still actively damped at all scales by other dissipative processes (e.g., background turbulence present in the upper ocean). This corresponds to modifying S_{ds}^{peak} to address the following conditions: (i) the contribution of energy losses from breaking due to nonlinear group modulation is cancelled when $(ak)_p < (ak)_r$ and (ii) other dissipative processes contribute actively to dissipation rates at the spectral peak and lower wavenumbers at any development stage, regardless of the dissipation rates associated with breaking due to group modulation.

A simple approach was used to verify if these modifications to S_{ds} would solve the problem of continuously growing mature wind-seas, without affecting the solution at earlier stages of development. This approach consisted in redefining the exponent p in equation (3.4) as a function of the ratio $(ak)_p/(ak)_r$ that becomes zero whenever $(ak)_p < (ak)_r$. Consistent with the conceptual framework presented in Chapter 3, this corresponds to shutting down dissipation rates due group modulation and, simultaneously, allowing S_{ds} to remain active due to other dissipative processes. As a first approximation, the contribution of background dissipation rates were assumed to be constant. Therefore, they were accounted for implicitly in the dissipation constant C_{ds}.

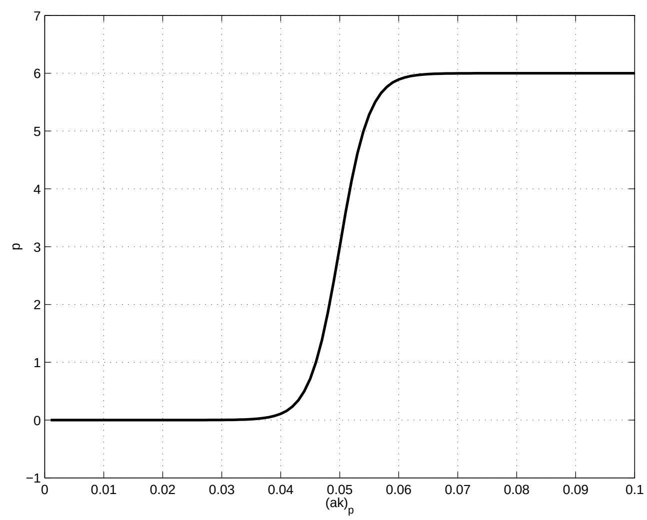

Figure 5.6: *Diagram of the exponent* p *as a function of* $(ak)_p$ *showing that equation (5.5) provides a sharp transition between* p_∞ *and zero that is not discontinuous.*

Preliminary tests showed that using a step-like function to specify the exponent p, in the form $p = \max(0, p_\infty)$, generated numerical instabilities during the transition between young and mature wind-seas. These problems were solved by defining p as a function of the ratio $(ak)_p/(ak)_r$ given by

$$p = \frac{p_\infty}{2} + \frac{p_\infty}{2} \tanh\left[10\left(\frac{(ak)_p}{(ak)_r} - 1\right)\right] \tag{5.5}$$

where $p_\infty = 6$ is the maximum value of p. Although providing a sharp transition between p_∞ and zero, as seen in Figure 5.6, equation (5.5) is still smooth enough to avoid numerical instabilities.

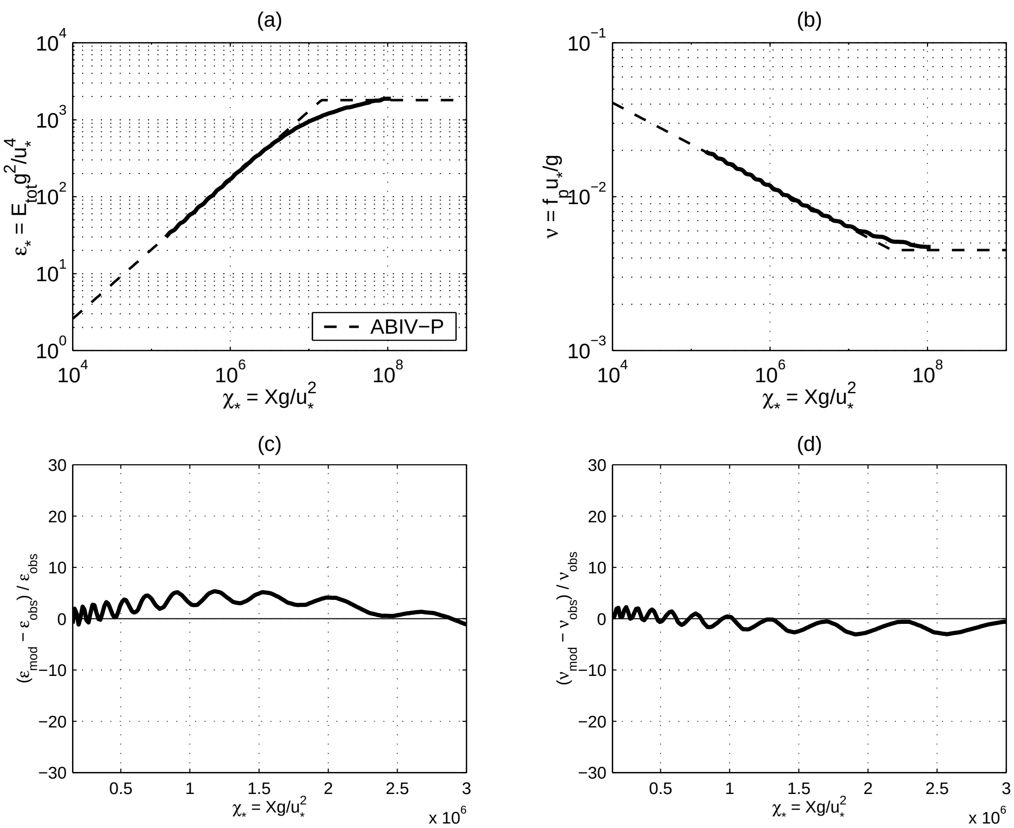

Figure 5.7: *Results from model run ABIV-P. The new definition of the exponent p provides proper dissipation rates in both fetch-limited and full-development ranges. Plots are (a) nondimensional total energy ε_* and (b) nondimensional peak frequency ν_*. Panels (c) and (d) show the percentage bias between these parameters and the corresponding Kahma and Calkoen (1992, 1994) evolution curves (shown as dash-dotted lines) within the range of available fetch-limited observations*

After adjustments to the parameters of S_{ds}^{peak}, a successful outcome was obtained with a model run designated ABIV-P. Results of this run are shown in Figure 5.7. Final values of the dissipation parameters are included in table 5.2. Source terms extracted from the output of run ABIV-P at two evolution stages are shown in Figure 5.8. Panels (a) to (c) show the azimuthally-integrated source terms at an early development stage, while panels (d) to (f) show the source terms at the point where the spectral evolution has become stationary. Source terms seem properly balanced in both situations. Consequently, model results and observations were in good agreement in all valid ranges of the target evolution curves.

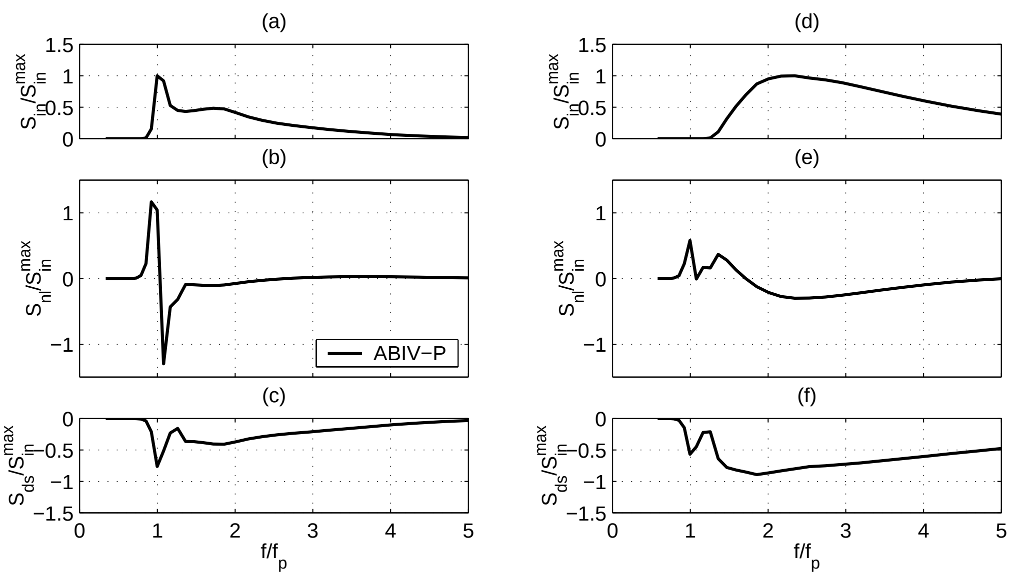

Figure 5.8: *Source term balance in run ABIV-P at an early development stage [panels (a), (b) and (c)] and at the point where spectral evolution has surpassed the full-development limits [panels (d), (e) and (f)]*

Further model runs using the short-fetch setup and three wind speeds $U_{10} = 7.5$, 10 and 15ms^{-1} were made to verify the robustness of these first successful results. The three extended runs were designated ABIV-XP7, ABIV-XP10 and ABIV-XP15, according to the forcing wind speed used in each case. Initial conditions consisted of a JONSWAP spectrum with peak frequencies defined in Table 5.1. Parameters of S_{ds}^{peak} were the same as in run ABIV-P. Results of runs ABIV-XP7, -XP10 and -XP15 are shown in Figure 5.9. Nondimensional evolution curves all collapsed approximately onto a single line, as expected from the similarity theory of Kitaigorodskii (1962). Small discrepancies may be explained by differences in resolution of the spatial stepping and of the spectral wavenumber grids associated with each model run. Apart from these discrepancies, Figure 5.9 shows good agreement between model results and the target fetch-limited evolution curves at all development stages.

These successful outcomes may be largely attributed to the fact that, by separating S_{ds} in two parts, dissipation rates at the spectral peak were allowed to have a wider dynamic range as the wave field evolved with fetch, due to its stronger nonlinear dependence on the local spectral peak steepness $(ak)_p$. This effect is illustrated in Figure 5.10, showing dissipation rates at two evolution stages corresponding to $c_p/u_* = 16$ [strongly forced wind-waves, panel (a)] and $c_p/u_* = 30$ [fully-developed seas, panel (b)]. To make this idea clearer, two directionally integrated forms of S_{ds}^{peak} with exponents $p = 4$ and $p = 6$ are shown. Both forms are normalised by the dissipation rates computed with $p = 6$ at $c_p/u_* = 16$.

The only differences in dissipation rates computed with $p = 4$ and $p = 6$ seen in Figure 5.10 occur within the spectral peak region of the diagrams in panel (a). In panel (b), the two forms overlap because in both cases $(ak)_p < (ak)_r$, which implies that $p = 0$. Both forms are also identical at higher wavenumbers, as they have the same specification of S_{ds} at $k > 9k_p$. Nevertheless, an intercomparison of S_{ds} reveals that the variation of relative dissipation rates within the spectral peak region between cases in panel (a) and (b) were of approximately 30% and 60% for cases

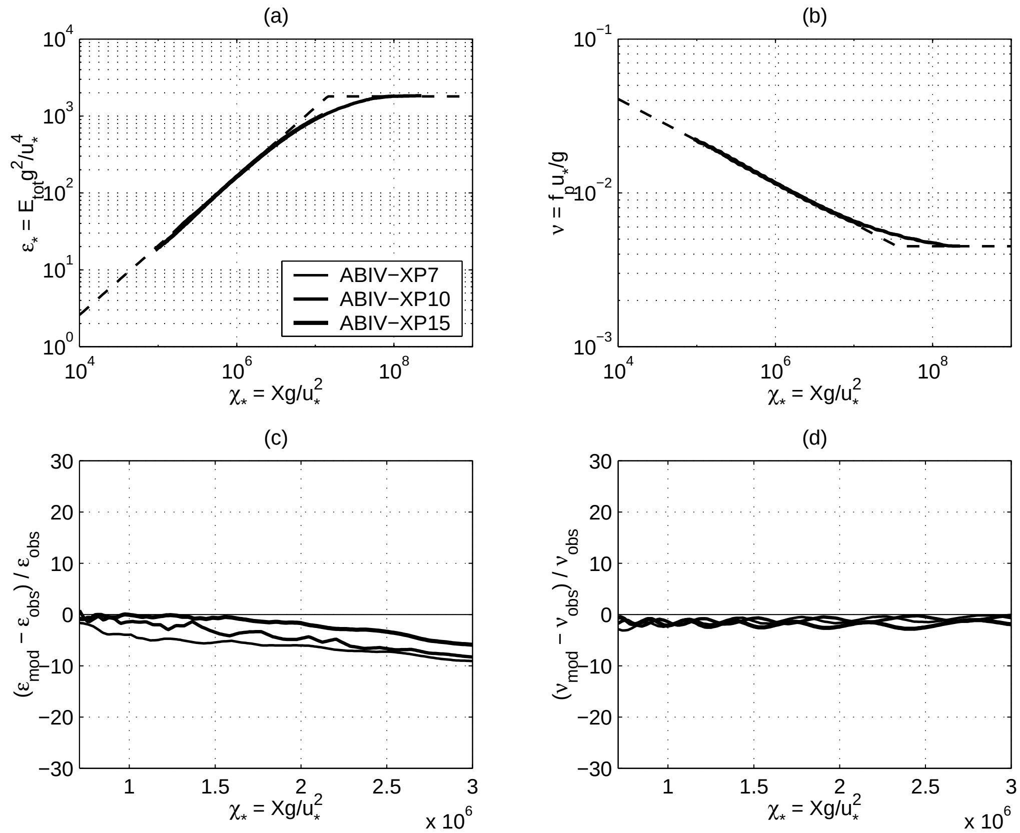

Figure 5.9: *Results from model runs ABIV-XP7, ABIV-XP10 and ABIV-XP15 demonstrate the robustness of agreement between model outcomes and the target KC curves. Plots are (a) nondimensional total energy* ε_* *and (b) nondimensional peak frequency* ν_**. Panels (c) and (d) show the percentage bias between these parameters and the corresponding Kahma and Calkoen (1992, 1994) evolution curves (shown as dash-dotted lines) within the range of available fetch-limited observations.*

with $p = 4$ and $p = 6$, respectively. Figure 5.10 thus demonstrates that a wider dynamic range of dissipation rates is obtained by increasing the nonlinearity of the dependence of S_{ds} on the spectral peak steepness $(ak)_p$.

The overall results in this section are qualitatively similar to those obtained by Tolman and Chalikov (1996), who independently proposed an alternative form of S_{ds} divided in two explicit constituents: a low-frequency dissipation part strongly dependent on the peak frequency f_p and a diagnostic high-frequency dissipation part

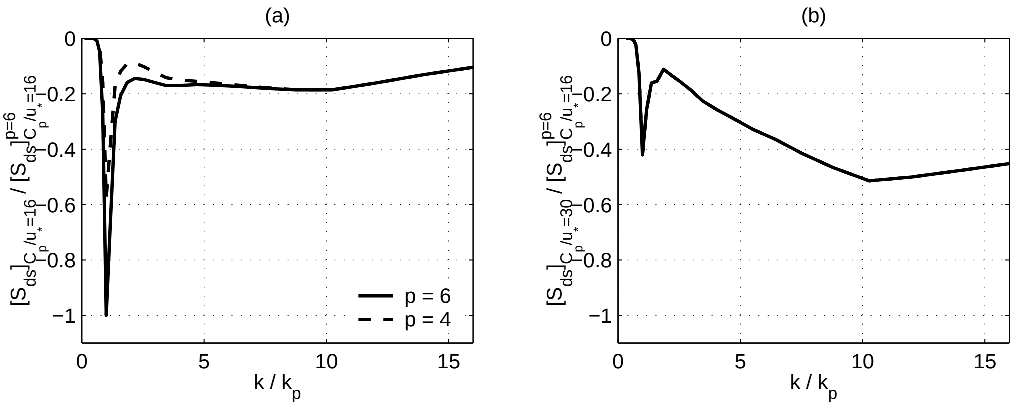

Figure 5.10: *Dissipation rates at two evolution stages (a) $c_p/u_* = 16$ and (b) $c_p/u_* = 30$. Two directionally integrated forms of S_{ds}^{peak} with exponents $p = 4$ (dashed line) and $p = 6$ (continuous line) are shown. Both forms are normalised by the dissipation rates computed with $p = 6$ at $c_p/u_* = 16$.*

designed to provide a balance to the input rates within that spectral range. In the case of fetch-limited evolution conditions, this results in dissipation rates that have a greater dynamic range within the spectral peak region, due to its strong dependence on f_p, while at the tail the dissipation rates are kept approximately constant.

5.3 Saturation-dependent dissipation rates

This section describes the results of experiments designed to validate the saturation-dependent dissipation function S_{ds}^b, given by equation 3.7. The validation of S_{ds}^b followed the same approach used in the previous sections, where dissipation parameters were adjusted manually to provide the best fit of model results to the fetch-limited evolution curves of Kahma and Calkoen (1992, 1994) and the asymptotic limit of Alves et al. (2000). This involved a large amount of computational effort, with single tests often extending over several days dedicated to the computations, the analysis of results and, in many cases, the repetition of the entire process until a robust outcome was achieved.

Validation tests were made with the exact nonlinear wave model of Tracy and Resio (1982), using the short-fetch setup and the form of S_{in} proposed by Yan (1987). As discussed previously, this input function provides a sound parametrisation of wind input rates at all scales of the wave spectrum. Forcing wind speeds were initially set to a single value $U_{10} = 10\text{ms}^{-1}$. Further validation of the robustness of the final form of S_{ds} were made with different specifications of S_{in} at several wind-speed regimes. The flexibility of the new dissipation function was also tested by fitting model results to the full-development limit proposed by Komen et al. (1984), based on the classic results of Pierson and Moskowitz (1964). Model runs were named according to the following convention: the first two characters identify the form of S_{ds}; the third character identifies the form of S_{in}, being either Y (Yan, 1987), S (Snyder et al., 1981) or J (Janssen, 1991); and the remaining characters identify particular properties of each individual test, such as wind speed or a particular parameter value.

The previous section analysed the performance of a two-component formulation of S_{ds} comprised of (i) a spectral peak term, with a strong nonlinear dependence on a local peak steepness parameter; and (ii) a high wavenumber term dependent on the integrated steepness $E_{tot}k_p^2$. In this section, the analysis focuses on the more general form S_{ds}^b, which is a single expression providing dissipation rates at all spectral ranges. As seen in Figure 3.10 of Chapter 3, its dependence on the local (azimuthally integrated) saturation spectrum $B(k)$ produces a wide dynamic range at the spectral peak as the wave field evolves from young wind-seas towards full development. On the other hand, dissipation rates at the spectral tail remain relatively unchanged. This property of S_{ds}^b, resulting from a strongly nonlinear dependence on the local saturation $B(k)$, provides a dynamical response that is in many ways analogous to that obtained with the division of S_{ds} in two distinct parts.

5.3.1 Validation of the saturation-dependent form

accommodates Results of the first successful test using S^b_{ds} are shown in Figure 5.11. Model predictions of nondimensional total energy ε_* and peak frequency ν_* are compared to the respective empirical fetch-limited evolution curves in panels (a) and (b). The percentage bias between model results and observations within the valid fetch-limited range of observational curves are shown in panels (c) and (d). Dissipation parameters of this model run, named ABYM0, were set to $C_{ds} = 1.2 \times 10^{-5}$, $B_r = 3.4 \times 10^{-3}$, $p_\infty = 6$ and $n = 2$. These values are listed in Table 5.3, along with a complete list of parameters used in other model runs described throughout this Chapter.

Predictions of ε_* and ν_* agree very well with the fetch-limited relations of Kahma and Calkoen (1992, 1994), as seen in Figure 5.11. Percentage bias between model estimates and target curves in both cases are within $\pm 5\%$. The maximum absolute discrepancies (around 5% in both ε_* and ν_*) occur at very short nondimensional fetches ($\chi_* \approx 1 \times 10^5$). At full development, model results are also in excellent agreement with the asymptotic limits proposed by Alves et al. (2000). Small oscillations of $\pm 1\%$ that become more apparent in the curves of panels (c) and (d) result from model adjustments to the shifting of k_p towards lower wavenumbers. As its numerical value “jumps” from one discrete spectral grid node to the next, the model rapidly to these changes and the outcome is a stable solution.

The effects of the new dissipation function on the behaviour of the spectral tail are

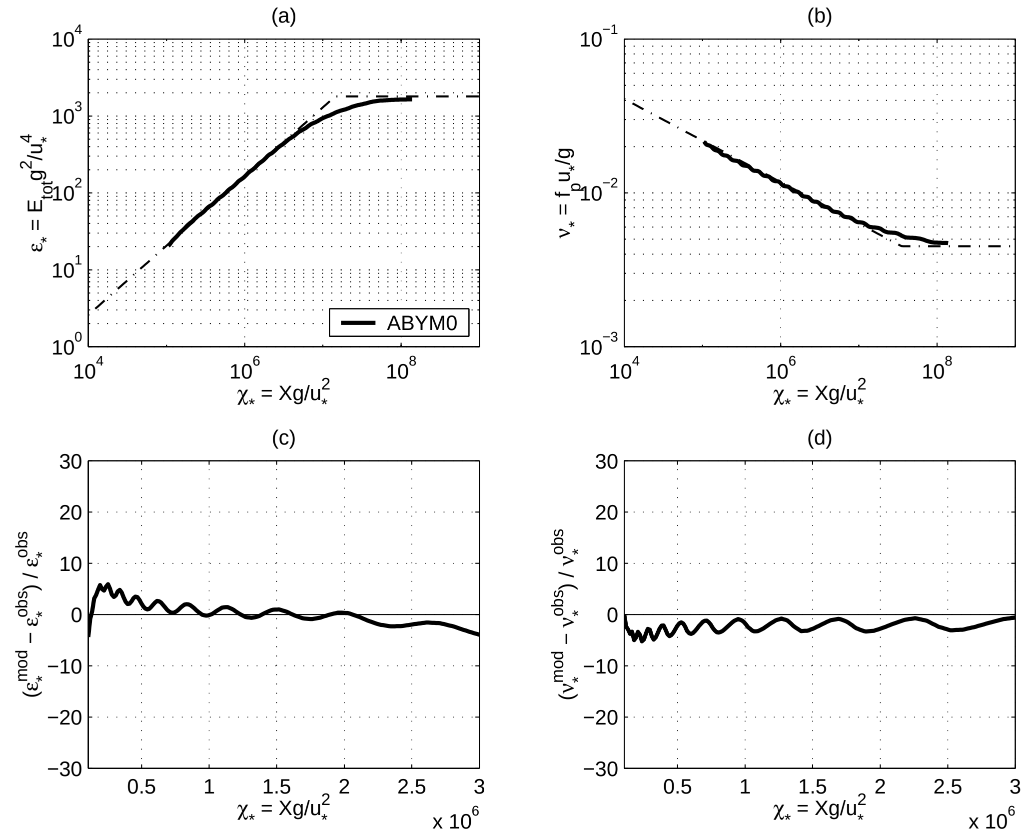

Figure 5.11: *Model predictions of nondimensional total energy ε_* (a) and peak frequency ν_* (b) from run ABYM0, compared to the respective empirical fetch-limited evolution curves (dashed lines). Percentage bias between model results and observations within the valid fetch-limited range of observational curves are shown in panels (c) and (d).*

summarised in Figure 5.12. Computed properties of the wavenumber spectral slice in the wind direction $F(k, \theta_{wind})$ are compared to the spectral tail shape and level parameters of Banner (1990), given by relations (4.37) and (4.40). The diagnostic parameters shown are: the average tail slope exponent $\overline{n}_B$ [panel (a)], with empirical value $\overline{n}_B = -4$; the tail level $\overline{\alpha}_B$, with empirical values indicated in panel (b) with a dashed line; and the ratio ϵ_B of computed tail energy density $F(k, \theta_{wind})$ and its empirical value $F_B k, \theta_{wind}$, evaluated at $k = 6.25k_p$ and $k = 12.25k_p$ [panels (c) and (d)], respectively. Spectral tail parameters are all plotted against the u_*-scaled wave age c_p/u_*.

Form of S_{ds}	Run code	S_{ds} C_{ds}	m	n	p_∞	B_r	δ
S_{ds}^{bs}	ABYM0	1.2×10^{-5}		2.0	8.0	3.4×10^{-3}	
	ABYM1	8.0×10^{-3}	1.0	2.0	6.0	4.2×10^{-3}	
	ABYM2	2.9	2.0	2.0	4.0	3.4×10^{-3}	
	ABYU	1.0×10^{-2}	1.0	2.0	6.0	4.2×10^{-3}	
	ABYPM	2.8×10^{-4}	0.35	2.0	8.0	4.5×10^{-3}	
	ABSU	4.1×10^{-3}	0.8	1.0	4.0	3.8×10^{-3}	
	ABSUS	4.0×10^{-3}	0.8	1.0	4.0	3.8×10^{-3}	
	ABSPM	3.7×10^{-4}	0.3	1.0	4.0	3.8×10^{-3}	
	ABJ	1.3×10^{-2}	1.0	2.0	8.0	3.1×10^{-3}	
S_{ds}^{w4}	W4YM2	9.4×10^{-5}	2.0				0.5
	W4YM3	2.4×10^{-5}	3.0				0.5
	W4YM4	1.2×10^{-5}	4.0				0.5
	W4YM5	0.8×10^{-5}	5.0				0.5
	W4YM4D4	0.6×10^{-5}	4.0				0.4
	W4YM3D3	0.4×10^{-5}	4.0				0.3
	W4YM3D6	1.9×10^{-5}	4.0				0.6

Table 5.3: Dissipation parameters of the saturation-dependent form of S_{ds}, corresponding to run codes with the prefix AB). Parameters adopted in the validation of the dissipation function used in the WAM Cycle 4 model (run codes with the prefix W4) are also indicated.

Panel (a) shows that the predicted spectral tail slope exponents $\overline{n}_B$ decrease with increasing wave age, instead of maintaining the constant k^{-4} slope inferred empirically. More significant, however, is the fact that the actual energy density levels at the tail provide an almost perfect match to the empirical levels, as indicated by a value of $\epsilon_B = 1$ at $k = 6.25k_p$ within a range of development stages extending up to $c_p/u_* = 22$. At the higher relative wavenumber position $k = 12.25k_p$, however, ϵ_B indicates an overestimation of energy densities that decreases as the wave field evolves from 40% to 20% of the empirical values. This reasonably stable behaviour of actual energy density levels at the tail, in combination with an increasing average slope $\overline{n}_B$, results in increasing values of $\overline{\alpha}_B$ seen in panel (b).

The good agreement between model predictions of energy density levels of the spectral tail and the empirical expressions of Banner (1990), indicated by values of ϵ_B

close to 1, are encouraging. However, the comparisons show that they are not yet optimal, particularly regarding $\overline{n}_B$ and $\overline{\alpha}_B$. Nevertheless, in relation to the results of Banner and Young (1994) shown in Figure 5.2, they provide a significant improvement relative to the form S_{ds}^{w3} proposed by Komen et al. (1984).

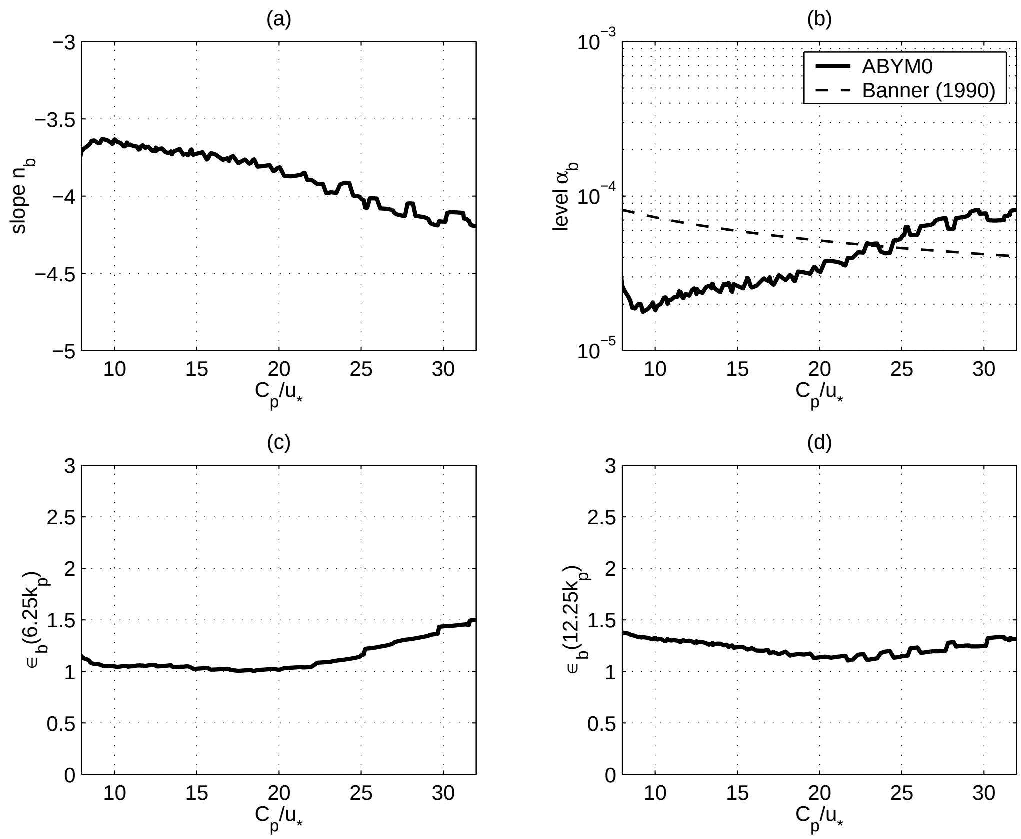

Figure 5.12: *Effects of the new dissipation function on the behaviour of the spectral tail. Computed properties of the wavenumber spectral slice in the wind direction $F(k, \theta_{wind})$ are compared to the spectral tail shape and level parameters of Banner (1990). The diagnostic parameters shown are: (a) the average tail slope exponent $\overline{n}_B$, (b) the tail level $\overline{\alpha}_B$ and the ratio ϵ_B of computed tail energy densities evaluated at (c) $k = 6.25k_p$ and (d) $k = 12.25k_p$. Parameters are all plotted against the u_*-scaled wave age c_p/u_**

As discussed in Chapter 3, dissipation rates within the spectral tail may be enhanced by processes other than breaking due to group modulation. These effects are added through an arbitrary $k/\overline{k}$ weighting parameter that, associated with the local dependence on $B(k)$, may not provide a complete representation of the dissipation rates required at higher wavenumbers. Therefore, further experiments were undertaken to assess the consequences of including an additional dependence of S^b_{ds} on an empirical parameter that has been shown to correlate well with properties of the spectral tail, as follows.

Observations of evolving wave spectra reported in Donelan et al. (1985) and Banner (1990) indicate that the energy levels of the spectral tail are well-correlated with the square root of the inverse wave age parameters $(U_{10}/c_p)^{1/2}$. The inclusion in S_{ds} of a term dependent on the wind speed, however, would contradict the assumption that dissipation rates are primarily related to the dynamics of the wave field alone. An alternative approach to describe the spectral tail behaviour using a property intrinsic to the wave field was proposed by Huang et al. (1981). Based on theoretical analysis and laboratory data, they express the observed decay of spectral tail levels with wave development in terms of a significant slope proportional to the integral steepness parameter $E_{tot}k_p^2$.

Field observations of fetch-limited wave growth reported by Donelan et al. (1992) have shown that E_{tot} and c_p/U are strongly correlated parameters. Therefore, their empirical relation for these two parameters, given by $E_{tot} \propto U^{4/5}c_p^{16/5}$, may be rewritten as $E_{tot}k_p^2 \propto (U/c_p)^{4/5}$ and combined with the expression for the tail level decay rate of Donelan et al. (1985) and Banner (1990), given by $F(k, \theta_{wind}) \propto (U/c_p)^{1/2}$. The result of this combination reconciles these relationships with the spectral-tail dependence on $E_{tot}k_p^2$ proposed by Huang et al. (1981), providing an alternative expression describing the decay rates of spectral tail energy densities that are proportional to a low power of the integral spectral steepness

$$F(k, \theta_{wind}) = \alpha_{ss}(E_{tot}k_p^2)^{0.63} k^{-n_{ss}}, \tag{5.6}$$

where α_{ss} and n_{ss} are level and slope parameters of the spectral tail, respectively.

The saturation-dependent function S_{ds}^b may, therefore, be modified to include this dependence on $E_{tot}k_p^2$, which results in the form

$$S_{ds}(k, \theta) = C_{ds} \left(\frac{B(k)}{B_r} \right)^{p/2} \left(E_{tot}k_p^2 \right)^m \left(\frac{k}{k_p} \right)^n \omega F(k, \theta), \tag{5.7}$$

where m is assumed to be a low power ≈ 1. This more general form of equation (3.7) will hereafter be represented by the symbol S_{ds}^{bs}.

The effect of including a linear dependence of S_{ds} on $E_{tot}k_p^2$ is illustrated in Figure 5.13. This figure shows a comparison of $(B(k)/B_r)^3$, in panel (a), and $E_{tot}k_p^2(B(k)/B_r)^3$, in panel (b), at two representative stages of development corresponding to young wind seas with $c_p/u_* = 8$ (continuous lines) and mature wind seas with $c_p/u_* = 15$ (dashed lines). Indicated parameters are normalised by their respective values at $c_p/u_* = 8$. A reference saturation level $B_r = 3 \times 10^{-3}$ is used. It is seen that by including $E_{tot}k_p^2$, the dynamic ranges of dissipation rates within the spectral tail (measured as the difference of level between the continuous and dashed lines at any given k/k_p) will increase up to two times relative to its original magnitude, while at the spectral peak this range will increase by only around 15%.

The impact of the new form S_{ds}^{bs} on predictions of fetch-limited spectral growth was investigated through run ABYM1, made with an exponent $m = 1$ and other dissipation parameters set according to the values listed in Table 5.3. The inclusion

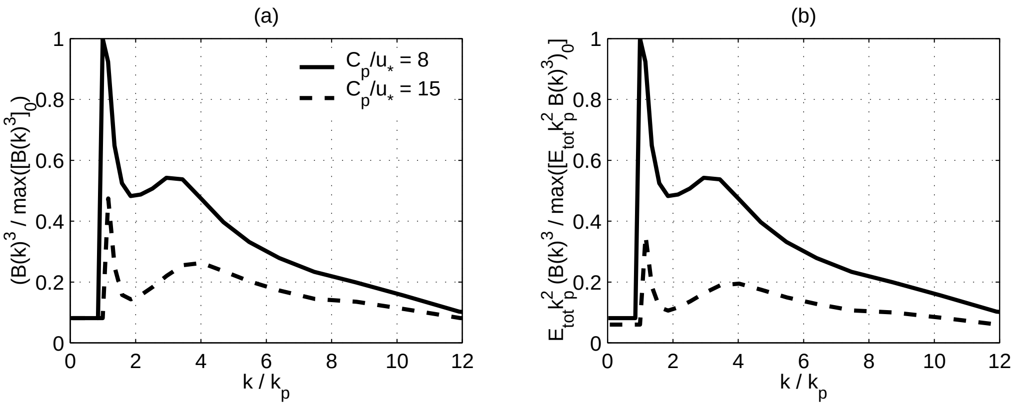

Figure 5.13: *Comparison of (a) $(B(k)/B_r)^3$ and (b) $E_{tot}k_p^2(B(k)/B_r)^3$ at two stages of development corresponding to young wind seas with $c_p/u_* = 8$ (continuous lines) and mature wind seas with $c_p/u_* = 15$ (dashed lines). Indicated parameters are normalised by their respective values at $c_p/u_* = 8$.*

of the new term in run ABYM1 resulted in increased dissipation levels relative to the previous form, as a consequence of an increase in the dissipation constant to $C_{ds} = 8 \times 10^{-3}$ needed to provide appropriate growth rates. To compensate for this effect, the nonlinearity of the term $(B(k)/B_r)^p$ had to be reduced by setting $p_\infty = 6$ and increasing B_r to 4.2×10^{-3}.

An intercomparison of the results from runs ABYM1 and ABYM0 is provided in Figures 5.14 and 5.15. Panels (c) and (d) show that the outcomes of run ABYM1 provide a better agreement with observations of ε_* and ν_* within the valid fetch-limited ranges of the empirical evolution curves, producing a mean percentage bias that is close to zero. After the transition towards full development, ε_* and ν_* both asymptote to values that are in good agreement with the full-development limits of Alves et al. (2000).

Figure 5.15 shows that the inclusion of the parameter $E_{tot}k_p^2$ has a substantial impact on the shape of the spectral tail. Although the range of variation in the spectral tail slope exponent $\overline{n}_B$ and in the tail level $\overline{\alpha}_B$ are comparable to those

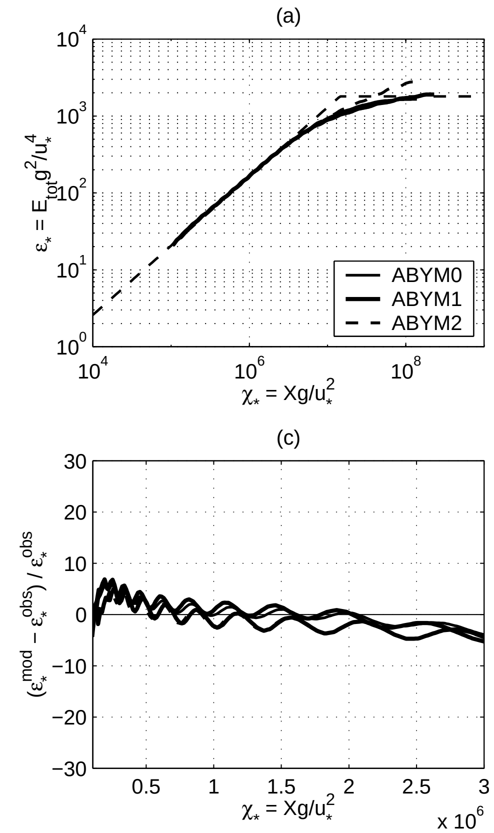

Figure 5.14: *Intercomparison of results from runs ABYM1, ABYM0 and ABYM2. Plotted parameters are (a) nondimensional total energy ε_* and (b) nondimensional peak frequency ν_*. Panels (c) and (d) show the percentage bias between these parameters and the corresponding Kahma and Calkoen (1992, 1994) evolution curves (shown as dash-dotted lines) within the range of available fetch-limited observations.*

of run ABYM0, their values now are generally closer to the empirical evolution curves. Energy densities at $6.25k_p$ still provide an excellent relationship with the empirical value of Banner (1990), providing a relative ratio close to 1. Computed levels at $12.25k_p$ were slightly improved, now ranging from a 30% overestimation at $c_p/u_* = 10$ to an almost perfect agreement at $c_p/u_* \approx 22$.

The effect of increasing the dependence of S_{ds}^{bs} on the integral spectral parameter $(E_{tot}k_p^2)^m$ was investigated in run ABYM2. Using an exponent $m = 2$ required a reduction in the strength of the term $(B(k)/B_r)^p$, achieved by setting $p = 4$

and $B_r = 3.4 \times 10^{-3}$. The dissipation constant was also retuned to $C_{ds} = 2.87$. Results of run ABYM2 are also shown in Figure 5.14. Computed integral spectral parameters were still in good agreement with the target evolution curves at short fetches. However, as the wave field evolved towards full development, the higher nonlinearity of $(E_{tot}k_p^2)^m$ resulted in a sharp reduction of the overall dissipation rates. In analogy to run ABIF-P, this led to an unbound net positive flux of energy towards the spectral peak, provided by the positive lobe of S_{nl}. Consequently, the wave spectrum and its associated integral parameters continued to evolve beyond the full-development limits.

Figure 5.15 shows that the effects of setting $m = 2$ were to stabilise even further the tail shape parameters $\overline{\alpha}_B$ and $\overline{n}_B$. However, the increased dissipation levels at short fetches resulting from the stronger dependence of S_{ds}^{bs} on $E_{tot}k_p^2$ resulted in values that were around 20% lower than the empirical energy densities of Banner (1990). This effect is indicated in panels (c) and (d).

Results from runs ABYM0, ABYM1 and ABYM2 suggest that there may be an optimal choice of S_{ds}^{bs} parameters that provide an improved model performance both in terms of the description of integral spectral properties and characteristics of the spectral tail. This, however, would benefit from using automatic optimisation techniques that were not available during this study. Efforts in that direction are envisaged in future research.

Further experiments were made to verify the robustness of the successful predictions of ε_* and ν_* obtained in runs ABYM0 and ABYM1. These consisted of forcing the wave model with two additional wind speeds $U_{10} = 7.5$ and 15m/s. Following the similarity theory of Kitaigorodskii (1962), model outcomes from runs made with

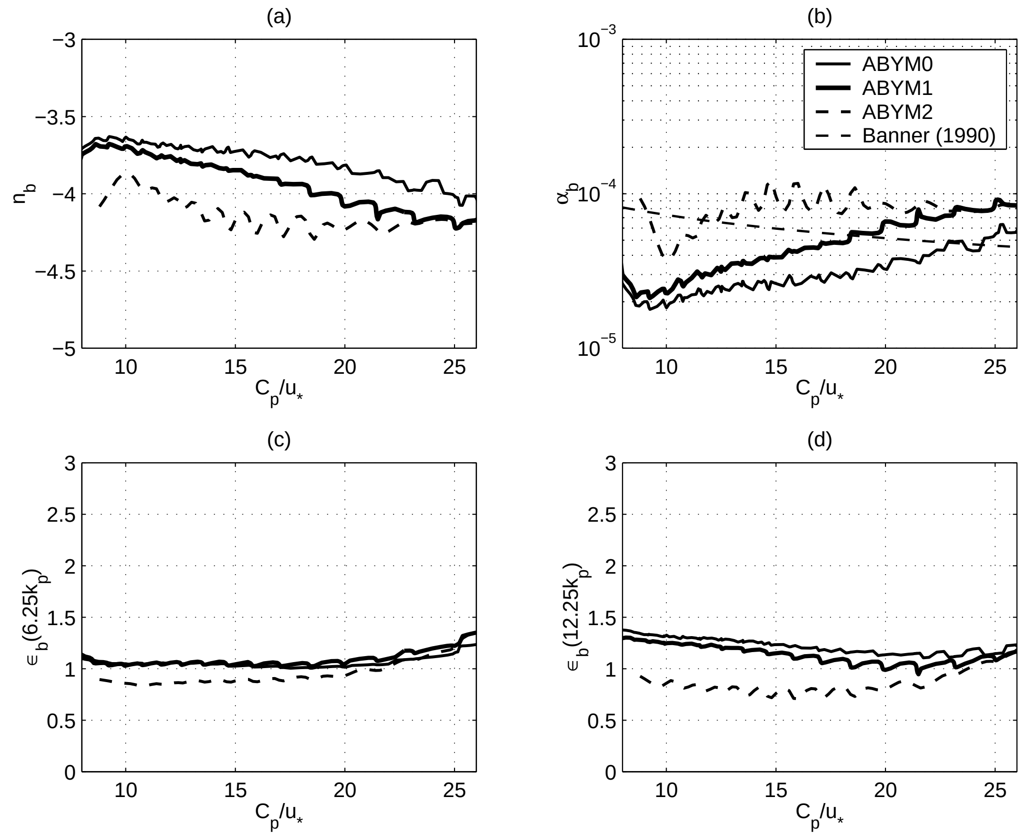

Figure 5.15: *Intercomparison of the spectral tail behaviour associated with runs ABYM1, ABYM0 and ABYM2. Validation is made against the empirical spectral tail parameters of Banner (1990): (a) average level* $\overline{\alpha}_B$*, (b) average slope* $\overline{n}_B$ *and relative energy density ratio* ϵ_B *of the wavenumber spectral slice in the wind direction at (c)* $k = 6.25k_p$ *and (d)* $k = 12.25k_p$*.*

different wind speeds are expected to produce values of nondimensional integral spectral parameters that collapse closely onto a single curve.

Results were initially compared to the u_*-scaled nondimensional curves of Kahma and Calkoen (1992, 1994), as the specification of the form of S_{in} proposed by Yan (1987) is made in terms of u_*. However, to increase the range of validation scenarios using the U_{10}-scaled empirical curves, this form of S_{in} was modified to become a function of U_{10}. Changes to S_{in} were made by replacing the parameter u_* in equation (2.19) by $U_{10}/26.26$. These two parameters are identical for $U_{10} = 10$m/s. With

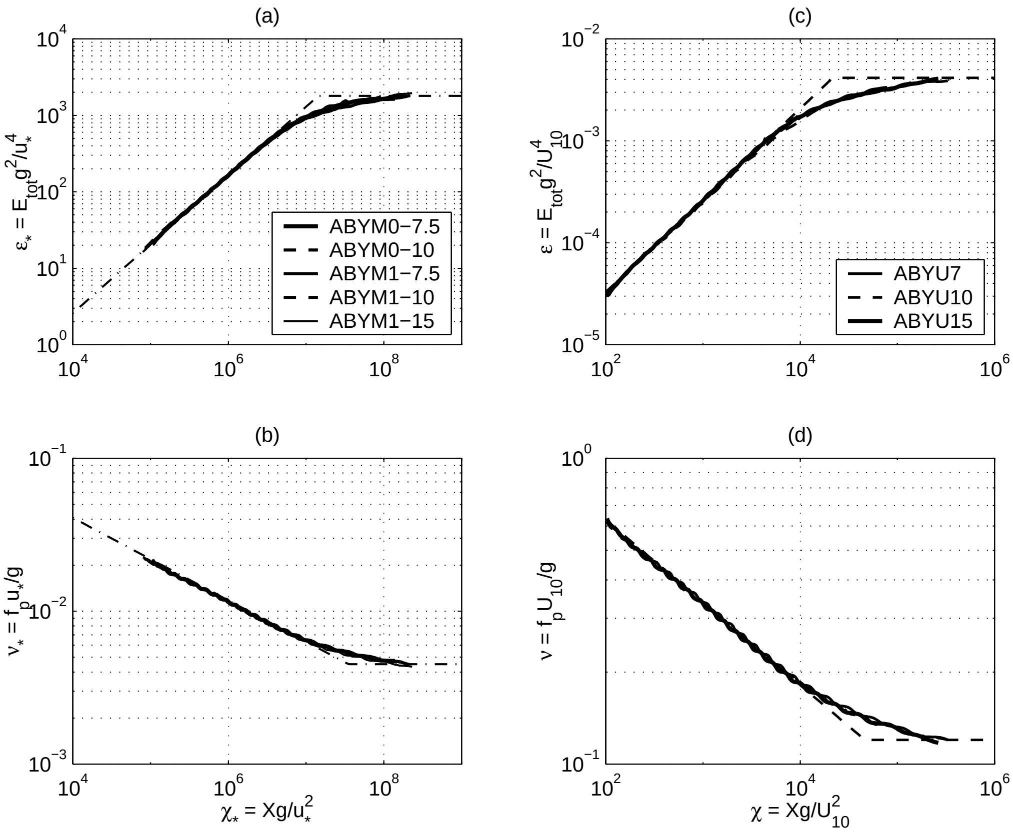

Figure 5.16: *Results of additional experiments to investigate the robustness of S_{ds}^{bs} under different wind forcing intensities. Panels on the left-hand side indicates the comparison with u_*-scaled empirical evolution curves. Panels on the right-hand side show a comparison against the U_{10}-scaled curves. Plotted parameters are (a) nondimensional total energy $\varepsilon_* = E_{tot}g^2/u_*^4$, (b) nondimensional peak frequency $\nu_* f_p u_*/g$, (c) nondimensional total energy $\varepsilon = E_{tot}g^2/U_{10}^4$ and (d) nondimensional peak frequency $\nu = f_p U_{10}/g$. Dash-dotted lines represent the Kahma and Calkoen (1992, 1994) growth curves.*

$U_{10} = 7.5$ and 20m/s, input rates changed by around -5% and +10%, respectively.

Figure 5.16 shows the results of these additional experiments. Run codes are named according to the original configuration of S_{ds}^{bs} (either ABYM0 or ABYM1), with the value of U_{10} added as a suffix. Panels (a) and (b) show the computed evolution curves of u_*-scaled integral parameters $\varepsilon_* = E_{tot}g^2/u_*^4$ and $\nu_* = f_p u_*/g$, respectively. The departure of the scaling assumption of runs with different wind speeds is negligible within the fetch-limited growth range ($1 \times 10^5 < \chi_* < 3 \times 10^6$). Small discrepancies of around 5 to 10%, however, occurred in the transition towards full development. Within the full-development range, runs with U_{10} =15m/s produced a small residual growth that may be eliminated through a more refined tuning of dissipation parameters. For the purposes of testing the robustness of the new form of S_{ds}, however, these results were considered satisfactory. Therefore, it is reasonable to conclude that the model results conform to the scaling behaviour predicted by similarity theory. These conclusions also apply to model runs made with S_{in} redefined in terms of U_{10}, as shown in panels (c) and (d).

A final experiment with S_{ds}^{bs} and the form of S_{in} due to Yan (1987) was made to test the flexibility of the new dissipation function. This consisted of readjusting the dissipation parameters, seeking a simultaneous fit of model results to both the empirical fetch-limited curves of Kahma and Calkoen (1992, 1994) and the full-development limit proposed by Komen et al. (1984), which is lower than the previously adopted asymptotic level due to Alves et al. (2000). Results of this model run are shown in Figure 5.17. Dissipation parameters were set to $C_{ds} = 3.2 \times 10^{-3}$, $p_\infty = 8$, $B_r = 4.2 \times 10^{-3}$ and $m = 0.35$. Figure 5.17 shows that these readjustments resulted in dissipation rates that were appropriate to produce model predictions of ε_* and ν_* in very good agreement with the empirical curves at all stages of evolution.

5.3.2 Comparative analysis with other dissipation terms

The potential impact of these results on wind-wave modelling applications may be assessed through a comparison to the analyses of Banner and Young (1994) on the performance of the dissipation function S_{ds}^{w3}, due to Komen et al. (1984), used

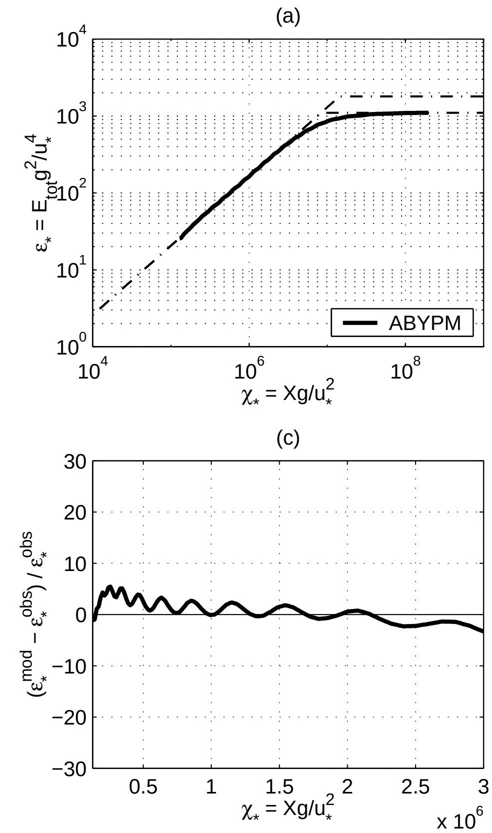

Figure 5.17: *Results of model run ABYPM, made to test the flexibility of S_{ds}^{bs} by fitting model results to the full-development limit of Komen et al. (1984) (lower horizontal dashed line), while maintaining good agreement with the empirical curves at shorter fetches. The full-development asymptote of Alves et al. (2000) (upper horizontal dashed line) is also shown. Plotted parameters are (a) nondimensional total energy ε_* and (b) nondimensional peak frequency ν_*. Panels (c) and (d) show the percentage bias between these parameters and the corresponding Kahma and Calkoen (1992, 1994) evolution curves (shown as dash-dotted lines) within the range of available fetch-limited observations.*

in the WAM Cycle 3 model. The major findings of Banner and Young (1994) were discussed in Section 5.1.5 and summarised in Figure 5.2. This figure shows that several variations of S_{ds}^{w3} [panels (a) and (b)] produced evolution curves of ε_* and ν_* with no portion approximating the power-law behaviour of the empirical relationships of Kahma and Calkoen (1992, 1994). In contrast, most of the results associated with the newly-proposed S_{ds}^{bs} [equation (5.7)] provided evolution curves of ε_* and ν_* that were nearly unbiased.

Although limited to a narrower range of wave ages c_p/u_*, the computations of Banner and Young (1994) revealed that S_{ds}^{w3} predicted dissipation rates that did not provide a proper source-term balance at higher wavenumbers within the spectral tail. This was indicated by their analyses of the empirical spectral tail parameters $\overline{n}_B$ and $\overline{\alpha}_B$ of Banner (1990), shown in panels (c) and (d) of Figure 5.2. In addition to these diagrams, Banner and Young (1994) reported on values of relative tail energy levels ϵ_b that were typically greater than 2. Conversely, the combination of the local saturation $(B(k)/B_r)^3$ with the integral steepness $(E_{tot}k_p^2)^m$ and the weighting function $(k/\overline{k})^n$ allowed more flexibility in tuning S_{ds}^{bs}, resulting in improved computed spectral tail properties. Improvements were particularly significant in respect to the relative tail energy levels ϵ_B.

Since the publication of the study by Banner and Young (1994), a more recent version of the WAM model, Cycle 4, has been released (Günther et al., 1992). This is a technically enhanced version of WAM Cycle 3 that includes the wind input and dissipation source terms proposed by Janssen (1991, 1989), given by equations (2.20) and (2.29) of Chapter 2, respectively. As shown in Figure 2.2 of that Chapter, the WAM Cycle 4 input term predicts growth rates that are similar to those provided by the form of S_{in} due to Yan (1987), as it also depends quadratically on the inverse wave age u_*/c_p. This dependence results in higher input rates at the spectral tail in relation to the form of S_{in} used in WAM Cycle 3.

The form of S_{ds} introduced in WAM Cycle 4 [hereafter represented by the symbol S_{ds}^{w4}] was designed to compensate for these higher S_{in} rates within the spectral tail. The new S_{ds}^{w4} is actually a modification of the S_{ds}^{w3} expression that kept its original form at the spectral peak, while increasing dissipation rates at the tail by introducing a linear combination of the ratio $k/\overline{k}$ in the form $(1-\delta)k/\overline{k}+\delta(k/\overline{k})^2$. The resulting S_{ds}^{w4} was, therefore, still consistent with the hypothesis of Hasselmann (1974) that dissipation rates across the spectrum are dependent on integral spectral properties only.

To provide a wider perspective on the performance of the new saturation-dependent function in relation to a form of S_{ds} presently used in operational applications, an analysis of S_{ds}^{w4} following the general procedure adopted in Banner and Young (1994) is included below. This analysis is based on computations of fetch-limited evolution with the same experimental framework used in the validation S_{ds}^{bs}. Consequently, C_{ds}, m and δ, the three parameters of S_{ds}^{w4}, were modified within a plausible range with the objective of providing an optimal fit to the u_*-scaled fetch-limited evolution curves of Kahma and Calkoen (1992, 1994).

Parameters of S_{ds}^{w4} in the standard WAM Cycle 4 configuration are set to $C_{ds} = 9.4\times10^{-5}$, $m=2$ and $\delta=0.5$. Results of a model run made with this initial setting (named W4YM2) are shown in Figure 5.18. Panels (c) and (d) indicate that results with this model setup diverge from the power-law behaviour of the target evolution curves within the valid range of fetch-limited observations. The percentage bias of predicted nondimensional total energy ε_*, shown in panel (c), indicates an underprediction of up to 40%, while nondimensonal peak frequencies ν_* (panel d) are overpredicted by up to 8%. Results of run W4YM2 also produce fully-developed values of $\varepsilon_* = 7\times10^2$, much lower than both asymptotic limits proposed by Alves et al. (2000) and by Komen et al. (1984), given by the levels $\varepsilon_*^{lim} = 1.76\times10^3$ and $\varepsilon_*^{lim} = 1.1\times10^3$, respectively. The computed fully-developed limit $\nu_* = 6.9\times10^{-3}$ is also significantly higher than both empirical asymptotes $\nu_*^{lim} = 4.7\times10^{-3}$ and

$\nu_*^{lim} = 5.6 \times 10^{-3}$, respectively.

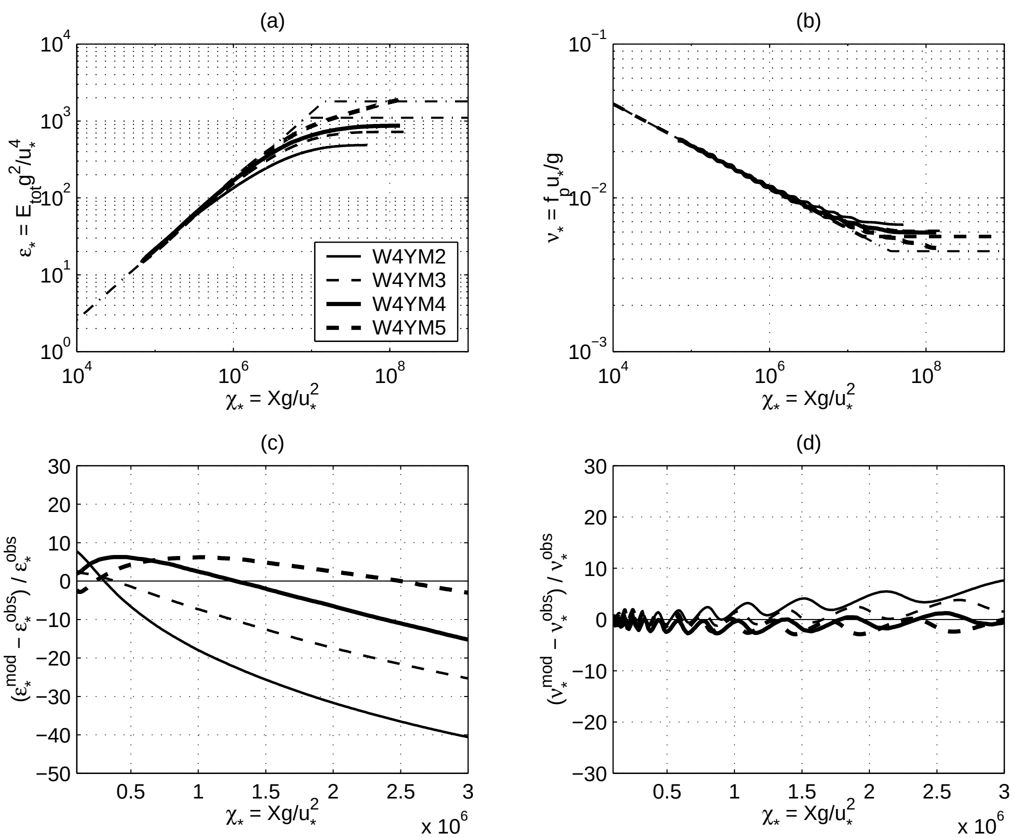

Figure 5.18: *Results of model runs made with S_{ds}^{w4} and several values of the dissipation parameter m. Empirical curves are shown as dashed lines. Both full-development asymptotes of Komen et al. (1984) (lower horizontal dashed line) and Alves et al. (2000) (upper line) are shown. Plotted parameters are (a) nondimensional total energy ε_* and (b) nondimensional peak frequency ν_*. Panels (c) and (d) show the percentage bias between these parameters and the corresponding Kahma and Calkoen (1992, 1994) evolution curves (shown as dash-dotted lines) within the range of available fetch-limited observations.*

Experiments made with S_{ds}^{peak} indicated that an increase of its nonlinear dependence on the steepness parameter $(ak)_p$ provided means of optimising model results. This dynamic behaviour of $(ak)_p$ is in many ways similar to that of $E_{tot}\bar{k}^2$, the integral steepness parameter used in S_{ds}^{w4}. Therefore, the effect of increasing the nonlinear dependence of S_{ds}^{w4} on $(E_{tot}\bar{k}^2/\alpha_{pm})^m$ was investigated in experiments made with the exponent m set to 3, 4 and 5. Values of the dissipation constant C_{ds} were also changed to accommodate the new exponents, as indicated in Table 5.3. Results are also shown in Figure 5.18.

Panels (c) and (d) of Figure 5.18 shows that increasing the values of m improved the agreement of computed ε_* and ν_* with their corresponding empirical evolution curves. The percentage bias, however, was still rather high for $m \leq 3$. With $m = 4$, the maximum percentage bias of ε_* and ν_* were reduced to less than 15% and 3%, respectively. Furthermore, the computed asymptotic limits of these two integral parameters approached very closely the full-development asymptotes of Komen et al. (1984). When an exponent $m = 5$ was used, however, the growth of ε_* overshot both this limit and the asymptote of Alves et al. (2000). Consistent with the experiments made with S_{ds}^{peak} and S_{ds}^{bs}, the higher nonlinear dependence of S_{ds}^{w4} on $(E_{tot}\overline{k}^2/\alpha_{pm})^m$ produced dissipation rates that, in the case of $m = 5$, became too low to balance the strong influx of energy provided by S_{nl} as the wave field approached full development.

These results indicate that tuning the exponent m in S_{ds}^{w4} provides a potential way of optimising model performance and the fit of its results to different fully-developed asymptotes. Depending on the choice of m, however, the percentage bias of computed integral spectral parameters at shorter fetches may become much larger than the bias associated with runs made with S_{ds}^{bs} (generally below 10% at any in development stage). Furthermore, high values of m in S_{ds}^{w4} led to an imbalance between S_{ds} and S_{nl} at very long fetches, resulting in continuous growth beyond the full-development limits. These limitations indicate that changes in m alone do not provide enough flexibility in adjusting S_{ds}^{w4}.

The consequences of further modifications in the dissipation parameters of S_{ds}^{w4}

were explored by setting δ, the linear combination factor of the weighting term $(1-\delta)k/\overline{k}+\delta(k/\overline{k})^2$, to values ranging from 0.3 to 0.6 (the original configuration uses $\delta = 0.5$). Since this parameter may change significantly the strength of S_{ds}^{w4} at higher wavenumbers, an analysis of the spectral tail behaviour is also provided, allowing a more detailed evaluation of the differences between S_{ds}^{w4} and S_{ds}^{bs}. Additional model runs were made with $m = 4$, as this choice of exponent provided a reasonably good fit of model results to the empirical curves of Kahma and Calkoen (1992, 1994) and to the asymptotic limit of Komen et al. (1984).

Computed integral spectral parameters from model runs using $m = 4$ and various values of δ are compared to empirical evolution curves in Figure 5.20. Names of runs with modified parameters are indicated by the two-character suffixes D3, D4 and D6 added to W4YM4, corresponding to values of $\delta = 0.3$, 0.4 and 0.6, respectively. Panels (c) and (d) indicate that the changes in δ had a marginal effect in the computations of ε_* and ν_* within the valid range of the target fetch-limited curves.

The percentage bias of ε_* (panel b), however, was slightly reduced when δ was set to 0.3 (run W4YM4D3), which implied in spectral tail dissipation rates that were lower relative to run W4YM4. Panel (a) shows that the outcomes of run W4YM4D3 were also in better agreement with the full-development limit of ε_* proposed by Komen et al. (1984). These results are in agreement the optimal parameter setup of S_{ds}^{w4} ($m = 3$ and $\delta = 0.31$) determined by Hersbach (1998) through inverse wave modelling using an adjoint version of the WAM model.

Figure 5.20 shows a comparison of computed tail parameters of the spectral slice in the wind direction with the empirical relations of Banner (1990). Panels (a) and (b) show the shape parameters $\overline{\alpha}_B$ and $\overline{n}_B$, while the ratio between the actual

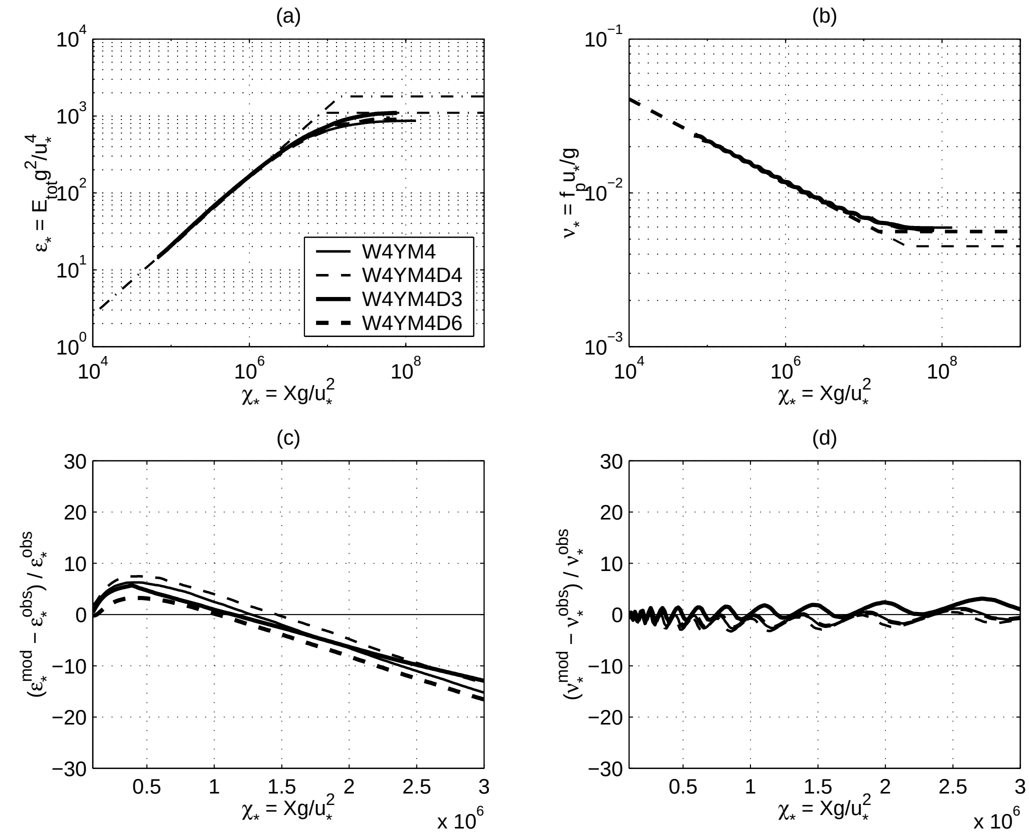

Figure 5.19: *Results of model runs made with S_{ds}^{w4} and several values of the dissipation parameter δ. Empirical curves are shown as dashed lines. Both full-development asymptotes of Komen et al. (1984) (lower horizontal dashed line) and Alves et al. (2000) (upper line) are shown. Plotted parameters are (a) nondimensional total energy ε_* and (b) nondimensional peak frequency ν_*. Panels (c) and (d) show the percentage bias between these parameters and the corresponding Kahma and Calkoen (1992, 1994) evolution curves (shown as dash-dotted lines) within the range of available fetch-limited observations.*

computed energy density $F(k, \theta_{wind})$ and the empirical value $F_B(k, \theta_{wind})$, given by equation (4.40), are shown in panels (c) and (d). In all cases, model results disagree substantially with the empirical parameters.

The initial setup of model run W4YM4 ($m = 4$ and $\delta = 0.5$) shown in Figure 5.20, produces a spectral tail that is too steep ($\overline{n}_b \approx -5$) in early development stages ($c_p/u_* \approx 10$) and too gentle at full development ($\overline{n}_b \approx -3.75$ at $c_p/u_* \approx 25$).

More importantly, the ratio ϵ_b shown in panel (c) indicates that the actual energy density at the lower limit of the spectral tail ($k = 6.25k_p$) progressively increases from 20% to 80% of the empirical value as the wave field evolves with fetch. This steadily increasing trend is also seen in the computed energy density at a higher wavenumber ($k = 12.25k_p$), but with a wider range of variation (from 50% lower to 100% higher than the empirical value), as shown in panel (d).

The strong decay of average spectral tail slopes with wave age obtained with $\delta = 0.5$ may be attenuated by setting δ to 0.3. This more stable behaviour, however, results in an average tail slope ($\overline{n}_B \approx 3.7$) that is lower than the empirical value, as seen in Figure 5.20, panel (a). Furthermore, it results in tail energy densities that are up to 250% higher than $F_B(k, \theta_{wind})$, as indicated by the parameter ϵ_B plotted in panels (c) and (d). Increasing the value of δ to 0.6, on the other hand, results in a much stronger disagreement of model results with the trends of all empirical relations proposed by Banner (1990).

Experiments made with S_{ds}^{peak} and S_{ds}^{bs} indicated that a proper description of energy densities at the spectral peak (i.e., a good fit between model results and empirical evolution curves of integral spectral parameters) and at the spectral tail (i.e., good agreement with the Banner (1990) empirical tail parameters) can only be achieved *simultaneously* if their levels of dissipation have different dynamic ranges. In other words, as the wave field evolves with fetch, the dissipation levels at the spectral peak should decay more rapidly than at the spectral tail. This behaviour matches the dynamic response of the other two source terms, S_{in} and S_{nl}. A well-known feature of S_{in} is the strong decay of input rates to the spectral peak as the wave field evolves from strongly forced to fully-developed seas. Input rates within the spectral tail, in contrast, remain comparable at any development stage.

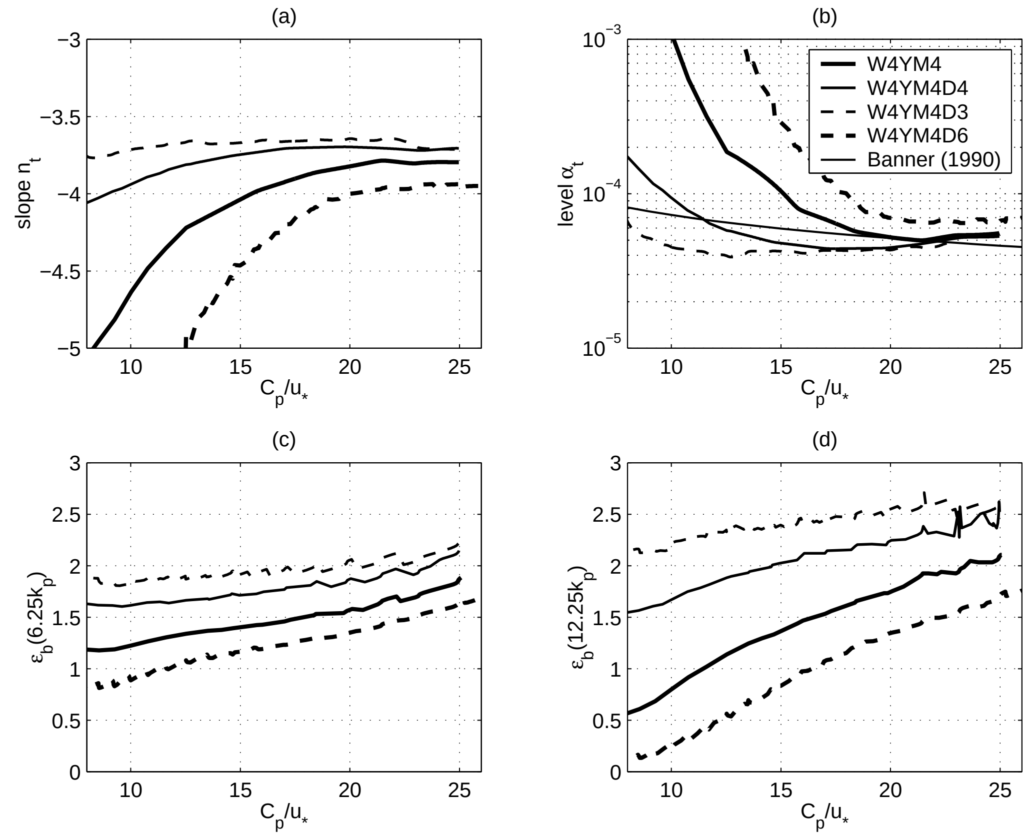

Figure 5.20: *Tail behaviour associated with runs made with S_{ds}^{w4} and several values of the dissipation parameter δ. Validation is made against the empirical spectral tail parameters of Banner (1990): (a) average level $\overline{\alpha}_B$, (b) average slope $\overline{n}_B$ and relative energy density ratio ϵ_B of the wavenumber spectral slice in the wind direction at (c) $k = 6.25k_p$ and (d) $k = 12.25k_p$.*

The dynamical behaviour of S_{nl} is less straightforward. Numerical computations made by Resio and Perrie (1991) and Young and Van Vledder (1993), however, have provided deep insight on how the nonlinear fluxes within the wave spectrum change with the stage of wave growth. According to Resio and Perrie (1991), S_{nl} shows little relative change within the spectral tail at different wave evolution stages. In opposition, the dynamics of nonlinear fluxes at the spectral peak are strongly affected by the spectral "peakedness", which becomes less pronounced as the wave field evolves in space or time. Young and Van Vledder (1993) show that this progressive broadening results in a reduction of nonlinear energy fluxes to the spectral peak.

Theoretical and empirical evidence shows that the changes of S_{in} and S_{nl} with wave growth, under active wind forcing, result in (i) a strong dynamic response of spectral components within the spectral peak and (ii) a small variation of spectral properties at the high wavenumber tail. The rates of decay in S_{ds}^{w3} and S_{ds}^{w4} are solely determined by the integral steepness term $(E_{tot}\overline{k}^2/\alpha_{pm})^m$, which is a constant value for all wavenumbers at any particular stage of wave growth. Consequently, the general structure of these two quasilinear forms of S_{ds} is not flexible enough to allow this needed differential tuning of dissipation rates across the spectrum. Alternatively, expressing S_{ds} as a function of a more local spectral parameter, such as the saturation-dependent term $(B(k)/B_r)^p$ of S_{ds}^{bs}, provides a viable conceptual framework that brings promising results when applied to wind-wave modelling.

5.3.3 Response of S_{ds}^{bs} to alternative wind input functions

Several parametrisations of the wind input source term S_{in} have been proposed since the advent of the critical-layer theory of wind-wave generation due to Miles (1957). Although sharing many of their basic features, these parametric forms of S_{in} have differences that may affect considerably the outcomes of numerical simulations on the evolution of wave spectra. The experiments described in previous sections of this Chapter were made with a form of S_{in} that synthesises the more robust observed properties of the momentum flux from wind to waves [i.e., a linear dependence on wave age at the spectral peak, as observed by Snyder et al. (1981), and a quadratic dependence on this parameter at higher wavenumbers, as reported in Plant (1982), Hsiao and Shemdim (1983) and Donelan and Pierson (1987)]. This section provides a brief investigation on the response of S_{ds}^{bs} to other commonly-used forms of S_{in}.

Snyder et al. (1981) form of S_{in}

The input source term S_{in}^{S}, given by equation (2.18) of Chapter 2, is a parametrisation of the growth rates of moderately-forced to mature waves ($1 < U_{10}/c < 3$) observed by Snyder et al. (1981) in the Bight of Abaco, in the Bahamas. This relatively limited range of stages of development in the observed waves led to a parametric form of S_{in} with a linear dependence on the inverse wave age parameter U_{10}/c. Despite the lack of observations of strongly-forced waves (higher wavenumber components with $U_{10}/c > 3$), applications of S_{in}^{S} in wind-wave modelling involve a simple extrapolation of its linear dependence towards the higher wavenumber spectral range.

Although more recent observational evidence has supported a quadratic dependence of input rates on wave age at higher wavenumbers, some operational implementations of wave models still adopt the form S_{in}^{S}, which was the standard input function of the WAM Cycle 3 model. An example is the modified version of WAM used at the Australian Bureau of Meteorology, AUSWAM, which is described in more detail in the next Chapter. Due to its wide usage and to the fact that by specifying much lower input rates to the high wavenumber spectral range, the use of S_{in}^{S} provides an alternative framework for the validation of S_{ds}^{bs}.

The results of five experiments designed to validate S_{ds}^{bs} using the form of S_{in} due to Snyder et al. (1981) are shown in Figure 5.21. These five model runs consisted of using two variations of S_{in}^{S} defined alternatively in terms of U_{10} and u_{*}. Experiments using U_{10}, which are named with the prefix ABSU, were made with three different

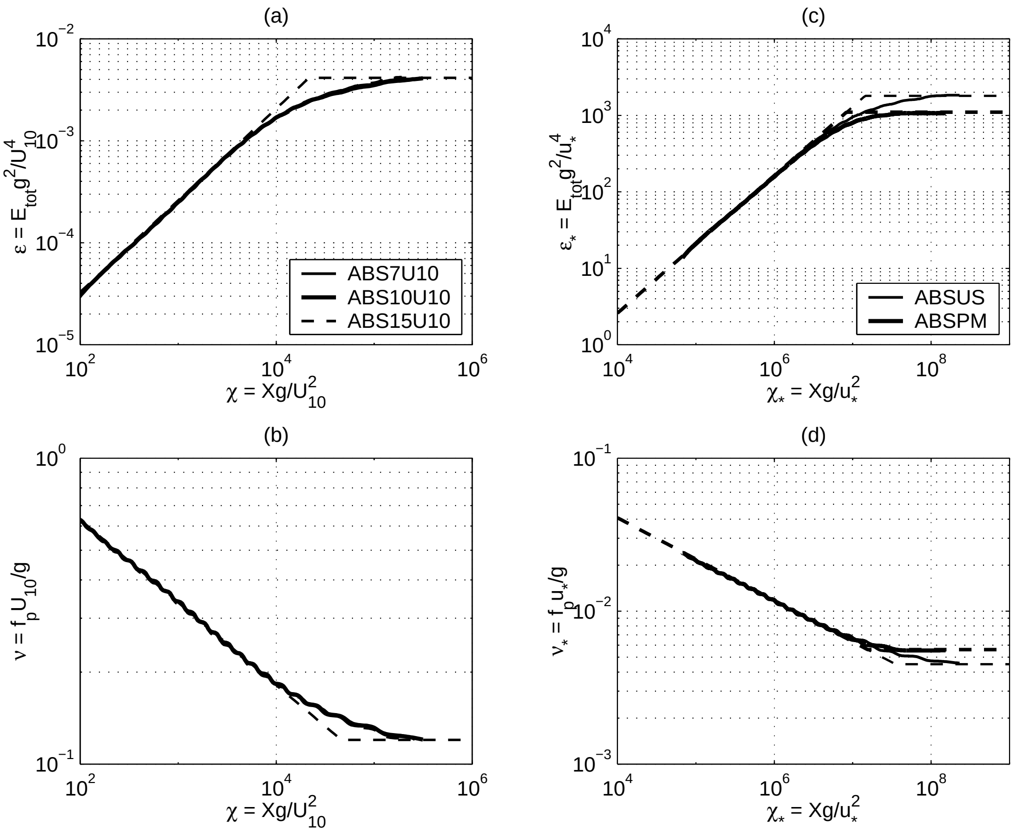

Figure 5.21: *Results of model runs made with* S_{ds}^{bs} *and the form of* S_{in} *due to Snyder et al. (1981). In the panels on the left-hand side, model results are compared to the* U_{10}*-scaled target evolution curves. Plotted parameters are (a) nondimensional total energy* ε *and (b) nondimensional peak frequency* ν*. On the right-hand side, model results are compared to the* u_**-scaled evolution curves and both full-development asymptotes of Komen et al. (1984) (lower horizontal dashed line) and Alves et al. (2000) (upper line). Plotted parameters are (c) nondimensional total energy* ε_* *and (d) nondimensional peak frequency* ν_**.*

wind speeds $U_{10} = 7.5$, 10 and 15m/s. The forcing intensity is indicated as a suffix in model run names (e.g., ABSU7 for $U_{10} = 7.5$m/s etc). Experiments using u_* were made to test the flexibility of S_{ds}^{bs}, by tuning its parameters to reproduce closely the evolution of integral spectral quantities towards (i) the full-development limits of Alves et al. (2000) or (ii) the asymptotes proposed by Komen et al. (1984). As these latter evolution limits are specified in terms of u_*, S_{in}^{S} was changed into a u_*-dependent form consistent with the WAM Cycle 3 model physics.

Due to the weaker input rates of S_{in}^{S} at wavenumbers higher than the spectral peak, both values of the exponents $n = 1$ and $p_{\infty} = 4$ in S_{ds}^{bs} were reduced in relation to previous experiments involving S_{in}^{Y}. Values of the constant C_{ds}, the exponent m and the reference saturation level B_r were tuned according to the values listed in Table 5.3. Figure 5.21 shows that the computed ε and ν were in good agreement with the target evolution curves within the valid range of fetch-limited. At full development, model runs at different wind speed also generated results that were consistent with the asymptotic limits proposed by Alves et al. (2000), which was initially used as a reference. The highest discrepancies amongst different model runs occurred in the transition towards full development. These, however, were always within the tolerance margin of $\pm 10\%$.

Model runs ABSUS and ABSPM were made with the alternative definition of S_{in}^{S} in terms of u_*. The suffix PM was used to indicate the experiment that targeted full-development limits of Komen et al. (1984), derived by integration of the analytical spectrum proposed by Pierson and Moskowitz (1964). Since S_{in}^{S} was specified as a function of the friction velocity, the results of these two model runs (shown on the right-hand side of Figure 5.21) were validated against the u_*-scaled evolution curves of Kahma and Calkoen (1992, 1994). Table 5.3 shows the changes in dissipation parameters required to accommodate the u_*-dependence of S_{in}^{S} and the evolution towards alternative asymptotic evolution limits.

Panels (c) and (d) of Figure 5.21 show the comparison of computed ε_* and ν_* from runs ABSUS and ABSPM against their respective target empirical evolution curves and full-development limits. In both cases, model results were consistent with the target fetch-limited growth curves within both the valid range of fetch-limited observations and at each respective full-development limit. The absolute percentage bias in any case was always under 10%.

The good agreement of model results with evolution curves with different scaling wind speeds and two distinct asymptotic growth limits demonstrates the flexibility provided by S_{ds}^{bs}. These results also indicate that the newly-proposed form S_{ds}^{bs} may be used as an alternative source term in wave models that prescribe wind input rates using the form of S_{in} due to Snyder et al. (1981). The impact of this combination of source terms on the skill of an operational wind-wave model used in the Australian region is examined in the next Chapter.

Janssen (1991) form of S_{in}

Recent advances in understanding the governing mechanisms of the momentum flux from wind to waves have been included in other parameterisations of S_{in}. Major improvements have been the inclusion of (i) the effects of the sea state on spectral rates of wind input (Janssen, 1991; Tolman and Chalikov, 1996) and (ii) the negative air-sea momentum flux within wave components travelling faster than the wind (Tolman and Chalikov, 1996; Makin et al., 1995; Donelan, 1999). Although evidence on the decay of laboratory waves propagating faster than or against the wind has been provided recently by Donelan (1999), this negative "input" has not yet been observed in the field. On the other hand, field experiments reported by Donelan (1982) and Maat et al. (1991) have provided strong evidence on the dependence of the roughness length z_0 and of the drag coefficient C_D on sea state. This implies that forms of S_{in} specified in terms of u_* should also depend on the sea state, as u_* is a function of z_0 and C_D. Experiments on the effects of including a form of S_{in} that accounts for negative momentum fluxes from spectral components propagating faster than or against the wind will be addressed in future research.

A preliminary assessment on the effects of using a sea-state dependent S_{in} on the performance of S_{ds}^{bs} is included below. This assessment was based on a single experiment using the form S_{in}^{J} due to Janssen (1991), which is presently the standard input source term used in the WAM Cycle 4 model. As seen in Chapter 2, this input source function is specified in terms of the sea-state-dependent friction velocity u_{**} (the double star subscript has been included to differentiate this parameter from the sea-state-independent friction velocity u_*). Although the rates of S_{in}^{J} at wavenumbers higher than the peak (i.e., strongly forced spectral components) are comparable to those of the form S_{in}^{Y} due to Yan (1987), they are significantly smaller than the S_{in}^{Y} rates for mature waves (see Figure 2.2 in Chapter 2). These two distinction between S_{in}^{J} and the two other input functions S_{in}^{Y} and S_{in}^{S} have, therefore, provided an alternative framework for the validation of S_{ds}^{bs}.

In the WAM Cycle 4 model, the dependence of u_{**} on the sea-state is calculated through an algorithm that couples the forcing wind field to the high wavenumber range of the wave spectrum. This algorithm solves iteratively the relation $u_{**}^2 = C_D U_{10}^2$, with $C_D = [\kappa/\log(z/z_0)]^2$, $z_0 = \alpha u_{**}^2/\sqrt{1 - \tau_w/u_{**}^2}$ and the wave induced stress τ_w given by a function of the integrated wind input rates at higher wavenumbers. Sensitivity tests indicated that the implementation of this coupled algorithm in the research model of Tracy and Resio (1982) generated numerical instabilities at high wavenumbers, leading to unreliable estimates of u_{**}. This was most likely a consequence of either (i) the adopted experimental setup, in which source terms were solved explicitly within a spectral range extending towards very high wavenumbers, limited at $25k_p$; and/or (ii) the use of an exact solution for the nonlinear interactions term S_{nl}. These problems are currently being investigated in more detail.

A more straightforward approach to calculating u_{**} was used to overcome the problems of high wavenumber instabilities. This approach consisted of using the parametric function expressing the sea-state dependence of z_0 proposed by Donelan et al. (1993), as follows:

$$z_0 = 3.7 \times 10^{-5} \frac{U_{10}^2}{g} \left(\frac{U_{10}}{c_p} \right)^{0.9}, \tag{5.8}$$

with

$$u_{**} = \frac{0.4 U_{10}}{\log(10/z_0)}, \tag{5.9}$$

where the wave age parameter U_{10}/c_p expresses the influence of sea maturity on the value of z_0.

Expression (5.8) is a simple parametric fit to measurements made during the HEXOS experiment (Katsaros et al., 1987). According to Janssen (1994), the coupled solution of S_{in}^J used in WAM Cycle 4 gives estimates of u_{**} that are in good agreement with the observed values of this parameter during HEXOS. Therefore, it is reasonable to expect that the input rates computed using the parametrised u_{**} of Donelan et al. (1993) would be consistent with those obtained with the coupled solution used in the WAM Cycle 4 model.

The numerical instabilities at high wavenumbers were eliminated with the replacement of the coupling algorithm of WAM Cycle 4 by the parametric u_{**} of Donelan

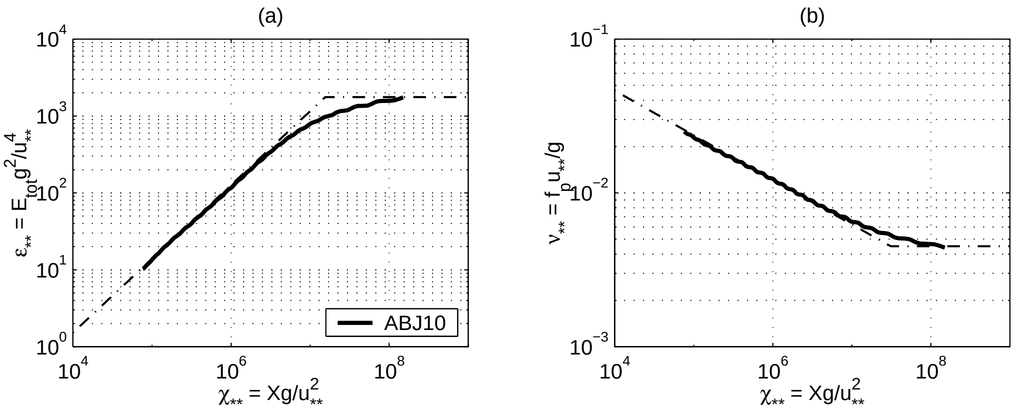

Figure 5.22: *Results of model runs made with S_{ds}^{bs} and the form of S_{in} due to Janssen (1991). Plotted parameters are (c) nondimensional total energy ε_* and (d) nondimensional peak frequency ν_*. Comparisons are made against the nondimensional evolution curves of Kahma and Calkoen (1994) and the asymptotic limit of Alves et al. (2000), using the sea-state-dependent friction velocity u_{**}.*

et al. (1993), which allowed one successful experiment using S_{in}^J to be made. Results from this model run, named ABJ, are shown in Figure 5.22. The wind speed was set to U_{10} =10m/s. Due to the quadratic dependence of S_{in}^J on the inverse wave age u_*/c, the dissipation parameters of S_{ds}^{bs} were re-tuned to values similar to those used in the experiments made with S_{in}^Y ($m = 1$, $n = 2$ and $p_\infty = 8$). The stronger input rates at high wavenumbers resulting from the dependence of S_{in}^J on u_{**} also required a reduction of the reference saturation level B_r to 3.1×10^{-3}, a value slightly smaller than those used in previous model runs.

Panels (a) and (b) of Figure 5.22 show that the computed ε_{**} and ν_{**} from run ABJ were in good agreement with the target evolution curves. Values of percentage bias were lower than 10% within the valid range of fetch-limited observations. Although some residual growth was observed in the approach towards the full-development limit of Alves et al. (2000), the results were considered satisfactory in terms of demonstrating that S_{ds}^{bs} may also be successfully used in conjunction with the input source term of the WAM Cycle 4 model. More importantly, the results reported in this section demonstrate the flexibility of the newly-proposed saturation-dependent form S_{ds}^{bs} in terms of providing proper dissipation levels to balance several well-accepted forms of S_{in}.

5.4 Directional spreading

The first successful attempt to determine an empirical function $D(k, \theta)$ describing the directional spreading of energy of the wave spectrum was reported by Longuet-Higgins et al. (1963). Since then, other analytical forms for $D(k, \theta)$ have been proposed by Mitsuyasu et al. (1975), Hasselmann et al. (1980) and Donelan et al. (1985). Although most of these analytical forms have distinctive shapes, they all agree that the directional spreading is narrower at the spectral peak wavenumber k_p, becoming broader at wavenumbers both above and below k_p. This very important structural feature can be used as a first criterion for assessing model performance in terms of directional properties of computed wave spectra.

The mean spectral width $\overline{\theta}(k)$, given by equation (4.39) of Chapter 4, provides a useful objective criterion for the purposes of model validation. Since this parameter is computed by integration of $D(k, \theta)$ within the entire range of directions, it is insensitive to asymmetries or small distortions in the shape of the directional spreading. Empirical values of $\overline{\theta}(k)$ may be obtained by integrating one of the available analytical forms of $D(k, \theta)$, following the relation (4.39). Young (1999) argues that the form of $D(k, \theta)$ proposed by Donelan et al. (1985) provides a better approximation to the directional spreading of actively-generated wind waves. In comparison with other forms, it is based on observations made with a more accurate spatial array of wave gauges and measured over a wider range of wave development stages. This form of $D(k, \theta)$ is given by equation (4.34) of Chapter 4.

The spreading function of Donelan et al. (1985) may be integrated directly by using the values of the parameter D_d given by equations (4.35). This implies assuming that the directional spreading of wind-waves at a given relative wavenumber k/k_p does not vary at different development stages. Although this seems to be a reasonable assumption based on the data of Donelan et al. (1985), recent results reported by Babanin and Soloviev (1998) have suggested a definite dependence of $D(k, \theta)$ on the wave age parameter c_p/U_{10}. To provide a wider range of validation scenarios, this alternative view is also included in the analyses presented in this section. Following Babanin and Soloviev (1998), the wave-age dependence of $D(k, \theta)$ may be expressed simply by redefining the spreading parameter D_d of equation (4.34) with the following empirical relation:

$$D_d \approx \frac{1}{2\pi} + 2.24 \left(\frac{c_p}{U}\right)^{1/2} \left(\frac{k}{k_p}\right)^{-0.48} . \tag{5.10}$$

Reference values of $\overline{\theta}(k)$ obtained with these two alternative definitions of D_d at $k = k_p$ and $k = 4k_p$ are indicated in Figures 5.23 and 5.24 by slanted dotted lines. The original definition of D_d proposed by Donelan et al. (1985) gives $\overline{\theta}(k = k_p) \approx 14.3°$ and $\overline{\theta}(k = 4k_p) \approx 33°$, within the entire range of wave ages. These values are indicated by horizontal dotted lines in Figures 5.23 and 5.24. The wave age dependent D_d of Babanin and Soloviev (1998) provides $\overline{\theta}(k)$ that decays from 24° to 15° at $k = k_p$ and from 40° to 25° at $k = 4k_p$, within the indicated ranges of c_p/u_*. As these two alternative results are supported by published data, outcomes of the wave model will be validated against the combination of both parameterisations, resulting in the range of $\overline{\theta}(k)$ indicated in Figures 5.23 and 5.24.

Computed $\overline{\theta}(k)$ from a selection of model runs using the newly-proposed saturation-dependent form S_{ds}^{bs} and the form S_{ds}^{w4} of the WAM Cycle 4 model are indicated in Figures 5.23 and 5.24, respectively. Panels on the left-hand side of both figures indicate $\overline{\theta}(k)$ at $k = k_p$, while the remaining panels illustrate the computed mean spreading width at $k = 4k_p$. A common feature of all model runs that was consistent with observations was the narrower directional spreading at k_p, which became broader at $4k_p$. Computed $\overline{\theta}(k)$, however, were generally broader than the range of empirical values at the peak and narrower at $4k_p$. When compared to the analyses of Banner and Young (1994) on the performance of S_{ds}^{w3}, these results suggest that the two alternative forms S_{ds}^{bs} and S_{ds}^{w4} do not bring improvements to model skill in terms of resolving the directional properties of the wave spectrum.

Figure 5.23 shows the computed $\overline{\theta}(k)$ from a selection of model runs made with S_{ds}^{bs}. Values of the mean width parameter obtained with experiments ABYM0, ABYM1, ABYM2 and ABYPM are included in panels (a) and (b). The major difference between these three model runs was the degree of nonlinear dependence on the integral steepness parameter $(E_{tot}k_p^2)^m$, controlled by values of the exponent m. These were set to $m = 0$, 1, 2 and 0.35, respectively. Comparisons with the empirical values of $\overline{\theta}(k)$ indicate that changes in the exponent m had little impact on the computed directional spreading, as they were generally compensated by adjustments of the parameter $(B(k)/B_r)^{p_\infty/2}$ needed to produce a good agreement of computed integral spectral parameters with fetch-limited observations.

Panels (c) and (d) of Figure 5.23 show the mean width of directional spreading from runs using S_{ds}^{bs} combined with different forms of S_{in}. These results reveal that changes in the specification of the wind input source term had a large impact on the behaviour of computed directional spreading widths. This may be explained by the differences of input rate levels and directionality prescribed by the forms S_{in}^{Y}, S_{in}^{S} and S_{in}^{J}, in conjunction with changes made in S_{ds}^{bs} to accommodate the different characteristics of these three wind input source terms, which were used in runs ABYM1, ABS and ABJ, respectively.

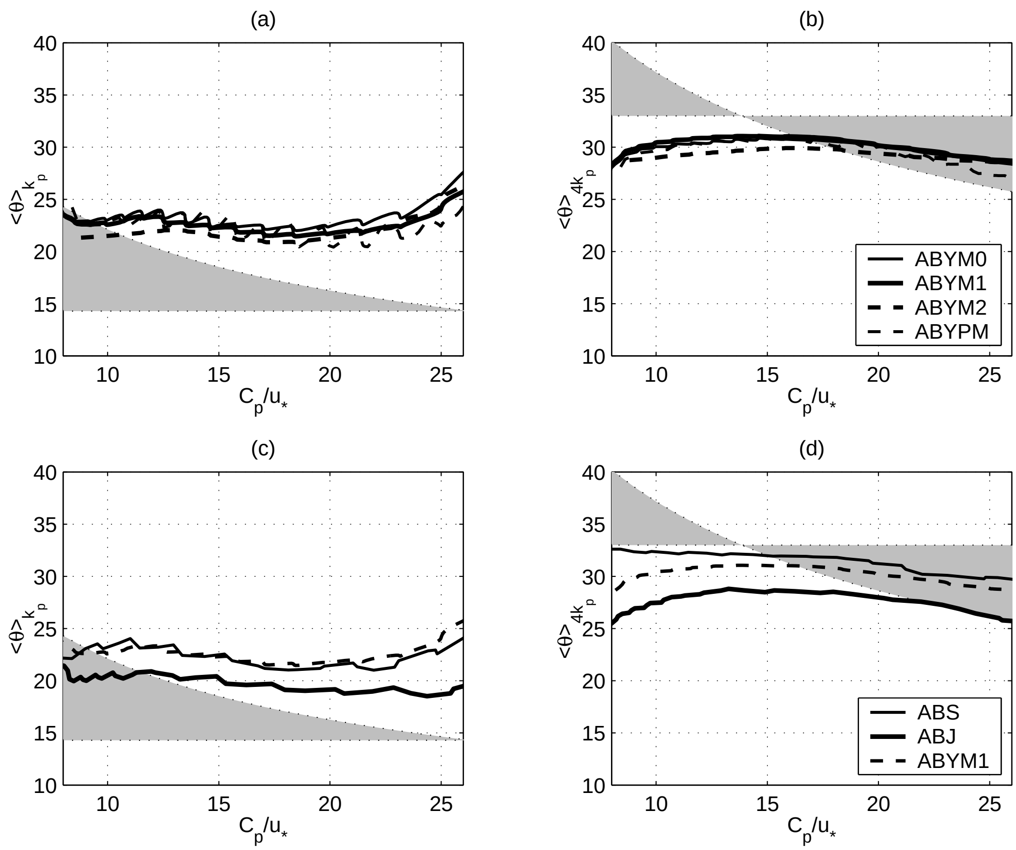

Figure 5.23: *Mean directional spreading width $\overline{\theta}(k)$ associated with runs made with S_{ds}^{bs}. Validation is made against a combination of empirical mean spreading widths based on results reported by Donelan et al. (1985) and Babanin and Soloviev (1998). The range of empirical values is indicated by the grey hatched area. Computed $\overline{\theta}(k)$ at $k = k_p$ and at $k = 4k_p$ are shown in the left- and right-hand sides of the figure, respectively. Run codes are indicated in the legends included in panels (c) and (d).*

The forms S_{in}^{Y} and S_{in}^{S} used in runs ABYM1 and ABS have very similar wind input rate levels and directionality at the spectral peak. Results presented in the previous section show that these two runs produced growth curves of integral spectral parameters that are in good agreement with parametric fetch-limited evolution curves, which indicates that the source-term balance at the spectral peak was similar in both cases. This explains why their estimates of $\overline{\theta}(k = k_p)$ are also comparable, as seen in panel (c). In both cases, the agreement with empirical values of $\overline{\theta}(k = k_p)$ was only acceptable at very low values of wave age c_p/u_* (i.e., strongly-forced wind seas). Above $c_p/u_* \approx 10$, computed $\overline{\theta}(k = k_p)$ do not become narrower as predicted by the Babanin and Soloviev (1998) data, thus leading to a strong departure between empirical and computed values. Computed mean directional widths at the peak from runs ABS and ABYM1 were also significantly broader than the Donelan et al. (1985) data at all ranges of c_p/u_*.

Estimates of $\overline{\theta}(k = 4k_p)$ from run ABS were slightly broader than those from ABYM1, as shown in panel (d) of Figure 5.23. This may be associated with the fact that the input rates of S_{in}^S at high wavenumbers were considerably lower than those prescribed by S_{in}^Y, as illustrated in Figure 2.2 of Chapter 2. These lower input rates at the spectral tail required a reduction of S_{ds}^{bs}, obtained by tuning the maximum exponent of the term $(B/B_r)^{p/2}$ to $p_\infty = 4$. While providing a proper balance of S_{in}^S for spectral components in the wind direction $\theta_m \equiv \theta_{wind}$, the reduction in S_{ds}^{bs} resulted in less damping of S_{nl} for $|\theta| > \theta_m$. These increased nonlinear fluxes towards larger angles may, therefore, explain the broader directional spreading of spectra generated by run ABS relative to the results of run ABYM1.

Figure 2.2 of Chapter 2 also shows that nondimensional input rates prescribed by S_{in}^J at the spectral peak are lower than those of S_{in}^S and S_{in}^Y, while at the spectral tail, S_{in}^J is stronger than S_{in}^Y. In general terms, however, the use of a sea-state dependent

u_{**} results in enhanced input rates, particularly at earlier stages of development (i.e., young wind seas). These characteristics of S_{in}^{J} required a stronger S_{ds}^{bs}, as indicated by the values of dissipation parameters listed in Table 5.3. This, in turn, resulted in a stronger damping of S_{nl} for $|\theta| > \theta_m$. Consequently, the directional spreading of spectra generated by run ABJ was narrower than in runs ABYM1 and ABS. Figure 5.23 shows that this led to a better agreement of computed $\overline{\theta}(k)$ with the empirical relations of Donelan et al. (1985) and Babanin and Soloviev (1998) at the spectral peak, but a stronger disagreement at $k = 4k_p$.

Computed mean directional spreading of spectra generated by experiments made with the dissipation term S_{ds}^{w4} used in the WAM Cycle 4 model are shown in Figure 5.24. As in the case of runs using S_{ds}^{bs}, all computed spectra had $\overline{\theta}(k)$ that were narrower at the spectral peak and broader at $k = 4k_p$, which is generally consistent with observations. Panels (a) and (b) of this figure show the impact on the estimates of $\overline{\theta}(k)$ produced by changing the nonlinear dependence of dissipation rates on the integral steepness parameter $(E_{tot}\overline{k}^2)^m$. The results shown were generated by runs W4M2, W4M4 and W4M5, which were made with values of m set to 2, 4 and 5, respectively.

Higher values of m resulted in better agreement of computed $\overline{\theta}(k)$ at the spectral peak, particularly in the case of run W4M5. On the other hand, the increased values of m in runs W4M4 and W4M5 led to a stronger overall disagreement with observations at $k = 4k_p$. Nevertheless, the trends of decaying $\overline{\theta}(k)$ prescribed by the empirical relation of Babanin and Soloviev (1998) seemed to be better described by run W4M5. These apparent benefits of run W4M5 on $(E_{tot}\overline{k}^2)^m$, however, had the side effect of producing dissipation rates at the spectral peak that became too low in the transition towards full development. This led to a continuous growth of integral spectral parameters beyond the full-development limits, as shown in Figure 5.18.

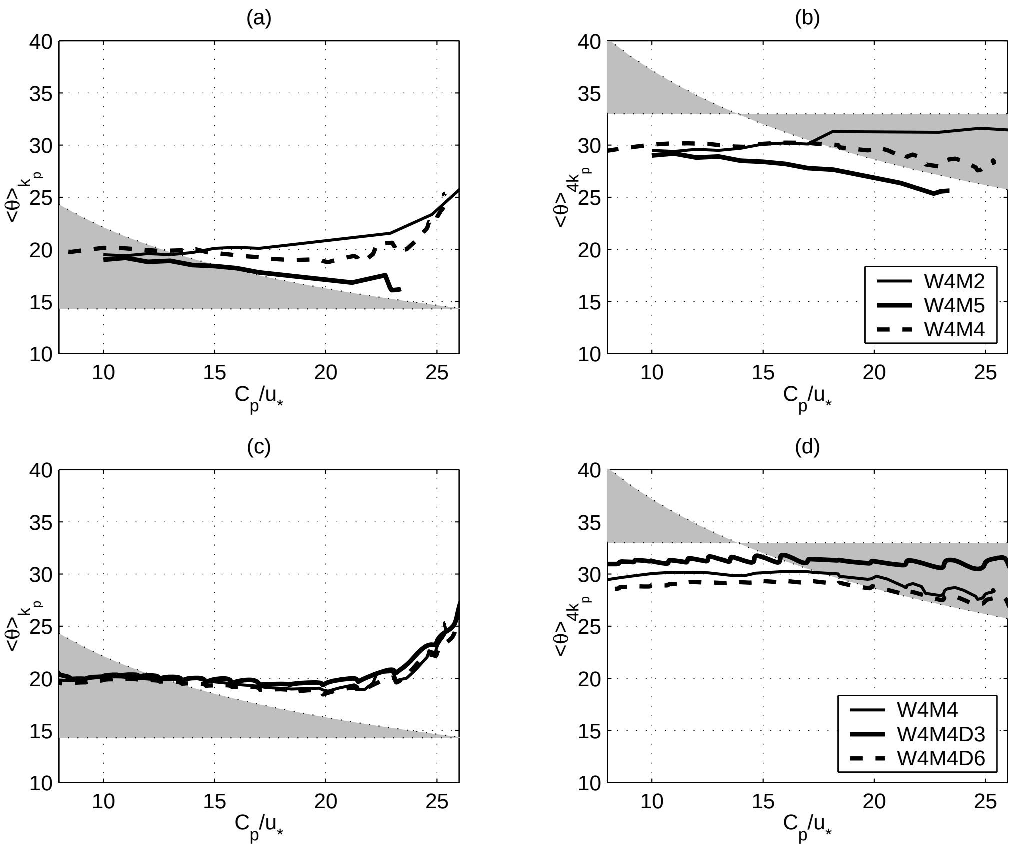

Figure 5.24: *Mean directional spreading $\overline{\theta}(k)$ associated with runs made with S_{ds}^{w4}. Validation is made against a combination of empirical mean spreading widths based on results reported by Donelan et al. (1985) and Babanin and Soloviev (1998). The range of empirical values is indicated by the grey hatched area. Computed $\overline{\theta}(k)$ at $k = k_p$ and at $k = 4k_p$ are shown in the left- and right-hand sides of the figure, respectively. Run codes are indicated in the legends included in panels (c) and (d).*

Panels (c) and (d) of Figure 5.24 show the results of model runs made with different values of the parameter δ, which controls the linear combination of terms in the weighting function $W_{k/k_p} = (1 - \delta)k/\overline{k} + \delta(k/\overline{k})^2$ in the dissipation source term S_{ds}^{w4}. The parameter δ of S_{ds}^{w4} was set to 0.3, 0.4 and 0.5 in runs W4M4, W4M4D3 and W4M4D6, respectively. These panels show that the variation of δ had very little effect on the values of $\overline{\theta}(k)$ at the spectral peak. This result was expected since at the spectral peak $W_{k/k_p} \approx 1$ regardless of the exact form of W_{k/k_p}. The mean directional spreading at $k = 4k_p$, however, was considerably improved when the linear combination parameter δ was reduced from the value $\delta = 0.5$ adopted in the WAM model to $\delta = 0.3$ in run W4M4D3. Nevertheless, the overall agreement of $\overline{\theta}(k)$ for most model runs made with various δ was fairly poor.

A comparison of the results shown in Figures 5.23 and 5.24 suggests that there is no clear advantage in using the present forms of either S_{ds}^{bs} or S_{ds}^{w4} to provide a better description or control of the directional spreading of computed wave spectra. The results reported in this section, however, provide useful insight for the design of future experiments aiming at the improvement of directional properties of computed spectra. These should focus on investigating the impacts of (i) using alternative parametrisations of the wind input source term, such as the forms of S_{in} proposed by Tolman and Chalikov (1996), Donelan (1999) or Makin and Kudryavtsev (1999) and (ii) replacing the dependence of S_{ds}^{bs} on the ratio $k/\overline{k}$ by a linear combination similar to the weighting function used in S_{ds}^{w4}.

Preliminary experiments were made to investigate a third potential source of improvement, which consisted of replacing the present dependence of S_{ds}^{bs} on the azimuthally-integrated saturation spectrum $B(k)$ by a dependence on the two-dimensional saturation spectrum $\mathcal{B}(k, \theta)$. Results from these experiments showed that dissipation rates of spectral components propagating with angles $|\theta| > \theta_m$ were too weak to balance the nonlinear energy transfers provided by S_{nl}, particularly at higher wavenumbers. This induced an unrealistic broadening of the wave spectrum due to the unbound growth of directional lobes. These sidelobes eventually became singularities that made the model solution diverge. These preliminary results suggested that future research on the applications of S_{ds}^{bs} should also investigate the impact of introducing a term expressing explicitly the dependence of dissipation rates on directional properties of the wave field.

5.5 Swell decay

Actively-generated wind-wave systems transition to swell when the wind forcing abates. Such swell systems propagating in deep water are composed typically of large wavelength waves with small amplitudes. The spectral signature of swell is, therefore, associated with low wavenumbers and very small energy densities. The combination of these two properties produces spectral saturation levels $B(k)$ that are generally much lower than typical reference values of the reference saturation parameter B_r used in S_{ds}^{bs}. This implies a negligible contribution of the term $(B(k)/B_r)^p$ to the dissipation rate, since $p \rightarrow 0$ whenever $B(k) < B_r$. Furthermore, the dependence of S_{ds}^{bs} on the weighting function $k/\overline{k}$ also vanishes at wavenumbers lower than the spectral peak. Consequently, the dissipation rates S_{ds}^{bs} of swell systems become a function of the form:

$$S_{ds}^{bs} = C_{ds} \left(E_{tot} k_p^2 \right)^m \omega F(k, \theta). \tag{5.11}$$

As discussed in previous sections, equation (5.11) provides the appropriate background dissipation levels to balance the positive lobe of S_{nl}, assuring the transition of the wave spectrum towards a fully-developed steady state. The impact of the background dissipation level specified by S_{ds}^{bs}, however, also affects the decay of swell. Therefore, additional experiments were made to examine the effect of this property of S_{ds}^{bs} on the propagation of spectral components with wavenumbers and energy densities typical of swell. These experiments consisted simply of "switching off" the wind input source term S_{in} to allow computed fully-developed wave spectra to propagate in space, with forcing specified only by S_{nl} and S_{ds}. A similar approach was used by Schneggenburger (1998) to validate a nonlinear dissipation function for applications in a shallow water wave propagation model.

This experimental setup is an approximate realisation of the field conditions observed by Snodgrass et al. (1966) during their investigations of swell propagation across the Pacific Ocean. Therefore, model results were compared to their empirical swell energy density decay curves. These empirical curves were based on average decay rates computed from measurements of swell systems generated by 12 major storm events observed near Australia and New Zealand. Despite the considerable levels of noise and data scatter, decay rates of $\approx 9\times10^{-4}$dB/km and $\approx 4.5\times10^{-4}$dB/km were determined for swell components with $f = 0.08$Hz and $f = 0.075$Hz, respectively. These decay rates were converted into values of the ratio between F, the energy density at any particular position x, and F_0, the initial energy density at the point where the swell systems became decoupled from the generating storm. Evolution curves of F/F_0 based on the data of Snodgrass et al. (1966) are shown in Figure 5.25.

Results of experiments made with two alternative forms of S_{ds}^{bs} used in model runs ABYM1 and ABS are shown in panels (a) and (b) of Figure 5.25. Results from the third experiment shown in panel (c) were obtained from an additional run (W4M2) made with the form S_{ds}^{w4} of the WAM Cycle 4 model. Since the dissipation rates predicted by S_{ds}^{bs} at these frequencies have been reduced to the form (5.11), the major differences between these three model runs is the degree of nonlinear dependence on

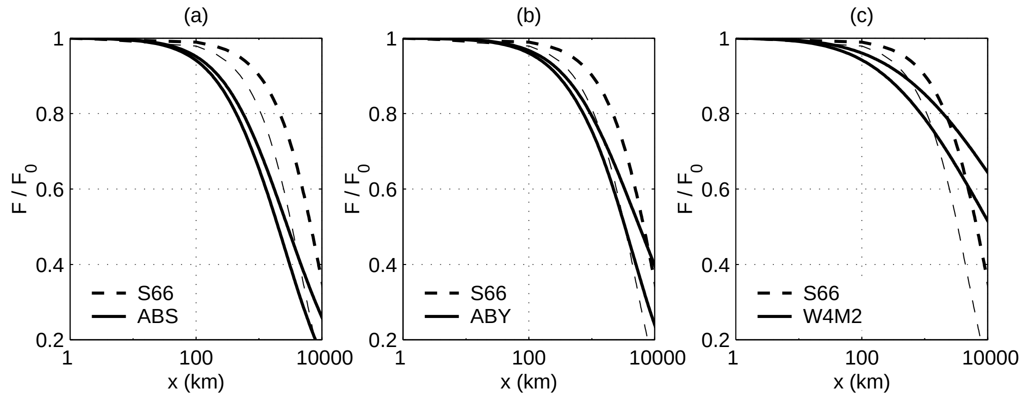

Figure 5.25: *Evolution curves of F/F_0 with distance x at two frequency bands typical of swell. Dashed lines indicate the empirical decay rates at $f = 0.075Hz$ and $f = 0.08Hz$ based on the data of Snodgrass et al. (1966). Computed decay rates of model runs ABS, ABYM1 and W4M2 at $f = 0.074Hz$ (right-hand curves) and $f = 0.082Hz$ (left-hand curves) are shown in panels (a), (b) and (c), respectively.*

the integral steepness term $(E_{tot}k_p^2)^m$ (in S_{ds}^{bs}) and $(E_{tot}\overline{k}^2)^m$ (in S_{ds}^{w4}). Values of m in each run are listed in Table 5.3.

Outcomes of model runs using the form S_{ds}^{bs} are generally more consistent with the data of Snodgrass et al. (1966). Nevertheless, decay rates in run ABS, which had the weakest dependence on the integral steepness parameter ($m = 0.80$), are consistently higher than those prescribed by the empirical curves. Decay rates of run W4M2 were also higher than the empirical values for the first 300km. Above $x = 300$km, however, decay rates relaxed due to the higher value of m in S_{ds}^{w4}, which led to a considerable reduction of decay rates. The setup of S_{ds}^{bs} used in run ABYM1 provided decay rates that were in better agreement with observations.

Limitations related to both the quality of the observational data and the oversimplified setup of the numerical experiments reduce the significance of these results. Nevertheless, these experiments indicated that the form S_{ds}^{bs} provides realistic estimates of dissipation rates for spectral ranges typical of swell systems, although model decay rates were generally higher than the data of Snodgrass et al. (1966). Further insight on the impact of the new saturation-dependent form of S_{ds} on swell decay is provided in the next Chapter.

Chapter 6

Sea-State Hindcasts in the Australian Region

This Chapter describes a first, exploratory series of experiments designed to validate the saturation-dependent form of S_{ds} using more realistic, two-dimensional wind fields. For this purpose, the new S_{ds} term was implemented in AUSWAM, a version of the WAM model used by the Australian Bureau of Meteorology (BoM) to produce sea-state forecasts within the Australian region. Performances of AUSWAM hindcasts using several configurations of the new dissipation function are compared to the operational model setup. Results are validated against fetch-limited evolution curves and *in situ* observations of integral spectral parameters from 12 buoys located in deep water sites off the Australian coast.

Results were significantly constrained by the reduced availability of observations of winds and waves in the Australian region. This major limitation did not allow a detailed examination of wave spectra and of the spatial distribution of simulated winds and waves. Consequently, the objectives of the experiments described in this Chapter were not to provide definitive answers on the impacts of a saturation-dependent dissipation source term on the performance of operational models. Nevertheless, these results offer a preliminary diagnosis that indicates the potential benefits of improved model physics on operational forecasting of wind-waves.

The sections of this Chapter are structured as follows. A brief historical overview of wind-wave modelling within the Australian region is made in Section 6.1. Section

6.2 provides a description of the implementation of the AUSWAM model. Buoy data and model validation strategies are described in Section 6.3. Fetch-limited experiments made to determine parameter values of the new saturation-dependent S_{ds} term are presented in Section 6.4. Results of model hindcasts of sea-state in the Australian region are described in Section 6.5. Finally, a refined model performance assessment using data from periods with optimal winds is presented in Section 6.6.

6.1 Wind-wave forecasting in Australia

Compared to other coastal nations, Australia has one of the longest and most diverse coastlines, containing a wide range of climatic and oceanographic regions. These areas support nearly 90% of Australia's population. A significant part of this coastal population is directly or indirectly involved in activities related to the ocean, which include fishing, offshore petroleum and tourism. Commercial and industrial activities related to the marine environment generate more than AUD$30 billion per year. Although sea-state forecasting provides important information for the success and safety of many of these activities, the history of operational wind-wave forecasting in Australia is surprisingly recent.

First-generation spectral wave models were introduced operationally at the BoM in 1986 (NMOC, 1986). They integrated a sea-state forecasting system composed of a hemispheric model at approximately 5° resolution and a nested regional model at approximately 2.5° resolution. The hemispheric model provided sea-state forecasts up to +48 hours at oceanic areas within the Southern Hemisphere, also providing boundary wave fields to the nested regional model, which generated forecasts at +12, +24 and +36 hours.

Several second-generation models were developed in Australia in subsequent years. They were mostly used in operational forecasting and hindcast studies conducted by private oil companies and the Australian Navy. Second-generation models were particularly useful in predicting and understanding the dynamics of hurricane-generated wave fields in the northwestern coast of Australia Sobey and Young (1986). Shallow water applications of these models, including the study of wave generation and propagation over the Great Barrier coral reef, are documented in Young (1988, 1989).

Despite the availability of these second-generation models, a broad upgrading of the sea-state forecasting system at the BoM was carried out only in 1994. The basis of the new system was the implementation of AUSWAM, a version of the WAM Cycle 4 model with the following modifications: (i) a third-order numerical propagation scheme and (ii) source terms from the Cycle 3 version of the WAM model. These two modifications of the standard WAM Cycle 4 release were based on numerical experiments reported in Bender and Leslie (1994) and Bender (1996).

AUSWAM currently comprises a global model at 3° spatial resolution, a regional model at 1° resolution (nested to the global model) and a mesoscale model at 0.25° resolution (nested to the regional model). The nested regional version covers an area from 60°S to 12°N and from 69°E to 180°E that involves the Australian continent, while the mesoscale model covers the southeast of Australia and ranges from 50°S to 24°S and 126°E to 164°E. The regional and global operational implementations of AUSWAM also include a system to assimilate significant save height H_s observations from the European Remote-Sensing Satellite ERS-2 (Greenslade, 2001).

6.2 Model Description

WAM is a third-generation spectral wind-wave model that simulates the evolution of the two-dimensional frequency spectrum $F(f, \theta)$ with respect to frequency f and direction θ. Spectral evolution is calculated by integrating the action balance equation in its spherical coordinate form

$$\frac{\partial F}{\partial t} + \cos^{-1}\phi \frac{c_\phi \cos\phi F}{\partial \phi} + \frac{\partial c_\lambda F}{\partial \lambda} + \frac{\partial c_\theta F}{\partial \theta} = S_{in} + S_{nl} + S_{ds}, \tag{6.1}$$

where $c_{\phi,\lambda,\theta}$ are components of the group velocity $\mathbf{c}_g = g/4\pi f$ and S_{in}, S_{nl} and S_{ds} are the wind input, nonlinear interactions and dissipation source functions, respectively.

6.2.1 Source terms

The source functions used in the AUSWAM implementation consist of the Discrete Interaction Approximation (DIA) of S_{nl}, following Hasselmann and Hasselmann (1985) and Hasselmann et al. (1985), and parameterised S_{in} and S_{ds} source terms consistent with the physics used in the WAM Cycle 3 release. The wind input source term follows the general form proposed by Snyder et al. (1981) [equation (2.18) of Chapter 2], with the proportionality constant $\beta = 0.25$.

Following Komen et al. (1984), the WAM model uses a variation of (2.18) defined in terms of the friction velocity u_*, where U_5 is replaced by $28u_*$. As u_* is generally a nonlinear function of U_5, this leads to an overestimation of spectral input rates relative to the original Snyder et al. (1981) form that increases nonlinearly with U_5

(e.g., for $U_5 = 10$ and 20 m/s the conversion $U_5 = 28u_*$ results in input rates that overestimate the original S_{in} by approximately 5% and 25%, respectively). In this study, model validation tests were done with two variations of S_{in} specified in terms of U_5 and $28u_*$.

In the operational AUSWAM implementation, whitecap dissipation is computed according to the quasi-linear source term proposed by Komen et al. (1984), given by equation (2.27) of Chapter 2. The value of the dissipation coefficient $C_{ds} = 6.74 \times 10^{-5}$ was set according to Bender and Leslie (1994), while Komen et al. (1984) suggest a somewhat lower constant $C_{ds} = 3.33 \times 10^{-5}$. Other S_{ds} parameters follow the default WAM Cycle 3 configuration: $m = 2$ and $n = 2$.

The main focus of this Chapter is to use realistic wind fields to validate the new form of S_{ds} that was proposed and tested under idealised condition in previous Chapters. For this purpose, the general S_{ds}^{bs} configuration given by equation (5.7) of Chapter 5 was implemented in AUSWAM. Although the validation tests described below are primarily directed towards validating the new S_{ds} form, they also provide a basis for comparing changes in model skill relative to the standard operational setup of AUSWAM.

6.3 General Validation strategy

Model results were first validated against parametric fetch-limited evolution curves and observations of significant wave height H_s and peak period T_p from 12 buoys deployed in intermediate- to deep-water sites near the Australian coast (Figure 6.1). Although the new dissipation function was extensively tested under idealised fetch-limited conditions, new tests were needed because of two major differences between the AUSWAM model and the research model used in the previous Chapter. These differences are (i) the dynamical treatment of the wave spectrum in wavenumbers above $6.25k_p$ (the spectral tail) and (ii) the numerical technique used in solving the nonlinear wave-wave interactions term S_{nl}.

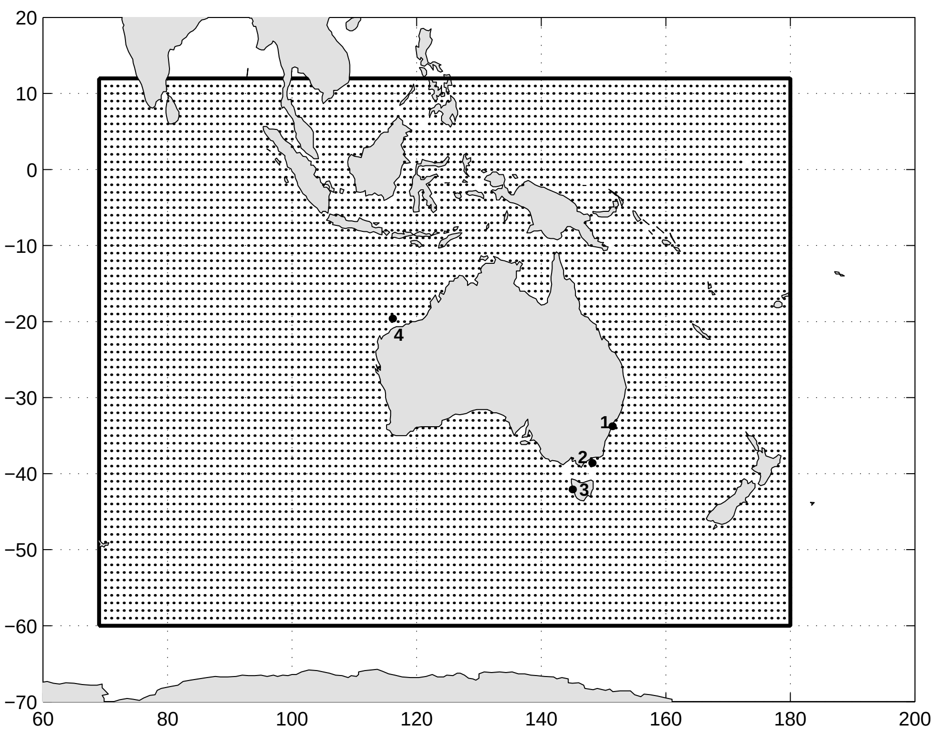

Figure 6.1: *Regional implementation of the AUSWAM model. The numerical grid is shown as an array of black dots at the model resolution of 1 °. Ocean and land boundaries of the numerical grid are indicated by thick continuous lines. Small islands represented by a single grid point appear as diamonds. Location of validation sites around the Australian coast are indicated by circles and labelled according to the definitions listed in Table 6.1.*

Numerical experiments presented in the previous Chapter were made with a model that uses the Tracy and Resio (1982) exact S_{nl} algorithm (WRT) described in Chapter 2. The WAM model uses the discrete interaction approximation (DIA) of S_{nl} developed by Hasselmann et al. (1985). The DIA is a parameterisation of S_{nl} that computes explicitly only one set of interacting spectral components satisfying the resonant conditions (2.24), while the exact solution evaluates millions of interacting sets. As shown by Hasselmann et al. (1985) and, more recently, by Van Vledder et al. (2000), results from the DIA and the exact S_{nl} solution may differ significantly in a variety of situations. A re-tuning of the other source terms is therefore needed to accommodate these distinctions between numerical models.

Other major difference between the research model used in the previous Chapter and the WAM model is the treatment of the spectral tail. The WAM model prescribes a fixed spectral tail proportional to f^{-5} at wavenumbers above $6.25k_p$ $(2.5f_p)$. This restricts the explicit computation of source terms to wavenumbers close to the spectral peak region. The consequence of this feature of the WAM model was investigated by Banner and Young (1994). Their results show that the specification of a fixed parametric tail at wavenumbers close to the spectral speak significantly affects model results not only in terms of details of the wave spectrum, but also regarding the evolution of integral spectral parameters such as E_{tot} and f_p.

Due to these major differences, fetch-limited experiments were undertaken with the primary objective of producing an array of S_{ds} configurations properly adjusted to the characteristics of the AUSWAM model, for subsequent use in the operational AUSWAM model runs with realistic two-dimensional wind fields. Although fetch-limited cases do not represent even roughly these more complex wind forcing conditions, this preliminary tuning exercise was the only alternative to optimising the number of experiments using the regional implementation of AUSWAM, leading to a more efficient usage of computer time.

Subsequent to the fetch-limited tuning experiments, regional hindcasts were made through two main groups of experiments. First, the six source term configurations with the best performance in the fetch-limited experiments were included in model runs made with wind fields from the 29 day period between February 1 00Z and February 29 00Z 2000. Winds were obtained from analysed data produced by the regional atmospheric model LAPS (Puri et al., 1998). The performances of the alternative S_{ds} configurations were compared and ranked according to the values of four statistical parameters [bias, root mean square (rms) error, scatter index and correlation coefficient] calculated in relation to H_s and T_p data at the 12 validation sites shown in Figure 6.1. These statistical parameters are formally defined in Section 6.3.2.1.

Label	Code	Location	Hull type	Payload	Position		Depth (m)	Wind height	Sample rate (h)
					Lat	Long			
1	55017	Byron Bay	Waverider	MHL	-28.69	153.73	72		1
2	55018	Coffs Harbor	Waverider	MHL	-30.34	153.27	73		1
3	55019	Crowdy Head	Waverider	MHL	-31.83	152.86	79		1
4	55011	Sydney	Waverider	MHL	-33.77	151.42	87		1
4	55025	Sydney	Waverider	MHL	-33.90	151.32	65	4.5	1
5	55014	Batemans Bay	Waverider	MHL	-35.71	150.34	73		1
6	55020	Eden	Waverider	MHL	-37.29	150.18	110		1
7	55039	Bass Strait	EMI Sensor	Esso	-38.60	148.19	75	44.0	1/6
8	55026	Strahan	Waverider	BoM	-42.08	145.01	100	19.5	1/2
9	56006	C Naturaliste	Waverider	WADoT	-33.36	114.78	50		1
10	56005	Rottnest Isl	Waverider	WADoT	-32.11	115.40	48		1
11	56004	Jurien	Waverider	WADoT	-30.29	114.91	42		1
12	56002	NW Shelf	Waverider	WP	-19.59	116.14	110	35.0	3

Table 6.1: Characteristics and locations of wind and wave measurement sites used for model validation. Acronyms refer to the Manly Hydraulics Laboratory (MHL), the Australian Bureau of Meteorology (BoM), the West Australian Department of Transport (WADoT) and, Woodside Petroleum (WP). Numbers in the first column correspond to labels in Figure 6.1. Codes are the World Meteorological Organization (WMO) index numbers.

As pointed out in previous studies (Cardone et al., 1994, 1996), the accuracy of the forcing wind fields is critical to the wave model performance. An examination of wind data at buoy sites with simultaneous wind and wave observations (see Table 6.1) revealed that in most cases the quality of LAPS model winds was not optimal during the hindcast period of February 2000. To address this limitation, wind fields from a 62-day long period between March 20 00Z and May 20 00Z 1998 were also examined. Comparisons with observations once more demonstrated that model winds were not adequate for a robust analysis of wave model performance in two validation sites (Sydney and Northwest Shelf). Consequently, a second round of analyses was carried out in the two remaining locations (Bass Strait and Strahan).

Limitations related to the coarse regional model grid resolution, however, were found to affect model predictions of peak periods T_p within Bass Strait. Therefore, a final refined analysis of two severe sea-state events associated with periods of optimal LAPS winds in Strahan was made. Criteria for selecting these two optimal wind periods were based on the analyses of Cardone et al. (1994). Details of numerical experiments and specific criteria for performance assessment are provided in sections 6.4 through 6.6. The remainder of this section provides a description of (i) the choice of parametric evolution curves used in the validation of fetch-limited experiments; (ii) the network of buoys used for validation of regional model runs; and (iii) the statistical parameters used to assess model performance.

6.3.1 Fetch-limited evolution curves

Model results of the fetch-limited experiments were compared to evolution curves according to whether the Snyder et al. (1981) wind input source function S_{in} is defined in terms of U_5 or the sea-state independent u_*. Consequently, only two classes of nondimensional fetch-limited evolution curves are used in the fetch-limited experiments presented in this Chapter. As U_5 is reasonably well approximated by a linear function of U_{10}, the U_{10}-scaled nondimensional curves given by equations (4.10) and (4.11) of Chapter 4 are adopted. The corresponding u_*-scaled parametric curves are given by equations (4.13) and (4.14).

The u_*-scaled evolution curves are valid approximately within the range of nondimensional fetches $1 \times 10^2 < \chi_* < 1 \times 10^4$, while the approximate range of validity of the U_{10}-scaled curves is within $3 \times 10^4 < \chi < 3 \times 10^6$. At longer nondimensional fetches, the evolution curves are extrapolated towards the asymptotic limits proposed by Alves et al. (2000), given by expressions (4.24), (4.26), (4.25) and (4.27) of Chapter 4.

6.3.2 Validation of regional model runs

Regional model runs were validated against H_s and T_p data from the 12 deep-water sites shown in Figure 6.1. Table 6.1 provides a detailed list of their relevant characteristics that includes the World Meteorological Organization (WMO) index numbers, hull type, payload, geographical position, depth of deployment, height of wind speed measurements (when present) and sampling rate. Most wave observations were made with Datawell Waverider buoys, the only exception being measurements at Bass Strait, provided by an electro-magnetic induction sensor attached to the leg of an oil platform. Although three buoy sites were located at depths ranging from 40m to 50m, all wave observations were assumed to be made in deep water.

Wind and wave data were generally provided at one-hourly intervals. Data from Bass Strait and Strahan, sampled at 10 and 30 min respectively, were reduced to one-hourly intervals by simple averaging. Following the approach of Cardone et al. (1994), the resulting hourly time series were smoothed by averaging three successive observations with weights 1/4, 1/2 and 1/4, to reduce sampling variability. Smoothed hourly time series were finally sub-sampled at three-hourly intervals at times corresponding to the wave model outputs.

Measurements of wind velocity and direction were made at a variety of anemometer heights, as indicated in Table 6.1. To enable validation of the hindcast 10m-height wind fields used to force AUSWAM, available observations were converted into corresponding 10m-height winds by assuming a neutrally-stable logarithmic atmospheric boundary layer. Converted U_{10} values were derived using the relation

$$U_z = U_{10}\ln(z/z_0)/\ln(10/z_0), \tag{6.2}$$

where the roughness length z_0 was determined from the Charnock relation and the drag coefficient parameterisation proposed by Wu (1982). Although in non-neutral atmospheric stability conditions the wind profile may deviate from this logarithmic profile, measurements of the air-sea temperature differences were not available. Therefore, neutral stability was assumed.

In most cases, nodes from the regional model grid did not match exactly the location of measurement sites. Because of the relatively coarse resolution of this numerical grid (i.e., 1°) and the proximity of measurement sites to the coast, it was not possible to spatially interpolate the model output into the exact buoy locations, as this would involve nodes over land boundaries. Consequently, model validation was performed using the output from grid nodes nearest to each buoy location.

6.3.2.1 Validation statistics

Our assessment of model results from regional model runs was based on the following four standard statistical parameters:

(i) Bias

$$bias = \frac{\sum_{i=1}^{N} M_i - O_i}{N}; \tag{6.3}$$

(ii) Root-mean-square error

$$\epsilon_{rms} = \sqrt{\frac{\sum_{i=1}^{N} (M_i - O_i)^2}{N}}; \tag{6.4}$$

(iii) Scatter index

$$SI = \frac{\sigma_M}{\overline{O}}; \tag{6.5}$$

(iv) Correlation coefficient

$$r = \frac{\sum_{i=1}^{N}(O_i - \overline{O})(M_i - \overline{M})/N}{\sqrt{\sum_{i=1}^{N}(O_i - \overline{O})^2}\sqrt{\sum_{i=1}^{N}(M_i - \overline{M})^2}} \tag{6.6}$$

where O_i and M_i represent observed and modelled values, respectively, of either wind speed U_{10}, wind direction θ_U, significant wave height H_s and spectral peak wave period T_p; σ_M is the standard deviation of modelled values; N is the number of observations; and over-bars denote ensemble averages. All statistics were determined by assuming that observations provided the best estimate of the true value of each diagnostic variable.

6.3.3 Experimental setup

6.3.3.1 Fetch-limited runs

The numerical grid used in the fetch-limited runs consisted of a rectangular basin with open south and north lateral and western-upwind boundaries and an eastern-downwind land boundary. Deep-water wave propagation was assured by specifying a constant depth equal to 4000m at all grid nodes, excluding the land boundary. The fetch-limited grid had 601x11 nodes extending from 0°E to 30°W (0.05° resolution) and -1°S to 1°N (0.2° resolution). The model was forced with two constant wind speeds U_{10} = 10 and 20m/s blowing at 90° offshore from the land boundary. As both wind regimes produce evolution curves that overlap in most cases after proper scaling with the wind speed used in the specification of S_{in}, figures included in this Chapter will show only results from experiments with U_{10} = 10m/s.

Model spectra were resolved at 33 frequency bins logarithmically spaced from 0.0418 Hz to 0.8819 Hz, at intervals of $\Delta f/f = 0.1$, and 12 directional bins with 30° resolution. Initial conditions were specified by a JONSWAP spectrum with $f_p = 0.4$Hz and parameters set to $\alpha_J = 0.018$, $\gamma = 3$, $\sigma_a = 0.07$ and $\sigma_b = 0.09$. Propagation time steps and source term integration intervals were both set to 60 s. Outputs of diagnostic variables were generated at 12 hour intervals. Computations simulated five days for cases with U_{10} = 10m/s and seven days for cases with U_{10} = 20m/s, resulting in stable steady-state model outcomes at the end of each simulation period. More than 20 model runs were initially made to assess the performance of the new saturation-dependent form of S_{ds}. The four best performing configurations are included in this Chapter.

6.3.3.2 Regional runs

Global and regional implementations of AUSWAM were both run for a total of 91 days over two hindcast periods representative of autumn and summer conditions: March 20 00Z to May 20 00Z 1998 and February 1 00Z to March 1 00Z 2000, respectively. Data assimilation was switched off so that the contrast between different wave model physics options could be emphasised. Initialisation occurred at day 1 of each hindcast period with analysed spectra obtained from the BoM operational archives.

The global model was run only once for each hindcast period with the standard BoM model physics, corresponding to S_{in} and S_{ds} prescribed by equations (2.18) and (2.27), respectively. Wave model spectra from the global model at the borders of the regional model were stored and used as boundary conditions for the nested regional model runs. Consequently, boundary conditions were identical in all regional simulations.

In both global and regional implementations of AUSWAM the propagation time step was set to 20 minutes, while source terms were integrated every 10 minutes. The discrete representation of the two-dimensional frequency spectrum $F(f, \theta)$ consisted of 25 frequency bins logarithmically spaced from 0.0418 Hz to 0.4114 Hz, at intervals of $\Delta f/f = 0.1$, and 12 directional bins with 30° resolution. At 1° spatial grid resolution, very few of the wave model grid points were in water depths of less than 100m. Therefore, the regional and global wave models were run with deep water physics only (i.e., bottom friction and refraction effects were switched off). Modelled wave spectra and diagnostic variables such as significant wave height H_s, mean wave direction θ_m and peak period T_p were stored in output files at 3 model-hour intervals.

The global wave model was forced with 12-hourly hindcast winds at 2.5° spatial resolution, obtained from the global atmospheric model GASP (Seaman et al., 1995) at the BoM. The global wind fields were interpolated into 3-hourly intervals and 3° spatial resolution. Winds used to force the regional wave model were obtained from the regional atmospheric model LAPS (Puri et al., 1998). Although the lowest level of LAPS is very close to 10m, proper U_{10} values are obtained via Monin-Obukhov theory with empirical stability functions given by Garratt (1992). This extrapolation is also done to reduce the 70m-level winds from GASP to U_{10}. The U_{10} fields were provided at 3-hourly intervals and 0.75° spatial resolution. These were interpolated into hourly intervals and to the spatial resolution of the regional wave model grid (i.e., 1°).

Both fetch-limited and regional hindcast experiments were made in a 32 vector processor NEC SX-4 supercomputer, which is largely dedicated to running operational models that produce weather and sea-state forecasts for the Australian region on a 12-hourly basis. The extension of the experiments reported in this Chapter was, therefore, largely limited by the availability of CPU time.

6.4 Results of fetch-limited runs

Fetch-limited experiments begun with a series of sensitivity tests to determine the best choice of numerical grid and initial and boundary conditions. Control runs with the standard AUSWAM source terms were then carried out. Subsequent experiments focused on tuning and validation of the saturation-dependent form of S_{ds}, with the objective of determining an array of optimal source term configurations to be used in the regional experiments.

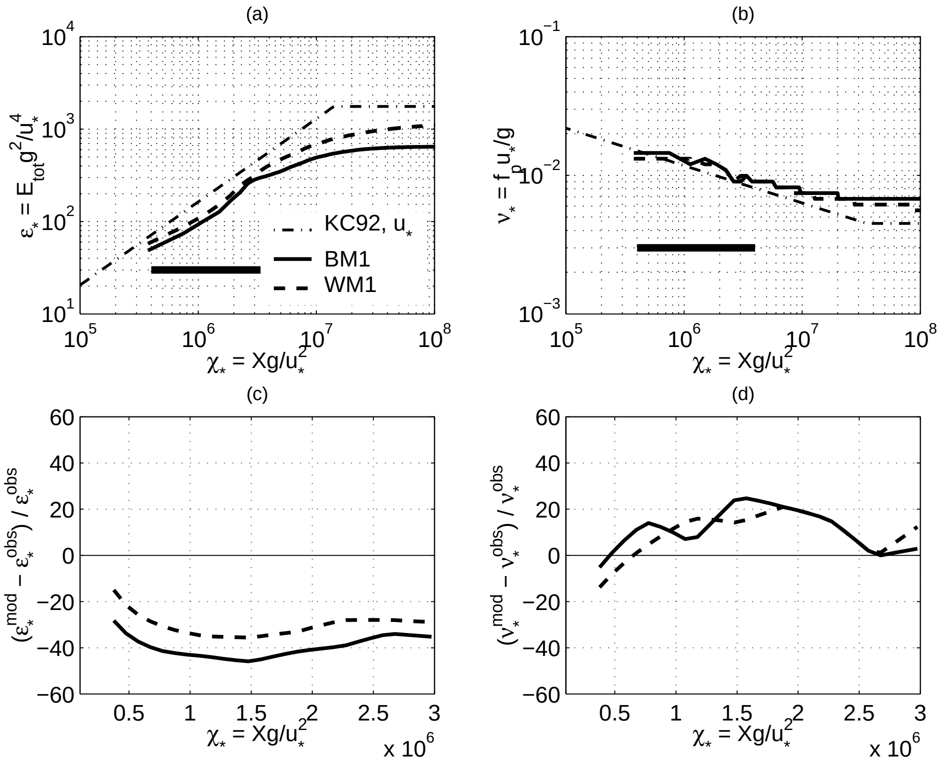

Figure 6.2: *Results from run BM1 and WM1. Non-dimensional total energy* $\varepsilon_* = E_{tot}g^2/u_*^4$ *and peak frequencies* $\nu_* = f_p u_*/g$ *are plotted against nondimensional fetch* $\chi_* = Xg/u_*^2$ *in panels (a) and (b), respectively. Model results (thick continuous lines) are compared to the parametric evolution curves (thin dashed lines indicated by the symbol KC92) of Kahma and Calkoen (1992, 1994). Lower panels show the discrepancy between model results and target curves as a percentage within the validity range of the Kahma and Calkoen (1992, 1994) relations [this is indicated by the thick horizontal lines in panels (a) and (b)].*

Model values of nondimensional total energy ($\varepsilon_* = E_{tot}g^2/u_*^4$ or $\varepsilon = E_{tot}g^2/U_{10}^4$) and peak frequency ($\nu_* = f_p u_*/g$ or $\nu = f_p U_{10}/g$) were validated against the parametric fetch-limited curves (4.13) and (4.14) or (4.10) and (4.11) according to whether S_{in} was specified in terms of u_* or U_5, respectively. At full development, validation was made against the corresponding asymptotes (4.25) and (4.27) or (4.24) and (4.26) proposed by Alves et al. (2000). Configurations of the new saturation-dependent term S_{ds}^{bs} were considered optimal when model values of ε and ν were within ±20% and ±10%, respectively, of the target curves within the fetch-limited range and also at full-development.

Experiments throughout this Chapter are labelled by three character codes. The first two characters represent the form of S_{ds} used and the third character represents the run number. Runs with either the standard AUSWAM dissipation term, an optimised variation of the WAM Cycle 3 term or the new saturation-dependent form S_{ds}^{bs} are, therefore, represented by the prefixes BM, WM and AB, respectively.

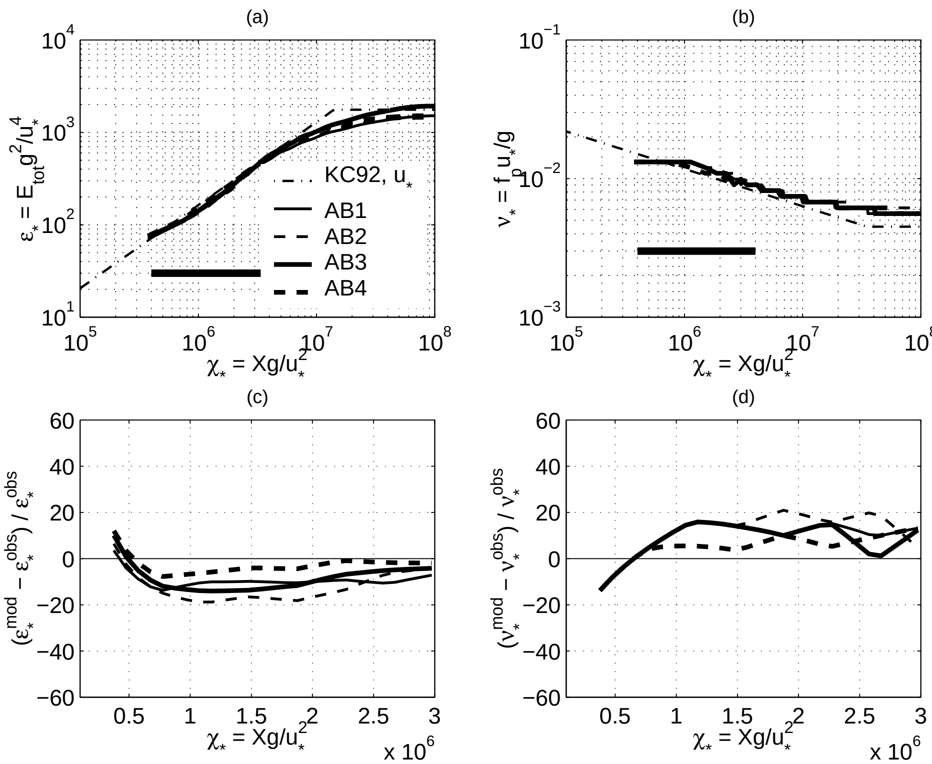

Figure 6.3: *Results from runs AB1, AB2, AB3 and AB4. Non-dimensional total energy $\varepsilon_* = E_{tot}g^2/u_*^4$ and peak frequencies $\nu_* = f_p u_*/g$ are plotted against nondimensional fetch $\chi_* = Xg/u_*^2$ in panels (a) and (b), respectively. Model results (thick continuous lines) are compared to the parametric evolution curves (thin dashed lines indicated by the symbol KC92) of Kahma and Calkoen (1992, 1994). Lower panels show the discrepancy between model results and target curves as a percentage within the validity range of the Kahma and Calkoen (1992, 1994) relations [this is indicated by the thick horizontal lines in panels (a) and (b)].*

6.4.1 Integral spectral parameters

The top panels (a) and (b) of Figure 6.2 show the nondimensional evolution curves of ε_* and ν_* obtained with the standard AUSWAM source term setup. Also shown are the u_*-scaled target evolution curves. This run was designated BM1. Friction velocity scaling is used, as the default WAM Cycle 3 S_{in} is defined in terms of u_*. The lower panels indicate the percentage bias between model results and corresponding target evolution curves only within the valid ranges of the fetch-limited region. AUSWAM clearly underestimates ε_* and ν_* values in up to 45% and 25% respectively. At full development, the underestimation is greater than 50%.

This poor performance in a fetch-limited scenario is a result of using a value of $C_{ds} = 6.74 \times 10^{-5}$ that is significantly higher than the original value ($C_{ds} = 3.33 \times 10^{-5}$) used in the WAM Cycle 3 release. This change was made on the basis of a validation study performed by Bender and Leslie (1994) over a one-month period. No wind speed validations were performed in this study. Therefore, it is possible that the need for higher dissipation rate levels arose due to an overprediction of winds used to force the wave model. Consequently, the significant underestimation of evolution rates in run BM1 is not unexpected.

The effects of reducing the dissipation constant to the original value $C_{ds} = 3.33 \times 10^{-5}$ were explored in run WM1. Results are also shown in Figure 6.2. In addition to a reduced C_{ds}, run WM1 was done with S_{ds} parameters $m = 2.65$ and $n = 2$, determined through model optimisation as reported in Monbaliu and Hasselmann (1994). Disagreement with the target growth curves within the fetch-limited range is reduced. Nevertheless, discrepancies at longer fetches are still considerable. At full development, the difference is enhanced due to the fact that the optimisation of

S_{ds} made by Monbaliu and Hasselmann (1994) targeted the Pierson and Moskowitz (1964) asymptotes, while in this Chapter the full-development limits of Alves et al. (2000) are used.

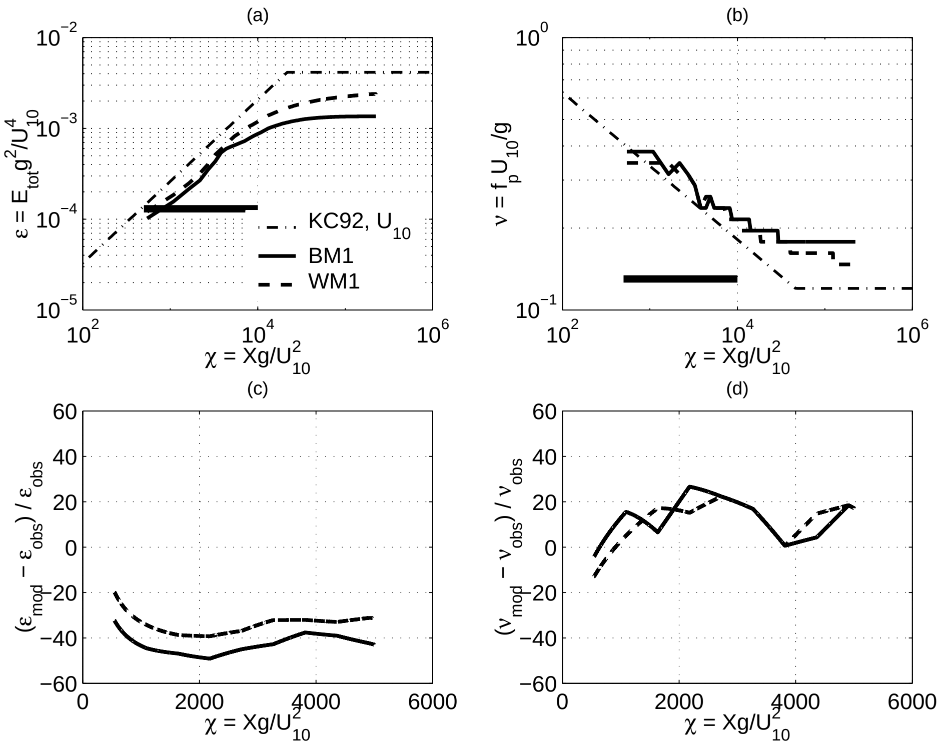

Figure 6.4: *Results from runs BM1 and WM1 using the Snyder et al. (1981) form of* S_{in} *with a dependence on* U_{10}*. Non-dimensional total energy* $\varepsilon = E_{tot}g^2/U_{10}^4$ *and peak frequencies* $\nu = f_pU_{10}/g$ *are plotted against nondimensional fetch* $\chi = Xg/u_{10}^2$ *in panels (a) and (b), respectively. Model results (thick continuous lines) are compared to the parametric evolution curves (thin dashed lines indicated by the symbol KC92) of Kahma and Calkoen (1992, 1994). Lower panels show the discrepancy between model results and target curves as a percentage within the validity range of the Kahma and Calkoen (1992, 1994) relations [this is indicated by the thick horizontal lines in panels (a) and (b)].*

As argued by Banner and Young (1994), further changes in the WAM Cycle 3 S_{ds} do not improve the agreement between model outcomes and observations of fetch-limited evolution. These results suggest that readjusting parameters may reduce the discrepancies at longer fetches and close to full development, but this will come at a cost of overestimating integrated energy levels at shorter fetches and vice-versa. Based on these results and having in mind the limited available computational resources, other alternative configurations of the WAM Cycle 3 S_{ds} were not tested as no further improvements were considered plausible.

Subsequent experiments were aimed at manually tuning the saturation-dependent form of S_{ds} to the target fetch-limited growth curves. The strategy was to first choose source term parameters that provided spectral dissipation rates as close as possible to those of the optimised WAM Cycle 3 S_{ds} term used in run WM1. These initial parameter values were then gradually changed, allowing a comprehensive assessment of how the new form of S_{ds} affects model skill as it becomes more strongly dependent on the term representing breaking due to group modulation $(B(k)/B_r)^{p/2}$. Table 6.2 summarises the run codes used throughout this section and their corresponding dissipation parameters.

Both the WAM Cycle 3 dissipation term and the saturation-dependent form of S_{ds} are predicated on concepts that differ in their most basic aspects. In practice, their major differences are (i) the inclusion in the new S_{ds} of a term dependent on the saturation spectrum $(B(k)/B_r)^{p/2}$ and (ii) a dependence in the new form of S_{ds} of an overall steepness parameter based on the peak wavenumber k_p rather than on the average wavenumber $\overline{k}$.

	S_{ds}				
Run code	C_{ds}	m	n	p_∞	B_r
BM1	6.74×10^{-5}	2.0	2.0		
WM1	3.33×10^{-5}	2.65	2.0		
AB1	7.71×10^{-2}	1.3	1.0	0.0	
AB2	2.63	2.0	0.0	4.0	7.5×10^{-3}
AB3	1.91	2.0	0.0	4.0	5.8×10^{-3}
AB4	8.80×10^{-3}	1.0	1.0	4.0	5.0×10^{-3}

Table 6.2: Summary of run codes and their corresponding dissipation parameters.

The term $(B(k)/B_r)^{p/2}$ is neutralised if the exponent p is set to zero for all values of $B(k)$. Dissipation rates of the new S_{ds} term would then, intuitively, be very similar to those provided by the WAM Cycle 3 S_{ds}, as the basic difference between both would only be the dependence on an integral steepness specified in terms of k_p (steepness= $E_{tot}k_p^2$) or $\overline{k}$ (steepness= $E_{tot}\overline{k}^2$), respectively. This hypothesis was tested by making $p = 0$ in run AB1, with other parameter values listed in Table 2.

Results of run AB1 are shown in Figure 6.3, which also summarises the outcomes of other runs made with the new form of S_{ds}. The discrepancies between model results and target fetch-limited curves are significantly reduced in relation to runs BM1 and WM1: values of ε_* and ν_* are now mostly within $\pm 15\%$ of valid ranges of the target evolution curves. At full development, the discrepancies are of the order of -10%. The increase in model skill relative to runs using the WAM Cycle 3 form of S_{ds} results mostly from replacing $\overline{k}$ with k_p in the definition of the integral steepness parameter $H_s k_p$ in (3.7). As the wave field evolves with fetch, k_p provides a slightly wider dynamic range than $\overline{k}$ as the wave field develops with fetch. The use of k_p, therefore, results in higher dissipation rates at short fetches and lower dissipation rates close to full development.

The nonlinear dependence of spectral dissipation rates on the ratio between the saturation spectrum and a reference saturation level $(B(k)/B_r)^{p/2}$ was activated in run AB2, with the exponent p set to 4, $m = 2$, $B_r = 7.5 \times 10^{-3}$ and $C_{ds} = 2.63$. To allow a better assessment of the impact of these changes, the short wave straining term k/k_p was turned off by making the exponent $n = 0$. Results of run AB2 are shown in Figure 6.3. The agreement between model results and target growth curves is comparable to those of run AB1 and slightly better than those of runs using the WAM Cycle 3 form of S_{ds}, BM1 and WM1.

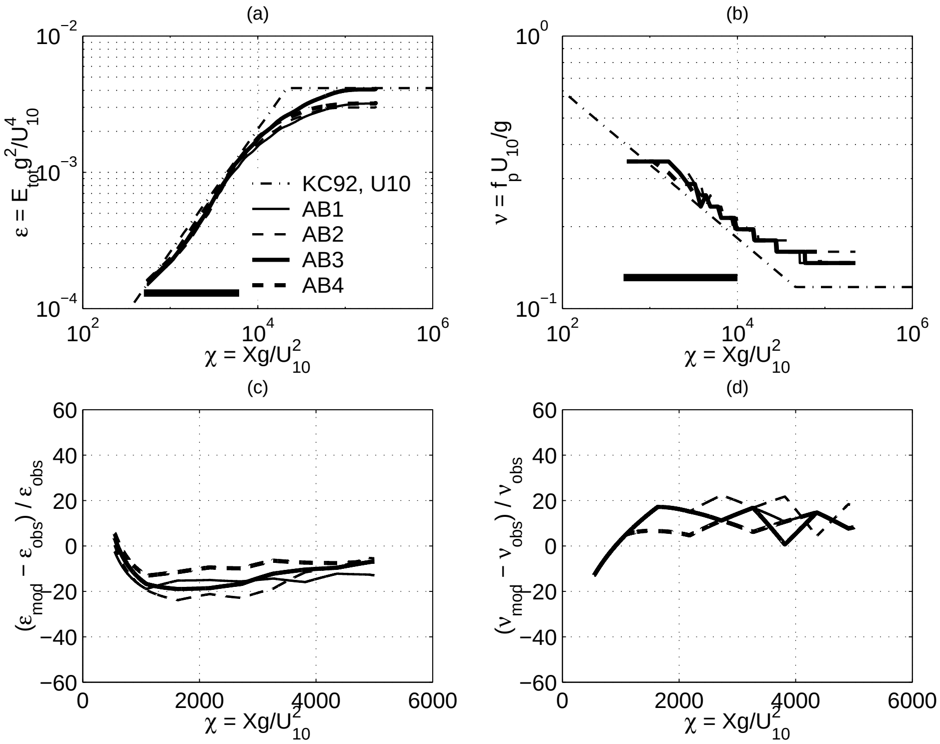

Figure 6.5: *Results from runs AB1,AB2,AB3 and AB4 using the Snyder et al. (1981) form of* S_{in} *with a dependence on* U_{10}*. Non-dimensional total energy* $\varepsilon = E_{tot}g^2/U_{10}^4$ *and peak frequencies* $\nu = f_pU_{10}/g$ *are plotted against nondimensional fetch* $\chi = Xg/u_{10}^2$ *in panels (a) and (b), respectively. Model results (thick continuous lines) are compared to the parametric evolution curves (thin dashed lines indicated by the symbol KC92) of Kahma and Calkoen (1992, 1994). Lower panels show the discrepancy between model results and target curves as a percentage within the validity range of the Kahma and Calkoen (1992, 1994) relations [this is indicated by the thick horizontal lines in panels (a) and (b)].*

In run AB3, the strength of the dependence of S_{ds} on $(B(k)/B_r)^{p/2}$ was increased by reducing the reference saturation level to $B_r = 5.8 \times 10^{-3}$, while the dissipation constant was reduced to $C_{ds} = 1.91$ and other parameters were kept at $p = 4$, $m = 2$ and $n = 0$. Figure 6.3 shows that the agreement of model results with the target curve within both the fetch-limited range and at full development is now improved relative to the previous model runs.

The agreement between model results and observations within the fetch-limited evolution range was further improved by reactivating the straining term $(k/k_p)^n$. This was done in run AB4 through setting the exponent n to unity. Other parameters were set to values listed in Table 6.2. Results are illustrated in Figure 6.3. Panels (c) and (d) of this figure show that activating the straining term results in some reduction of the percentage bias in both estimates of ε_* and ν_*. The changes, however, are not dramatic because above $6.25k_p$, where the ratio (k/k_p) becomes increasingly large, no explicit source term computations are done due to the presence of a fixed parametric spectral tail.

The robustness of results obtained with wind input levels specified in terms of u_* were further verified by changing the specifications of the input term S_{in}. This was done by replacing $U_0 = 28u_*$ with $U_0 = U_{10}$ in equation (2.18) and reducing the proportionally constant C_{in} to 0.23. These changes amount to recovering the original form and levels of S_{in} proposed by Snyder et al. (1981), which was directly obtained from observations of growth rates of deep water waves. All runs described previously were repeated with this alternative configuration of S_{in} and unchanged S_{ds} parameters, as listed in Table 6.2.

Results of these additional runs are summarised in Figures 6.4 and 6.5. Figure 6.4 illustrates the outcomes of runs BM1 and WM1, while Figure 6.5 shows the results of runs AB1, AB2, AB3 and AB4. In most cases, model performance was essentially the same as that of previous tests using $U_0 = 28u_*$. Major differences were found in results from the test using the S_{ds} setup of run AB4. Although this configuration provided the best overall model performance within the valid range of fetch-limited target evolution curves, as in the $U_0 = 28u_*$ tests, it underestimated considerably (by more than 20%) the U_{10}-scaled full-development limit. The best match between model results and target U_{10}-scaled fetch-limited evolution curves , including the full-development limits, was achieved with the S_{ds} setup of run AB3.

6.4.2 One-dimensional frequency spectra

The results of the previous section indicates that model outcomes are strongly affected by the chosen form of S_{ds}. Alternative dissipation functions result in significant differences in the computed evolution curves of integral spectral parameters. The differences are most significant in the computed values of nondimensional energy ε. The simulated evolution curves of nondimensional peak frequency ν are less sensitive to alternative forms of S_{ds}, as seen in panels (b) and (d) of Figures 6.4 through 6.5.

It is well-established that the peak frequency shifting observed in the fetch-limited evolution of wind-waves is governed by nonlinear wave-wave interactions (Hasselmann et al., 1973; Young and Van Vledder, 1993). Numerical experiments conducted by Hasselmann et al. (1985), Young and Van Vledder (1993) and Van Vledder et al. (2000) have demonstrated that the choice of parameterisation of the nonlinear interactions source term S_{nl} not only affects the rate of peak frequency down-shifting with fetch, but also determines the shape of the wind-wave spectrum. A comparison between fetch-limited spectra computed using AUSWAM and the research model used in the previous Chapter provides a confirmation of these earlier results. The DIA form of S_{nl} is used in AUSWAM, while the research model of the previous Chapter uses an exact algorithm to calculate S_{nl}.

Figure 6.6 shows the spectra computed using the original WAM Cycle 3 form of S_{ds} (run WM1) and the newly-proposed saturation-dependent form of S_{ds} (run AB3). This figure shows two different stages of evolution, corresponding to an intermediate

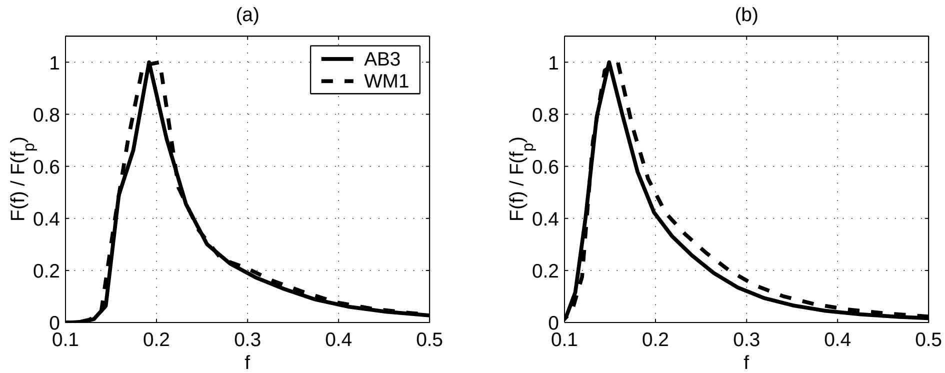

Figure 6.6: *Fetch-limited spectra computed using the original WAM Cycle 3 form of S_{ds} (run WM1: dashed line) and the newly-proposed saturation-dependent form of S_{ds} (run AB3: continuous line). Panels (a) and (b) represent two different stages of evolution, corresponding to an intermediate fetch ($\chi = 1 \times 10^{-4}$) and to full development ($\chi = 1 \times 10^{-5}$). Energy densities $F(f)$ are normalised by the peak energy density $F(f_p)$.*

fetch and to full development. Spectra were by the peak energy density $F(f_p)$ to allow a better inter-comparison of their shapes. Despite minor changes, the shapes of spectra from runs WM1 and AB3 are virtually identical. The position of the spectral peak in frequency space, kept in the original dimensional form, is also very similar. Run AB3 produces a slightly lower f_p, which explains its slightly better performance relative to runs BM1 and WM1, as seen in Figures 6.3 and 6.5.

In Figure 6.7, spectra produced by run AB3 is compared to fetch-limited spectra computed using the exact S_{nl} algorithm. Results from run ABS of Chapter 5 are used because forms of S_{in} and S_{ds} similar to those used in run AB3 were used in that experiment. This figure shows two different stages of evolution, corresponding to an intermediate fetch and to full development. Both vertical and horizontal axis maintain the dimensional values of energy density $F(f)$ and frequency f.

The differences in spectral shape are striking. Spectra produced with the DIA form of S_{nl} (run AB3) are much broader than the corresponding spectra computed using

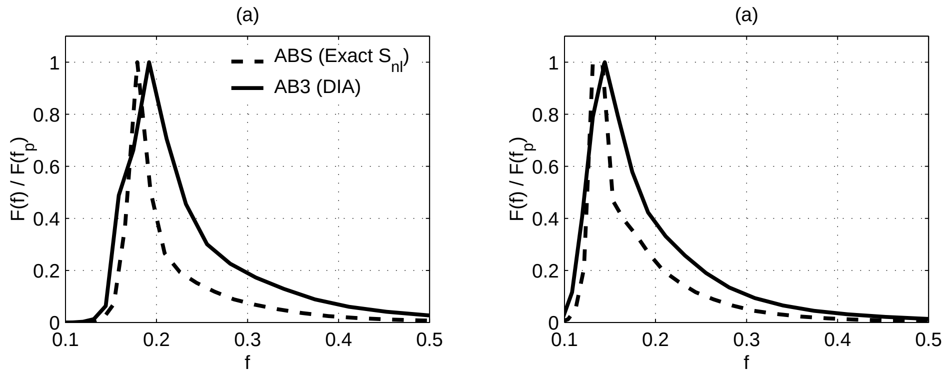

Figure 6.7: *A comparison of fetch-limited spectra produced by run AB3 (continuous line) with spectra computed using the exact S_{nl} algorithm (run ABS: dashed line). Panels (a) and (b) represent two different stages of evolution, corresponding to an intermediate fetch ($\chi = 1 \times 10^{-4}$) and to full development ($\chi = 1 \times 10^{-5}$).*

the exact S_{nl} (run ABS). Despite the differences in shape, both spectra provide values of integrated energy that are quite similar. Significant wave heights H_s from spectra in panel (a) are 0.95m (ABS) and 0.85m (AB3), while in panel (b) the values are 1.50m (ABS) and 1.31m (AB3), representing a discrepancy of around 10%. This explains why in both experiments ABS and AB3 there was close agreement between computed and empirical evolution curves for ε.

The distribution of wave energy within frequency bands, which determines the strong differences in the shapes of the spectra from runs ABS and AB3, is also crucial in determining the value of the peak frequency f_p. As seen in panels (a) and (b), the values of f_p from run AB3 (0.21Hz and 0.15Hz, respectively) are more than 15% higher than the calculated peak frequencies of spectra from run ABS (0.18Hz and 0.13Hz, respectively). These results suggest strongly that the poorer match between computed f_p and empirical evolution curves is a consequence of using the DIA, a simplified parametric form of S_{nl}. This feature of the DIA may partly explain why hindcast peak periods T_p obtained with AUSWAM and alternative forms of S_{ds} also perform poorly under more realistic wind forcing conditions, as will be seen in the following sections of this Chapter.

6.5 Hindcasts in the Australian Region

The six alternative configurations of dissipation source terms described in the previous section were intercompared through a series of regional AUSWAM model hindcasts. Model results were validated against measurements from the 12 measurement sites indicated in Figure 6.1. The performance of these six model setups with alternative S_{ds} configurations was assessed according to the four statistical parameters described in section 6.3. Experiments were initially made with wind fields from the hindcast period of February 2000.

Figure 6.8 shows the scatterplots of AUSWAM hindcasts against corresponding observations of H_s and T_p aggregated during this first hindcast period. Lines representing a perfect 1-to-1 correlation and the linear least squares fit through the cloud of co-located data are indicated. Corresponding performance statistics shown in Table 6.3 were computed from co-located model and observed data aggregated from all buoy locations.

A striking feature in Figure 6.8 is the systematic trend of hindcast H_s in underestimating observations higher than around 2m, while overestimating lower values. Wave heights predicted with the standard AUSWAM form of S_{ds} [run BM1 in panel (a)], however, underestimated observations in all ranges. Less apparent bias was observed in runs WM1, AB2 and AB3 [panels (d) and (e)]. Another conspicuous feature seen in Figure 6.8 is the degree of scatter of values greater than 4m. The scatter of high H_s values is greater in both runs made with the WAM Cycle 3 form

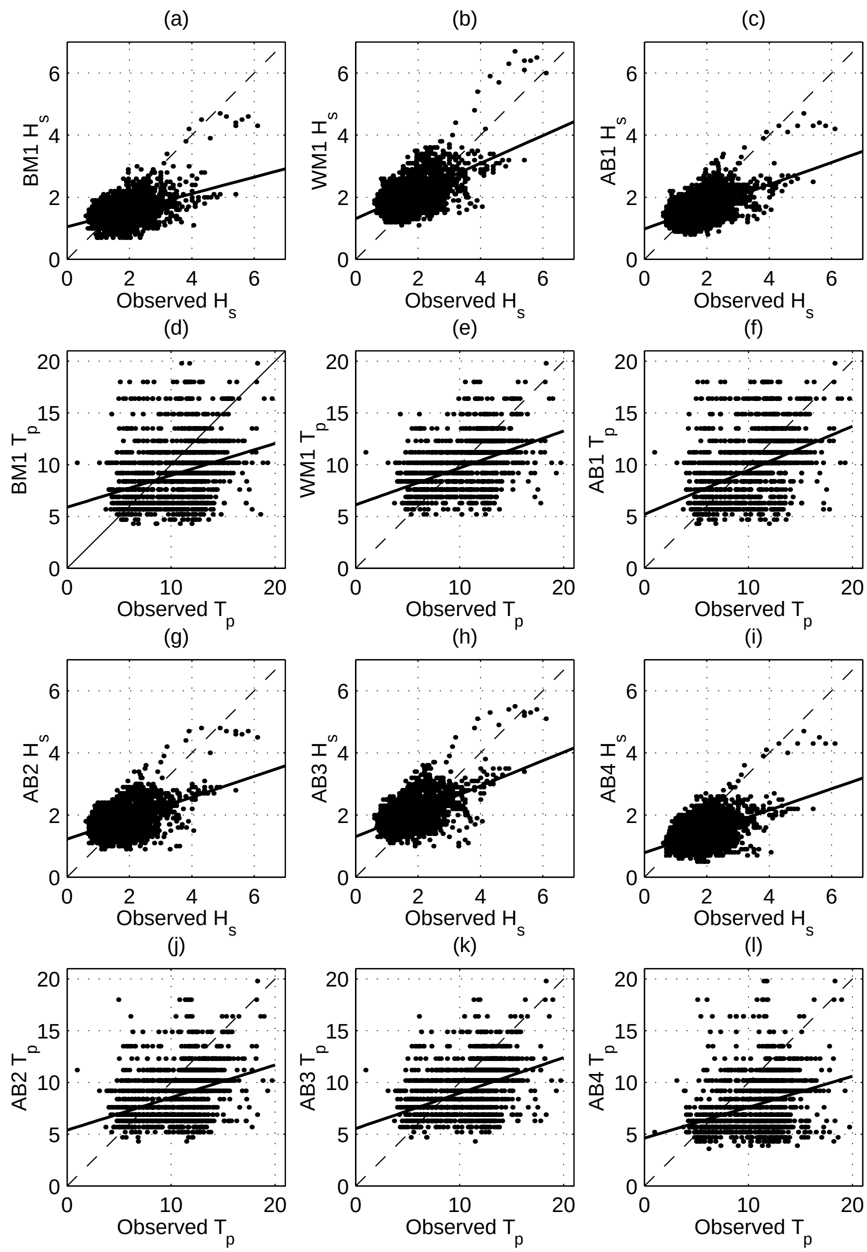

Figure 6.8: *Scatterplots of AUSWAM hindcasts generated by the six experiments with alternative S_{ds} configurations against observed significant wave heights H_s [panels (a), (b), (c), (g), (h) and (i)] and peak periods T_p [panels (d), (e), (f), (j), (k) and (l)] during Febuary 2000. Data was aggregated from the 12 validation sites indicated in Figure 6.1. Thin dashed lines indicate a perfect 1-to-1 correlation and continuous lines indicate the linear least squares fit through the cloud of co-located data.*

	H_s								T_p							
	bias		ϵ_{rms}		*SI*		*r*		*bias*		ϵ_{rms}		*SI*		*r*	
Run code	m/s		m/s						sec		sec					
BM1	-0.24	3	0.67	4	0.36	6	0.49	6	-0.96	4	3.23	5	0.31	6	0.34	6
WM1	0.33	5	0.67	5	0.33	2	0.60	1	-0.26	1	2.48	1	0.25	1	0.49	1
AB1	-0.15	2	0.60	1	0.33	1	0.59	2	-0.48	2	2.94	3	0.29	5	0.44	3
AB2	0.06	1	0.62	2	0.35	5	0.52	5	-1.40	5	3.03	4	0.27	3	0.41	4
AB3	0.26	4	0.65	3	0.34	3	0.57	3	-0.96	3	2.70	2	0.25	2	0.47	2
AB4	-0.37	6	0.70	6	0.34	4	0.56	4	-2.32	6	3.69	6	0.29	4	0.36	5

Table 6.3: Validation statistics from hindcasts of significant wave height H_s and peak period T_p produced by the operational WAM Cycle 3 implementation AUSWAM at the BoM, Australia, during 1-29 February 2000. Observations from 11 deep water buoys are used. Listed statistical parameters are bias, root mean square error ϵ_{rms}, scatter index SI and correlation coefficient r. Values of statistics at each model run are followed by a rank indicator. For a detailed description of run codes, see Table 6.2.

of S_{ds} [BM1 and WM1 in panels (a) and (b)] and smaller in hindcasts from experiments made with the new form of S_{ds}, particularly in data from run AB3 [panel (h)].

Table 6.3 shows that experiments using the saturation-dependent form S_{ds}^{bs} provided hindcasts of H_s that performed better than the standard AUSWAM configuration of run BM1. When compared to results from the optimised WAM Cycle 3 S_{ds} parameters (run WM1), statistics of H_s from all the AB experiments were significantly improved in terms of bias and rms-error and unaltered or marginally degraded in terms of scatter index and correlation coefficient. An exception was run AB4, which provided the highest absolute values of bias and rms-error, although still delivering better performance than the standard AUSWAM configuration in terms of scatter index and correlation coefficient.

Validation statistics of hindcast T_p shown in Table 6.3 show that most alternative S_{ds} configurations provided better performance than the standard AUSWAM setup. An exception was run AB4. The best performance in terms of hindcast T_p was associated with run WM1, which had significantly less bias than other experi-

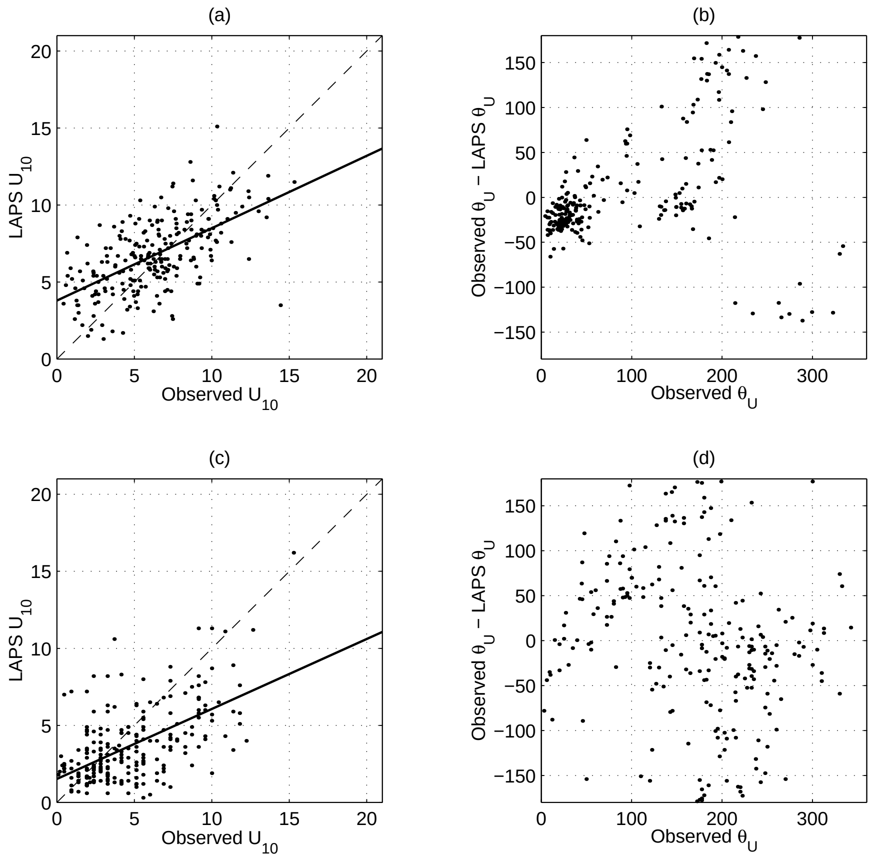

Figure 6.9: *Scatterplots of LAPS model winds against observations of 10m-height wind speeds U_{10} and associated directions θ_U measured in Strahan (site 55026) [panels (a) and (b)] and Sydney (site 55011) [panels (c) and (d)] during the hindcast period of February 2000. Thin dashed lines indicate a perfect 1-to-1 correlation and continuous lines indicate the linear least squares fit through the cloud of co-located data.In panels b and d, absolute bias between modelled and observed directions are plotted against observations of θ_U.*

ments. Nevertheless, the remaining statistical parameters from this run were only marginally better than those from runs AB1 and AB3. Despite these distinctions, the common feature of most experiments was the considerable scatter of hindcast T_p and the underestimation of values greater than 10s, as seen in Figure 6.8.

This first assessment of wave model performance indicates that even subtle changes in model physics can produce large impacts on the predicted sea state, with no modifications of the forcing winds. Therefore, this contradicts the belief that a more accurate description of the wind fields alone results in good quality wave predictions. Nevertheless, the validation strategy adopted so far leads to inconclusive evidence about model skill as it suffers from at least two major limitations: (i) except for a few locations, the quality of LAPS model winds is unknown and (ii) there is no way of ensuring that swell propagation into the regional domain is properly specified via boundary conditions prescribed from the global hindcast run.

		U_{10}				θ_U			
Buoy	$\overline{U_{10}^{obs}}$ m/s	$bias$ m/s	ϵ_{rms} m/s	SI	r	$bias$ deg	ϵ_{rms} deg	SI	r
55011	6.32	0.45	2.51	0.39	0.61	-13.97	83.63	0.92	0.36
55026	4.74	-1.06	2.81	0.55	0.57	9.05	109.77	0.64	0.42

Table 6.4: Assessment of LAPS model wind speeds U_{10} and directions θ_U against measured data from buoys 55011 (Sydney) and 55026 (Strahan) during February 2000. Listed statistical parameters are bias, root mean square error ϵ_{rms}, scatter index SI and correlation coefficient r. Mean observed values of wind speed $\overline{U_{10}^{obs}}$ are also indicated.

6.5.1 Validation of modelled winds

Implications of incorrect specification of swell properties are difficult to verify as there were no observations of the wave spectrum anywhere near the regional model grid boundaries during the hindcast periods considered in this study. The quality of the forcing wind fields provided by the LAPS atmospheric model, however, was assessed using wind measurements from sites 55011 (Sydney) and 55026 (Strahan), available during February 2000. Scatterplots of modelled wind speeds U_{10} and wind directions θ_U against measurements made at Sydney and Strahan in this period are shown in Figure 6.9. Corresponding statistics are provided in Table 6.4.

Wind speeds from the atmospheric model LAPS in Sydney were underestimated for observed U_{10} above 5m/s. Conversely, measured winds under 5m/s were overestimated by LAPS. At Strahan, model winds generally underestimated the observations in all ranges of U_{10} values. At both locations, the scatter of model directions was considerably high. Consequently, to compensate for the absence of higher quality wind fields and the unavailability of wind observations from other measurement sites during February 2000, LAPS model winds from the period between March 20 and May 20 1998 were examined and used to generate a second series of sea-state hindcasts. The analysis of winds and waves during this second period had the benefit of the availability of measurements at two other locations (Bass Strait and Northwest Shelf).

		U_{10}				θ_U			
Buoy	$\overline{U_{10}^{obs}}$ m/s	$bias$ m/s	ϵ_{rms} m/s	SI	r	$bias$ deg	ϵ_{rms} deg	SI	r
55039	6.53	0.48	2.15	0.32	0.86	11.27	74.80	0.38	0.69
55011	6.35	0.74	3.22	0.49	0.48	-1.78	88.71	0.52	0.50
55026	6.41	1.45	2.79	0.37	0.81	30.99	97.07	0.44	0.54
56002	5.07	-0.21	2.35	0.46	0.58	23.49	98.05	0.70	0.38

Table 6.5: Validation of wind speed U_{10} and direction θ_U at the validation sites 55039 (Bass Strait), 55011 (Sydney), 55026 (Strahan) and 56002 (Northwest Shelf) during the second hindcast period of March 20 to May 20 1998. Listed statistical parameters are bias, root mean square error ϵ_{rms}, scatter index SI and correlation coefficient r. Mean observed values of wind speed U_{10}^{obs} are also indicated.

Scatterplots of modelled and observed wind speeds U_{10} and directions θ_U at sites 55011 (Sydney), 55039 (Bass Strait), 55026 (Strahan) and 56002 (Northwest Shelf) during March through May 1998 are shown in Figures 6.10 and 6.11, respectively. Corresponding validation statistics are listed in Table 6.5. Statistics of wind speeds at Sydney [panel (a) of Figure 6.10] were substantially degraded relative to the previous hindcast period. The scatter of modelled estimates was very large (0.49) and its correlation with observations was very low ($r = 0.48$). Modelled wind directions at Sydney during this second hindcast period were also significantly scattered, as seen in panel (a) of Figure 6.11.

Modelled winds from Northwest Shelf also compared poorly with observations. Despite the relatively low bias (-0.21), wind speeds at this location had a high rms error (nearly 50% of the mean observed U_{10}), large scatter index ($SI = 0.46$) and a relatively low correlation with measurements ($r = 0.58$). Modelled wind directions on the Northwest Shelf were characterised by a very large scatter index ($SI = 0.70$) and low correlation with measurements ($r = 0.48$). This large scatter is seen clearly in panel (d) of Figures 6.10 and 6.11.

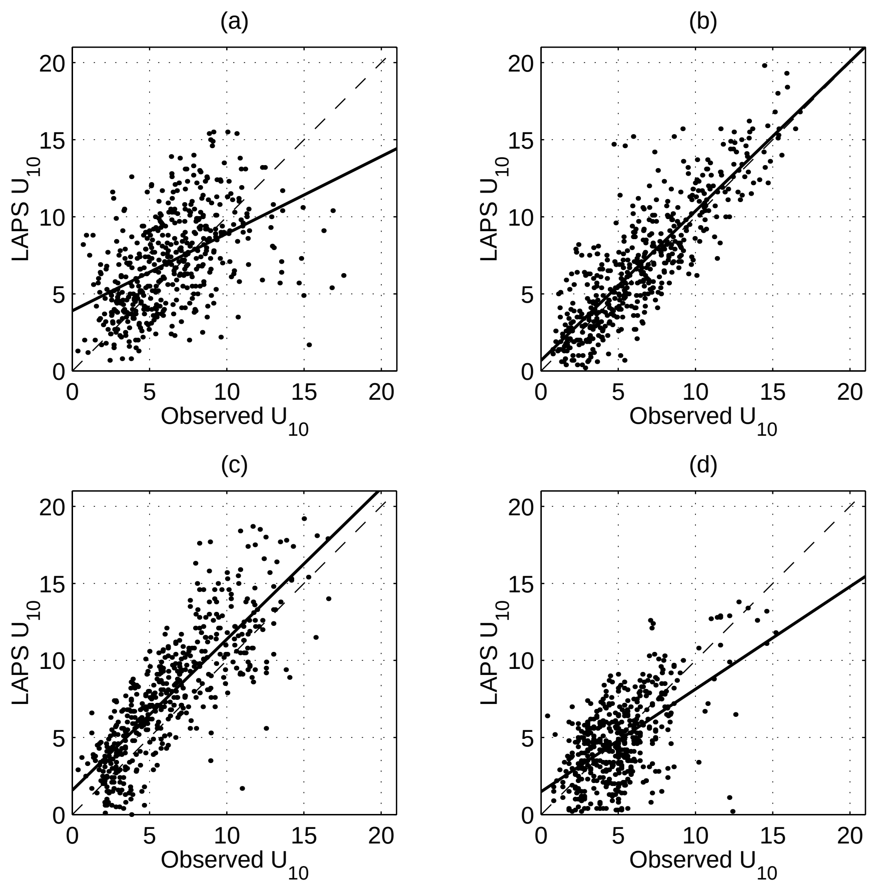

Figure 6.10: *Scatterplots of LAPS model winds against observations of the 10m-height wind speed U_{10} at four validation sites during the period of March to May 1998. Panels show comparisons at four validation sites: (a) 55011, Sydney; (b) 55039, Bass Strait; (c) 55026, Strahan; and (d) 56002, Northwest Shelf.*

LAPS model wind speeds in Bass Strait and Strahan were in better agreement with observations. In both cases, correlation coefficients were above 0.8 and scatter indices were much improved compared to the two other validation sites ($SI = 0.32$ and 0.37, respectively). Modelled wind directions were also more consistent with measured data. These improvements are clearly seen in panels (b) and (c) of Figures 6.10 and 6.11. Although validation statistics shown in Table 6.5 indicate that the bulk of LAPS model wind fields is not ideal for a critical overall evaluation of wave model performance, the better quality of model winds in Bass Strait and Strahan allowed a refinement of the overall wave model performance analysis presented above. This refined analysis was based on AUSWAM hindcasts of H_s and T_p at these two locations during the second hindcast period of March 20 to May 20 1998.

6.5.2 Hindcasts of H_s and T_p

Scatterplots of hindcast and observed H_s and T_p from the second hindcast period in Bass Strait are shown in Figures 6.12 and 6.13, respectively. In all cases, hindcast H_s seem much more consistent with observations than in the analysis of aggregated data from the 12 validation sites. The superimposed linear least squares fit through the cloud of co-located data suggests that most experiments provided good hindcasts of significant wave heights. An exception was run WM1, which produced hindcasts with a strong bias towards overestimating most measurements of H_s. On the other hand, hindcast T_p from all model runs had a consistent trend towards underestimation of measurements greater than approximately 8s.

Table 6.6 lists the validation statistics corresponding to the Bass Strait hindcasts shown in Figures 6.12 and 6.13. Statistics of hindcast H_s in this location indicate a best overall performance of runs BM1, AB1 and AB2. Hindcasts from runs AB3 and

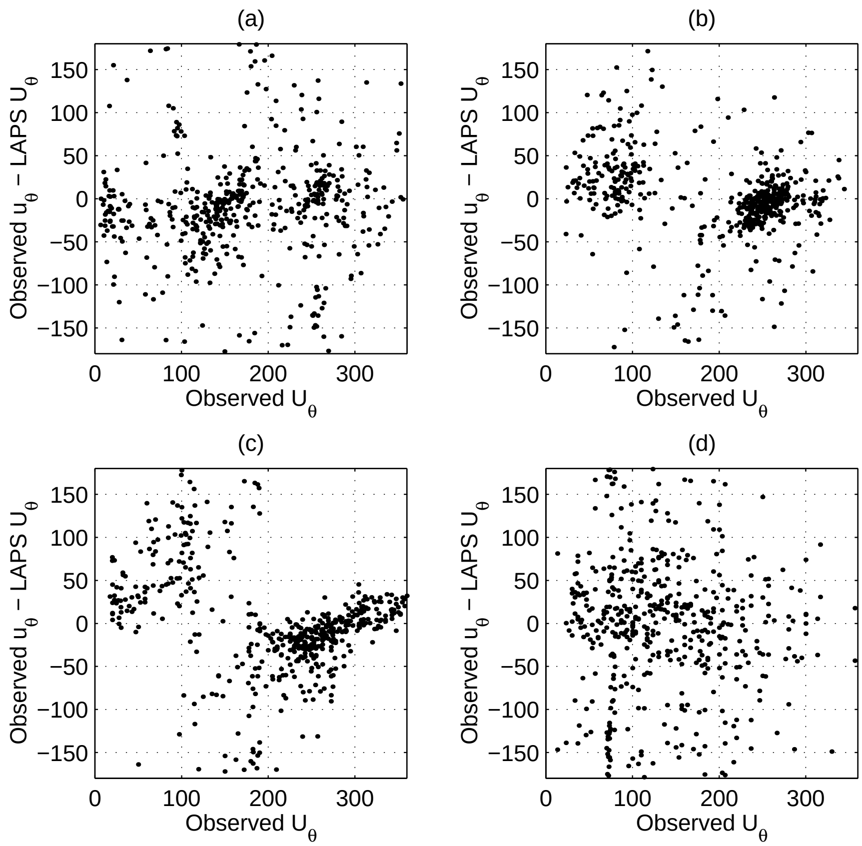

Figure 6.11: *Scatterplots of LAPS model predictions against observations of wind directions θ_U at four validation sites during the period of March to May 1998. Panels show comparisons at four validation sites: (a) 55011, Sydney; (b) 55039, Bass Strait; (c) 55026, Strahan; and (d) 56002, Northwest Shelf. The absolute bias between modelled and observed directions are plotted against observations of θ_U.*

AB4 also produced good statistical scores. Run WM1, however, generated hindcast H_s with high values of positive bias, rms error and scatter index. The generally good agreement of modelled and observed H_s from most experiments, however, was not repeated in the case of hindcast peak periods. Although values of bias, rms error and scatter index were comparable to those of hindcast H_s, the correlation coefficients of hindcast T_p were remarkably low (under 0.35 in all cases).

This lower correlation of hindcast T_p values in Bass Strait, which was particularly strong at larger values of this parameter (e.g., $T_p > 8$s), implies that the ratio between the energy of low- and high-frequency spectral components is often incorrect in the wave model results. This may be associated with at least four factors: (i) the use of the DIA algorithm to compute S_{nl}; (ii) the poor specification of swell properties at the external boundary of the regional model grid; (iii) the excessive dissipation of low frequency spectral components in the different specifications of S_{ds}; and (iv) the coarse resolution of the regional model grid within Bass Strait.

Figure 6.7 indicates clearly that some of the underestimation of hindcast T_p may be attributed to the use of the DIA algorithm to compute S_{nl}. The second and third factors cannot be directly assessed due to the lack of observed wave spectra near the outer regional grid boundaries. The effects of grid resolution within Bass Strait, however, may be examined in more detail.

March/May 1998			H_s				T_p			
Location	Mean obs	Run	*bias* m/s	ϵ_{rms} m/s	*SI*	*r*	*bias* sec	ϵ_{rms} sec	*SI*	*r*
Bass Strait	$\overline{H_s^{obs}} = 1.57$m	BM1	-0.16	0.49	0.29	0.86	-1.39	2.81	0.28	0.32
	$\overline{T_p^{obs}} = 8.79$s	WM1	0.37	0.65	0.34	0.85	-0.23	2.40	0.27	0.31
		AB1	-0.12	0.43	0.27	0.87	-1.28	2.58	0.26	0.33
		AB2	0.09	0.42	0.26	0.86	-1.68	2.70	0.24	0.26
		AB3	0.30	0.52	0.27	0.86	-0.97	2.38	0.25	0.25
		AB4	-0.23	0.51	0.29	0.86	-2.67	3.57	0.27	0.13
Strahan	$\overline{H_s^{obs}} = 3.44$m	BM1	-0.73	1.12	0.25	0.77	-2.62	3.67	0.20	0.36
	$\overline{T_p^{obs}} = 12.99$s	WM1	0.53	1.06	0.27	0.80	-0.58	2.30	0.17	0.41
		AB1	-0.41	0.85	0.22	0.79	-1.74	2.75	0.16	0.38
		AB2	-0.38	0.89	0.23	0.77	-3.43	4.06	0.17	0.31
		AB3	0.10	0.79	0.23	0.81	-2.50	3.33	0.17	0.33
		AB4	-1.10	1.40	0.25	0.74	-4.56	5.11	0.18	0.26

Table 6.6: Validation statistics from hindcasts of significant wave height H_s and peak period T_p provided by AUSWAM at sites 55039 (Bass Strait) and 55026 (Strahan) during the period of March 20 to May 20 1998. Listed statistical parameters are bias, root mean square error ϵ_{rms}, scatter index SI and correlation coefficient r.

Figure 6.1 shows that the complex land features within Bass Strait were considerably misrepresented due to the coarse resolution (1°) of the regional model grid. This misrepresentation does not affect local operational sea-state forecasts, as these are based on the results of a higher resolution (0.25°) mesoscale implementation of AUSWAM covering the southeastern region of the Australian continent in more detail. This implementation, however, was not available at the time of the experiments described in this Chapter. Consequently, an examination of the available time series of regional hindcasts and observations of T_p generated with alternative forms of S_{ds} revealed that model data within Bass Strait systematically omitted wave events with peak periods typically greater than 12s, usually associated with the occurrence of weak local winds.

The combination of higher T_p values with weak local winds is a well-recognised characteristic of swell events. Due to the frequent development of mid-latitude cyclones within the Southern Ocean, these swell systems may often penetrate Bass Strait through its western entrance. This passage, however, is almost completely blocked in the regional model grid, as seen in Figure 6.1. Consequently, this numerical boundary may have obstructed the passage of swell in the regional simulations, leading to a disagreement between model hindcasts and observations of T_p, as seen in Table 6.6 and in Figure 6.13.

Joint measurements from Bass Strait and Strahan confirm this hypothesis. They suggest that actual swell systems penetrated into the Bass Strait during the second hindcast period, occasionally superimposing the local wind-seas when winds were low. An example is given in the time series of measured U_{10}, H_s and T_p shown in Figure 6.14. Observations in Strahan from the 30th of April to the 3rd of May [dashed line in Figure 6.14, panel (b)] were dominated by high peak periods associated with waves generated within the extensive westerly wind fetches that extend over the Southern Ocean, south of Australia.

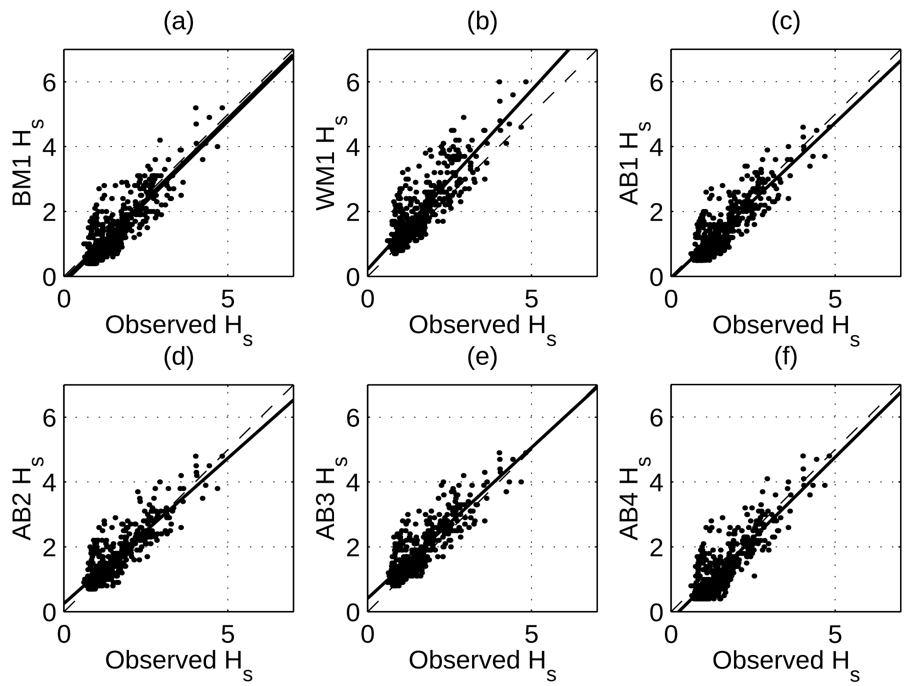

Figure 6.12: *Scatterplots of hindcast and observed significant wave heights H_s in Bass Strait during the second hindcast period of March 20 to May 20 1998. Model runs are indicated in the vertical axis. Thin dashed lines indicate a perfect 1-to-1 correlation and continuous lines indicate the linear least squares fit through the cloud of co-located data.*

The time series of T_p from Bass Strait shown in panel (b) of Figure 6.14 suggests that these swell systems that dominated the sea state in Strahan were superimposed locally by wind seas or were not present prior to the 1st of May. Swell penetration into Bass Strait, however, caused a sudden rise in measured T_p (from 7 to 16s) on the 1st of May. Careful analysis of surface wind fields prior to this event indicated that there were no apparent sources of swell other than storms located west of Bass Strait, within the Southern Ocean. This swell signal, which is clear in the observational data, was not present in the model hindcasts, as seen in panel (b) of Figure 6.14. This effect resulted from the misrepresentation of Bass Strait's western entrance in the regional numerical grid. Therefore, hindcast T_p were considerably lower than observations during most of of this swell event.

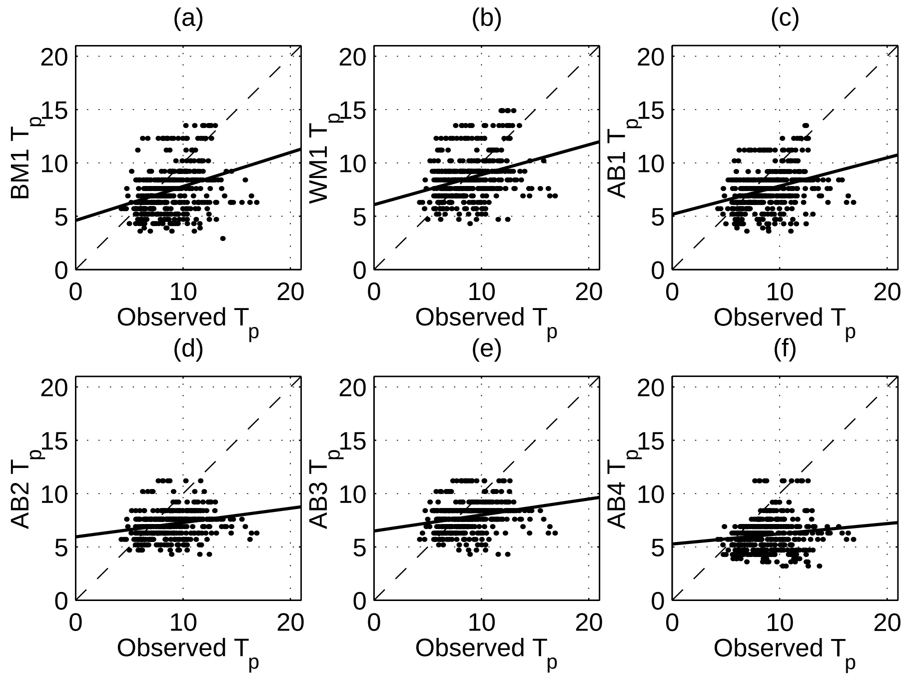

Figure 6.13: *Scatterplots of hindcast and observed significant peak periods T_p in Bass Strait during the second hindcast period of March 20 to May 20 1998. Model runs are indicated in the vertical axis. Thin dashed lines indicate a perfect 1-to-1 correlation and continuous lines indicate the linear least squares fit through the cloud of co-located data.*

Figures 6.15 and 6.16 show the comparisons of hindcast and observed H_s and T_p in Strahan during the second hindcast period. The difference of results from alternative model configurations is greater in Strahan than in the data from Bass Strait. Lines of the least squares fit through the co-located data suggest that hindcasts of H_s from runs BM1, AB1, AB2 and AB4 systematically underestimated the observations. On the other hand, hindcast H_s produced by run WM1 overestimated the observed values. Only hindcast H_s from run AB3 repeated in Strahan the good performance in Bass Strait, producing a low bias. The general trends seen in the scatterplots of hindcast and observed T_p from Strahan, however, repeat those seen in data from Bass Strait: most model runs underestimated higher values of peak period. An exception was the results from run WM1, which was closer to the line of perfect agreement.

Validation statistics shown in Table 6.6 indicate that the hindcasts of H_s from run AB3 had the lowest bias and rms error, and thus the best overall performance. The low scatter index of this experiment is comparable to that of runs AB1 and AB2. These two cases also delivered a good performance in terms of bias and rms error. Runs BM1 and AB4 produced significant negative bias and high rms errors. Their scatter-indices, however, were slightly improved relative to run WM1, which generated considerable positive bias and high rms error.

Run WM1 provided the lowest values of bias in terms of hindcast T_p in both Strahan and Bass Strait. The lowest rms errors in these two locations were associated with runs WM1, AB1 and AB3, while scatter indices of these three test cases and those of runs AB2 were all remarkably low. The poor performance of run AB4 in Strahan and Bass Strait indicates that its configuration of S_{ds}^{bs} may be predicting too much dissipation at wavenumbers lower than the peak. Despite these apparent differences, all model runs correlated poorly with the trends of measured T_p, as suggested by the low values of the parameter r.

Since Strahan is completely exposed to wave systems propagating from the east, the discrepancies in hindcast T_p can no longer be attributed to topography constraints, as in Bass Strait. Consequently, the generally poor agreement of hindcast T_p with observations from Strahan supports the idea that the use of the DIA form of S_{nl} may be producing spectra with peak frequencies biased towards values higher than those expected from observations, in analogy to Figure 6.7. This effect might also be enhanced due to improper specification of swell systems at the AUSWAM regional model boundaries, and to the possibility that the forms of S_{ds} used in this Chapter

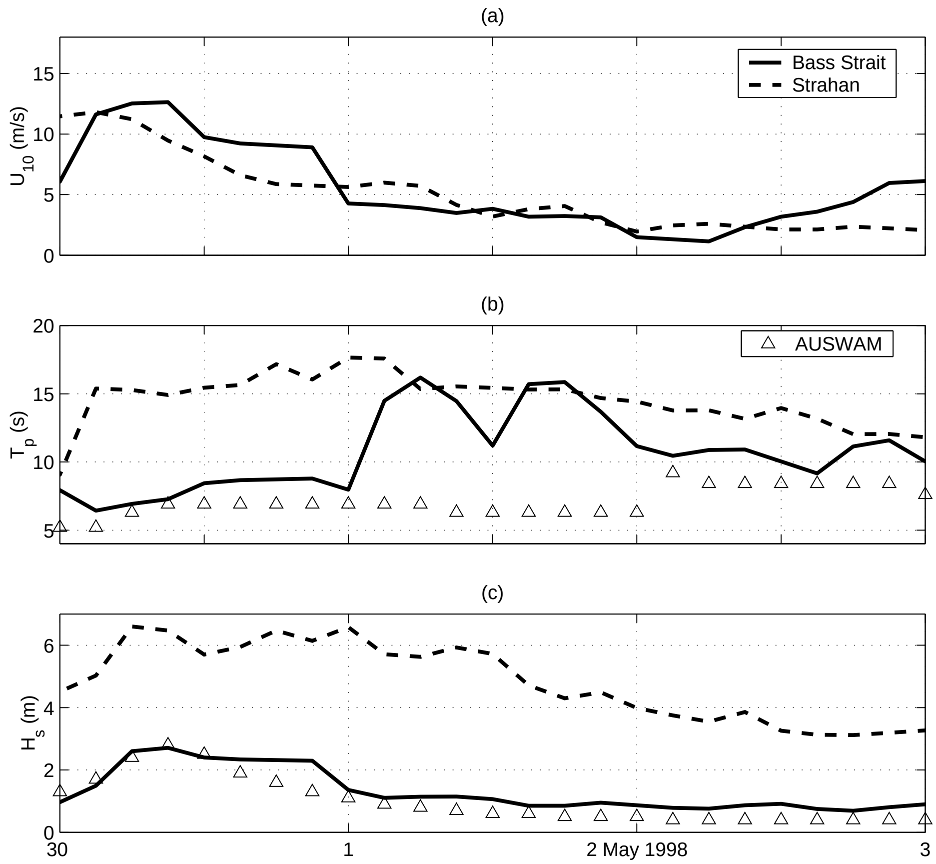

Figure 6.14: *Time series of (a) wind speed U_{10}, (b) peak period T_p and (c) significant wave height H_s in Bass Strait (55039) [continuous line] and Strahan (55026) [dashed line] during three days of the second hindcast period. It shows a strong correlation between observed parameters at these two sites, including a noticeable rise in peak periods after the 1st of May. Panel (b) shows that this observed rise is not present in the hindcast T_p in Bass Strait (triangles) produced by the regional implementation of AUSWAM (run BM1).*

predict dissipation rates that are too high at low wavenumbers.

The results of alternative hindcasts of H_s and T_p in Strahan and Bass Strait may be summarised as follows:

- the configuration of S_{ds} used in the standard AUSWAM model setup (run BM1), consisting of the WAM Cycle 3 dissipation function S_{ds}^{w3} with an increased value of the constant C_{ds}, produced hindcasts of H_s and T_p that

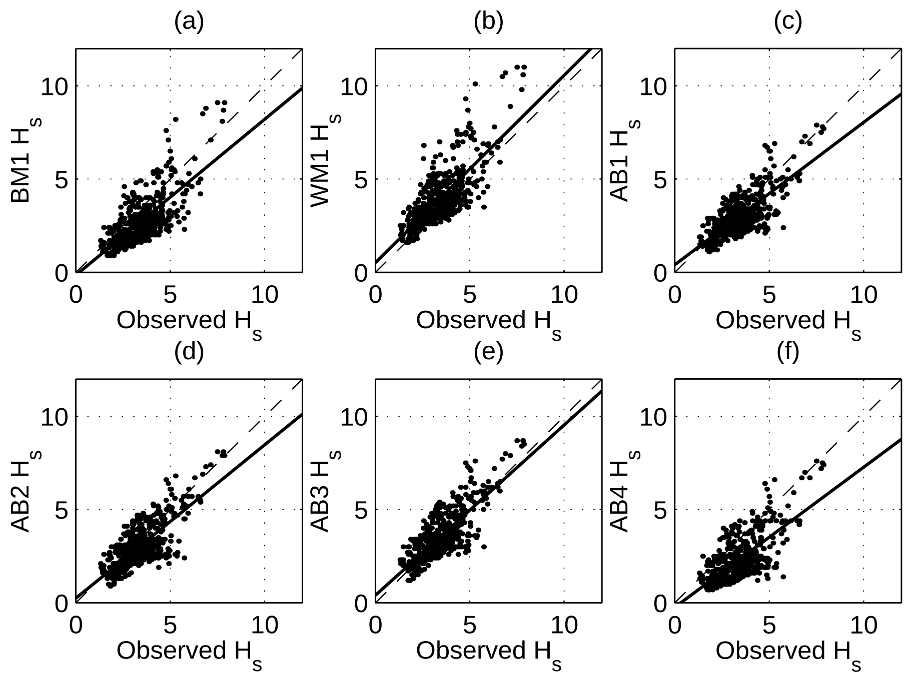

Figure 6.15: *Scatterplots of hindcast and observed significant wave heights H_s in Strahan during the second hindcast period of March 20 to May 20 1998. Model runs are indicated in the vertical axis. Thin dashed lines indicate a perfect 1-to-1 correlation and continuous lines indicate the linear least squares fit through the cloud of co-located data.*

generally underestimated measured data;

- the alternative configuration of S_{ds}^{w3} used in run WM1 provided the least degraded hindcasts of T_p. This slight improvement is probably related to its stronger nonlinear dependence ($m = 2.65$) on the integrated steepness parameter $(E_{tot}\overline{k}^2)^m$. In association with a lower value of C_{ds} relative to the standard AUSWAM configuration, this may have significantly reduced the dissipation levels of old wind seas, leading to a less constrained propagation of swell components of the wave spectrum. These improved hindcast T_p estimates, however, had as a tradeoff the systematic overestimation of hindcast H_s at both validation sites;

- the aim of run AB1 was to examine the effect of redefining the integral steepness parameter of S_{ds}^{w3} as a function of the peak wavenumber k_p (i.e., the form $E_{tot}\overline{k}^2$ used in S_{ds}^{w3} was replaced by $E_{tot}k_p^2$). This change may explain why this experiment provided improved hindcast H_s when compared to results of runs BM1 and WM1. Hindcasts of T_p from run AB1 were also comparable to the best performing results of run WM1 in statistical terms;

- statistics of hindcast H_s from runs AB2 and AB3, made with the saturation-dependent form S_{ds}^{bs} were in excellent agreement with measurements. Therefore, in statistical terms they were consistently superior to cases using the WAM Cycle 3 form of S_{ds} (BM1 and WM1). Statistics of hindcast T_p from runs AB2 and AB3, however, indicated that the dissipation rates of spectral components within the swell range predicted by S_{ds}^{bs} may need to be reduced;

- run AB4 produced the most degraded hindcasts of H_s and T_p. This may be a consequence of its stronger dependence on the weighting term $(k/\overline{k})^n = 1$, which increases the dissipation rates at wavenumbers higher than the peak and of incorrect tuning of other dissipation parameters;

- the strong discrepancies between hindcast and observed T_p from all model runs indicate that the DIA form of S_{nl} may need to be significantly improved or replaced by more appropriate parameterisations of the nonlinear wave-wave interactions.

These conclusions indicate that the newly-proposed saturation-dependent form S_{ds}^{bs} generally improves the hindcasts of sea-state produced by the AUSWAM model in terms of H_s. Discrepancies in the hindcasts of peak periods, however, indicate that further adjustments are needed in the specification of dissipation rates at wavenumbers lower than the spectral peak, in conjunction with improvements in the parametric form of S_{nl} used for operational wave model applications. Nevertheless, validation statistics of hindcast T_p from test cases using S_{ds}^{bs} were in most cases still better than those associated with the standard AUSWAM setup (run BM1).

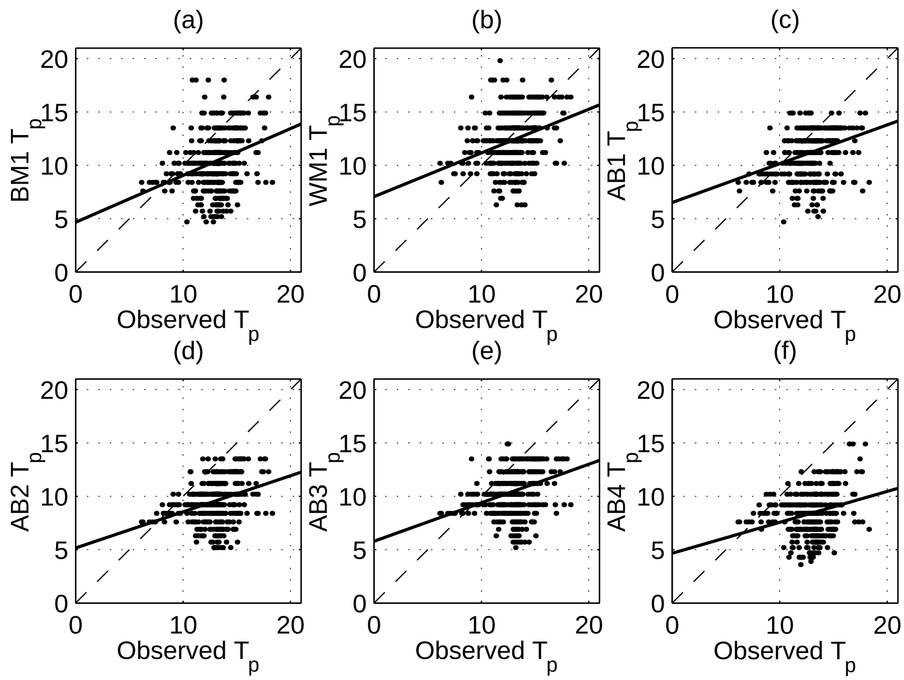

Figure 6.16: *Scatterplots of hindcast and observed peak periods T_p in Strahan during the second hindcast period of March 20 to May 20 1998. Model runs are indicated in the vertical axis. Thin dashed lines indicate a perfect 1-to-1 correlation and continuous lines indicate the linear least squares fit through the cloud of co-located data.*

6.6 Severe sea states

This section presents a more refined assessment of wave model performance using wind and wave data recorded during two severe sea-state events at Strahan. These events were selected after a careful analysis of the available data, made with the objective of identifying periods of optimal agreement between wind fields produced by the LAPS atmospheric model and the observations. Objective criteria for selecting these two periods of optimal winds were based on the investigation of Cardone et al. (1994). Data from Strahan were chosen due to the complete exposure of this site to storm systems propagating over the Southern Ocean from the west, with few constraints associated with the coarse resolution of the regional AUSWAM model grid.

The two selected severe sea state events (SSE1 and SSE2) were characterised by strong modelled winds satisfying the following statistical criteria:

- scatter indices SI below 0.3,
- bias relative to the mean observed U_{10} below 20%,
- root-mean-square errors ϵ_{rms} relative to the mean lower than 30%, and
- correlation coefficients higher than 0.8.

Model winds were compared to observations made at a single point near the location of the wave measurements in Strahan. Using point measurements of wind fields to assess the quality of model winds and waves is far from being representative of the full atmospheric systems involved in the generation of wind-waves at any point. Nevertheless, due to the restricted availability of measurements within the Australian region, this was as much as could be done. Future research is planned to address these limitations.

The first period of severe sea states (SSE1) consisted of data from the 9th to the 16th of April 1998. The second storm period (SSE2) was recorded between the 25th of April and the 3rd of May 1998. Validation statistics of LAPS model winds corresponding to SSE1 and SSE2 are shown in Table 6.7. This table also includes statistics of combined data from both storm events.

			U_{10}				θ_U			
Code	Buoy	$\overline{U_{10}^{obs}}$ m/s	$bias$ m/s	ϵ_{rms} m/s	SI	r	$bias$ deg	ϵ_{rms} deg	SI	r
SSE1	55026	5.94	1.28	2.28	0.29	0.88	55.70	112.90	0.51	0.37
SSE2	55026	6.50	0.94	2.30	0.30	0.82	31.86	88.43	0.38	0.48
Aggregate		6.23	1.10	2.29	0.29	0.85	42.16	100.71	0.44	0.42

Table 6.7: Validation statistics of LAPS model winds during the two storm events in Strahan. Average observed wind speeds U_{10}^{obs} of each storm are indicated. Other listed statistics are bias, rms error ϵ_{rms}, scatter index SI and correlation coefficient r.

Synoptic weather conditions prevailing during the duration of SSE1 are illustrated in panels (a) and (b) of Figure 6.17. At the beginning of this period, a frontal system associated with a small low-pressure vortex developed close to the southwestern Australian coast. This system is indicated by a circle in panel (a). At the same time, a larger-scale low-pressure vortex (indicated by an ellipse) is seen propagating over the Southern Ocean. These two systems eventually converge south of Tasmania, as seen in panel (b), generating an extensive patch of strong southwesterly winds (U_{10} > 15m/s) reaching Strahan on April 14 1998. Time series of U_{10} and θ_U associated with this event are shown in the left-hand side of panels (a) and (b) in Figure 6.18.

During the second severe sea state event (SSE2), two consecutive storm systems were observed in Strahan within a period of seven days. The first storm is indicated in panel (c) of Figure 6.17. It is an example of a family of storms known as east-coast cyclones, which develop over coastal waters in autumn and spring due to strong sea-surface temperature gradients (Holland et al., 1987). The system shown in panel (c) migrated south from a latitude of around 30° to form strong wind patches over Tasmania, due to interactions with the higher topography of southeastern Australia.

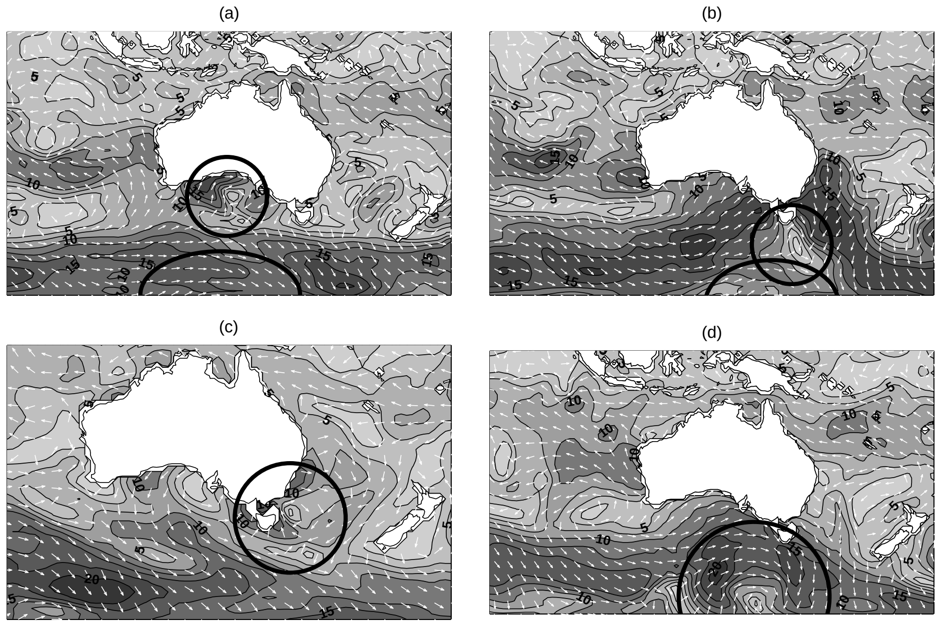

Figure 6.17: *Surface wind fields at a 10m height U_{10} produced by the atmospheric model LAPS during two storm events recorded at Strahan. The two converging mid-latitude low-pressure systems of SSE1 are indicated in panels (a) and (b) by circles at their positions on 11/04/98 09 Z and 12/04/98 15 Z, respectively. Panel (c) shows the east-coast low of SSE2 at its position on 25/04/98 18 Z, while panel (d) shows a larger-scale mid-latitude low-pressure system reaching the Tasmanian coast on 29/04/1998 18Z.*

The second storm of SSE2 was associated with the large-scale low-pressure system indicated in panel (d). Systems of this kind develop regularly all year round in higher latitudes due to instabilities in the interface between sub-tropical and polar air masses. They are frequently associated with the passage of cold fronts and have a typical periodicity of one week. Time series of U_{10} and θ_U recorded during SSE2 are shown in the right-hand side of panels (a) and (b) in Figure 6.18.

Time series of observed H_s and T_p during SSE1 and SSE2 are indicated by crosses in Figures 6.19 and 6.20, respectively. Values of H_s in excess of 5m, observed in day 6 of SSE1, were generated by the arrival in Strahan of strong southwesterly winds associated with the two low-pressure vortices seen in panel (b) of Figure 6.17.

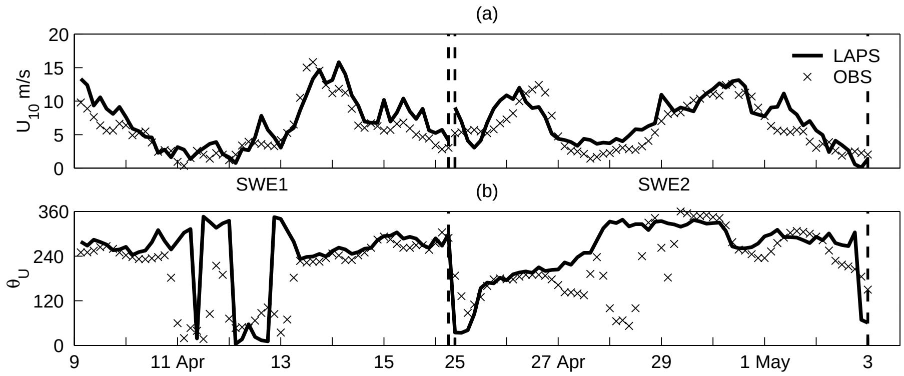

Figure 6.18: *Time series of wind speeds U_{10} [panel (a)] and directions θ_U [panel (b)] during the two storm events in Strahan. Observations are represented by crosses and LAPS model products by continuous lines. Tick marks show one-day intervals. Details of wind characteristics during each storm event are provided in Table 6.7.*

The two consecutive periods of higher H_s recorded during SSE2, on the right hand side of Figure 6.19, were associated with the arrival in Strahan of the east-coast low ($H_s \approx 4$m) and of the large-scale low-pressure system ($H_s > 6$m) indicated in panels (c) and (d) of Figure 6.17, respectively. Hindcast H_s and T_p produced by experiments with alternative S_{ds} configurations are shown in panels (a) through (f) of Figures 6.19 and 6.20. Alternative runs are identified by a legend included in each panel.

A visual inspection of Figure 6.19 reveals that hindcast H_s from the experiment using the standard AUSWAM S_{ds} configuration (BM1), shown in panel (a), significantly underestimate the observations during most of the two storm events. This also applies for the results of run AB4, shown in panel (f). On the other hand, the experiment made with the optimised S_{ds}^{w3} setup (WM1), shown in panel (b), overestimates the maximum observed H_s of SSE1 by 30%. Run WM1 also significantly overestimates the two storm peaks in SSE2.

The remaining experiments shown in panels (c), (d) and (e) of Figure 6.19 were

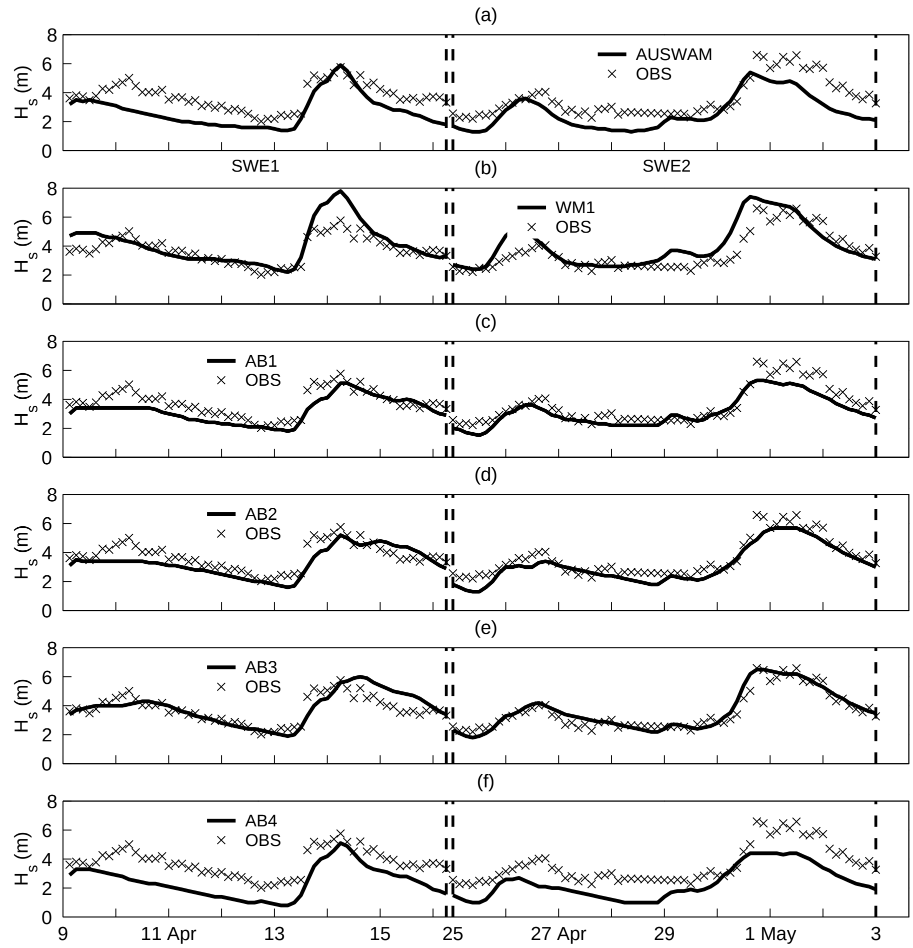

Figure 6.19: *Time series of significant wave heights H_s during the two storm events in Strahan. Observations are represented by crosses and model products by continuous lines. Tick marks are scaled in one-day intervals. Panels show results from runs (a) BM1, (b) WM1, (c) AB1, (d) AB2, (e) AB3 and (f) AB4.*

made with the new saturation-dependent form S_{ds}^{bs}. Both runs AB1 and AB2 produced hindcasts of H_s that were more consistent with observations than those of the standard AUSWAM configuration. Nevertheless, in both cases the maximum H_s from both storm events was underestimated. Run AB3, however, had an excellent agreement with measured data in all ranges of the two storm events. This agreement is particularly good during SSE2. Values of H_s during the last two days of SSE1 were slightly overestimated by the hindcasts of run AB3. However, this overestimation corresponds to a period in which LAPS model winds were also high compared to measurements of U_{10}, as seen in panel (a) of Figure 6.18.

Time series of T_p in Figure 6.20 show that most model runs produced hindcasts that systematically underestimated the observations. The agreement between hindcast and observed T_p from run WM1, however, was better than for the other experiments. Consistent with the analyses presented in the previous section, this seems to be related to the fact that the optimised configuration of S_{ds}^{w3} used in that experiment has a higher nonlinear dependence on the integrated steepness parameter $(E_{tot}\overline{k})^m$. This improved performance in terms of T_p, however, had the drawback of producing hindcast H_s that overestimated significantly the measured data. Run AB1, shown in panel (c), also generated hindcasts of T_p that were in better agreement with the measured data. Hindcasts of H_s from this model run, however, underestimated the measurements during the storm peaks of SSE1 and SSE2.

Other experiments produced T_p that were systematically lower than observations. In most cases, however, hindcasts were more consistent with observations during SSE1 than SSE2. A stronger disagreement occurred in the period between the two storm peaks of SSE2, when most model runs predicted a moderate-to-sharp decrease in T_p, while the measurements indicated that the local wave climate remained almost continuously dominated by longer period waves. A visual inspection of two-dimensional wind fields prior to the second storm peak of SSE2 suggested that the higher measured T_p values were associated with swells generated by a sequence of large mid-latitude storms propagating eastwards within the Southern Ocean. One of these storm systems is seen in panel (d) of Figure 6.17.

Although these swell systems appear in the model hindcasts during SSE2, as suggested by the fluctuations in the time series of T_p from runs BM1 and AB1 seen in panels (c) and (d), their actual strength was clearly underestimated. The reasons for this underestimation cannot be determined objectively. However, they may possibly be related to factors identified in the analyses of the previous sections: distortions in the spectral shape due to the use of the DIA form of S_{nl}, poor specification of swell properties at the regional model grid boundaries and/or too-high dissipation rates of low frequency spectral components in most alternative configuration of S_{ds}. They could also be related to the "garden-sprinkler effect", which arises from coarse spatial resolution of the model grid associated with a poor directional resolution in the spectral grid. This effect causes swell systems to disintegrate into smaller systems as they propagate over long distances.

Table 6.8 shows the validation statistics of the six model runs during SSE1 and SSE2. Statistics of data aggregated from these two storm events are also included in this table. The listed statistics confirm that model runs using the new saturation-dependent form S_{ds}^{bs} performed significantly better in terms of hindcast H_s, when compared to runs using the WAM Cycle 3 dissipation S_{ds}^{w3} (BM1 and WM1). An exception, however, was run AB4. Compared to all other cases, this model run provided hindcasts of H_s and T_p that were substantially degraded in terms of both systematic and time-varying errors. The validation statistics also confirm that run WM1 produced the best hindcasts of T_p, while indicating that other model runs provided hindcasts that were in fair overall agreement with observations.

The quality of hindcast H_s produced by run AB3 was particularly good. Compared to the experiments made with the standard AUSWAM configuration of S_{ds}^{w3} (BM1), run AB3 generated, on an overall basis, hindcast H_s with 90% less bias, around 50% less rms error, 20% less scatter and a substantial increase in the correlation

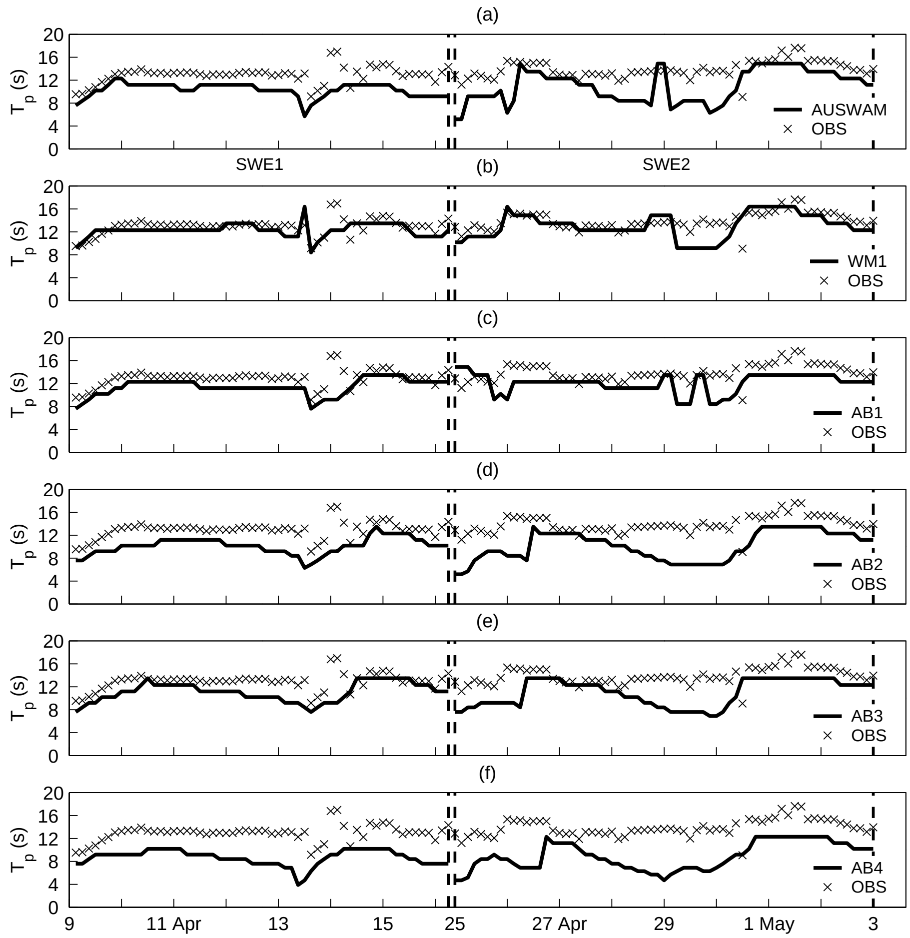

Figure 6.20: *Time series of peak periods T_p during the two storm events in Strahan. Observations are represented by crosses and model products by continuous lines. Tick marks are scaled in one-day intervals. Panels show results from runs (a) BM1, (b) WM1, (c) AB1, (d) AB2, (e) AB3 and (f) AB4.*

coefficient r. The improvements were also significant in comparison to run WM1, which produced H_s with considerable positive bias and the highest levels of scatter. Other experiments made with variations of S_{ds}^{bs} confirm these trends. Although the validation statistics of hindcast T_p generated by run AB3 were comparable or inferior to those associated with test cases using the WAM Cycle 3 form of S_{ds}, the improved performance of this model run in terms of H_s is encouraging.

Period	Mean obs	Run	H_s bias m/s	H_s ϵ_{rms} m/s	H_s SI	H_s r	T_p bias sec	T_p ϵ_{rms} sec	T_p SI	T_p r
SSE1	$\overline{H_s} = 3.74$m	BM1	-1.01	1.17	0.16	0.85	-2.61	2.98	0.11	0.43
	$\overline{T_p} = 12.93$s	WM1	0.37	0.82	0.20	0.87	-0.65	1.46	0.10	0.52
		AB1	-0.52	0.69	0.12	0.86	-1.52	2.08	0.11	0.51
		AB2	-0.43	0.70	0.15	0.82	-2.81	3.15	0.11	0.50
		AB3	0.11	0.63	0.17	0.82	-1.84	2.47	0.13	0.44
		AB4	-1.31	1.40	0.14	0.89	-4.27	4.57	0.13	0.31
SSE2	$\overline{H_s} = 3.59$m	BM1	-0.95	1.16	0.18	0.86	-2.94	3.78	0.17	0.55
	$\overline{T_p} = 13.90$s	WM1	0.44	0.90	0.22	0.84	-0.84	1.94	0.13	0.60
		AB1	-0.45	0.66	0.14	0.94	-1.80	2.64	0.14	0.26
		AB2	-0.43	0.58	0.11	0.96	-3.77	4.35	0.16	0.51
		AB3	0.08	0.39	0.11	0.96	-2.94	3.65	0.16	0.43
		AB4	-1.25	1.37	0.16	0.90	-4.99	5.41	0.15	0.51
Aggregate	$\overline{H_s} = 3.66$m	BM1	-0.98	1.16	0.17	0.85	-2.78	3.42	0.15	0.50
	$\overline{T_p} = 13.44$s	WM1	0.41	0.87	0.21	0.84	-0.75	1.73	0.12	0.58
		AB1	-0.48	0.68	0.13	0.91	-1.67	2.39	0.13	0.40
		AB2	-0.43	0.64	0.13	0.91	-3.31	3.83	0.14	0.47
		AB3	0.09	0.52	0.14	0.91	-2.42	3.15	0.15	0.40
		AB4	-1.28	1.39	0.15	0.88	-4.65	5.03	0.14	0.43

Table 6.8: Validation statistics of significant wave height H_s and peak period T_p during the two storm events recorded in Strahan. Listed statistical parameters are bias, root mean square error ϵ_{rms}, scatter index SI and correlation coefficient r.

A final remark on the results reported in this Chapter regards the choice of alternative S_{ds} configurations used in the numerical experiments. Dissipation parameters used in the saturation-dependent form S_{ds}^{bs} were tuned manually to parametric fetch-limited evolution curves, as described in Section 6.4. The performance of alternative configurations of S_{ds}^{bs} was then compared to other model configurations that used variations of the form S_{ds}^{w3} with dissipation parameters determined either (i) through previous validation experiments using field data, as in the case of the standard AUSWAM setup; or (ii) through the automatic optimisation techniques described in Monbaliu and Hasselmann (1994).

Intuitively, model setups based on these two latter approaches should have provided a better model performance, when compared to a manually-tuned configuration based on a restricted set of wave evolution conditions. Nevertheless, the outcomes of experiments described in this Chapter contradict this intuition. They show that increased model performance may benefit from improved parametrisations of S_{ds}.

In view of these results, a potential source of improvements in the performance of the newly-proposed form of S_{ds} is the optimisation of its dissipation parameters through more objective techniques, made with a wider range of sea-state and wind conditions, also focusing on a proper specification of dissipation rates of swell systems. The proper specification of spectral dissipation rates will also depend on improvements in the parametric function used to calculate the nonlinear wave-wave interactions. These are the topic of ongoing and future research activities. Nevertheless, based on the experiments described in this Chapter, the positive results obtained in terms of hindcasts of H_s in the Australian region demonstrate the potential benefits of using S_{ds}^{bs} in operational wave forecasting applications.

Chapter 7

Concluding Remarks

The major theme of this thesis is the development and evaluation of a new formulation of the spectral dissipation source term S_{ds}. This new form of S_{ds} features a nonlinear dependence on the local wave spectrum, expressed in terms of the azimuthally integrated saturation parameter $B(k) = k^4 F(k)$. The underlying form of this saturation-dependent S_{ds} is based on a new framework for the onset of deep-water wave breaking due to the nonlinear modulation of wave groups. The new form of S_{ds} is succesfully validated through numerical experiments that include exact nonlinear computations of fetch-limited wind-wave evolution and hindcasts of two-dimensional wave fields made with an operational wind-wave model.

Exact nonlinear computations of fetch-limited growth made with the newly-proposed form of S_{ds} generate integral spectral parameters that agree more closely with observations when compared to other dissipation source terms used in state-of-the-art wind-wave models. It also provides more flexibility in controlling properties of the wave spectrum within the high wavenumber range. Tests using a variety of wind speeds, three commonly-used wind input source functions and two alternative full-development evolution limits further demonstrate the robustness and flexibility of the new saturation-dependent dissipation source term. Finally, improved wave hindcasts obtained with an implementation of the new form of S_{ds} in a version of the WAM model demonstrate its potential usefulness in operational wind-wave forecasting applications.

The following sections serve to highlight and summarise the new results arising from the investigations conducted in this thesis and to outline the directions for future research.

Summary of Conclusions

A. Exact nonlinear simulations of fetch-limited evolution

Simulations of the fetch-limited evolution of wind waves made using the exact nonlinear wave model of Tracy and Resio (1982) consisted of experiments designed to investigate (i) a two-component form of S_{ds} with a strong nonlinear dependence on an integrated spectral steepness parameter and (ii) a general saturation-dependent form of S_{ds}. Experiments with the two-component form of S_{ds} [equation (3.4) of Chapter 3] provided the following conclusions:

(1) the strong nonlinear dependence of spectral peak dissipation rates on an integrated spectral steepness parameter that represents breaking due to nonlinear group modulation provides a close agreement between computed integral steepness parameters and observations within the fetch-limited evolution range;

(2) the transition of the wave field towards a fully-developed stationary state requires significant dissipation rate levels even when the contribution of breaking due to group modulation has ceased. These residual dissipation rates are needed to balance the strong positive energy flux towards the spectral peak produced by S_{nl};

(3) a proper source-term balance and, therefore, closer agreement of model results with parametric fetch-limited curves at all ranges, including full development, are achieved through the use of a variable-exponent dependence of S_{ds} on an integrated spectral steepness parameter. This variable-exponent approach allows "switching off" the dissipation rates associated with wave breaking due to group modulation, while simultaneously maintaining background dissipation rates that are strong enough to balance S_{nl} in the transition towards full development;

(4) using a two-component form of S_{ds} allows the prescription of dissipation rates that have a wider dynamic range at the spectral peak than at the high wavenumber spectral range. This differential behaviour of S_{ds} leads to a better agreement between model results and observations at several development stages, including fully-developed seas.

A general saturation-dependent dissipaton function [equation (5.7) of Chapter 5] was developed to provide estimates of dissipation rates at all ranges of the wave spectrum, on the basis of a nonlinear dependence of S_{ds} on a spectral saturation parameter. The following conclusions may be drawn from experiments made with this extended form of S_{ds}:

(1) the nonlinear dependence of S_{ds} on the local azimuthally-integrated saturation spectrum generates predictions of integral spectral parameters that agree closely with both observations of fetch-limited wind-wave evolution and fully-developed seas;

(2) a general form of S_{ds} that combines a dependence on the local saturation with

a weighting function proportional to the ratio $k/\overline{k}$ provides an effective method for controlling the general properties of the high wavenumber spectral tail;

(3) the inclusion of a weak dependence of S_{ds} on $E_{tot}k_p^2$ provides means of further increasing the control of properties of the spectral tail without affecting the general behaviour of S_{ds} at the spectral peak;

(4) a stronger dependence of S_{ds} on $E_{tot}k_p^2$ may cause unbounded positive S_{nl} fluxes towards the spectral peak, leading to a continued growth of integral spectral parameters beyond the full-development limits;

(5) integral spectral parameters generated with the new form of S_{ds} under different wind intensities collapse onto closely-superposed nondimensional evolution curves as predicted by the similarity theory of Kitaigorodskii (1962);

(6) dissipation parameters of the newly-proposed S_{ds} may be tuned to adjust the fit of computed integral spectral parameters to alternative parametrisations of fetch-limited evolution curves and/or fully-developed limits;

(7) the new form of S_{ds} may be successfully used in combination with several commonly-used forms of S_{in};

(8) background dissipation rates of low wavenumber spectral components estimated by the new form of S_{ds} show qualitative agreement with observations of swell decay.

An analysis of the new saturation-dependent form of S_{ds} and of the dissipation source terms used in the WAM model (Cycles 3 and 4) reveals that:

(1) the new saturation-dependent S_{ds} provides evolution curves of integral spectral parameters that agree more closely with fetch-limited observations and have more flexibility in controlling properties of the spectral tail;

(2) the form of S_{ds} used in the WAM Cycle 4 model provides more tuning flexibility when compared to the previous dissipation source function of the WAM Cycle 3 model, resulting in a closer agreement of computed integral spectral parameters with fetch-limited observations;

(3) computed properties of the high wavenumber range in spectra generated in runs using the new saturation-dependent form of S_{ds} provides improved agreement with empirical data compared with results from runs using the WAM Cycle 4 form of S_{ds};

(4) all forms of S_{ds} generate spectra with directional spreading that is narrower at the spectral peak and wider at the high wavenumber spectral range, which is generally consistent with observations. Nevertheless, computed mean values of angular spreading width generated by all forms of S_{ds} differ significantly from observations for most development stages.

B. Operational hindcasts of wind-waves

Numerical experiments with an operational implementation of the WAM model were made to demonstrate the potential benefits of using the newly-proposed saturation-dependent form of S_{ds} in wind-wave forecasting applications. Results of these experiments provide the following conclusions:

(1) simulations of fetch-limited wind-wave evolution made with an implementation

of the new saturation-dependent form of S_{ds} in the WAM model, which uses a parametrisation of S_{nl} based on the DIA, confirm the good overall results obtained with the exact nonlinear model of for S_{nl};

(2) a more accurate analysis and the proper specification of spectral dissipation rates for operational applications still depends heavily on improving the parametrisation of S_{nl};

(3) the DIA form of S_{nl} produces fetch-limited spectra that are much broader than corresponding spectra computed with the exact form of S_{nl}, leading to a significant overestimation of the spectral peak frequency f_p;

(4) changes in the specification of the dissipation source term have a profound impact on the quality of hindcasts produced by an operational wind-wave model;

(5) alternative configurations of the dissipation source term used in the WAM Cycle 3 model do not provide means of improving the quality of model hindcasts of significant wave heights;

(6) the newly-proposed saturation-dependent form S_{ds}^{bs} provides an overall improvement of hindcast of sea-states in terms of significant wave heights;

(7) discrepancies in the hindcasts of peak periods generated by model runs using the new form of S_{ds} indicate that further adjustments are needed in the specification of dissipation rates at wavenumbers lower than the spectral peak, in combination with improvements in the paramtric form of S_{nl} used in operational wind-wave models;

(8) model runs using the new form of S_{ds} provided greatly improved hindcasts of significant wave heights during severe sea-state events.

Future directions

Suggestions of future directions based on the results presented in this thesis are divided into three major areas: scientific research, operational wind-wave forecasting applications and extensions of the available observational database. Future directions within these major topics are discussed separately, as follows.

A. Research and Model Development

Simulations of the fetch-limited evolution of wind-waves using exact nonlinear models should focus on the development and validation of refined versions of the saturation-dependent form of S_{ds} aiming at:

(1) improving model predictions of the directional spreading through the introduction of a term expressing more explicitly the dependence of dissipation rates on directional properties of the wave field;

(2) increasing the control of the high wavenumber spectral tail behaviour;

(3) providing more flexibility in modelling the propagation and decay of swell systems travelling over long distances; and

(4) investigating the impact of combining these refined forms of S_{ds} with alternative parametrisations of the wind input source term, such as the forms of S_{in} proposed by Tolman and Chalikov (1996), Donelan (1999) or Makin and Kudryavtsev (1999).

B. Operational applications

Although the new dissipation source term has shown the potential to improve hindcasts of sea state within the Australian region, its impact on more recently proposed wind-wave models (e.g., WAVEWATCH-III and SWAN) should be investigated for more complex sea state scenarios. Moreover, further refinements of the general form of S_{ds} proposed in this thesis would benefit from:

(1) improved parametrisations of the nonlinear wave-wave interactions source term S_{nl},

(2) finer tuning of dissipation parameters through optimization techniques using inverse modelling or adjoint techniques; and

(3) extending its validation to a wider range of wave generation conditions, using higher quality forcing wind fields.

C. Observational database

Many of the validation analyses presented in this thesis were largely constrained by the unavailability or unreliability of observations. The success of future investigations, therefore, requires refinements of the observational database that may be achieved through

(1) increasing the available database of fetch-limited observations;

(2) refining the database of measurements of the directional spreading of the wave spectrum made with directional arrays or instruments able to measure the

directional wavenumber spectrum in more detail;

(3) generating an inventory of test cases from available state-of-the-art measurements of wind-wave evolution under a variety of scenarios including turning and adverse winds, cumulative fetches, stable and unstable atmospheric conditions, amongst others; and

(4) extending the investigation made by Snodgrass et al. (1966) on the long-distance propagation of swell using more sophisticated wave measurement instrumentation developed in recent years.

References

Al Zanaidi, M. A. and W. H. Hui (1984), 'Turbulent air flow over water waves', *J. Fluid Mech.* **148**, 225–246.

Alves, J. H .G. M., M. L. Banner and I. R. Young (2000), 'Revisiting the asymptotic limits of fully-developed seas', *J. Phys. Oceanogr.* . Submitted.

Babanin, A. V. and Y. P. Soloviev (1998), 'Variability of directional spectra of wind-generated waves, studied by means of wave staff arrays', *Mar. Freshwater Res.* **49**, 89–101.

Banner, M. L. (1990), 'Equilibrium spectra of wind waves', *J. Phys. Oceanogr.* **20**(7), 966–984.

Banner, M. L., A. V. Babanin and I. R. Young (2000), 'Breaking probability for dominant waves on the sea surface', *J. Phys. Oceanogr.* . Accepted for publication.

Banner, M. L. and D. H. Peregrine (1993), 'Wave breaking in deep water', *Annu. Rev. Fluid Mech.* **25**, 373–397.

Banner, M. L. and I. R. Young (1994), 'Modeling spectral dissipation in the evolution of wind waves. Part I: Assessment of existing model performance', *J. Phys. Oceanogr.* **24**(7), 1550–1570.

Banner, M. L., I. S. F. Jones and J. C. Trinder (1989), 'Wavenumber spectra of short gravity waves', *J. Fluid Mech.* **198**, 321–344.

Banner, M. L. and X. Tian (1998), 'On the determination of the onset of breaking for modulating surface gravity waves', *J. Fluid Mech.* **367**, 107–137.

Barnett, T. P. and J. C. Wilkerson (1967), 'On the generation of ocean wind waves as inferred by airborne radar measurements of fetch-limited spectra', *J. Marine Res.* **25**, 292–328.

Bender, L. C. (1996), 'Modification of the physics and numerics in a third-generation ocean wave model', *J. of Atmos. Oceanic Tech.* **13**(3), 726–750.

Bender, L. C. and L. M. Leslie (1994), Evaluation of a third-generation ocean wave model for the australian region, BMRC Research Report 43, Bureau of Meteorology Research Centre, Melbourne, Australia.

Booij, N., I. Haagsma and A. Kieftenburg (1998), Swan implementation manual, Technical report, Delft University of Technology.

Booij, N., L. H. Holthuijsen and R. C. Ris (1999), 'A third-generation wave model for coastal regions. 1. model description and validation', *J. Geophys. Res.* **104**((C4)), 7649–7666.

Bradford, S. F. (2000), 'Numerical simulation of surf zone dynamics', *J. Water. Port Coast. Oc. Engng.* **126**(1), 1–13.

Bretschneider, C. L. (1966), Wave generation by wind, deep and shallow water, *in* A. T.Ippen, ed., 'Estuary and coastal hydrodynamics', McGraw-Hill Book Co., New York, pp. 744–762.

Burling, R. W. (1959), 'The spectrum of waves at short fetches', *Dtsch. Hydrogr. Z.* **12**, 96–117.

Cardone, V. J., H. C. Graber, R. E. Jensen, S. Hasselmann and M. J. Caruso (1994), 'In search of the true surface wind field in SWADE IOP-1: Ocean wave modelling perspective', *Global Atm. Ocean Syst.* **3**, 107–150.

Cardone, V. J., R. E. Jensen, D. T. Resio, V. R. Swail and A. T. Cox (1996), ‘Evaluation of contemporary ocean wave models in rare extreme events: The “Halloween storm of October 1991 and the “storm of the century” of March 1993’, *J. Atm. Ocean. Tech.* **13**, 198–230.

Cavaleri, L. and P. M. Rizzoli (1981), ‘Wind wave prediction in shallow water: theory and application’, *J. Geophys. Res.* **86**, 10961–10973.

Chalikov, D. V. and M. Yu. Belevich (1993), ‘One-dimensional theory of the wave boundary layer’, *Bound. Layer Meteorol.* **63**, 65–96.

Chalikov, D. V. and V. K. Makin (1991), ‘Models of the wave boundary layer’, *Bound. Layer. Meteorol.* **56**, 83–89.

Charnock, H. (1955), ‘Wind stress on the water surface’, *Q. J. Royal Meteorol. Soc.* **81**, 639–640.

Darbyshire, J. (1959), ‘A further investigation of wind generated waves’, *Deut. Hydrograph. Z.* **12**, 1–13.

Davidan, I. N. (1996), ‘New results in wind-wave studies’, *Meteorology and Hydrology* **4**, 65–72. In Russian.

Dean, R. G. and R. A. Dalrymple (1990), *Water Wave Mechanics for Engineers and Scientists*, World Scientific, Singapore. pp.

Dobson, F. W. (1971), ‘Measurements of atmospheric pressure on wind-generated sea waves’, *J. Fluid Mech.* **48**, 91–127.

Dold, J. W. and D. H. Peregrine (1986), Water-wave modulation, *in* ‘20th International Conference on Coastal Engineering’, Vol. 103, ASCE, Taipei, pp. 163–176.

Donelan, M. A. (1982), The dependence of the aerodynamic drag coefficient on wave parameters, *in* 'Proc. 1st International Conference on Meteorological and air/sea interactions of the coastal zone', American Meteorological Society, Boston, pp. 381–387.

Donelan, M. A. (1990), Air-sea interaction, *in* 'The sea', Vol. 9 of *Ocean Engineering Sciences*, J. Wiley, New York.

Donelan, M. A. (1996), Air-water exchange processes, *in* J.Imberger, ed., 'Physical Limnology: Coastal and Estuarine Studies', American Geophysical Union.

Donelan, M. A. (1999), Wind-induced growth and attenuation of laboratory waves, *in* S. G.Sajjadi, N. H.Thomas and J. C. R.Hunt, eds, 'Wind-over-wave couplings: perspectives and prospects', University of Salford, pp. 183–194.

Donelan, M. A., F. W. Dobson, S. D. Smith and R. J. Anderson (1993), 'On the dependence of sea surface roughness on wave development', *J. Phys. Oceanogr.* **23**, 2143–2149.

Donelan, M. A., J. Hamilton and W. H. Hui (1985), 'Directional spectra of wind-generated waves', *Phil. Trans. R. Soc. Lond.* **A315**, 509–562.

Donelan, M. A., M. Skafel, H. C. Graber, P. Liu, D. Schwab and S. Venkatesh (1992), 'On the growth rate of wind-generated waves', *Atmosphere-Ocean* **30**, 457–478.

Donelan, M. A. and W. J. Pierson (1987), 'Radar scattering and equilibrium ranges in wind-generated waves with application to scatterometry', *J. Geophys. Res.* **92**(C5), 4971–5029.

Donelan, M. A., W. M. Drennan and A. K. Magnusson (1996), 'Nonstationary analysis of the directional properties of propagating waves', *J. Phys. Oceanogr.* **26**, 1901–1914.

Donelan, M. A. and Y. Yuan (1994), Wave dissipation by surface processes, *in* G. J. Komen et al., ed., 'Dynamics and modelling of wind waves', Cambridge University Press, Cambridge, pp. 143–155.

Donelan, Mark A., M. S. Longuet-Higgins and J. S. Turner (1972), 'Periodicity in whitecaps', *Nature* **239**, 449–451.

Ebuchi, N., H. Kawamura and Y. Toba (1992), 'Growth of wind waves with fetch observed by the GEOSAT altimeter in the Japan Sea during winter monsoon', *J. Phys. Oceanogr.* **97**, 809–819.

Ewing, J. A and A. K. Laing (1987), 'Directional spectra of seas near full development', *J. Phys. Oceanogr.* **17**, 1696–1706.

Fabrikant, A. L. (1976), 'Quasilinear theory of wind wave generation', *Izv. Atmos. Ocean. Phys.* **12**, 524–526.

Garratt, J. R. (1992), *The atmospheric boundary layer*, University Press, Cambridge. 316pp.

Gelci, R., H. Cazalé and J. Vassal (1957), 'Prévision de la houle. La méthode des densités spectroangulaires', *Bull. Inf. Comité Central Océnogr. Etude Côtes* **8**, 416–435.

Gent, P. R. and P. A. Taylor (1976), 'A numerical model of the flow above water waves', *J. Fluid Mech.* **77**, 105–128.

Glazman, R. E. (1994), 'Surface gravity waves at equilibrium with steady wind', *J. Geophys. Res.* **99**(C3), 5249–5262.

Greenslade, D. (2001), 'The assimilation of ERS-2 significant wave height data in the Australian region', *J. Mar. Systems* **28**, 141–160.

Günther, H., S. Hasselmann and P. A. E. M. Janssen (1992), The WAM model Cycle 4, Technical Report 4, German Climate Research Center - DKRZ, Hamburg.

Hasselmann, D. E. and Bösenberg (1991), 'Field measurements of wave-induced pressure over wind-sea and swell', *J. Fluid Mech.* **230**, 391–428.

Hasselmann, D. E., M. Dunckel and J. A. Ewing (1980), 'Directional wave spectra observed during JONSWAP 1973', *J. Phys. Oceanogr.* **10**(8), 1264–1280.

Hasselmann, K. (1962), 'On the nonlinear energy transfer in a gravity-wave spectrum. Part 1: General theory', *J. Fluid Mech.* **12**, 481–500.

Hasselmann, K. (1974), 'On the spectral dissipation of ocean waves due to white-capping', *Bound. Layer Meteor.* **6**, 107–127.

Hasselmann, K., D. B. Ross, P. Müller and W. Sell (1976), 'A parametric wave prediction model', *J. Phys. Oceanogr.* **6**, 200–228.

Hasselmann, K., T. P. Barnett, E. Bouws, H. Carlson, D. E. Cartwright, K. Enke, J. A. Ewing, H. Gienapp, D. E. Hasselmann, P. Kruseman, A. Meerburg, P. Müller, D. J. Olbers, K. Richter, W. Sell and H. Walden (1973), 'Measurements of wind-wave growth and swell decay during the joint North Sea wave project (JONSWAP)', *Dtsch. Hydrogh. Z. Suppl. A* **8**(12), 1–95.

Hasselmann, S. and K. Hasselmann (1981), 'A symmetrical method of computing the nonlinear transfer in a gravity-wave spectrum', *Hamb. Geophys. Einzelschr.* **52**, 1–138.

Hasselmann, S. and K. Hasselmann (1985), 'Computations and parameterizations of the nonlinear energy transfer in a gravity-wave spectrum. Part 1: a new method for efficient computations of the nonlinear transfer integral', *J. Phys. Oceanogr.* **15**, 1369–1377.

Hasselmann, S., K. Hasselmann, E. Bauer, Janssen P. A. E. M., G. I. Komen, L. Bertotti, P. Lionello, A. Guillaume, V. Cardone, J. A. Greenwood, M. Reistad, L. Zambresky and J. A. Ewing (1988), 'The WAM model – a third generation ocean wave prediction model', *J. Phys. Oceanogr.* **18**(12), 1775–1810.

Hasselmann, S., K. Hasselmann, J. H. Allender and T. P. Barnett (1985), 'Computations and parameterizations of the nonlinear energy transfer in a gravity-wave spectrum. Part 2: Parameterizations of the nonlinear energy transfer for applicaitons in wave models', *J. Phys. Oceanogr.* **15**, 1378–1391.

Hersbach, H. (1998), 'Application of the adjoint of the WAM model to inverse wave modeling', *J. Geophys. Res.* **103(C5)**, 10469–10487.

Holland, G., A. H. Lynch and L. Leslie (1987), 'Australian east-coast cyclones. Part I: Synoptic overview and case study', *Mon. Weath. Rev.* **115**, 3024–3036.

Holthuijsen, L. H. and T. H. C. Herbers (1986), 'Statistics of breaking waves observed as whitecaps in the open sea', *J. Phys. Oceanogr.* **16**(2), 290–297.

Holthuijsen, L., R. C. Ris, N. Booij and E. Cecchi (2000), Swell and whitecapping, *in* '27th International Conference on Coastal Engineering (Abstracts)', Vol. 1, ASCE, Sydney.

Hsiao, S. V. and O. H. Shemdim (1983), 'Measurements of wind velocity and pressure with a wave follower during MARSEN', *J. Geophys. Res.* **88**, 9841–9849.

Huang, N. E., S. R. Long, C. Tung, Y. Youen and L. Bliven (1981), 'A unified teo-parameter wave spectral model for a general sea state', *J. Fluid Mech.* **112**, 203–224.

Janssen, P. A. E. M. (1989), 'Wave-induced stress and the drag of air flow over sea waves', *J. Phys. Oceanogr.* **19**, 745–754.

Janssen, P. A. E. M. (1991), 'Quasi-linear theory of wind-wave generation applied to wave forecasting', *J. Phys. Oceanogr.* **21**, 1631–1642.

Janssen, P. A. E. M. (1994), Wave growth by wind, *in* G. J. Komen et al., ed., 'Dynamics and modelling of wind waves', Cambridge University Press, Cambridge, pp. 71–112.

Janssen, P. A. E. M., G. J. Komen and W. J. P. Voogt (1987), 'Friction velocity scaling in wind-wave generation', *Boundary Layer Meterol.* **38**, 29–35.

Jonsson, I. G. (1990), Wave-current interactions, *in* B.Le Mehaute and D. M.Hanes, eds, 'The Sea (9): Ocean Engineering Science', Wiley and Sons, pp. 65–120.

Kahma, K. (1981), 'A study of the growth of the wave spectrum with fetch', *J. Phys. Oceanogr.* **11**, 1502–1515.

Kahma, K. and C. J. Calkoen (1992), 'Reconciling discrepancies in the observed growth of wind-generated waves', *J. Phys. Oceanogr.* **22**, 1389–1405.

Kahma, K. and C. J. Calkoen (1994), Growth curve observations, *in* G. J. Komen et al., ed., 'Dynamics and modelling of wind waves', Cambridge University Press, Cambridge, pp. 143–155.

Katsaros, K. B., S. D. Smith and W. A. Oost (1987), 'HEXOS - Humidity Exchange Over the Seas. a program for research on water-vapor and droplet fluxes from sea to air at moderate to high wind speeds', *Bull. Amer. Meteor. Soc.* **68**, 466–476.

Kitaigorodskii, S. A. (1962), 'Application of the theory of similarity to the analysis of wind-generated water waves as a stochastic process', *Bull. Acad. Sci. USSR, Geophys. Ser.* **1**, 1–73.

Kitaigorodskii, S. A. (1973), *The physics of air-sea interactions*, Israel Program for Scientific Translations, Jerusalem.

Kolaini, A. R. and M. P. Tulin (1995), 'Laboratory measurements of breaking inception and post-breaking dynamics of steep short-crested waves', *Int. J. Offsh. Polar Engng.* **5**(3), 212–218.

Komen, G. J., L. Cavaleri, M. Donelan, K. Hasselmann, S. Hasselmann and P. A. E. M. Janssen (1994), *Dynamics and modelling of ocean waves*, Cambridge University Press, New York. 532pp.

Komen, G. J., S. Hasselmann and K. Hasselmann (1984), 'On the existence of a fully developed wind-sea spectrum', *J. Phys. Oceanogr.* **14**(8), 1271–1285.

Kuik, A. J., G. Ph. van Vledder and L. H. Holthuijsen (1988), 'A method for the routine analysis of pitch-and-roll buoy wave data', *J. Phys. Oceanogr.* **18**, 1020–1034.

Lavrenov, I.V. and F. J. Ocampo-Torres (1999), Non-linear energy transfer to the spectrum of waves opposite to wind direction, *in* M. L.Banner, ed., 'Air-sea interface: wave dynamics and turbulence; electromagnetic and acoustic sensing', University of New South Wales, Sydney.

Lewis, A. W. and R. N. Allos (1990), 'JONSWAP's parameters: sorting out inconsistencies', *Ocean Engng.* **17**, 409–415.

Lin, P. Z., K. A. Chang and P. L. F. Liu (1999), 'Runup and rundown of solitary waves on sloping beaches', *J. Water. Port Coast. Oc. Engng.* **125**(5), 247–255.

Lin, R. (1998), 'Comments on "the Goddard coastal wave model": Reply', *J. Phys. Oceanogr.* **28**, 1291–1318.

Lin, R. Q. and N. E. Huang (1996*a*), 'The Goddard coastal wave model. Part I: Numerical method', *J. Phys. Oceanogr.* **26**(6), 833–847.

Lin, R. Q. and N. E. Huang (1996*b*), 'The Goddard coastal wave model. Part II: Kinematics', *J. Phys. Oceanogr.* **26**(6), 848–862.

Liu, P. C. and D. B. Ross (1980), 'Airborne measurements of wave growth for stable and unstable atmospheres in Lake Michigan', *J. Phys. Oceanogr.* **10**, 1842–1853.

Liu, P. L. F., P. Z. Lin, K. A. Chang and T. Sakakiyama (1999), 'Numerical modeling of wave interaction with porous structures', *J. Water. Port Coast. Oc. Engng.* **125**(6), 322–330.

Longuet-Higgins, M. S. (1984), 'Statistical properties of wave groups in a random sea state', *Phil. Trans. R. Soc. Lond.* **A 312**, 219–250.

Longuet-Higgins, M. S., D. E. Cartwright and N. D. Smith (1963), Observations of the directional spectrum of sea waves using the motions of a floating buoy, *in* 'Ocean Wave Spectra', Englewood Cliffs, New York, pp. 111–136.

Longuet-Higgins, M. S. and E. D. Cokelet (1976), 'The deformation of steep surface waves on water. Part 1: A numerical method of computation', *Proc. Roy. Soc. London* **A358**, 1–26.

Maat, N., C. Kraan and W. A. Oost (1991), 'On the roughness of wind waves', *Boundary Layer Meterol.* **54**, 89–103.

Makin, V. K. and D. V. Chalikov (1979), 'Numerical modeling of air structure above waves', *Izv. Atmos. Ocean Phys.* **15**, 199–204.

Makin, V. K. and V. N. Kudryavtsev (1999), 'Coupled sea surface-atmosphere model. Part 1. Wind over waves coupling', *J. Geophys. Res.* **104**((C4)), 7613–7623.

Makin, V. K., V. N. Kudryavtsev and C. Mastenbroek (1995), 'Drag of the sea surface', *Bound. Layer Meteor.* **73**, 159–182.

Masuda, A. (1981), 'Nonlinear energy transfer between wind waves', *J. Phys. Oceanogr.* **10**(12), 2082–2093.

Mei, C. C. (1983), *The Applied Dynamics of Ocean Surface Waves*, John Wiley and Sons.

Melville, W. K. (1996), 'The role of surface-wave breaking in air-sea interaction', *Annu. Rev. Fluid Mech.* **26**, 279–321.

Miles, J. W. (1957), 'On the generation of surface waves by shear flows', *J. Fluid Mech.* **3**, 185–204.

Mitsuyasu, H. (1966), Interactions between water waves and wind, Report of the Research Institute of Applied Mechanics 14, Kyushu University.

Mitsuyasu, H. (1968), 'On the growth of the spectrum of wind-generated waves', *Rep. Res. Inst. Appl. Mech. Kyushu University* **16**, 251–264.

Mitsuyasu, H., F. Tasai, T. Suhara, S. Mizuno, M. Okhuso, T. Honda and K. Rikiishi (1975), 'Observations of the directional spectrum of ocean waves using a cloverleaf buoy', *J. Phys. Oceanogr.* **5**, 750–760.

Monbaliu, J. and S. Hasselmann (1994), Optimization of the WAM source functions by direct cost function minimization, *in* G. J. Komen et al., ed., 'Dynamics and modelling of wind waves', Cambridge University Press, Cambridge, pp. 442–447.

Moskowitz, L. (1964), 'Estimates of the power spectrums for fully-developed seas for wind speeds of 20 to 40 knots', *J. Geophys. Res.* **69**, 5161–5179.

Müller, P. (1976), 'Parameterizations of one-dimensional wind-wave spectra and their dependence on the state of development', *Hamburger Geophysikalische Einzelschriften* **31**, 1–177.

Mutsuda, H. and T. Yasuda (2000), Physical mechanisms based on numerical simulations of strongly turbulent air-water mixiing layer within surf-zone, Proceedings, Int. Conf. Coast. Engng., Sydney, Australia.

Nepf, H. M., C. H. Wu and E. S. Chan (1998), 'A comparison of two- and three-dimensional wave breaking', *J. Phys. Oceanogr.* **28**, 1496–1510.

NMOC (1986), Implementation of spectral sea-state models, H. O. Publ. 5, National Meteorological Operations Centre, Australian Bureau of Meteorology, Melbourne.

Phillips, O. M. (1957), 'On the generation of waves by turbulent wind', *J. Fluid Mech.* **2**, 426–434.

Phillips, O. M. (1958), 'The equilibrium range in the spectrum of wind-generated ocean waves', *J. Fluid Mech.* **107**, 465–485.

Phillips, O. M. (1960), 'The dynamics of unsteady gravity waves of finite amplitude', *J. Fluid Mech.* **9**, 193–217.

Phillips, O. M. (1966), *The dynamics of the upper ocean*, Cambridge University Press, London. 265pp.

Phillips, O. M. (1981), 'Wave interactions - the evolution of an idea', *J. Fluid Mech.* **106**, 215–227.

Phillips, O. M. (1984), 'On the response of short ocean wave components at a fixed wavenumber to ocean current variations', *J. Phys. Oceanogr.* **14**, 1425–1433.

Phillips, O. M. (1985), 'Spectral and statistical properties of the equilibrium range in wind-generated gravity waves', *J. Fluid Mech.* **156**, 505–531.

Phillips, O. M. and M. L. Banner (1974), 'Wave breaking in the presence of wind drift and swell', *J. Fluid Mech.* **66**, 625–640.

Pierson, W. J. (1964), 'The interpretation of wave spectrums in terms of the wind profile instead of the wind measured at a constant height', *J. Geophys. Res.* **69**, 5191–5203.

Pierson, W. J. (1991), 'Comment on "Effects of sea maturity on satellite altimeter measurements"', *J. Geophys. Res.* **96(C3)**, 4973–4977.

Pierson, W. J., G. Neumann and R. James (1955), Practical methods for observing and forecasting ocean waves by means of wave spectra and statistics, H. O. Publ. 603, U. S. Navy Hydrographic Office.

Pierson, W. J. and L. Moskowitz (1964), 'A proposed spectral form for fully-developed wind seas based on the similarity theory of A. A. Kitaigorodskii', *J. Geophys. Res.* **69**, 5181–5190.

Plant, W. J. (1982), 'A relationship between wind stress and wave slope', *J. Geophys. Res.* **87**, 1961–1967.

Polnikov, V. G. (1994), 'Numerical modelling of flux spectra formation for surface gravity waves', *J. Fluid Mech.* **278**, 289–296.

Puri, K., G. S. Dietachmayer, G. A. Mills, N. E. Davison, R. A. Bowen and L. W. Logan (1998), 'The new BMRC limited area prediction system', *Aust. Met. Mag.* **47**, 203–233.

Rapp, R. J. and W. K. Melville (1990), 'Laboratory measurements of deep-water breaking waves', *Phil. Trans. R. Soc. Lond.* **A331**, 735–800.

Resio, D. T.and V. R. Swail, R. E. Jensen and V. J. Cardone (1999), 'Wind speed scaling in fully-developed seas', *J. Phys. Oceanogr.* **29**, 1801–1811.

Resio, D. and W. Perrie (1991), 'A numerical study of nonlinear energy fluxes due to wave-wave interactions. Part 1. Methodology and basic results', *J. Fluid Mech.* **223**, 603–629.

Riley, D. S., M. A. Donelan and W. H. Hui (1982), 'An extended miles' theory for wave generation by wind', *Bound. Layer Meteorol.* **22**, 209–225.

Ris, R. C. (1997), Spectral modelling of wind waves in coastal areas, Communications on Hydraulic and Geotechnical Engineering 97-4, Technical University of Delft, Delft.

Ross, D. B. (1978), On the use of aircraft in the observation of one- and two-dimensional ocean wave spectra, *in* M. D.Earle and A.Malahoff, eds, 'Ocean Wave Climate', Plennum Press, pp. 253–267.

Schneggenburger, C, . (1998), Spectral wave modelling with nonlinear dissipation, Phd dissertation, GKSS-Forschungszentrum Geesthacht GmbH, Hamburg.

Seaman, R, W. Bourke, P. Steinle, T Hart, G. Embery, M. Naughton and L. Rikus (1995), 'Evolution of the Bureau of Meteorology's global assimilation and prediction system. Part 1: analyses and initialization', *Aust. Met. Mag.* **44**, 1–18.

She, K., C. A. Greated and W. J. Easson (1997), 'Experimental study of three-dimensional breaking wave kinematics', *Appl. Oc. Res.* **19**, 329–343.

Shen, Z. and L. Mei (1993), 'Equilibrium spectra of water waves forced by intermittent wind turbulence', *J. Phys. Oceanogr.* **23**, 2019–2026.

Snodgrass, F. E., G. W. Groves, K. F. Hasselmann, G. R. Miller, W. H. Munk and W. H. Powers (1966), 'Propagation of swell across the pacific', *Trans. Roy. Soc. London* **A259**, 431–497.

Snyder, R. L. (1974), 'A field study of wave-induced pressure fluctuation above surface gravity waves', *J. Marine Res.* **32**, 497–531.

Snyder, R. L. and C. S. Cox (1966), 'A field study of the wind generation of ocean waves', *J. Marine Res.* **24**, 141–178.

Snyder, R. L., F. W. Dobson, J. A Elliot and R. B. Long (1981), 'Array measurements of atmospheric pressure fluctuations above surface gravity waves', *J. Fluid Mech.* **102**, 1–59.

Snyder, R. L. and R. M. Kennedy (1983), 'On the formation of whitecaps by a threshold mechanism. Part I: Basic formalism', *J. Phys. Oceanogr.* **13**, 1482–1518.

Sobey, R. J. and I.R. Young (1986), 'Hurricane wind waves: A discrete spectral model', *J. Waterways, Port, Coast. Ocean Engng.* **112**, 370–389.

Sverdrup, H. V. and W. H. Munk (1947), Wind sea and swell: Theory of relation for forecasting, Hydrographic Office Publication 601, U. S. Navy.

SWAMP (1985), *Ocean wave modeling*, Plennum Press, New York.

Toba, Y. (1973), 'Local balance in the air-sea boundary process', *J. Oceanogr. Soc. Japan* **29**, 209–220.

Tolman, H. L. (1992), 'Effects of numerics on the physics in a third generation wind-wave model', *J. Phys. Oceanogr.* **22**(10), 1095–1111.

Tolman, H. L. (1997), User manual and system documentation of WAVEWATCH-III, version 1.15, Technical report, NCEP/NOAA, Washington D. C.

Tolman, H. L. and D. Chalikov (1996), 'Source terms in a third-generation wind wave model', *J. Phys. Oceanogr.* **26**(11), 2497–2518.

Tolman, H. L., L. C. Bender and W. L. Neu (1998), 'Comments on "the Goddard coastal wave model"', *J. Phys. Oceanogr.* **28**, 1291–1318.

Tracy, B. A. and D. T. Resio (1982), Theory and calculation of the nonlinear energy transfer between sea waves in deep water, WIS Report 11, US Army Engineer Waterways Experiment Station, Washington, D.C.

Tucker, M. J. (1991), *Waves in ocean engineering*, Ellis Horwood, London.

Van Vledder, G. Ph., T. H. C. Herbers, R. E. Jensen, D. T. Resio and B. Tracy (2000), Modelling of nonlinear quadruplet wave-wave interactions in operational coastal wave models, *in* 'Proc. 27th Int. Conf. Coast. Eng.', ASCE. in press.

Walsh, E. J., D. W. Hancock III, D.E Hines, R. N. Swift and J. F Scott (1989), 'An observation of the directional wave spectrum evolution from shoreline to fully developed', *J. Phys. Oceanogr.* **19**, 670–690.

Watson, K. M. and B. J. West (1975), 'A transport-equation description of nonlinear ocean surface wave interactions', *J. Fluid Mech.* **70**, 815–826.

Webb, D. J. (1978), 'Nonlinear transfers between sea waves', *Deep-sea Res.* **25**, 279–298.

Wiegel, R. L. (1963), Some engineering aspects of wave spectra, *in* 'Ocean Wave Spectra', Prentice-Hall, New York, pp. 309–321.

Wu, C. H. and H. M. Nepf (2000), 'Breaking criteria and energy losses for three-dimensional wave breaking'. unpublished.

Wu, J. (1982), 'Wind-stress coefficients over the sea surface from breeze to hurricane', *J. Geophys. Res.* **87 (C12)**, 9704–9706.

Yan, L. (1987), An improved wind input source term for third generation ocean wave modelling, Scientific Report WR-87-8, Royal Netherlands Meteorological Institute-KNMI.

Young, I. R. (1988), A parametric model for tropical cyclone waves, Research Report 28, Australian Defence Force Academy.

Young, I. R. (1989), 'Wave transformation over coral reefs', *J. Geophys. Res.* **94 (C7)**, 9779–9789.

Young, I. R. (1995), 'The determination of confidence limits associated with estimates of the spectral peak frequency', *Ocean Engng.* **22**, 669–686.

Young, I. R. (1999), *Wind generated ocean waves*, Oxford-Elsevier, Amsterdam.

Young, I. R. and G. Holland (1996), *Atlas of the oceans: wind and wave climate*, Pergamon Press.

Young, I. R. and G. Ph. Van Vledder (1993), 'A review of the central role of nonlinear interactions in wind-wave evolution', *Phil. Trans. R. Soc. Lond.* **342**, 505–524.

Young, I. R. and L. A. Verhagen (1996), 'The growth of fetch limited waves in water of finite depth. Part 1: total energy and peak frequency', *Coastal Engng.* **29**, 47–78.

Zakharov, V. E. (1968), 'Stability of periodic waves of finite amplitude on the surface of a deep fluid', *J. Appl. Mech. Techn. Phys.* **9**, 190–194.

List of Tables

List of Figures

List of Symbols

Lowercase Greek

α Phillips' parameter

$\overline{\alpha}_B$ mean spectral tail level

γ nondimensional growth rate

ϵ relative spectral tail level

η sea-surface elevation

ι peak enhancement exponent

λ wavelength

ρ fluid densities

ϕ velocity potential

$\overline{\varphi}$ frequency spectrum

ω angular frequency

$\hat{\alpha}$ integral spectral steepness

β growth rate parameter

δ linear combination parameter

ε nondimensional total energy

θ direction

κ von Karman constant

ν nondimensional peak frequency

τ seas surface stress

φ directional frequency spectrum

χ nondimensional fetch

$\daleth$ peak enhancement factor

Lowercase Arabic

a wave amplitude

c wave phase speed

g gravity acceleration

m,n generic exponents

p,s generic exponents

u_* friction velocity

x,y,z spatial dimensions

b_T breaking probability

c_g wave group velocity

$\mathbf{k}$,k wavenumber vector and scalar

$\overline{n}_B$ mean spectral tail slope

t time

u_{**} sea-state-dependent u_*

Uppercase Greek

Γ breaking crest per unit area

Υ wind input parameter

Φ frequency wavenumber spectrum

Uppercase Arabic

B saturation spectrum

C generic proportionality constant

C_D drag coefficient

D directional distribution function

E_{tot} total energy

F wavenumber spectrum

H_s significant wave height

Q strength of breaking

N action density

S source terms

T_p dominant wave period

U wind speed

X wind fetch